Alma Mater Studiorum – Università di Bologna

DOTTORATO DI RICERCA IN

Ingegneria Civile, Chimica, Ambientale e dei Materiali

Ciclo **XXXII**

Settore Concorsuale: 08A1

Settore Scientifico disciplinare: ICAR/01

Numerical modelling and structural optimization of multifunctional maritime structures aimed to protect harbours and produce energy

Presentata da: Giuseppina Palma

Coordinatore Dottorato	**Supervisore**
Prof. Ing. Luca Vittuari	Prof. Barbara Zanuttigh
	Co – Supervisore
	Ing. Juan Carlos Alcerreca

Esame finale anno 2020

Acknowledgements

I would not be able to perform and complete this PhD work, without the help and the support of many persons that I would like to acknowledge.

Firstly, I would like to thank my Prof. Barbara Zanuttigh. If I had not met her, I would not be able to do all the things that I did in these past years. I am infinitely grateful for the opportunities, the responsibilities and the trust that her gave to me over these years. Her support and esteem were fundamental to me to face the challenges that I met. I would like also to thank my colleague Sara for the advices, the support and the strong collaboration that we developed during this period.

During my PhD, I had the opportunity to spend 3 months in Chetumal (Mexico), conducting my research at the ECOSUR company, under the supervision of the Dr. Juan Carlos Alcerreca. It was the best experience of my life. I learnt so much and not only from a professional point of view. I am very grateful to him for the time he dedicated to me and the encouragement that I always found in his words.

There are not the right words to thank my family. My parents and my sister were, are and always will be my pillars. They continuously gave me the strength and the opportunity to do whatever I wanted to do with limitless understanding and patience. Thank you.

I have also to thank the family that I met in Bologna, my friends. If I had not known them, probably I would not be here. In this big family, there are people who are not or not anymore in this city, but despite this they have always been close to me. I am deeply grateful to the ones who were constantly beside me and I would like also to thank the ones that shared just part of this journey with me. Without them, I would not be the person that I am today.

Abstract

The increasing number of extreme events and the sea level rise due to climate change have recently posed new challenges to the design of coastal structures. The design has also to face the increasing environmental impacts due to the extremely high anthropic pressure and to seek the social acceptance to maintain and eventually boost the recreational use. The design of coastal structures has therefore to be resilient, ecologically friendly and socially attractive. To achieve these goals, innovative designs have been developed, a. o. the design of multifunctional structures such as Wave Energy Converters (WECs) for coastal and harbour defence. These hybrid systems ensure the proper safety level by reducing the wave actions at the inshore area, while capturing wave energy to be converted for local use and/or storage. The nearshore location of such systems allows to decrease the construction, maintenance and energy transfer costs, with respect to offshore installations. However, these systems still require design optimisation and therefore a combined analysis of their hydraulic and structural performance is of paramount relevance.

The main objective of this PhD thesis is to optimize a specific multifunctional maritime structure for harbour protection and energy production, named Overtopping Breakwater for Energy Conversion (OBREC), developed by the team of the University of Campania. This device is provided with a sloping plate followed by a unique reservoir, which is linked with the machine room (where the energy conversion occurs) by means of a pipe passing through the crown wall, provided with a parapet on top of it. Therefore, the potential energy of the overtopping waves, collected inside the reservoir located above the still water level, is then converted by means of low – head turbines.

In order to improve the understanding of the wave – structure interactions with OBREC, several methodologies have been used and combined together:
  i.   analysis of recent experimental campaigns on wave overtopping discharges and pressures at the crown wall on small – scale OBREC cross sections, carried out in other laboratories by the team of the University of Campania;
  ii. new experiments on cross sections similar to the OBREC device, planned and carried out in the hydraulic lab at the University of Bologna in the framework of this PhD work;
  iii. numerical modelling with a 1 – phase incompressible fluid model IH – 2VOF, developed by the University of Cantabria, and with a 2 – phase incompressible fluid model OpenFOAM, both available from the literature;
  iv. numerical modelling with a new 2 – phase compressible fluid model developed in the OpenFOAM environment within this PhD work;
  v.   analysis of the data gained from the monitoring of the OBREC prototype installation.

The analysis of the experimental data at small scale available from the literature and the numerical modelling performed with the 1 – phase IH – 2VOF code prompted the definition of some fundamental guidelines for the design of the prototype to be installed in the port of Naples. The numerical results suggest the introduction of a submerged quasi – vertical part in the frontal part of the sloping plate, without compromising its hydraulic performance in terms of overtopping discharge rates inside the reservoir. The double inclination improves i) the ramp resistance to bending and to fatigue, and ii) the interlocking between the rocks of the armour layer and the device, leading to a more general cross section, which can be easily installed on top of existing breakwaters. The reservoir width does not strongly affect the hydraulic and structural

performance. Therefore, its selection can be subordinated to the height of the sloping plate, which has to be tuned on the specific site of installation. The presence of the parapet is fundamental to guarantee the harbour safety at the inshore area of the structure. An angle of 45° is capable of maximizing its effectiveness that increases as the dimension of the reservoir width decreases, ensuring an adequate safety level even if the site – specific spatial constraints does not allow the implementation of a wide reservoir.

The new laboratory campaign at the University of Bologna was planned to investigate on the crown wall shape, by testing simple dikes provided with crown walls with and without parapets. A simple smooth geometry was preferred to the complex OBREC cross section to reduce the parameters under analysis and focus on the discharges and wave loads acting along the crown walls. Furthermore, specific objective was also to improve the knowledge about the role of the entrapped air during the wave impacts, in case of breaking and non – breaking waves. A qualitative analysis of the pressure distributions along the crown walls verified that the nature and the magnitude of the impact loads and the shape of the pressure signal consequent to the wave impact are strongly dependent on the breaker type and the amount of air pockets entrapped.

In case of breaking/broken waves, the increasing of the crest width significantly contribute to reduce the magnitude of the impacts, which are more severe in presence of a parapet. This latter dynamic is more pronounced in case of non – breaking waves, were the effect of crest width is negligible.

With the purpose of replicating and extending these experimental data, a new solver that represents the compressibility of the fluids, has been developed in the openFOAM environment. It has been compiled to account for the presence of both porous and impermeable obstacles. The comparison of the results with the corresponding incompressible solver show that the fluid compressibility increases the magnitude of the pressures during the wave impact. However, both the numerical models tend to underestimate the laboratory results, but the discrepancy characterizing the incompressible solver is much bigger than the one associated to compressible one, i.e. 62 vs. 34% and 26% vs. 4% for the maximum and the statistical values, respectively. Therefore, the new compressible solver could represent a valuable tool for the analysis of the structural response of traditional, but even more complicated coastal structures.

The gathered field data (incident waves, pressures on the slope and crown wall) at prototype highlighted the differences between the small – scale tests and the performance in the real environment. The qualitative analysis of the pressure signals, in the latter case, show high – aeration conditions during the wave – structure interactions, which could enhance the loads with respect to the small – scale results.

The multiphase code openFOAM, and specifically the toolbox *waves2foam,* was adopted to compare the numerical results with the monitored data of the prototype under a real monitored storm. The numerical prototype has been tested also under the typical wave climate of the installation site, to assess the ordinary hydraulic and the structural performance of the device. The analysis performed were useful to give an indication about how to maximize the operational time and an estimation of the available hydraulic head. These information are useful for the selection of the suitable turbine, to maximize the energy production.

Table of Contents

List of Notations

$a, b\ c$	-	Darcy-Forchheimer and Polubarinova-Kochina coefficients
A_c	m	Freeboard of a dike
B_r	m	Reservoir width
B_s	m	Longitudinal extension of the sloping plate
c_A	-	Added mass coefficient
D_{50}	m	Nominal rock diameter
d_w	m	Height of the sloping plate
f_p	Hz	Peak frequency
Fr	-	Frequency of occurrence of a specific wave condition
g	m/s^2	Gravity acceleration
H	m	Wave height
h	m	Water depth
H_{m0}	m	Zero moment wave height
H_{max}	m	Maximum wave height
h_n	m	Parapet height
H_s	m	Significant wave height
h_{tot}	m	Total hydraulic head
h_w	m	Wall height
K_r	-	Reflection coefficient
L	m	Wave lenght
N	-	Number of waves
n	-	Porosity
n_{vec}	-	Normal vector
P	-	Permeability
p_{100}	Pa	Statistical pressure, representing the non – exceedance level of 90%
p_{250}	Pa	Statistical pressure, representing the non – exceedance level of 99.7%
$Pabs$	kW/m	Energy flux per unit of wave – crest length
p_{dyn}	Pa	Dynamic pressure
$p_{h,q}$	pa	Quasi hydrostatic pressure
p_{max}	Pa	Maximum pressure
p_{stat}	Pa	Quasi static pressure
p_{tot}	Pa	Total pressure
$P_{turbine,nom}$	kW	Theoretical nominal power of the turbine
$P_{turbine,ws}$	kW	Theoretical power produced in a year (according to a specific sea state)
$P_{turbine,year}$	kWh	Absolute theoretical estimation of the yearly produced power
P_{year}	kW/m	Energy flux per unit of wave – crest length in a year
Q	m^3/s	Prototype scale discharge rate
q	m^3/s or l/s	Small scale test Discharge rate per unit length
R_c	m	Freaborad OBREC rear wall
R_r	m	Freaborad OBREC sloping plate
S	-	Coeffiecient of damage
$s_{m-1,0}$	-	Wave steepness
T	s	Wave period
t	s	Time
$T_{\%full}$	-	Percentage of time in which the OBREC pipe works in saturated condition

t_A	s	Compression time
t_D	s	Duration of the impact
t_E	s	Expansion time
T_m	s	Mean wave period
T_p	s	Peak wave period
t_{stat}	s	Time to reach the quasi static pressure
t_{stat2}	s	Time to decay from the quasi static pressure
U	m/s	Velocity
U_r	m/s	Compression velocity
α	°	Offshore slope angle
α_F	-	Linear friction coefficient
β_F	-	Non linear friction coefficient
γ	-	Peak enhancement factor in JONSWAP spectrum
γ_b	-	Berm influence factor
γ_f	-	Roughness influence factor
γ_β	-	Oblique wave influence factor
ε	°	Parapet angle
θ_m	°	Wave direction
κ	-	Curvature of the interface
λ	-	Ratio h_n/h_w
μ_{eff}	Ns/m²	Effective viscosity
μ_t	Ns/m²	Turbulent viscosity
ρ	Kg/m³	Density
σ	-	Surface tension
β	°	Angle of wave attack
γ_{phase}	-	Phase fraction
$\xi_{m-1,0}$	-	Surf similarity parameter

List of Figures

List of Tables

1.   Introduction

Many megacities around the world are located in coastal areas [10, 90], which have been subjected to a tremendous increase of their development and utilisation in the last decades, with relevant socio – economic and environmental changes [24, 72]. Furthermore, climate change is posing a significant additional challenge to sustainable management, as it cannot be considered as a static issue for planning and management purposes. All these aspects highlight an increased exposure to coastal flooding and a consequent increase of social, economic and environmental damages [113].

Traditional structures have already shown their limits (New Orleans), and risk cannot be reduced to zero [116]. One of the most interesting design is based on the concept to use the same structure for contemporarily producing energy and protecting the harbour area, to minimize the use of space and the construction/maintenance costs. These hybrid systems produce energy under ordinary wave states, to avoid too high costs due to oversizing the power energy conversion system, but have to contemporarily satisfy the survivability standards, i.e. to withstand extreme loads [33]. For this reason, the joint analysis of their hydraulic and structural response is fundamental to improve their design.

Indeed, the main objective of this PhD thesis is to optimize the design of multifunctional maritime structures aimed to protect harbours and produce energy. The study case here analysed is represented by an Overtopping Breakwater for Energy Conversion (hereafter OBREC), developed by the University of Campania [106]. It is a concrete top element, which can be installed in new and existing breakwaters, composed by a sloping ramp followed by a unique reservoir. It is linked with the machine room by means of a pipe passing through a crown wall provided with a bullnose on top of it. The analysis of the performance of such a peculiar structure was performed by means of several methodologies, combined to each other to overcome their own limits.

Recent small – scale laboratory campaigns, carried – out at the Aalborg University by the team of the University of Campania. They were focused on the hydraulic and structural performance of the OBREC device. The results analysed were extended by means of a single – phase numerical model for incompressible fluids, i.e. IH – 2VOF, developed by the University of Cantabria [63]. The results obtained were useful to define some fundamental guidelines for the design of the first OBREC full – scale prototype installation in the port of Naples (Italy).

The monitoring activity at the installation site was performed in the context of the project BRIGAID (www.brigaid.eu). The aim was to enhance the knowledge about the wave – structure – device interactions under a real wave climate. The gathered field data were useful to close the gaps related to the small – scale effects, which can affect the laboratory results. Furthermore, a more sophisticated multi – phase numerical model of the prototype, was developed by means of the library *waves2foam* [50]. It was tested under a real storm event and the typical wave climate of Naples to analyse both the hydraulic and structural performance in extreme and ordinary conditions, respectively.

The analysis of the OBREC prototype structural response, moreover in extreme conditions, highlighted the complexity of the wave – structure interactions due to its peculiar geometry. Indeed, one of the most concerning factors came out from the prototype observations, was the effect water – air mixtures, which can have an effect on the magnitude of the wave loads during the wave impact [12, 25, 26, 27, 82, 83]. Indeed, the compressibility of the trapped or entrained air affect the dynamics and is often thought to reduce the maximum pressures due to cushioning effect. However, a trapped air pocket will also tend to distribute the impact pressures more widely

so that the overall force on the wall may not be reduced [82] and the impulse may be increased due to rebound [114].

To deepen the knowledge about this topic, a new experimental campaign on cross sections similar to the OBREC device, was planned and carried – out at the hydraulic lab of the University of Bologna, in the framework of this PhD work. It was focused on the air – entrainment effect on the nature and the magnitude of the loads against crown wall with and without a bullnose. Based on these experiments, a new plug – in solver, accounting for the compressibility of the fluid, was developed in openFOAM environment. The aim was to produce a valuable numerical tool to support the wave – structure interaction analysis of traditional, but event more complicated coastal structures.

The present thesis is structured as follows.

Chapter 2 gives a description of traditional coastal structures aimed to protect harbours and coasts, providing a review of the prediction methods available to assess their hydraulic and structural performance. It also describes innovative multifunctional coastal structures, which integrate the wave energy conversion principle in the traditional systems, with specific focus on the most common technologies existing at prototype – scale, i.e. Oscillating Water Column OWC and Overtopping OTD devices. In this context, the study case for this research, the Overtopping Breakwater for the Energy Conversion (hereafter OBREC), developed by the team of the University of Campania, is presented.

Chapter 3 gives a general overview of the RANS VOF models, used to solve the Computational Fluid Dynamic problems. The mathematical formulations and equations are provided together with the discretization techniques. The codes used in this work to support the analysis and the optimization of the OBREC device, from the proof of concept stage up to the prototype installation, are here briefly described.

Chapter 4 presents the experimental and numerical database derived from the literature and gained from new experiments and prototype measurements, aimed to support the numerical modelling analysis. The first data set is related to the small – scale OBREC laboratory campaigns, performed at the Aalborg University. The principal aim was to assess the reliability of the OBREC system with respect to a traditional rubble mound breakwater with similar overall dimensions and to investigate some geometrical parameters of the device cross section. The second data set concerns the field measurements performed at the OBREC prototype installation in the Gulf of Naples. The monitoring activity was useful to analyse the hydraulic and the structural OBREC performance under real storm events and the site – specific typical wave climate. The third data set was obtained by means of a new laboratory campaign, performed during the Hydraulic Laboratory of the University of Bologna during this PhD program, aimed to improve the knowledge about the role of the fluid compressibility during the wave impact against crown walls.

Chapter 5 describes the numerical investigation, performed with the single – phase code IH – 2VOF, aimed to complete and extend the experimental analysis carried – out during the firsts OBREC small – scale laboratory campaigns. The performed simulations increased the knowledge about i) the OBREC general performance and ii) the effects of some geometric changes on its hydraulic and structural response. The main objective was to define, together with the results obtained from the laboratory investigations, some fundamental guidelines for the design of the first full – scale OBREC pilot plant, installed in the port of Naples (Italy).

Chapter 6 discusses the numerical investigations, performed with the multi – phase code openFOAM, aimed to test the performance of the OBREC prototype under a single storm event and under the real wave climate characterizing the Gulf of Naples, i.e. the installation site. A qualitative analysis of the pressures acting on the structure allowed the wave loads classification, highlighting the differences with the small – tests laboratory tests. Furthermore, by analysing the device response under the typical wave climate, it was possible to give an indication about the theoretical energy production at the site.

Chapter 7 is devoted to the development of a new multi – phase solver, which accounts for the fluid compressibility. The complexity of the wave – structure interactions for the peculiar cross sections analysed in this work was worth the deepening of the knowledge about the water – air mixture effects during the wave impacts against crown walls. The new plug – in solver was developed in the openFOAM environment. The preliminary results of the new solver were compared with a sub – set of the tests related to the new laboratory campaign presented in Chapter 4.

Chapter 8 draws the conclusions, while Chapter 9 presents the further research that will be performed.

2. Coastal and harbours structures and interaction processes

This Chapter presents traditional (Section 2.1) and the innovative coastal structures (Section 2.2), with a specific attention to the Overtopping Breakwater for Energy Conversion (hereafter OBREC, see Section 2.3), developed by the team of University of Campania.

Traditional coastal structures are mainly employed as coast/harbour defence, while the development of innovative hybrid systems became a valuable solution to combine several functions, such as the shoreline protection and the energy production, without increasing exponentially the costs.

The hydraulic and structural responses of these systems are here commented by analysing the main wave – structure interactions (sub – Section 2.4.1) and the wave impacts/loadings due to wave actions (sub – Section 2.4.2), respectively.

2.1 Traditional coastal structures

Detached breakwaters are coast – parallel structures, usually located inside or close to the surf – zone, aimed to protect the activities performed near and/or along the coasts. Therefore, their principle aim is to reduce the intensity of the wave action in the inshore waters to i) control the coastal erosion, ii) lower the risk of flooding and/or iii) provide safe harbourage.

In the coastal management practice, the shoreline protection is achieved by designing a breakwater capable of ensuring prescribed safety level of a sensitive area for a specific return period, in terms of overtopping and transmission (see sub – Section 2.4.1). The design of a breakwater, therefore, has to withstand the abovementioned hydraulic standards, providing a good structural response with respect to a given extreme wave condition. The conventional breakwaters can be classified in 2 main categories:

- rubble – mound breakwaters (sub – Section 2.1.1); and
- vertical breakwaters (sub – Section 2.1.2).

2.1.1 Rubble – mound breakwaters

Traditional rubble – mound breakwaters are generally composed by a (Figure 1):
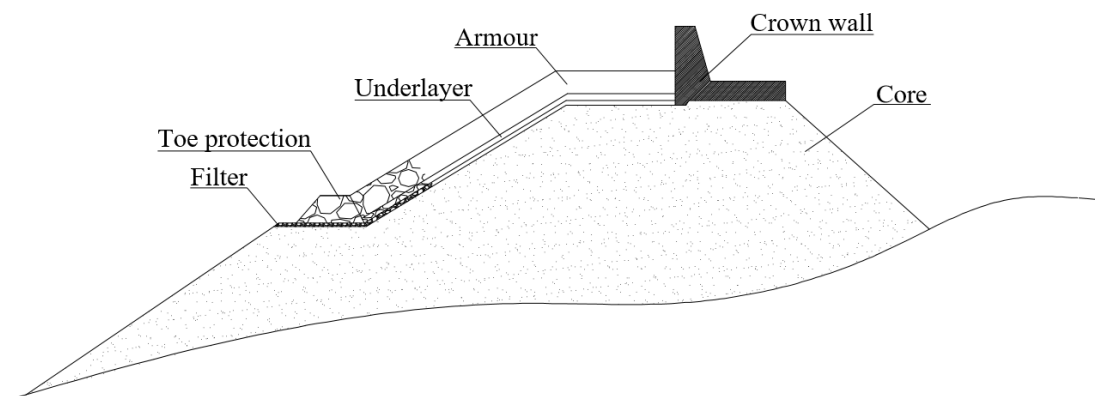
Figure 1. General scheme of a rubble – mound breakwater, provided with a crown wall.

- *core*, which has to prevent the wave transmission thanks to its fine granulometry;
- *filter*, also called *underlayer*, which avoids the wash – out of the core material through the armour layer;

- *armour*, which is directly exposed to the wave attack, with the principal aim to dissipate its energy. Historically it is made by large natural rocks, while nowadays artificial concrete armour units such as cubes, tetrapods, acropodes, xblocs (Figure 2) are available to increase the interlocking, and so the stability, of the most external layer.
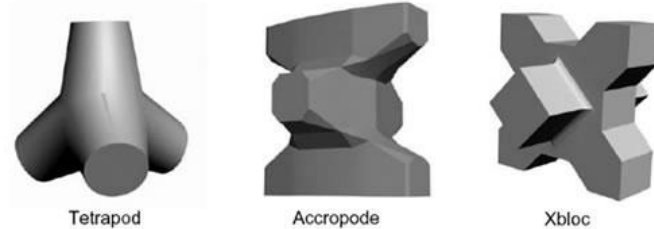
Figure 2. Example of artificial concrete units, i.e. tetrapod, accropode, xbloc.

The design of this kind of structure usually involves the introduction of a *superstructure* (Figure 1), to reduce the crest elevation and/or the wave overtopping, allowing if needed the presence of a roadway for traffic or pipelines at the rear side of the structure itself.

The rubble – mound breakwaters dissipate the wave energy by means of 4 main processes, which will be extensively explained in Section 2.4: i) the wave run – up/down, ii) the wave overtopping, iii) the wave transmission and iv) the wave reflection. The design process is usually based on laboratory tests, which allowed the development of theories aimed to ensure hydraulic and structural standards. However, in the last decades, the numerical modelling of the wave – structure interactions, combined with the experimental investigations, became a significant tool in the design process, because of the improvement of the computer capabilities.

The design formulae used to assess the structure characteristics were developed at the Delft University by Van der Meer [97], to satisfy both hydraulic and structural standards. The armour layer results to be the most sensitive part of the structure, being directly in contact with the wave action. Therefore, its stability is strictly connected to the stability of the overall structure. The aforementioned formulae take into account some fundamental factors related to the wave (wave height H_s, wave period T, breaking wave conditions $\xi_{m-1,0}$, number of waves N), the rock (nominal diameter D_{50}, sieve curve), the cross section (permeability P) characteristics and the structural response (damage level S). The alternative to a straight slope cross section is the introduction of a berm, which acts as a foundation for the armour layer. Besides, the berm may catch armour units displaced, contemporarily increasing the energy dissipation of the wave action. It is normally composed of large stones of quarry run or the most coarse units of the filter layer [97].

As anticipated, rubble – mound breakwater can be provided with crown walls to reduce wave overtopping. Several studies and laboratory campaigns have been performed to analyse the pressure distributions along simple crown walls placed on rubble–mound breakwaters to improve their stability. The main theories, developed by Pedersen [81] and Martin [68], were based respectively on irregular wave and regular waves generated in intermediate/deep water. Nørgaard [73] extended the work of Pedersen [81], with a new set of physical model tests to assess the wave loads on wall superstructures in deep and shallow water conditions.

2.1.2 Vertical breakwaters

Vertical breakwaters are composed by prefabricated monolithic reinforced concrete caissons, which are typically floated or installed on a rubble mound foundation and then filled with sand and/or concrete. They are also called "upright" or "vertically – composite" or "caisson" breakwaters (a unified nomenclature is still lacking) [36]. Their main purpose is to protect

harbours by mainly reflecting them (see Section 2.4). Indeed, the main processes related to these kind of structures are the wave reflection and the wave transmission, deeply investigated by Takahashi [92]. Their structural response, against breaking wave attacks, has been widely investigated by several researches, remaining an open issue, mainly due to the highly stochastic nature of wave impact forces. Oumeraci et al. [74] proposed a general method to assess quasi – static and impulsive loads, then extended by Cuomo [25] for caisson breakwaters and seawalls. Based on field measurements, Hiroi [47] suggested a formula in which the pressure acts uniformly over the full height of the upright section, while Sainflou [86] applied by non – linear theory for standing (i.e. non – breaking) regular waves, finding a good agreement with the field measurements performed on vertical walls. However, the assessment of the impulsive loads remained an uncovered field up to the observations made by Bagnold [6], who discovered the importance of the air entrainment phenomenon during these kind of impacts, which were not sufficient to develop a standalone theory. Eventually, the reference formulae, for the wave loads acting on vertical breakwaters, was suggested by Goda [39] based on laboratory data and theoretical considerations. They were later extended by Tanimoto et al. [94], Takahashi et al. [93] and Takahashi & Hosoyamada [92] to take into account of the effect of the berm, sloping top element, wave breaking type and incident wave angle. However, several full – scale laboratory campaigns proved that impact pressures in the field are generally lower than those measured during laboratory tests, mainly due to the high percentage of air entrained [7]. This discrepancy was taken into account during the project PROVERBS, by performing large and small – scale physical tests. This resulted in a new methodology capable of predicting wave impact forces on vertical breakwaters [3, 4], recommended also by Oumeraci et al. [74]. Among vertical breakwaters, it is possible to distinguish several types, even if 2 typologies are the most used, i.e. the conventional vertical caisson and the composite caisson breakwaters (Figure 3). The latter ones are usually built on rubble – mound breakwaters, while the formers on a thin rubble layer. In general, these kind of structures are preferred with respect to the traditional rubble – mound breakwaters for the reduced amount of materials needed for their construction, for the high durability, the low maintenance costs and the rapid installation on site, characterized by a reduced risk of damage during the construction process [36].
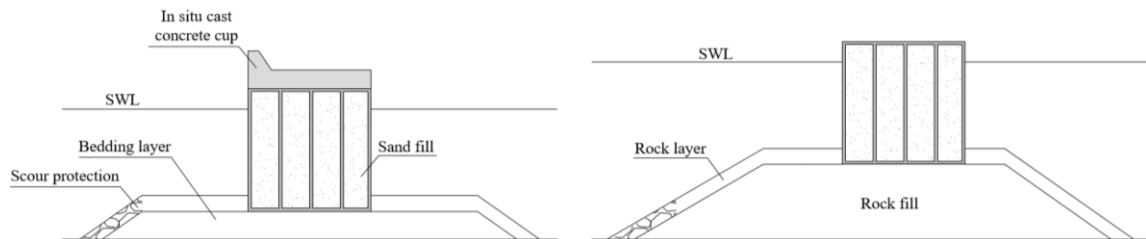
Figure 3. Conventional caisson breakwater and vertical composite breakwater.

2.2   Multifunctional coastal structures

The development of multifunctional/innovative coastal structures is one of the non – direct consequences of the oil crisis, which brought the attention, and consequently the investments, on new energy sectors. This new perspective can be declined in several advantages, such as the extension of the numbers of alternative renewable energy resources, the decreasing of several countries dependency from the fossil fuels; the reduction of the land use for the energy production and the creation and growth of a new industrial and scientific sector. Among the others, one of the most interesting and promising field is represented by the marine energy sector, aimed to

exploit the wave power resource. However, the cost – effective utilization of wave energy is still a major engineering challenge. Indeed, a successful product innovation, a Wave Energy Converter (hereafter WEC), has to comply 3 main aspects: the technical reliability, the economic feasibility and the appealing for end – users. For the latter case, the trend of the increasing of public investments supports the positive perception of this new kind of technologies, while the technical and economic aspects are dependent to each other. Up to now, these technologies require a higher capital and operational expenditures (CAPEX/OPEX) compared to other renewable energy technologies, such as solar or wind ones.

The assessment of the performance of such devices is still a difficult issue and often requires a full – prototype installation to better understand its behaviour under a real sea state, including extreme events. Very few devices in the world are developed in a prototype scale to demonstrate the technical capabilities and structural reliability, reaching high Technology Readiness Levels (TRL). However, in order to fully describe and quantify the status of WEC technology a further metric is required which focuses on the level of techno – economic performance of the WEC system, which is the Technology Performance Levels (TPLs) [110]. The TRL defines how ready a technology is from the commercial point of view, while the TPL how well a technology performs from the economic perspective. Figure 4 shows the possible paths of the development of a WEC. The achievement of the final stage in terms of TPL and TRL does not ensured the successful commercialisation of a WEC. For the purpose a new metric has to be introduced, i.e. the Levelized Cost of Energy (LCoE). The LCoE is an economic indicator on the costs of energy – generating system over its lifetime, allowing the comparison between different sources. Typically it is shown in cents/kWh or Euro/MWh, and includes the initial capital and the costs of operation and maintenance. At this stage, the ocean energy is characterizes by a high LCoE compared to other sources. However, even if the LCoE calculation indicates a non – successful commercialisation, there is still the chance to improve the TPL and TRL to eventually lower the economic indicator.
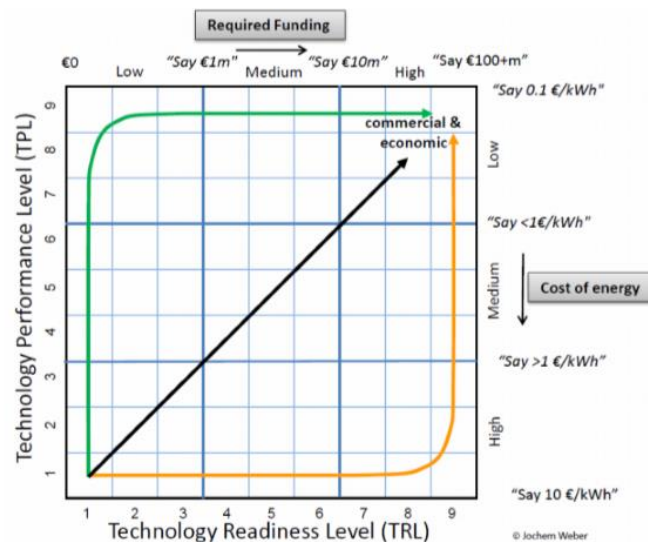
Figure 4. The potential trajectories for a WEC [110].

In this context, the main purpose of the marine energy sector is to lower the construction, operational and maintenance costs, while improving the WECs performance moreover in real sea state conditions. To achieve these objectives, the research carried – out nowadays are developing hybrid devices, which can be installed in existing breakwaters. Therefore, the multifunctional coastal structures have been developed to combine several functions, such as the coastal defence

and the marine energy exploitation, without exponentially increasing the costs. There are 2 kind of technologies thought to be integrated in existing breakwaters or constructed with them, i.e. the Oscillating Water Column (OWC) and the OverTopping Device (OTD).

The OWC structures are capable of harvesting energy from the oscillation of the seawater inside a semi –submerged chamber caused by the wave action, keeping a trapped air pocket above a water column as shown in Figure 5. The wave motion force the column to act like a piston, moving the air out of the chamber and back to it. Due to this movement, the PTO consists in a bidirectional turbine capable of converting the high – velocity airflow into energy.
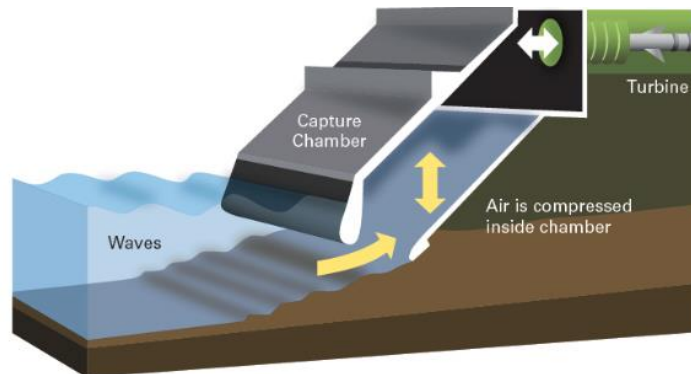
Figure 5. Oscillating Water Column scheme.

There are several examples of this kind of devices around the world such as the REWEC3 [9] installed in the Civitavecchia harbour (Italy), the PICO [80] the LIMPET [8].

The need to use a different principle of exploitation and several issues related to some of these installations, such as the acoustic pollution as for the MUTRIKU experience [67] brought the attention to the overtopping devices as the Sea – wave Slot – cone Generator [11, 107]. It employs several reservoirs placed on top of each other, in which the energy of incoming waves is stored as potential energy (Figure 6). Then, the captured water runs through turbines for electricity production. The system works under a wide spectrum of different wave conditions, giving a high overall efficiency. It can be suitable for shoreline and breakwater applications and presents particular advantages, such as sharing structure costs, availability of grid connection and recirculation of water inside the harbour, as the outlet of the turbines is on the rear part of the system (Figure 6). The system has undergone six years of research and demonstration at Aalborg University, in Denmark. The research has focused mainly on the maximization of wave power capturing [66] and on the nature and magnitude of wave loadings [11, 66]. However, this technology was economically unfeasible due to the complex geometry of the reservoirs.
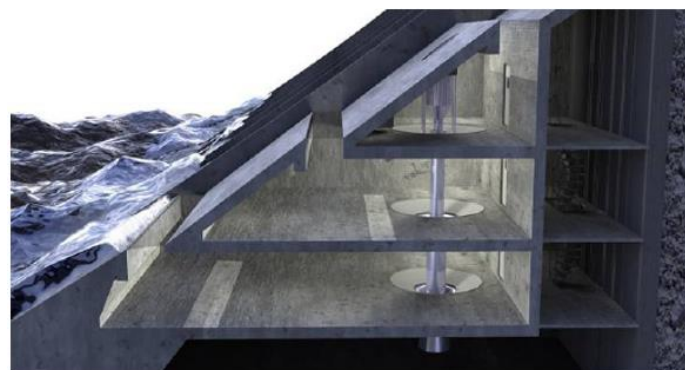
Figure 6. Sea – wave Slot – cone Generator.

2.3 Overtopping BReakwater for Energy Conversion

Based on the experience of the SSG device (see Section 2.2), a different device named OBREC (Overtopping Breakwater for Energy Conversion), was developed by the Research Team of the University of Campania (Italy). The idea behind this technology is to capture and collect part of the energy from the incident waves that overtop the structure, instead of dissipating it.

Figure 7 shows a rendering view of OBREC compared to a traditional rubble – mound breakwater. The former is a concrete superstructure provided with a frontal sloping plate, followed by a single reservoir. A crown wall, including a bullnose placed on top of it, anticipates a rear wave chamber where the turbines should be installed (Figure 7). The overtopping waves are collected inside the reservoir, which is located above the still water level. Eventually, the water flows towards the hydraulic turbines, where the potential energy is converted into kinetic, using the difference between the reservoir bottom edge and the sea water level. Besides the energy production, the OBREC device is capable of protecting the inshore area by absorbing part of the overtopping waves and reflecting the extreme ones thanks to the presence of the crown wall, provided with a bullnose. The added value of this technology is to share the costs because of the integration with a rubble – mound breakwater, that would be built even without the inclusion of OBREC. Its design can be applied to harbour expansions, existing breakwaters reparation or upgrade due to climate change [48]. Furthermore, the inshore location of this WEC i) simplifies the accessibility to the grid connection and infrastructure, ii) improves the recirculation of water inside the harbour and iii) allows an easy installation and maintenance procedures, lowering the costs. Indeed, all the expenditures for deep – water installation, such as the mooring system or the underwater electrical cables for the energy transfer to the shoreline are avoided.

The challenge related to this technology is to define and optimize, in a comprehensive way, its hydraulic and structural performance, which are strictly connected to each other. As anticipated in the previous Section, the improvement of the TPL and TRL is fundamental to assess its applicability by improving its reliability in terms of technical and economic standards. The definition of some standard criteria for the OBREC design depending on the installation site, would be extremely helpful to increase the exploitability of such a device, and is one of the aims of this thesis. The numerical investigations are particularly focused on the wave – structure interactions and the structural response of the device in extreme conditions. These analyses are intended to improve the device as a defence structure, maximizing the energy production.
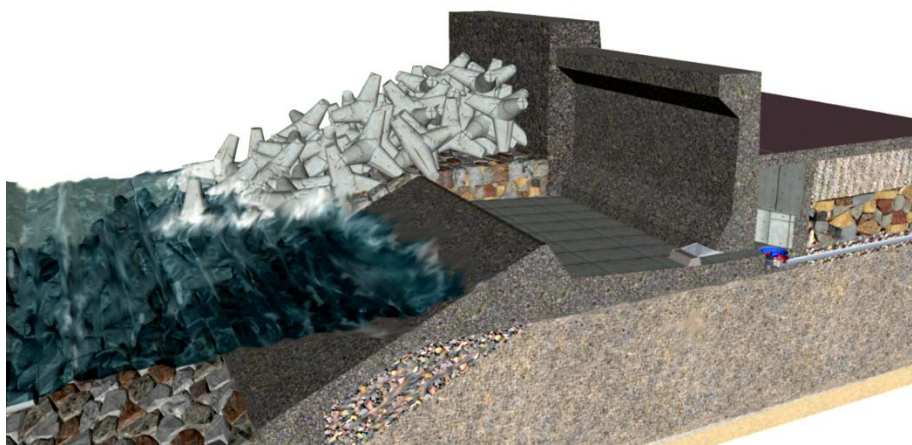
Figure 7. 3D rendering of a traditional rubble – mound breakwater and OBREC.

2.4 Wave – structure interactions

Both traditional and multifunctional/innovative coastal structures are designed to achieve reliable hydraulic and structural standards. The main hydraulic responses to wave conditions are the wave run – up and run – down, the wave overtopping, the wave transmission and the wave reflection (sub – Section 2.4.1).

All these processes imply the direct contact between the wave and the structure, which produces loads, due to wave impact, deeply analysed and presented in the sub – Section 2.4.2.

2.4.1 Main interaction processes

The wave conditions are characterized by the incident wave height at the toe of the structure H, usually as the significant wave height H_s (average of the highest 1/3 of the waves) or H_{m0} ($4\sqrt{m_0}$, based on the spectrum); the mean or the peak wave period T_m or T_p (based on the statistical or spectral analysis); the angle of wave attack β, and the water depth, h [97].

The wave action causes the water oscillation on the structure. The minimum and the maximum levels reached by water surface, with respect to the still water level (SWL), are known as run – down and run – up, respectively. Both of them are fundamental for the design of coastal structures. Specifically, the run – up determines the structure crest level, the presence of a superstructure, directly influencing the overtopping and the transmission processes; while the run – down influences the extension of the armour layer or a possible toe protection. The reference value is usually the 2% exceedance level of the expected run – up for dikes, while for breakwaters and offshore rubble – mound structures it can varies between 5% and 40% [99].

The wave overtopping implies that part of the waves pass over the structure. It is usually quantified as the average discharge per linear meter of width. In reality, there is no constant discharge over the crest of a structure during the overtopping process, which is very random in time, space and volume. The highest waves will push a large volume of water over the crest in a short period of time (less than a wave period), whereas lower waves may not produce any overtopping. The main formulae used for the design procedure are reported in the EurOtop manual (www.overtopping-manual.com) [32], and are aimed to minimize this phenomenon to avoid severe consequences at the inshore area.

One of the consequences of the overtopping phenomenon is the creation of new waves behind the structure. This process is known as wave transmission. It occurs in case of low – crest and/or permeable structures. It is defined by a coefficient that is the ratio between the incident and the transmitted wave height. Further investigations were performed by d'Angremond et al. [28], to provide design formulae aimed to minimize this phenomenon.

Part of the energy associated to the incident wave is reflected towards the sea by the structure. The reflection phenomenon is influenced by the characteristics of the obstacle, such as its geometry and material (roughness). In case of an impermeable structure, the 100% of the incident wave is reflected, while a permeable one is capable of absorbing part of the associated energy. Zanuttigh and Van der Meer [117] proposed a new simple formula to quantify the wave reflection in case of rock permeable, rock impermeable, armour unit and smooth slopes structures.

To summarize the wave – structure interactions, part of the wave energy is dissipated during the breaking process, while other portion is reflected or dissipated during the wave transmission inside the structure. All these processes have to be controlled to ensure a proper hydraulic response of the structure that has to capable of providing proper coastal protection and safe harbourage, without compromising the stability of the structure itself.

2.4.2 Wave loads

The wave action and its interaction with coastal structures generates pressure, loads and therefore forces, which are extremely important to ensure the overall stability. Particular attention has to be paid to the breaking process over the structure, which can compromise the proper functioning of the system producing structural damages.

The wave loads and the associated forces can be classified in 2 main groups [112]: i) quasi – static forces (hydrostatic forces) and ii) dynamic forces. For the latter category, [13], distinguished 3 different behaviours resulting in i) quasi – static/standing/non – impact and impact loads, ii) uplift loads, iii) cyclic loads and vibrations.

The main difference between impact (i.e. non – breaking wave with $\xi_{-1.0,m} > 2$) and non – impact loads (i.e. breaking wave with $\xi_{-1.0,m} < 2$) can be noticed by performing a time – history analysis of the pressure signal. The former is characterized by a "church spire" shape and is composed by a first peak due to the wave impact itself, followed by a quasi – static component. Figure 8 shows a parametrization of the impact load, in which it is possible to distinguish:

- the maximum pressure due to wave motion (p_{max}). The maximum pressure is referred to the pressure induced only by wave motion excluding hydrostatic pressure resulting from water depth (h) at the SWL;
- the compression time (t_A). Also called rise time, it is the time needed for the pressure to reach its maximum value and it must be shorter than the wave period;
- the duration of the impact (t_D). It is the sum of the compression and the expansion time and belongs to the duration of the impact component;
- the expansion time ($t_E = t_D - t_A$). It is the time needed for the pressure to reduce from the maximum pressure to a hydrostatic value.
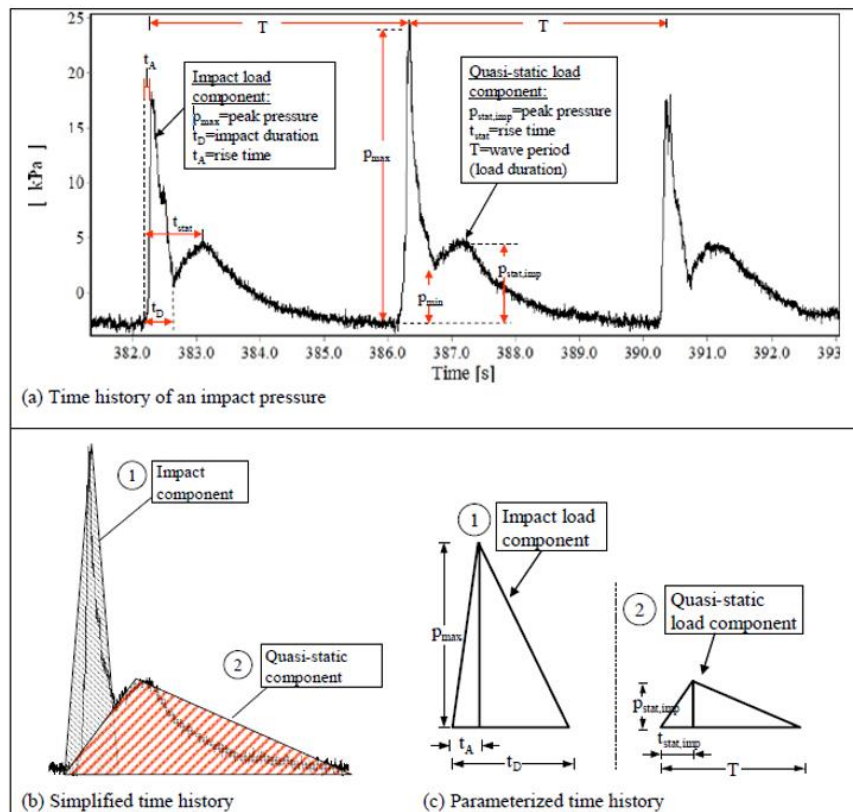
Figure 8. Pressure time series developed at large – scale tests with PBA revetments and parameterization of the signal for impact loads [76].

The shape, and therefore the parametrization, of the non – impact loads is very similar to the quasi – static component of the impact loads, and needs the definition of 3 parameters:

- maximum pressure due to wave motion (p_{max}), referred to the pressure induced only by wave motion excluding hydrostatic pressure. In the case of quasi – static loads the maximum pressure is defined as p_{stat};
- rise time, that is the time needed for the pressure to reach its maximum value and it must be shorter than the wave period (t_{stat}). If a trapezoidal form is used to idealize the time history, the rise time is divided into the rise time t_{stat1} and the time till the pressure starts to decrease t_{stat2};
- load duration, that depends to the period of the incident waves T.
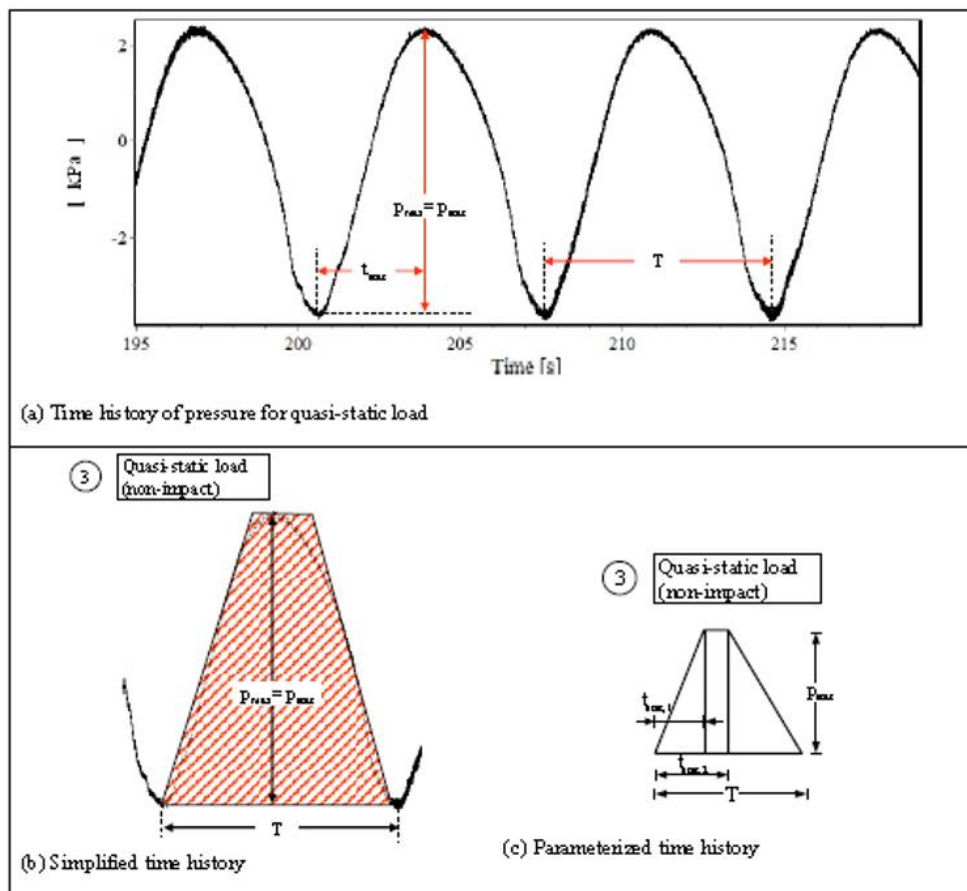
Figure 9. Parametrization of non – impact loads [76].

Between these 2 categories, it is possible to define an intermediate condition which usually occurs in case of plunging breakers [83], producing slightly breaking loads (Figure 10). Figure 11 shows the map produced by Oumeraci et al. [74] during the PROVERBS project, in which it is possible to combine several structure and wave parameters to obtain an indication about the probability of occurrence of a certain breaker type. Input for this map are geometric and wave parameters, which in combination yield an indication on the breaker type, here fully described:

- *quasi – static/standing loads* for which the formulae developed by Goda [39] (Figure 10a);
- *slightly breaking loads* which already consist of some breaking waves but not significantly exceeding the Goda loads (Figure 10b);

- *impact load* for which new formulae including impact duration are to be used (Figure 10c); and
- *broken loads*, i.e. the waves already broke before reaching the structure.
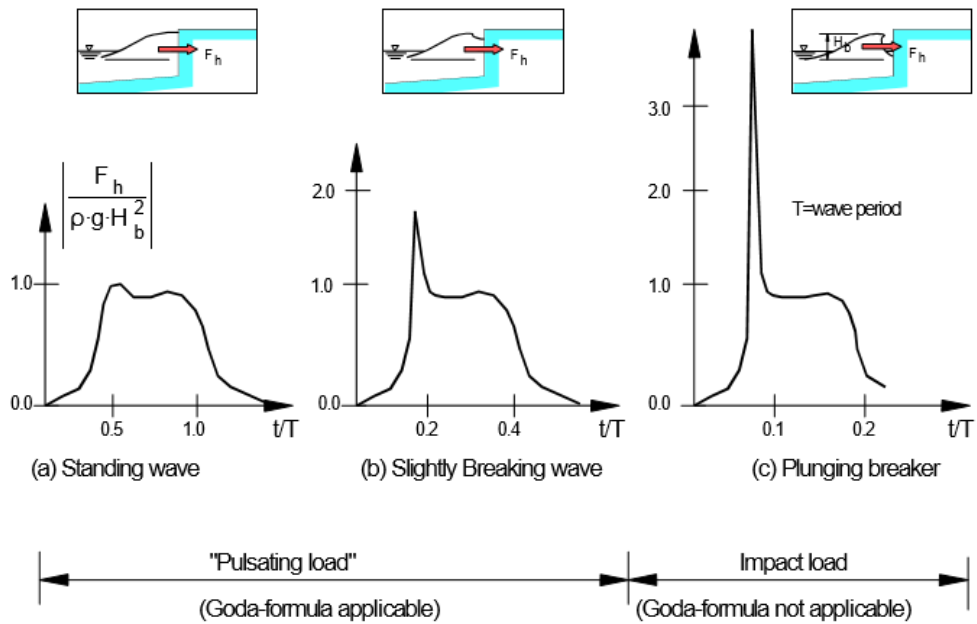
Figure 10. Distinction between pulsating and impact loads [74].
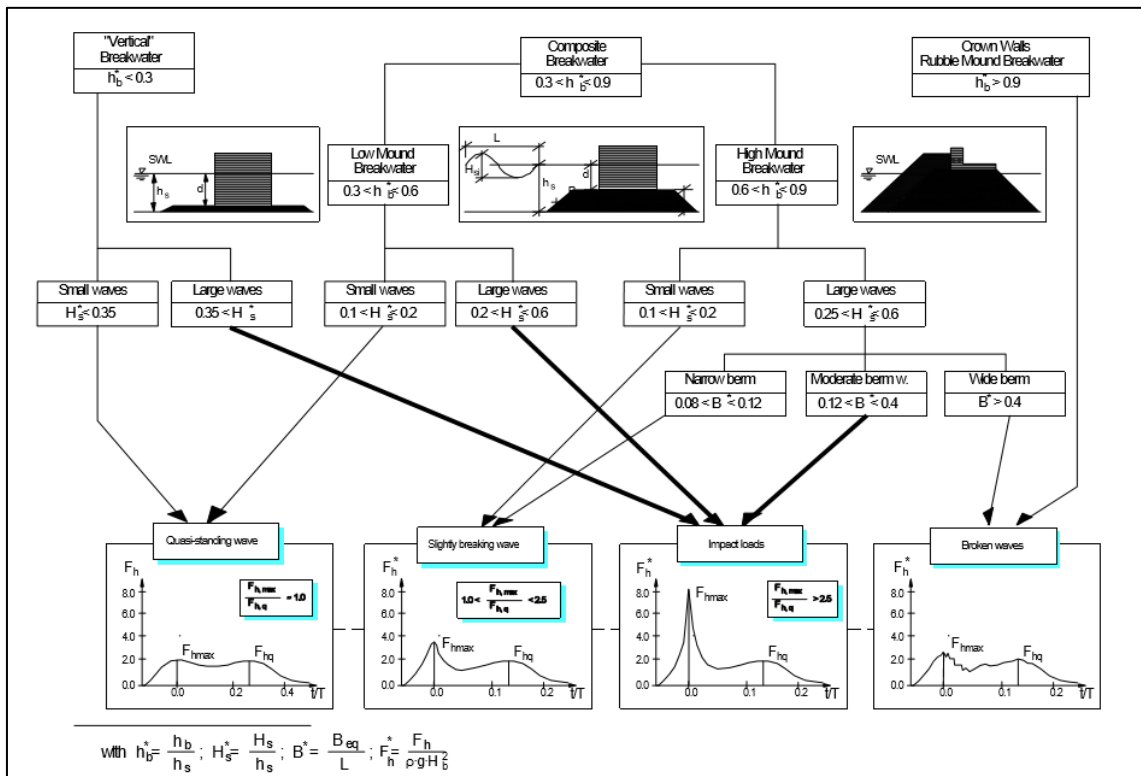
Figure 11. PROVERBS map to classify the wave loads [74].

Most of the wave impacts on wall involve air entrapment by the water. There are 2 different manner to be present: i) entrapment of an air pocket, ii) entrainment of a collection of air bubbles. It is important to take into account of the aeration effects analysing the impact loads. Figure 12

35

shows the difference between pressure signals according to the amount of air trapped by a breaking wave [12]. In case of low – aeration, the water adjacent to the revetment slope contains relatively small amount of air (considering a void ratio < 5%), while in case of high – aeration the water contains a bigger amount of air. This latter case is usually due to plunging waves breaking on the cover of the external layer. In the case of low – aeration, the duration of the impact load is of about 80 to 200 ms, while for high – aeration the duration is increased and the range of it is about 100 to 450 ms [12]. However, it is not so straightforward to distinguish between the 2 conditions according to the impact time duration. However, the pressure signals measured from large scale tests show the difference that exists due to aeration. Figure 12 shows damped oscillations for the high – aeration case, due to air entrainment such as air pockets or because of the presence of bubbles. The trapped air interacts with the surrounding fluid in a pulsating motion wherein the fluid energy is alternatively stocked and released (compression/expansion of the aerated water) [12]. The latest causes the mentioned oscillations in the pressure signals, which are damped afterwards due to the leakage of the trapped air and the disintegration of the air pocket into a bubbly flow. The presence of an air pocket is usually given by a specific dynamic in which the water reaches the highest transducers before the lowest ones. Furthermore, the high – aeration is characterized by a frequently presence of sub – atmospheric pressures after the impact takes place, specifically after the first expansion phase. The latest was observed experimentally in largescale tests [71, 74].
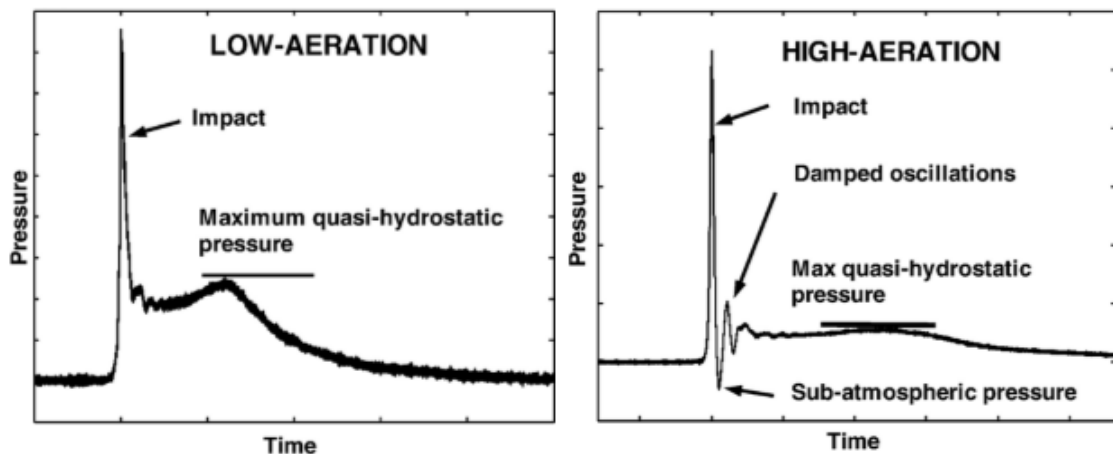
Figure 12. Schematic representations of (a) a low – aeration impact and (b) a high – aeration impact [12].

3.   RANS VOF numerical modelling

This Chapter presents the numerical models adopted in this work. The aim is to achieve a better and more comprehensive understanding of the wave – structure interactions, by analysing the hydraulic and structural responses of coastal structures.

3.1   CFD for wave – structure interactions

The use of the computers to model mathematically natural phenomena is increased enormously in the last decades. The improvement of their computational capacity allowed these machines to become a new fundamental tool capable of i) applying theories to support the description and the resolution of these phenomena; ii) handling and processing a huge amount of data.

The aforementioned theories are implemented in terms of mathematical equations. The aim is to evaluate all the variables, in a time/space domain, which satisfy the equations, which are generally not provided with a closed analytical solution.

The problems related to the fluid mechanic processes can be solved thanks to a set of methodologies known as Computational Fluid Dynamics (CFD). The simulations allow to numerically solve the laws governing the movement of fluids, in or around a material system, where its geometry is also modelled in the computer environment. Therefore, the whole system is *virtual* and is completely equivalent to the physical one, as in an experimental investigation [44]. Therefore, CFD represent an interesting tool not only for scientific, but also for engineering purposes. Working as a virtual laboratory, the numerical simulations can be used also to develop new expressions to fully describe a phenomenon or the performance of a specific structure. Therefore, the development of more reliable mathematical models, combined with the improvement of the computers computational power, makes the CFD approach a valuable instrument capable of compensating or extending, and in some cases fully replacing, the physical investigations avoiding huge investments.

3.1.1 Governing equations

The fundamental basis of almost all CFD problems are the Navier – Stokes (NS) equations, which are a set of non – linear partial differential equations which describe the fluid motion. These equations, in addition to the free surface boundary conditions, have been incorporated in the last 2 decades in the numerical models to study the wave – structure interaction processes. They are able to calculate flows in complex geometries and provide very refined information on the velocity, pressure and turbulence field [60]. Specifically, from these equations, once the velocity field is determined, other quantities such as pressure or drag forces can be estimated. The number of simplifying assumptions in this kind of models is lower than in other approaches. However, in order to solve the NS equations, several considerations and simplifications are normally made. Among the others, the shallow waters equations, the Reynolds – Averaged Navier Stokes (RANS) equations and the Volume – Averaged Reynolds Averaged Navier Stokes (VARANS) equations were derived to simplify the original ones and to solve practical problems. The shallow water and the RANS equations are used to observe the wave propagation, while the VARANS include the effects of porous media into the flow motions. In the present work, numerical models based on the RANS and VARANS formulations were adopted. The RANS equations are time – averaged equations of motion for fluid flow. The idea behind the equations is the Reynolds decomposition, where the instantaneous quantity is decomposed into a mean (time – averaged) and a fluctuating terms.

Here below, the continuity equation together with the VOF method to track the free surface are reported in Eq.s (1) and (2), respectively. The VOF method is used in the numerical model, such as openFOAM, to track the free surface, in which γ_{phase} represents the fluid fraction in a computational cell, ranging from 1 to 0, where a cell fully filled by one of the fluids (phase 1) takes a value of 1, while a cell filled with the void phase (phase 2) should be 0. Furthermore, in OpenFOAM the interface between the 2 phases is compressed by the introduction of an extra artificial compression term in the VOF equation to keep a sharp interface between the faces.

The equations, an unsteady, incompressible, viscous and immiscible 2 phase flow, are defined as follows:

$$\nabla U = 0 \tag{1}$$

$$\frac{\partial \gamma}{\partial t} + \nabla \cdot (\gamma_{phase} U) + \nabla \cdot (\gamma_{phase}(1 - \gamma_{phase})U_r) = 0 \tag{2}$$

where U_r is a velocity field capable to compress the interface and defined as $U_r = U \cdot n_{vec}$, with n being a vector normal to the interface ($n_{vec} = \nabla\gamma_{phase}$). The extra term in the VOF equation is active only in the 2 phase interface. Additionally, the density at the cells of the domain is calculated as a weighted average of the densities of the phases, according to the volume fraction occupied by each phase into a cell (Eq. (3)). The latest is calculated trough the scalar function γ_{phase}.

$$\rho = \gamma_{phase}\rho_{phase1} + (1 - \gamma_{phase})\rho_{phase2} \tag{3}$$

Eq. (4) presents the momentum equation that solves the fluid dynamics:

$$\frac{\partial \rho U}{\partial t} + \underbrace{\nabla(\rho U U)}_{\text{Convective term}} - \underbrace{\nabla^2(\mu_{eff}U)}_{\text{Diffusive term}} = -\nabla p + F_s \tag{4}$$

The terms composing the momentum equation are the time derivative, the convective term, the viscosity, the total pressure ($p_{tot} = p_{dyn} + \rho g h$) and the surface tension. The latter, defined in Eq. (5), represents the tension between the 2 fluids at the interface:

$$F_s = \sigma\kappa(x)n_{vec} \tag{5}$$

Where σ is the surface tension, κ represents the curvature of the interface and n_{vec} is the normal vector. The viscous term, because of the Reynolds decomposition, is split in 2 contributions known as a dynamic and a turbulent term (Eq. (6)).

$$\mu_{eff} = \mu + \mu_t \tag{6}$$

To describe surface wave motions near to a coastal structure, which could be either impermeable or a permeable structure or a combination of both, the Volume – Averaged Reynolds – Averaged Navier Stokes (VARANS) equations were developed. Here, the Volume – Averaged Reynolds stress is modelled by adopting the nonlinear eddy viscosity assumption [45]. In simple words, the VARANS equations are the integral of the RANS over a representative volumetric element, larger than the pore structure but smaller than the length of the flow.

Considering the porosity constant for each cell, the continuity equation is equivalent to the RANS formulation, Eq. (1). The momentum equation is affected by the presence of the porosity field and the coefficient c_A that takes into account of the added mass effects, as shown in Eq. (7):

$$\frac{(1 + c_A)}{n}\frac{\partial \rho U}{\partial t} + \frac{1}{n^2}\nabla(\rho U U) = -[\nabla p + F_s] + \frac{1}{n}\nabla \mu_{eff}\nabla U - \left[\frac{\alpha_F(1-n)^2}{n^3 D_{50}^2}\mu U + \frac{\beta_F(1-n)}{n^3 D_{50}}\rho|U| \cdot U\right] \quad (7)$$

By applying the volume averaging procedure the new terms related to the presence of the porous media need to be closed. The Darcy – Forchheimer equation, reported in Eq. (8), appears on the right hand side of the momentum equation, where the Polubarinova – Kochina term (PK – term) is included in the time derivative to account for the added mass effect, while the coefficients *a* and *b* are explicitly defined in Eq.(9):

$$aU + b|U|U + c_A\frac{\partial}{\partial t}\rho U \quad (8)$$

$$\left[\frac{\alpha_F(1-n)^2}{n^3 D_{50}^2}\mu U + \frac{\beta_F(1-n)}{n^3 D_{50}}\rho|U| \cdot U\right] \rightarrow \quad \rho\left[\frac{\alpha_F(1-n)^2}{n^3 D_{50}^2}\nu U + \frac{\beta_F(1-n)}{n^3 D_{50}}|U| \cdot U\right] \rightarrow \quad \rho[aU + b|U|U] \quad (9)$$

Eq. (9) shows the definition of the coefficients *a* and *b* given by Ergun[31], while in Eq. (10) and (11) by Engelund [30] and van Gent [104], respectively, characterized by small differences. Furthermore, Eq. (12) reports the added mass coefficient c_A formula given by van Gent [104].

$$a = \frac{\alpha_F(1-n)^3}{n^2 D_{50}^2}\nu; \quad b = \frac{\beta_F(1-n)}{n^3 D_{50}} \quad (10)$$

$$a = \frac{\alpha_F(1-n)^2}{n^3 D_{50}^2}\nu; \quad b = \beta_F\left(1 + \frac{7.5}{KC}\right)\frac{(1-n)}{n^2 D_{50}} \quad (11)$$

$$c_A = \frac{1 + \gamma\frac{(1-n)}{n}}{ng} \quad (12)$$

where *γ* is usually taken equals to 0.34.

3.1.2 Turbulence closure models

As anticipated in the previous section, the RANS and therefore the VARANS equations implied the splitting of the variables in a mean and a turbulent components. The latter one has to be modelled, to provide the model closure.

The classification of the turbulence models in order of increasing complexity is: i) First Order Models (Zero –, One – and Two – Equation Models) and ii) Second Order Models (Algebraic Stress Models and Reynolds Stress Models). Particularly the Two – Equation models (e.g., $k - \varepsilon$, $k - \omega$, SST models) are widely used due to the simplicity of implementation if compared to second order models and are able to model the turbulent kinetic energy (*k*) and the rate of energy dissipation. Further classifications of turbulence models may be found based on the scale for modelling the turbulence:

- RAS (Reynolds Averaged Simulation) which uses averaged form of the governing equations for turbulence;

- LES (Large Eddy Simulation) solve the large turbulent structures in the flow while modelling the small eddies;
- DES (Detached eddy simulation) is a hybrid method between RAS and LES models; and
- DNS (Direct numerical simulation) resolves all scales of turbulence by solving directly the NS equations (supplied by OpenFOAM).

3.1.3 Discretization schemes

One of the most important step in the CFD approach consists in the set – up of the algorithm, namely the discretization phase (see Figure 13). The definition of the computational approach deals with the choice of the discretization method of the selected mathematical model and involves 2 components, the space discretization and the equation discretization.

The space discretization consists in setting up a mesh, or a grid, by which the continuum of space is replaced by a finite number of points where the numerical values of the variables are determined. It is intuitively obvious that the accuracy of a numerical approximation will be directly dependent on the size of the mesh that is the closer the points, the better the discretized space approaches the continuum, the better the approximation of the numerical scheme. For complex geometries, the solution will also be dependent on the form of the mesh, since in these cases we will tend to develop meshes, which are adapted to the geometrical complexities [44]. The grid can be classified as structured or unstructured (see Figure 14), the latter being of more general nature. The formers are composed by families of lines (one for each space dimension), each mesh point being at the intersection of one line of each family and correspond to Cartesian grids in the mathematical space of the curvilinear coordinates. In unstructured grids, the mesh point distribution is arbitrary since they are not localized on identified lines and they can be connected through various polynomials in 2D or polyhedrals in 3D [44]. The grid quality is essential to determine the computational cost if the simulation, but moreover the accuracy of the results.
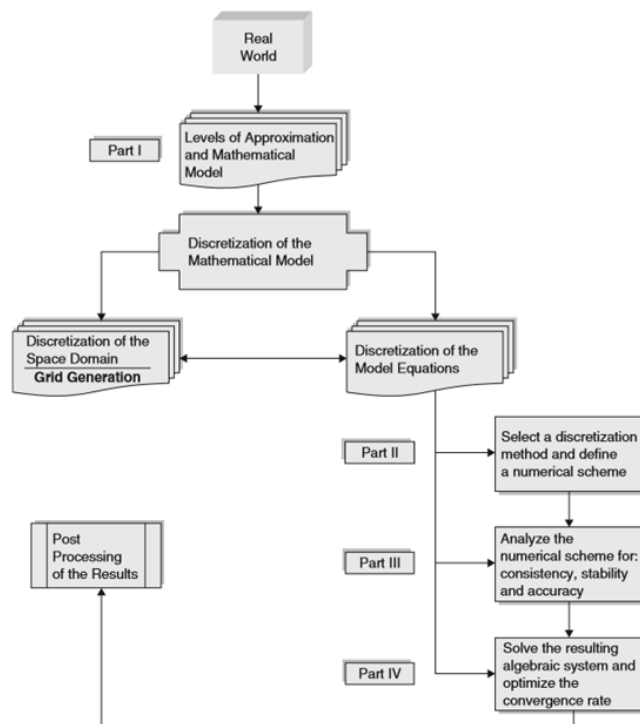
Figure 13. Structure of the discretization and resolution steps in the numerical model [44].
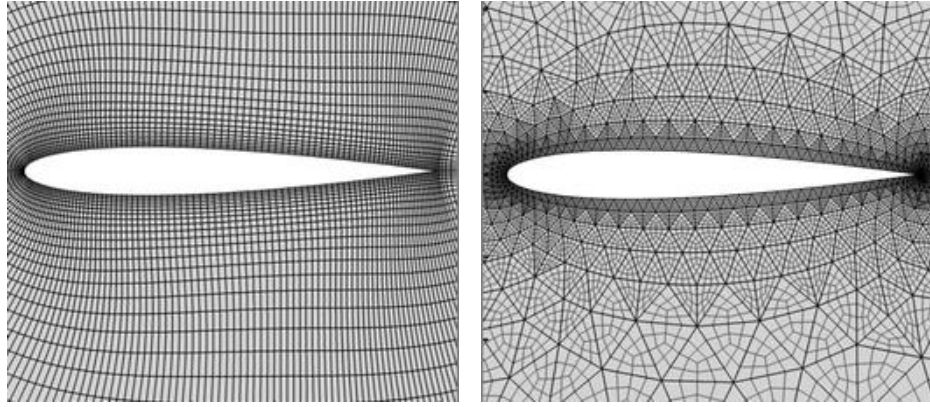
Figure 14. Structured mesh vs. unstructured mesh.

Once the mesh has been defined, the equations can be discretized leading to the transformation of the differential or integral equations to discrete algebraic operations involving the values of the unknowns related to the mesh points. The basis of all numerical methods consists in this transformation of the mathematical model into an algebraic, linear or non - linear, system of equations for the mesh – related unknown quantities. The definition of the algorithms adopted to solve the problem, depend on the nature of the problem itself, which could be time – dependent with a transient flow behaviour or connected to time varying boundary conditions, or steady state problem. In this work, only the former will be considered.

With time – dependent numerical formulations, 2 families of methods can be distinguished, i.e. explicit or implicit methods. In explicit methods, the matrix of the unknown variables at the new time is a diagonal matrix while the right – hand side of the system is being dependent only on the flow variables at the previous times. This leads to minimize the number of arithmetic operations for each time step, while the stability and convergence conditions impose severe restrictions on the maximum admissible time step. In implicit methods, the matrix to be inverted is not diagonal since more than one set of variables are unknown at the same time level. In many cases however, the structure of the matrix will be rather simple, allowing simple algorithms for the solution of the system at each time step, although the number of operations required will be higher when compared to the explicit methods. This is compensated by the fact that many implicit methods have, at least for linear problems, no limitation on the time step and hence a lesser number of iterations will be needed to reach the steady state.

To discretize the space derivatives, 3 families of methods are available:

- the finite difference method (FDM), which is the most traditional and oldest method for numerical discretization, although it is only applicable in practice to structured grids;
- the finite volume method (FVM), which the most widely applied method today in CFD is which discretizes directly the integral form of the conservation laws. Its popularity is due to its generality, its conceptual simplicity and the relatively ease of application to both structured as unstructured grids. However, it leads to similar formulas as a FDM when applied to structured grids.
- the finite element method (FEM), which is mainly adopted in structural mechanics models. Its application to CFD is of interest, but is not dominant.

According to the numerical models used in this work, only the first 2 methods have been deployed.

3.2 Numerical models

Nowadays, a number of CFD numerical models are based on the resolution of the RANS and the VARANS equations, coupling with the VOF method, for coastal engineering applications, to track the interface between the water and the air/void. The differences among the codes depends on the modelling of the closure terms or on the techniques applied to finally solve the RANS equations such as the volume averaging and/or the numerical and discretization schemes used. In the next sub – Sections, the CFD models adopted in this thesis are commented.
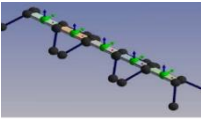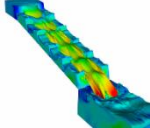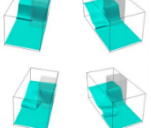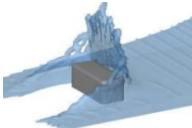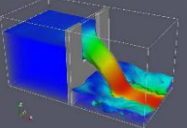
Specifically, the first part of this research was performed with the commercial single – phase software IH – 2VOF (see sub – Section 3.2.1) that works only in 2 dimensions. The simplicity of this numerical model was useful to preliminary investigate the OBREC concept, from both the hydraulic and structural points of view.

To analyse the OBREC prototype, installed in the port of Naples, a more sophisticated numerical model was needed, which has to be capable of solving 3D problems and multi – phase flows. Table 1 shows a series of numerical models together with their main characteristics, i. e. governing equations, base programming language, free surface track method, grid definition, turbulence model adopted, presence of porous media and type of software. The selection of openFOAM (sub – Section 3.2.2) was based on the following reasons:

- it is capable of solving problems that involve complex structures (permeable/impermeable combination), as for the OBREC case;
- it has been extensively validated for wave – structure interactions occurring at the inshore area [41, 42, 42, 51];
- being an open source software, it can be modified to develop new solvers, which is one of the objectives of this PhD work (Chapter 7).

Furthermore, the plug – in solver *waves2foam*, implemented in the openFOAM environment for the wave generation/absorption, is presented in the sub – Section 3.2.3.

Table 1. Examples of 3D numerical models available for coastal engineering applications.

	Ansys – Fluent	Flow 3D	IH - 3VOF	ComFlow	OpenFOAM
Governing Equations	VARANS	VARANS	VARANS	RANS	VARANS
Program Languages	Fortran	Fortran	/	Python	C++ (object oriented)
Track of free surface	VOF	VOF	VOF	VOF	VOF
Grid Definition	Finite Volume method	Finite Volume method	Finite Volume method	Finite Volume Method	Finite Element method
Turbulence model	Spalart-Allmaras, k-ε and k-ω	k-ε, RNG k-ε, and k-ω	SST model (k-ε and k-ω)	qr model	Possibility to apply k-ε, k-ω and SST
Porous media	Considered	Considered	Considered	Not considered	Possibility to implement it
Type of Software	Commercial	Commercial	Commercial	Open Source	Open Source
Examples of simulation					

3.2.1 IH – 2VOF

The IH – 2VOF code [60, 63] is an updated version of the COrnell BReaking waves and Structures (COBRAS – UC) [62], a model based on the RIPPLE code developed at Los Alamos National Laboratory by Kothe [58]. RIPPLE is a general program for transient, 2 – dimensional incompressible fluid flows with free surfaces. The IH – 2VOF is a 2DV numerical model capable of solving the RANS equations at the clear fluid region and the VARANS ones inside the porous media regions. As anticipated in the previous Section, it is based on the decomposition of the instantaneous velocity and pressure fields into a mean plus a turbulent component. In this 2D code, the latter element is modelled by means of the $\kappa - \varepsilon$ turbulence model, composed by 2 equations related to the kinetic energy and its dissipation rate, respectively.

The VOF method performs the track of the free surface for one phase only, i.e. water and void. The cutting cell method, firstly presented by Clarke [17], is used to replicate the solid bodies in the mesh. The discretization of the numerical domain can be performed only by means of orthogonal structured meshes to speed up, in terms of time, the numerical simulations. The VOF approach, combined with the definition of a regular grid, involves the definition of an openness function θ to recognize the fraction of volume of free space in the cell. If $\theta = 0$ is a solid cell, if $\theta = 1$ is a fluid cell and if $0 < \theta < 1$ is a partial cell. All the variables, satisfying the governing laws, are redefined by multiplying the function θ by the original variables.

Furthermore, IH – 2VOF includes a set of wave generation boundary conditions, covering a wide range of wave theories. Among the others, the Dirichlet boundary condition and a moving boundary method are available, which are linked with an active wave absorption system to avoid an increase of the still water level and the agitation inside the numerical domain.

The discretization of the equations is performed by means of the central finite difference method (FDM) (see Section 3.1.3). The basic idea is to estimate a derivative by the ratio of 2 differences according to the theoretical definition of the derivative (Eq. (13)). For a function *u(x)*, the derivative at point *x* is defined by:

$$u_x = \frac{\partial u}{\partial x} = \lim_{\Delta x \to 0} \frac{u(x + \Delta x) - u(x)}{\Delta x} \tag{13}$$

The smaller is the quantity Δx, the more accurate is the approximation of the value u_x even if an error is introduced, i.e. truncation error. The power of u_x with which this error tends to zero is called the order of accuracy of the difference approximation, and it can be obtained from a Taylor series development of $u(x + u_x)$ around point *x* (Eq. (14)).

$$u(x + \Delta x) = u(x) + \Delta x \frac{\partial u}{\partial x} + \frac{\Delta x^2}{2} \frac{\partial^2 u}{\partial x^2} + \frac{\Delta x^3}{3!} \frac{\partial^3 u}{\partial x^3} + .. \tag{14}$$

The approximation shown in Eq. (14), obtained by applying Eq. (13), can involves an increment of the value of u_x on the right or on the left hand side, leading to a one – side difference formula which implies a first order error of truncation. A more precise method is characterized by a truncation error of the second order, involving the points to the left and to the right with respect to the unknown, leading to a central difference formula (Eq. (15)).

$$(u_x)_i = \frac{u_{i+1} + u_{i-1}}{2\Delta x} - \frac{x^2}{6} (u_{xxx})_i + ... \tag{15}$$

The wave generation consists in converting the computational domain into a numerical wave flume and defining the velocity field and the free surface elevation at the wave – generating boundary. As for a physical laboratory, the generation of incident waves trains in the computational domain, using the wave – paddle mode of generation, brings up the problem of the absorption of the waves reflected, because of the presence of an obstacle. Nevertheless, in numerical modelling, the problem of wave absorption at the wave generating boundary is still a challenging task. For a numerical model based on RANS equations, the problem is even more difficult to solve, as the model requires the velocity distribution as well as the free surface displacement at the boundary and is therefore very sensitive to errors from the boundary [61].

3.2.2 openFOAM

OpenFOAM (Open Field Operation And Manipulation) is a free and open source CFD code capable of solving continuum mechanics problems, developed at the Imperial College [49]. It is a C++ object oriented library, used primarily to create executables known as *applications,* which can be classified in 2 main categories, i.e. *utilities* and *solvers.* The first ones are aimed to perform tasks involving data manipulation, while the second ones solve specific problems in continuum mechanics.

All the solvers adopt the Finite Volume discretization Method (FVM) (see Section 3.1.3), which is one of the most versatile techniques, which implies the division of the domain into a number of control volumes, i.e. cells or elements, where the variable of interest is located at its centroid. Then the differential governing equations are integrated over each control volume. Interpolation profiles are assumed to describe the variation of the concerned variable between cell centroids.

An OF case is composed by 3 folders, in which all the needed files are contained:

- *0* folder*,* where the initial conditions of particular fields, selected according to the case, are usually stored. When the simulation starts, a series of time folders are produced, taking the name of the time step selected to write the output variables;
- *constant* folder, which contains a full description of the case mesh in a subdirectory *polyMesh*, and files specifying physical properties for the application concerned;
- *system* folders, which includes all the input files associated with the solution procedure itself. It contains at least the *controlDict* where run control parameters are set; the *fvSchemes* where discretisation schemes used in the solution may be selected at run – time; and, *fvSolution* where the equation solvers, tolerances and other algorithm controls are set for the run.

The *utilities* cover both the pre and post – processing steps, leading to a consistent data handling and processing. For the former, OF includes the mesh generation tools such as *blockMesh* and *snappyHexMesh*, capable of defining, and refining in case of obstacles, structured mesh. However, the code is compatible also with external mesh generators, such as Gmsh [38], supporting if needed also unstructured mesh. The principle behind the native utilities, i.e. *blockMesh* and *SnappyHexMesh* is to decompose the domain into a set of one or more 3D hexahedral blocks, where the edges can be straight lines, arcs or splines. Each dimension of the numerical domain has to be characterized by a number of cells, whit the possibility to produce a graded mesh to optimize the computational cost. The *SnappyHexMesh*, taking as input the obstacle defined by stereo lithography surface (STL file), involves 3 steps to perform the mesh refinement:

- the *cell splitting*, which selects a certain number of cells located in the proximity of a specified edge features within the domain;
- the *cell removal*, requires one or more regions enclosed entirely by a bounding surface (of the defined body) within the domain. The region in which cells are retained are simply identified by a location vector within that region. Cells are retained if the 50% or more of their volume lies within the region. The remaining cells are removed;
- the *snapping* phase, which involves the movement of cell vertex points onto the surface geometry, above mentioned, to create a body – fitted mesh.

The pre – processing phase implies also the initialization of the variables and the definition of the boundary conditions of the domain. Once the problem has been set properly, the OF library can move towards the problem resolution, being supported by a large range of solvers each designed for a specific class of problem. The equations and algorithms differ from one solver to another, implying different initial choices on the modelling of the problem according to the test case. The main characteristic of the simulation, such as the solver, the duration, and the output interval of the variables, are stated in the *controlDict* file, where it is possible to introduce a snippet code for the evaluation of some variables in run – time, such as the pressures.

Several post – processing utilities are available to extrapolate the output variables, such the velocity or the VOF values in a specific region, once the simulation has been performed. Furthermore, OF is supplied with a post – processing utility *paraFoam* that uses *ParaView*, an open source visualisation application (Figure 15).
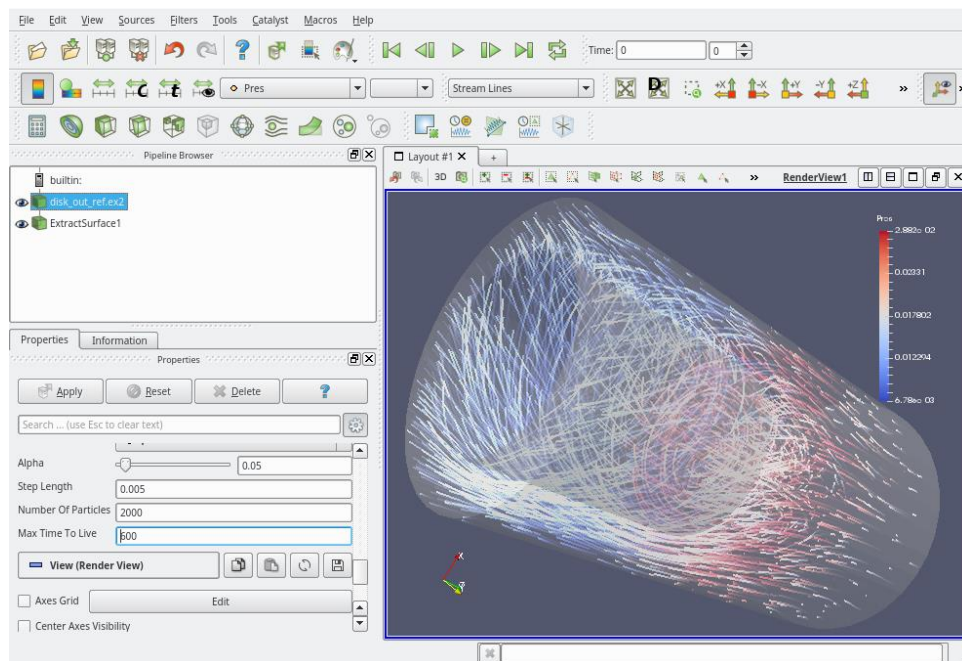
Figure 15. Layout of the *ParaView* application.

3.2.3 waves2foam

For coastal application, Jacobsen et al. [50] developed a plug – in solver in the openFOAM environment, by modifying the native solver *interFoam*, capable of solving problems for 2 incompressible, isothermal immiscible fluids using the VOF method. The porosity module was introduced thanks to the collaboration with Jensen [51], at the Technical University of Denmark.

The new solver implied the introduction of the wave generation/absorption. The latter is performed by introducing the relaxation zone technique, based on a weighting between the computed solution of the velocity field and the indicator field with a target solution at the boundary of the domain, to avoid spurious reflection phenomena.

All the utilities supplied by OF, related to the set – up and the resolution of the problem, are compatible with the toolbox *waves2foam*. However, the latter offers specific pre and post – processing tools, more suitable for the analysis of the wave – structure interactions, such as:

- *waveGaugesNProbes* and/or *surfaceElevation* → analysis of the free surface elevations inside the domain;
- *setWaveParameters* → elaboration of the information related to the implemented wave condition and relaxation zones;
- *relaxationZaoneLayout* → study the of the layout related to the relaxation zones;
- *sampleIncidentWaveField* → evaluation of the incident wave field based on its algebraic form;
- *setWaveField* → set up the initial conditions according to the wave theory implemented;
- *faceSetToSTL* → definition of non – convex impermeable/permeable regions, taken as input for the refinement made by means of *snappyHexMesh;*
- *postProcessWaves2Foam* → processing of the data acquired during the simulation.

The simulations performed in this work use a combination of native and *waves2foam* utilities, to carry – out a comprehensive analysis of the wave – structure interaction and of the variable fields.

4.   Data sets and measurements for model calibration and validation

To optimize the multifunctional maritime structures, several laboratory and field data were used i) to calibrate and validate the numerical models adopted, ii) to improve the knowledge related to the wave – structure interactions and to better understand the role of the fluids compressibility during the wave impact. Specific objectives were:

- the improvement of the understanding of the OBREC concept and the role of some geometric parameters on the device performance;
- the increasing of the knowledge about the wave – structure interactions, with a specific attention to the wave impact against crown walls provided with a bullnose;
- the design of the full – scale OBREC prototype in the Gulf of Naples;
- the analysis of the structural and the hydraulic performance of the prototype under i) a real storm event, and ii) the typical wave climate, characterizing the Gulf of Naples;
- the development and the stabilization of a new plug – in solver developed in the OF environment, which takes into account the compressibility of the fluids.

The Chapter is organized as follows. Section 4.1 presents the laboratory campaigns, performed by the team of University of Campania. They represent the reference literature to further investigate OBREC by means of single – phase numerical model developed in this thesis. Section 4.2 involves the monitoring activities performed on the OBREC prototype in collaboration with the project BRIGAD (www.brigaid.eu). The data collected were useful to set – up and validate a 2D multi – phase numerical model, aimed to investigate the prototype under the typical wave climate of the Gulf of Naples. The new laboratory campaign, discussed in Section 4.3, was set – up and performed in the context of this PhD thesis, to improve the understanding of the wave impacts against crown, focusing on the air – entrainment phenomena.

4.1   Laboratory campaigns with OBREC device

In the 2012 and 2014, 2 laboratory campaigns were carried – out at Aalborg University (Denmark) in 1:30 scale [20, 21, 48]. This Section presents the numerical set – up and the results obtained.

4.1.1 Laboratory set – up and measurements

The tests were performed in the wave flume, which was 25 m long, 1.50 m wide and 1.20 m deep, and included ordinary and extreme wave conditions.

In both the campaigns, the wave series were irregular and generated based on the 3 parameters of the JONSWAP spectrum, i.e. the wave height H_{m0}, the frequency f_p and the so – called peak enhancement factor γ ($\gamma = 3.3$ in all tests), containing at least 1000 waves. The tests are synthetized in Table 2, according to the wave conditions and crown wall characteristics for the 2012 campaign and the geometric configuration for the 2014 tests.

Figure 16 shows the cross sections tested during the laboratory campaigns, with the indications of all the main geometric characteristics. The common characteristics of the configurations are:

- the average size of the rocks (in terms of nominal diameter D_{n50}), i.e. $D_{n50} = 50$ mm for the armour layer, $D_{n50} = 20$ mm for the filter layer, $D_{n50} = 2$ mm for the core part;

- the OBREC offshore slope α equal to 34° (armour and plate), with the exception of the 2014 curved configuration (see Figure 16d), where the sloping plate is characterized by 2 slope angles, i.e. 52° and 17° in the upper part.

The first test campaign (AAU2012) was aimed to compare and evaluate the difference in the hydraulic performance [106], between OBREC and a traditional rubble mound breakwater provided with a simple crown wall and already tested by Nørgaard et al.[73], characterized by the same overall dimensions. A total of 48 tests (Table 2) were carried – out, considering 2 cross sections, which differ only for the height of the sloping plate, i.e. $d_{w,low} = 0.075$ m and $d_{w,high} = 0.125$ m, at model scale (Figure 16a and b, respectively). The laboratory structure width at the bottom is 2.56 m, whereas the width of the reservoir is $B_r = 0.6$ m. For the extreme conditions, a special configuration provided with a parapet (named bullnose), placed on top of the crown wall, was tested to reduce the overtopping discharge at the rear side of the structure, i.e. the q_{rear} [100]. The 2014 configurations were then all designed with such a parapet (as shown in Figure 16c and d), because of its effectiveness.

The second laboratory campaign (AAU2014) was focused on the influence of some geometrical parameters on the hydraulic performance, such as the horizontal reservoir width and the sloping plate shape and length:

- a flat profile with a slope angle equal to 34° (Figure 16c), according to the research conducted by Kofoed [55], aimed to maximize the overtopping discharge $q_{reservoir}$;
- a curved sloping plate, where the slope angle varies linearly between 52° to 17°, which represents an adaptation from the convex profile tested by Kofoed [54].

A submerged prolongation of the sloping plate was introduced, with respect to the 2012 configuration, to improve the overtopping process. The reservoir width B_r, i.e. the horizontal distance between the crown wall and the beginning of the sloping plate ΔB_r (see Figure 16c and d), was set equal to: 0.10 m for the small configuration; 0.20 m for the large configuration and 0.30 m for the extra – large configuration. Iuppa et al. [48] already presented the results of this second laboratory campaign, in which a total of 200 tests were carried – out (Table 2).
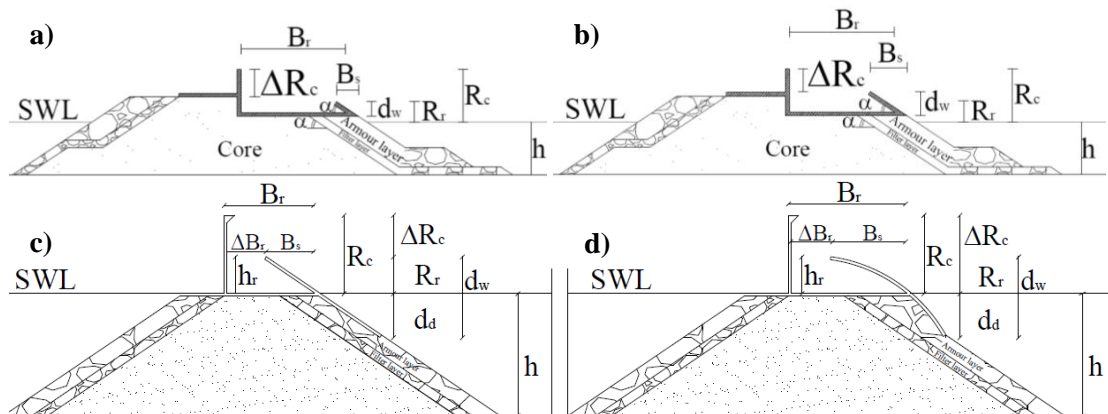
Figure 16. OBREC configurations of the 2012 campaign: a) $d_{w,low}$, b) $d_{w,high}$ configurations; and of the 2014 campaign: c) flat, d) curved configurations.

Table 2. Main wave and geometrical characteristics of the OBREC laboratory campaigns [20, 21, 48], at model scale.

	h [m]	H_{m0} [m]	$T_{m-1,0}$ [s]	R_c [m]	R_r [m]	B_r [m]
2012	(min–max)	(min–max)	(min–max)	(min–max)	(min–max)	(min–max)
Extreme conditions	0.30-0.34	0.141-0.177	1.68-2.26	0.20-0.24	0.075-0.125	0.415-0.488
Extreme conditions with nose	0.34	0.145-0.161	1.66-2.28	0.20	0.035-0.085	0.415-0.488
Production conditions	0.27	0.037-0.138	1.05-2.14	0.27	0.105-0.155	0.415-0.488
2014						
Small structure	0.27-0.35	0.02-0.12	0.76-2.2	0.147-0.227	0.045-0.129	0.219-0.460
Large structure	0.27-0.35	0.05-0.13	0.76-2.2	0.147-0.227	0.045-0.129	0.219-0.460
Extra-Large structure	0.27-0.35	0.05-0.118	0.76-2.2	0.147-0.227	0.045-0.129	0.219-0.460

The assessment of the hydraulic and structural performance of the OBREC device was performed thanks to several instruments to measure:

- the wave reflection from the structure, i.e. K_r;
- the pressures acting along the OBREC profile;
- the average overtopping discharge rate flowing inside the reservoir $q_{reservoir}$; and
- the average overtopping discharge rate at the rear side of the structure q_{rear}.

The water collected inside the reservoir was controlled by depth gauges, which activated the pumps to allow the water to flow out from the reservoir when a fixed threshold level was achieved. The wave volumes overtopping the crown wall were collected into a box inshore the structure, where a similar control was installed. In both cases, the values of $q_{reservoir}$ and q_{rear} were reconstructed by the combination of the signals acquired from the depth gauges and the pumps.

The wave reflection coefficient K_r was derived from 4 wave gauges positioned in front of the structure, according to Klopman and Van der Meer [53] recommendations.

In the 2012 campaign, 3 and 6 pressures transducers were installed on the $d_{w,low}$ and the $d_{w,high}$ configurations respectively, while 5 were placed across the reservoir outside bottom, to evaluate the uplift pressures and 17 on the upper/lower crown wall. In the 2014 campaign, a total of 14 pressure transducers were used to estimate the pressures/forces induced by the waves on the structure. Specifically, 5 probes were located along the sloping plate, 2 across the reservoir outside bottom, 5 on the lower/upper crown wall and 1 on the parapet.

4.1.2 Results of the laboratory campaigns

The first laboratory campaign showed that OBREC is characterized by similar or reduced values of K_r with respect to traditional rubble mound breakwaters. Figure 17 shows the main results for the 2 tested configurations, compared with the main existing formulae for the wave reflection [2, 84, 117]. The values of $q_{reservoir}$ can be compared with existing prediction methods [32, 54, 98, 108], as shown in Figure 18, considering a friction reduction factor $\gamma_f = 0.7$. The introduction of a parapet in the OBREC cross section reduced the values of q_{rear} up to the 80% with respect to the simple crown wall (Figure 19). The qualitative analysis of the wave loads highlighted a quasi – static load time history over the sloping plate and the reservoir bottom, which can be predicted by applying Tanimoto and Kimura [91], used in the Goda formulation [39] (see Figure 20). The hydrodynamic behaviour of the crown wall is similar to that one analysed by Pedersen [81] for simple crown wall anticipated by a berm. However, the impulsive behaviour should be investigated by modifying the method developed by Norgaard [73] (shallow water conditions), to account for the differences in the structure configuration [106].
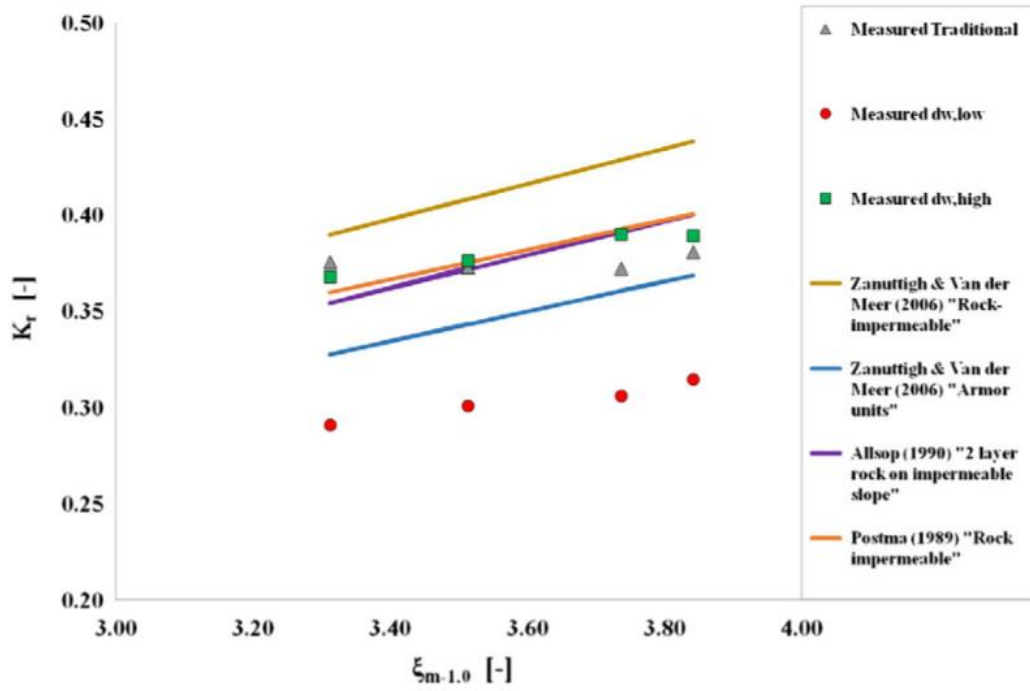
Figure 17. Comparison between the values of K_r obtained during the first laboratory campaign with the existing formulae [106].
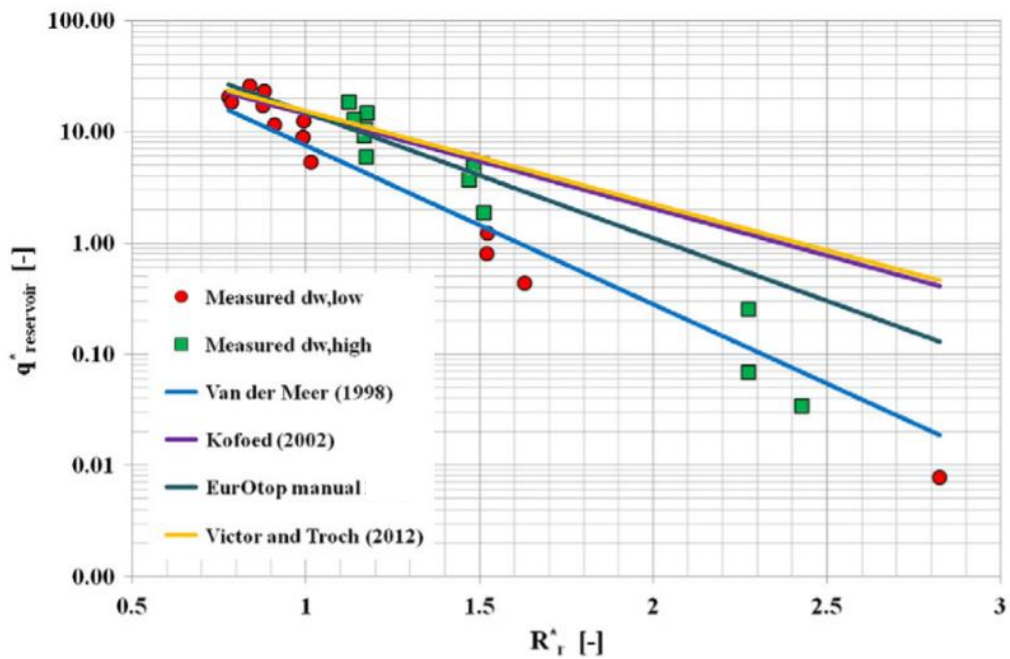
Figure 18. Comparison between different design formulae vs. measured non – dimensional average front reservoir overtopping discharge [106].
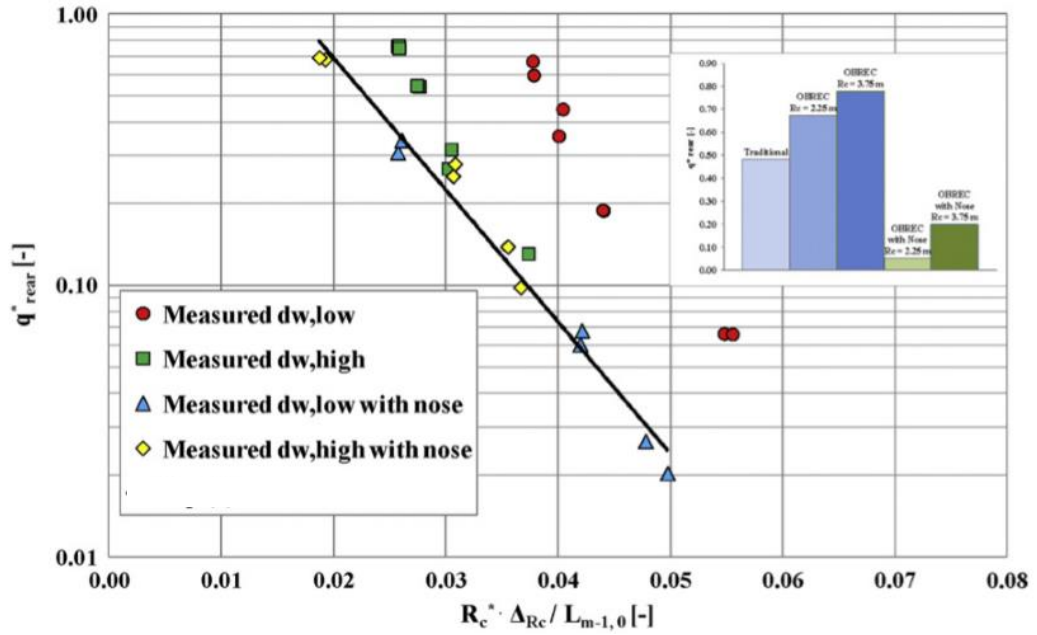
Figure 19. Non – dimensional average overtopping discharge (q^*_{rear}) rear OBREC crown wall with "nose" vs. $R_c^* \ \Delta R_c \ / \ L_{m-1,0}$ [106].
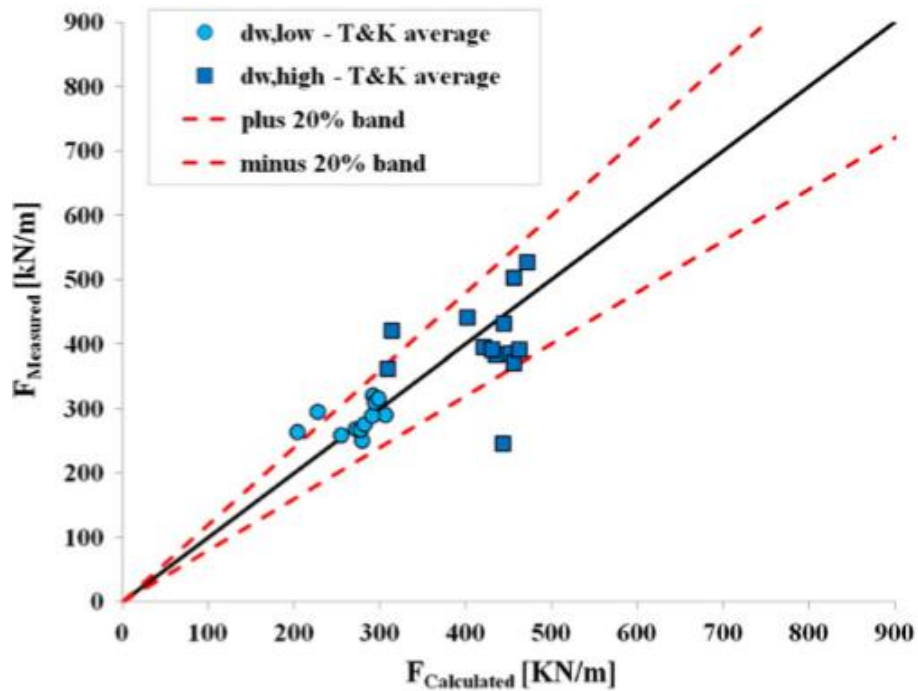
Figure 20. Measured versus calculated forces using Tanimoto and Kimura [91] average of impulsive and non – impulsive Goda formula [39] on the front sloping wall [106].
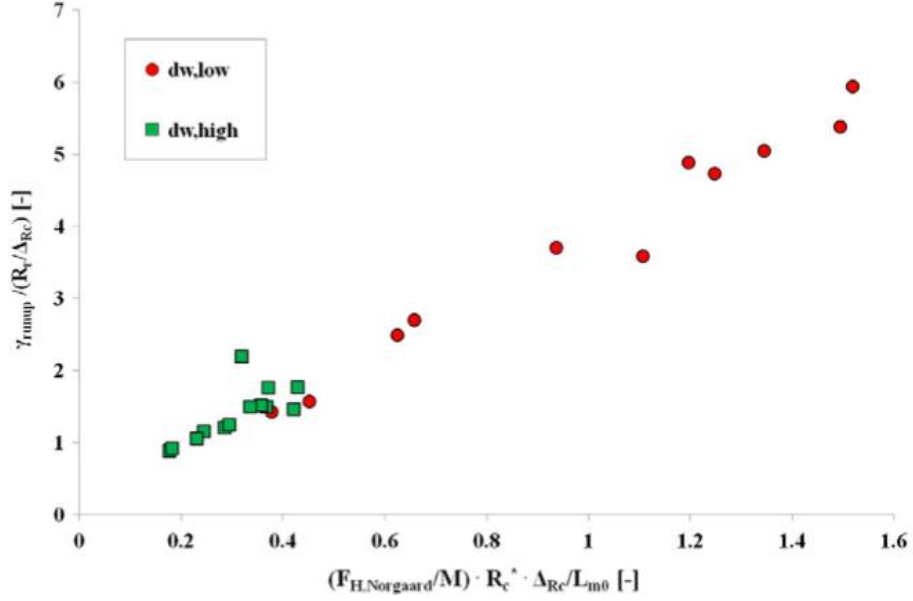
Figure 21. Functional law between γ_{runup}, horizontal forces calculate by Nørgaard formula [73], moment flux and main geometrical parameters of OBREC [106].

During the second laboratory campaign, the overtopping process was improved by including a submerged part of the sloping plate that slightly increases the wave reflection. This aspect was more evident because of the absence of the berm in the 2014 configuration, as expected according to Zanuttigh et al. [118]. Iuppa et al. [48] demonstrated that the curved configuration is less efficient with respect to the flat one in terms of hydraulic performance, leading to lower overtopping discharge rates, approximately 22% less. Figure 22 shows the results obtained according to different values of R_r, i.e. freeboard of the plate [48]. However, the structural response of the latter was characterized by higher normal forces acting on the sloping plate (+30%, see Figure 23), lower uplift pressures on the reservoir bottom edge [20] and similar behaviour of the crown wall with respect to the curved configuration. Eventually, the best profile of the sloping plate should be further investigated to balance the energy production, the structural response and the coastal defence function, i.e. reduction of q_{rear}.
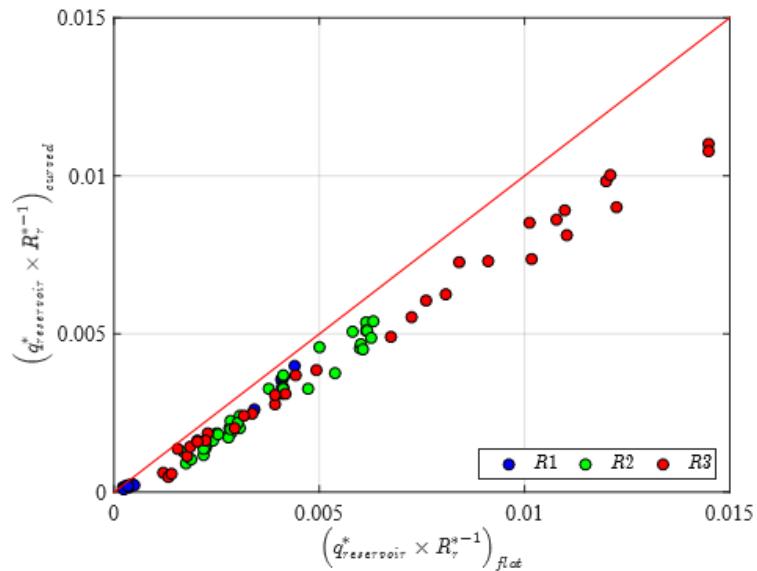
Figure 22. Overtopping into the front reservoir: $q^*_{reservoir}/R^*_r$ observed in the presence of the flat configuration versus $q^*_{reservoir}/R^*_r$ observed in the presence of the curved configuration [48].
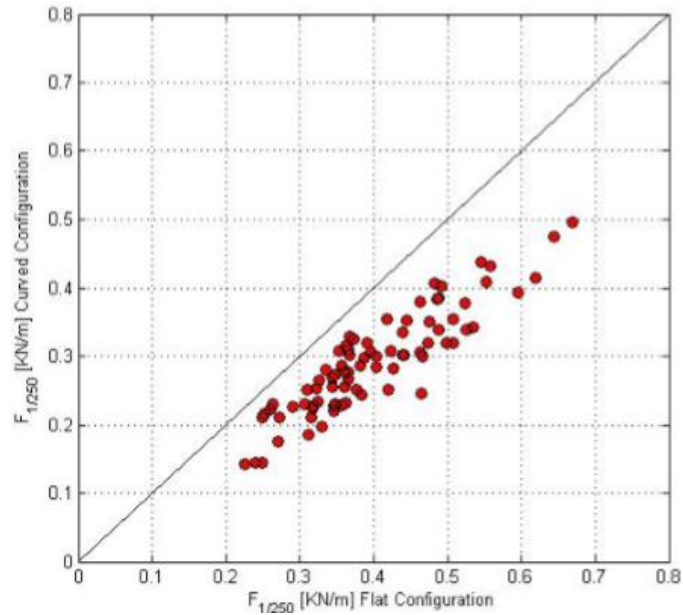
Figure 23. Measured forces on the front ramps between curved and flat configurations [20].

4.2   Field measurements at the OBREC prototype installation

The OBREC prototype was constructed in the port of Naples (Italy) in Middle Tyrrhenian Sea (Figure 24). The geographical coordinates of the site are 40°49'58.68'' N and 14°16'03.64'' E. According to the data gathered by the Italian Wave Buoys Network [105], the installation site is characterized by an average wave power flux of 2.5 KN/m. The low occurrence of extreme events makes this site ideal for a first installation. Indeed, few WEC technologies were constructed at a prototype scale, showing a common technical issue, i.e. the weak reliability with respect to the extreme events. Therefore, the pilot plant installation represents a fundamental step for the OBREC design improvement and the achievement of a commercial stage.

The OBREC was casted in – situ on the existing San Vincenzo breakwater, which protects the harbour inshore area. It is a traditional rubble – mound breakwater, provided with an armour layer made of Antifers, a filter layer made of rocks and a quarry run core. The freeboard level of the structure is about 4.50 m above the mean water level (i.e. 26 m at the toe of the breakwater), while the offshore slope is approximately 1:2 [22]. The construction process implied the removal of a portion of the layer of Antifers; the installation of the foundation composed by concrete micropiles (to improve the stability against sliding and overturning); the casting in – situ of the main body of the device (i.e. the reservoirs and the machine room) and the location of the prefabricated ramps [22]. This installation substituted a portion of the external layer damaged during several storm events (Figure 25a, b). Therefore, OBREC can be used as an innovative design option during the maintenance operations [19]. The prototype is composed by 2 configurations, i.e. OBREC RS – LAB (Real Scale Laboratory) and OBREC NW – LAB (Natural Waves Laboratory), which differ only for the height of the sloping plate above the mean low water level, i.e. 1.78 m and 0.98 m, respectively (Figure 25c and d, respectively). The selection of this parameter was based on the typical wave climate characterizing the installation site. The NW – LAB configuration is intended to capture the most frequent waves, while the RS – LAB the highest ones. For the prototype installation, a double plate configuration was considered, according also to the results obtained from the numerical investigations performed by Palma et

53

al. [77] (Section 5). Furthermore, a submerged quasi – vertical part of the ramp was introduced to i) improve its resistance to bending and fatigue, and to ii) enhance the interlocking between the rocks of the armour layer and the device. The longitudinal dimension of the installation is the same in both cases, having in common the crown wall and the machine room, where the turbines should be installed (see the prototype in Figure 24, and the OBREC sections in Figure 25c, d). This spatial constraint results in a different dimension of the reservoir width for the 2 configurations, i.e. 2.56 m and 3.7 m in Figure 18c, d. The wider reservoir is associated to the lower sloping plate, which is the more frequently overtopped; and vice versa. The sensitivity of the reservoir width with respect to the hydraulic and structural performance, as demonstrated by the experimental and numerical investigations [48, 77], can be neglected. Therefore, its definition, during the design procedure, can be subordinated to the height of the sloping plate.

The OBREC prototype was provided with a monitoring system (see Section 4.2.1) capable of associating the sea states, occurring in real time in the Gulf of Naples (see Section 4.2.3), with the hydraulic and the structural responses of the device. This monitoring activity was useful to assess the reliability of the prototype numerical model developed with the multi – phase code OF, and specifically with *waves2foam* (see Chapter 6). The numerical investigations were then extended to analyse the device performance under the typical wave climate of Naples, reconstructed thanks to the Italian Wave Buoy Network [105], and presented in sub – Section 4.2.2.

Figure 24. OBREC prototype installed in the port of Naples.
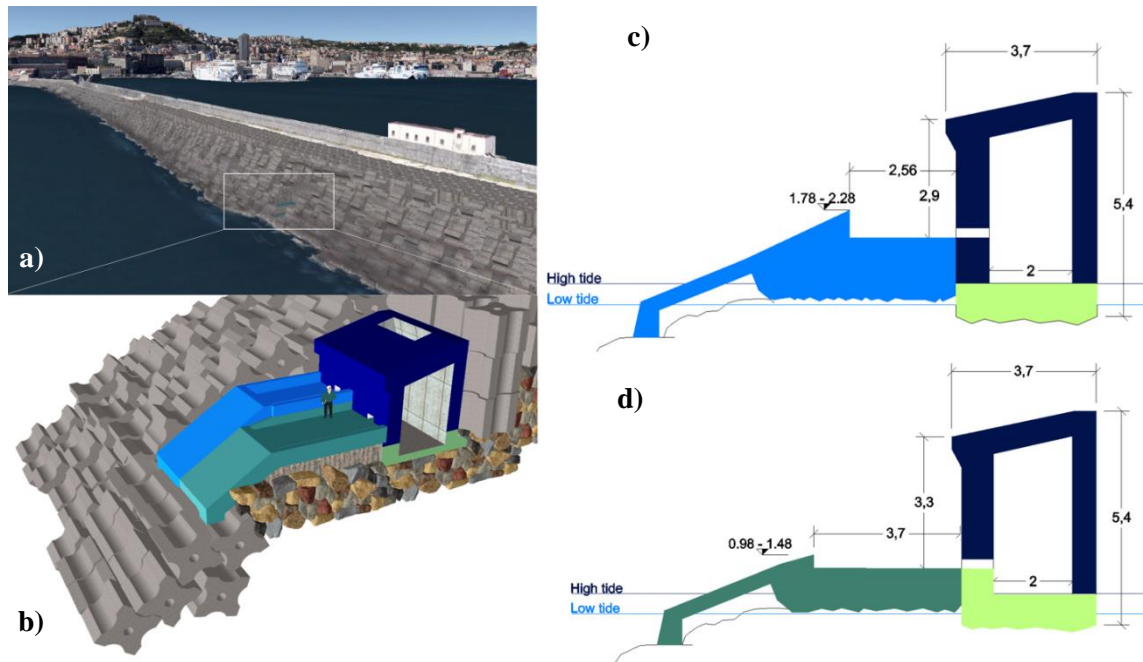
Figure 25. a, b) Render views of the location and the prototype installation; c) RS – LAB configuration and d) NW – LAB configuration composing OBREC.

4.2.1 Monitoring system and measurements

The full – scale pilot plant was provided with several instruments to measure the parameters useful to assess the OBREC performance under a real sea state. The objective is to increase the understanding of the response of the device, in order to improve its design according to the specific wave climate, to highlight the gaps of the laboratory experiments and numerical simulations due to scale effects and to simplify the description of the wave – structure interaction. The information gained have been combined with physical testing and numerical modelling to reach a more exhaustive and comprehensive understanding of all the processes.

The wave conditions occurring in the Gulf of Naples are measured by means of a wave buoy named Directional Wave Spectra Drifter (DWSD) and developed by the Scripps Institution of Oceanography (San Diego, US), using the Global Positioning System (GPS) technology [15]. The buoy is located 100 m far from the OBREC device and in 26 m water depth, with a bottom mounted Acoustic Doppler current profiler (ADCP), one directional radar and one moored waverider buoy [15]. The main information recorded are the significant incident wave height H_s and the associated wave period named T_m.

The structural response of the device has been analysed by means of 7 pressure transducers installed along the OBREC profile (Figure 26), here listed going from the lower part of the sloping plate going towards the bullnose. The transducers F, G and H were placed on the sloping plate of the RS – LAB configuration (Figure 27); while A, B and C on the crown wall and N on the bullnose of the NW – LAB configuration (Figure 28). Their characteristics have been selected based on the hydrodynamic loads theoretically expected and on the results obtained during the laboratory campaigns [106], and numerical simulations [35, 77]. They are capable of measuring i) the fluid temperature from - 40° to 125°, and ii) the pressures ranging from 0 to 100 bar, with a full scale F.S. precision at 25° of 0.4%. The output signals vary between 4 and 20 mA.

The OBREC principle of operation consists of using the potential energy of the water due to the difference between the still water level and the reservoir bottom edge. The available head is then exploited by means of turbines, which resulted to be the most reliable power take – off (PTO)

system for this kind of WEC [95]. To maximize the energy exploitation, the water flowing towards the turbines has to be as constant as possible. To this purpose, a shunt tank is located just after the pipe, linking the reservoir with the machine room. The hydraulic head in the shunt tank has been measured by means of a resistive gauge, characterized by an acquisition frequency of 10 Hz.

Figure 26. Pressure transducers installed on the OBREC device.

Figure 27. a) Longitudinal and b) flat sections of position of the pressure transducers for the RS – LAB configuration.

Figure 28. a) Longitudinal and b) flat sections of position of the pressure transducers for the NW– LAB configuration.

4.2.2. Meteomarine climate conditions at the site

The typical wave climate of Naples was assessed thanks to the Italian Buoys Network [105]. From the 1989, the buoys measured the significant wave height H_s smaller than 1.5 m every 3 hours; while greater than 1.5 m every 30 minutes, together with the mean wave period T_m and the mean wave direction θ_m.

Table 3 shows 8 sea states, which were reconstructed to describe the typical climate of the Gulf of Naples, characterized by H_s, T_m and a certain frequency of occurrence Fr during the year. As from Table 3, the sum of the frequencies does not cover the entire year, to account for the calm sea states, i.e. those characterized by $H_s < 0.25$ m.

The wave properties determine the energy flux P_{abs} per unit of wave – crest length, defined in Eq. (16).

$$P_{abs} = \frac{\rho g^2}{64} T_m H_{m0}^2 \frac{1}{1000} (kW/m)$$

(16)

By multiplying P_{abs} with n Fr, it is possible to obtain the annual theoretical energy flux per unit length P_{year}, as reported in Table 3. The values of P_{year} give a rough estimate of the hydraulic energy produced, by neglecting all the losses. This estimate could suggest the definition of some fundamental guidelines for the optimized OBREC design, with specific focus on the height of the sloping plate, which directly influences the overtopping process and so the energy production.

Table 3. Characteristics of the wave conditions of the typical climate of Naples.

Sea states	H_{m0} [m]	T_m [s]	P_{abs} [kW/m]	Fr [/]	P_{year} [kW/m]
1	0.25	2.25	0.06	0.3740	0.02
2	0.75	3.90	1.01	0.3171	0.32
3	1.25	5.03	3.61	0.1753	0.63
4	1.75	5.95	8.37	0.0705	0.59
5	2.25	6.75	15.68	0.0295	0.46
6	2.75	7.46	25.90	0.0130	0.34
7	3.25	8.11	39.33	0.0041	0.16
8	3.75	8.71	56.25	0.0034	0.19

4.2.3 The storms occurred in the monitoring period

During the first semester of 2018, 5 storm events were recorded, whose characteristics, including the peak period T_p, the significant and the maximum wave heights H_s and H_{max}, respectively, are reported in Table 4. The events show similar values of the parameters, however the storm event A was selected because of the clear distinction of a rising, a peak and a decay phase (see Figure 29). The analyzed field measurements belong to the peak phase, characterized by $H_s = 2.13$ m and a peak period $T_p = 8.37$ s. Specifically, the pressures signals are related to 6 hours of monitoring, in which the characteristics of the wave condition did not vary from their representative values.

Table 4. Storm events occurred at the beginning of the 2018, characterized by the mean period T_m and the significant and maximum wave heights H_s and H_{max}, respectively.

Storm event	Date	Duration [days]	H_s [m]	H_{max} [m]	T_m [s]
A	(6 – 10)/1/2018	5	1.99	2.47	5.58
B	(15 – 18)/1/2018	4	1.72	2.02	5.20
C	(1 – 4)/2/2018	4	1.98	3.07	5.85
D	(20 – 22)/3/2018	3	1.93	2.21	5.52
E	(31 – 2)/4/2018	3	2.47	2.81	6.36
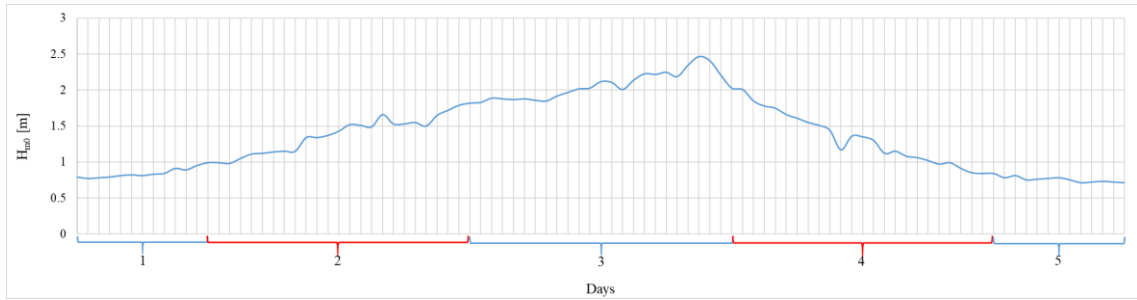
Figure 29. Variation of the significant wave height H_s during the storm event A, described in Table 4.

4.3 New laboratory campaigns on smooth dikes provided with a crown wall

This Section presents a new laboratory campaign on wave overtopping at smooth dikes with crown walls, which were carried – out in the small – scale wave flume of the University of Bologna in breaking and non – breaking wave conditions. The experiments were focused on the analysis of the wave loads acting along the crown walls, with specific attention to the effects induced by the inclusion of a sloping parapet on top. Different offshore slopes, dike crest widths, crown wall heights and dike crest freeboards were considered. A parametric analysis of the variation of the pressure distribution along the wall is performed, highlighting that a relevant role is played by the crest width under breaking waves.

This work was performed to increase the knowledge about the wave – structure interactions, with a specific attention to the wave loads acting on crown wall also in presence of a bullnose, as in the OBREC case. A small sub – set of the tests have been considered to stabilize and calibrate the new plug – in solver developed within the OF environment, to represent the role of the compressibility of the fluids.

4.3.3 Experimental setup and tested configurations

The experiments were performed at the wave flume of the Hydraulic Laboratory of the University of Bologna, which is 12 m long, 0.5 m wide and 1.0 m deep. The wave flume is equipped by a piston – type wave – maker that can generate regular and irregular wave attacks, with a maximum significant wave height H_s of approximately 0.06 m and a maximum wave length $L_{m-1,0}$ of $\approx$ 3 m. The water depth h at the wave – maker should not exceed $0.4 – 0.45$ m. All the experiments consisted of irregular waves, characterized by a Jonswap spectrum with a peak enhancement factor $\gamma = 3.3$, wave heights H_s in the range $0.05 – 0.06$ m and spectral wave periods $T_{m-1,0}$ in the range $0.85 – 1.45$ s, giving wave steepnesse $s_{m-1,0} \approx 0.03 – 0.04$.

The instruments installed in the wave – flume for the experiments consisted of:

- 4 resistive wave gauges (wgs), characterized by a sample frequency of 100 Hz and used to record the time series of the free – surface elevation; the first 3 wgs were placed at approximately 1.5·times the maximum $L_{m-1,0}$ ($\approx$ 3 m) to reconstruct the incident and reflected waves, based on the methodology proposed by Zelt and Skjelbreia [119]. The last wg was installed above the crest of the structures to measure the thickness of the overtopping layer.
- 3 pressure transducers characterized by the following mean features: sample frequency of 1 kHz; range of measurement from 70 mbar to 700 mbar; accuracy $\pm 0.04\%$ full scale; diameter of 25 mm, with internal diameter of 3 mm for the effective measurement of the pressures.
- A recirculation system, composed by a recirculation conduit, a pump and a flowmeter.
- A full HD camera employed to film the wave run – up and overtopping processes.

The full scheme of the wave flume with reference to the position of the wave gauges can be found in Zanuttigh & Formentin [115].

All the tested structures consisted of plain, smooth dikes with a finite crest width (G_c) and crown wall at its inshore edge. The crown walls are built with and without a parapet. Figure 30 provides a schematic representation of the typical cross section, with reference to the symbols used to describe the main structural and hydraulic parameters. Note that a simplified notation is adopted in the present contribution to characterize the geometry of the structures, with respect to the standardized schematization suggested by the EurOtop manual [32]. The dike offshore slope (α) is constant from the toe to the crest, the crest is horizontal and placed at the still water level ($A_c = 0$) or emerged ($A_c > 0$). The water depth in front of the structure ($wd = h$) is the same at the wave maker, as no foreshore, toe or berm is included.

Exactly in correspondence of the middle of the dike crest (i.e. at $G_c/2$), a wg was installed to record the free surface elevation of the overtopping events, allowing the reconstruction of the overtopping layer thickness. To measure the wave loads along the crown walls, the 3 pressure transducers – namely P1, P2 and P3 – were installed at 3 different positions along the wall, and specifically: P1 at the basis of the wall, P3 in correspondence of the basis of the parapet (both in case the parapet is present or not) and P2 in the middle between P1 and P3. These positions – detailed in Figure 31 for the 2 wall heights configurations, $h_w = 0.04$ and 0.05 m and shown in the picture of Figure 30 – were kept constant for all the tests. The axes of the pressure transducers were installed perpendicularly to the wall itself facing directly the incident waves. P2 was set in the mid front section of the wall, while P3 and P1 where placed to the left and to the right of P2 and as close as possible to the center, to avoid/reduce to a minimum the side effects induced by the walls of the wave flume.
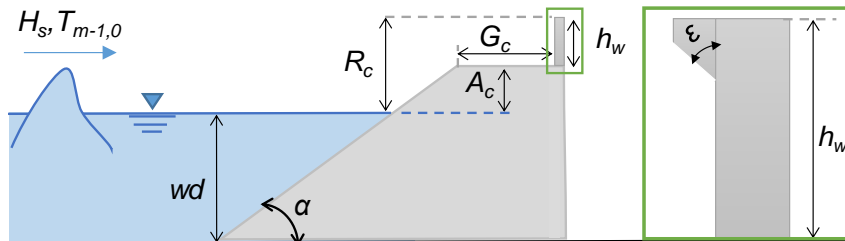
Figure 30. Scheme with hydraulic and structural parameters of the tested configurations.
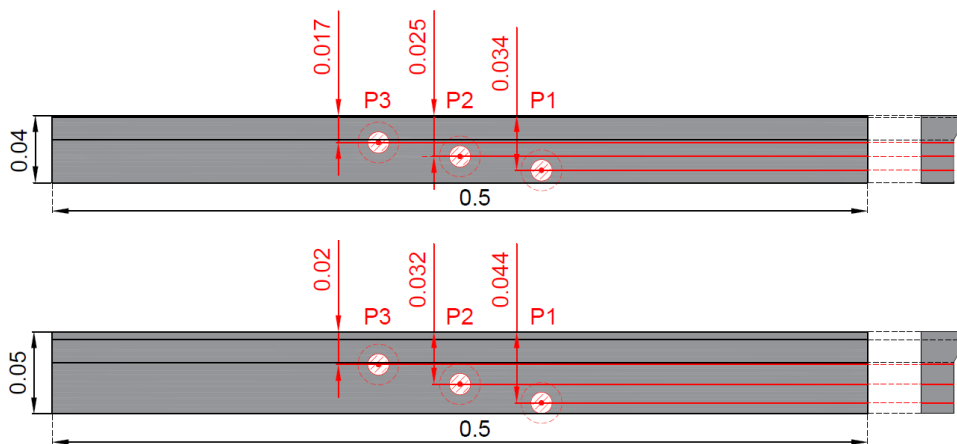
Figure 31. Front and cross sections of the 2 crown walls configurations ($h_w = 0.04$ and 0.05 m, respectively) tested in the lab with reference to the position of the pressure transducers P1, P2 and P3. Measures in m.

Overall, 128 tests were carried – out in scale 1:20. The hydraulic and structural features of the tested configurations reproduce exactly the tests conducted within the previous campaign of experiments on wave overtopping at dikes with crown walls and bullnoses by Zanuttigh & Formentin [115]. The wave attacks, characterized by $H_s = 0.05$ or 0.06 m and $s_{m-1,0} = 0.03$ or 0.04, were performed against 4 basic dike configurations, whose cross – sections differ for $G_c = 0.15$ or 0.3 m, and/or $\cot(\alpha) = 2$ or 4. Above each dike, was installed a vertical crown wall (wall heights $h_w = 4$ or 5 cm) with or without the parapet. The geometry of the parapet was fixed and characterized by a value of the parapet to wall height ratio $h_n/h_w = \lambda = 0.375$ and of the parapet inclination $\varepsilon = 30°$.

All the structures were 0.35 m high plus the crown wall heights h_w (so, 0.39 or 0.40 m) and were positioned at the same distance of 10.75 m from the wave maker (considering the dike offshore crest edge). Each dike configuration was tested at 2 crest – freeboard conditions, $A_c/H_s = 0$ or 0.5, giving total freeboard conditions R_c/H_s (see Figure 30) in the range 0.67 - 1.50. The 128 tests are the result of the combination of all the structural/hydraulic configurations obtained by varying each of the following parameters singularly: A_c/H_s, H_s, $s_{m-1,0}$, A_c/H_s, G_c, $\cot(\alpha)$, h_w, inclusion of the parapet.

The summary of the tested configurations is given in Table 5. The experiments include both breaking and non – breaking waves, where the value of the Iribarren – Battjes breaker parameter $\xi_{m-1,0}$ varied between 1.23 and 4.0. Figure 32 shows 3 frames show a plunging breaker reaching the wall in broken conditions, while 2 frames of an overtopping event for a surging wave (non-breaking wave type), where the breaking process occurs against the wall.

Table 5. Summary of the target conditions of the 128 experiments.

A_c/H_s	0	0.5
H_s [m]	0.05; 0.06	0.05; 0.06
$s_{m-1,0}$ [-]	0.03; 0.04	0.03; 0.04
$\cot(\alpha)$ [-]	2; 4	2; 4
G_c [-]	0.15; 0.30	0.15; 0.30
h_w [-]	0.04; 0.05	0.04; 0.05
parapet (ε, λ)	no; yes (30°, 0.375)	no; yes (30°, 0.375)
#	64	64

4.3.4 Analysis of the wave pressures

Oumeraci et al. [75] proposed a method to classify the type of the wave impacts for seawalls based on the distance between the breaking point and the wall: the lower the distance, the lower the entrapment of air pockets due to the turbulence induced by the wave breaking and – generally – the higher the magnitude of the pressure peak. Many studies demonstrated that the pressure peaks at walls are strongly affected by the amount of air pocket entrapment [83].

Considering the values of $\xi_{m-1,0} = 1.23 – 4.0$, the tested conditions present breaker types varying from plunging ($\xi_{m-1,0} < 2.0 – 3.0$) to surging ($\xi_{m-1,0} > 2.0 – 3.0$). As long as $A_c = 0$, it is assumed that the breaking point occurs before the structure crest, in case of plunging breaker, while it may be closer or rightly in front of the crown wall, in case of surging breaker. This hypothesis is indeed verified by the visual examination of the wave impacts: Figure 32 and Figure 33 show consecutive frames of 2 overtopping events reaching the crown wall respectively in broken conditions and breaking before the crown wall. The 2 events correspond to 2 tests at $A_c = 0$ and respectively characterized by plunging and surging break types. In case of $A_c > 0$, the wave breaking always

occurs along the dike slope in the wave run – up phase, before the wave reaches the crest. In such conditions, the flow over the crest is fully broken, with a significant level of air pocket entrapment.

In summary, according to Oumeraci et al. [75], the tested conditions can be classified as:

- impact type "c": plunging breakers, with small air pocket entrapments, in case of $A_c = 0$ and $\xi_{m-1,0} < 2.0$ (tests carried – out with $cot(\alpha) = 4$);
- impact type "d": surging breakers, where the wave hits violently against the wall before breaking and it is upward deflected, in case of $A_c = 0$ and $\xi_{m-1,0} > 2.0 – 3$ (tests carried - out with $cot(\alpha) = 2$);
- impact type "a": broken waves, where a turbulent bore flow impacts the wall, in case of $A_c > 0$.
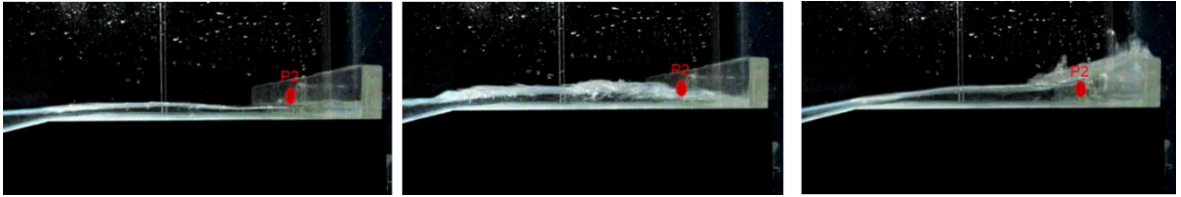
Figure 32. Consecutive frames of an overtopping event reaching the wall in broken flow conditions (plunging breaker). Test $A_c/H_s = 0.0$, $H_s = 0.05$ m, $s_{m-1,0} = 0.03$, $G_c = 0.30$ m, $cot(\alpha) = 4$, $h_w = 0.05$ m.
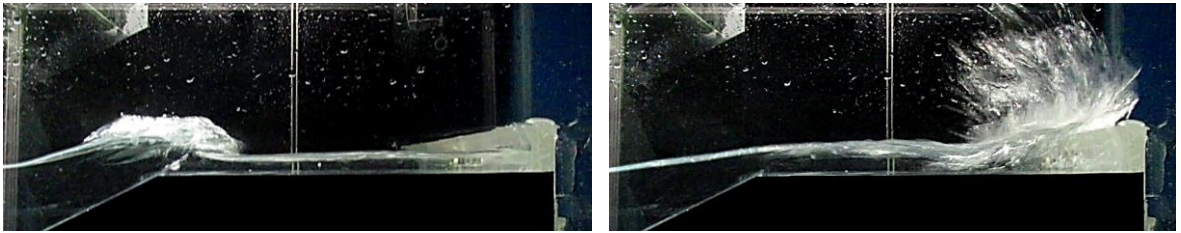
Figure 33. Consecutive frames of an overtopping event breaking rightly in front of the wall (surging breaker). Test $A_c/H_s = 0.0$, $H_s = 0.06$ m, $s_{m-1,0} = 0.03$, $G_c = 0.30$ m, $cot(\alpha) = 2$, $h_w = 0.04$ m with parapet.

Examples of the different pressure signals associated to the 3 breaker types are given in Figure 34. The 3 charts show 3 different impact events associated to: a surging breaker (panel a); a plunging breaker (panel b); a fully – broken wave (panel c). In each panel, the 3 differently coloured plots correspond to the p signals recorded at P1, P2 and P3. For all the tested conditions, P2 (orange signals) appears to be the most stressed pressure transducer, as it is subjected to the maximum pressures and it is reached by the wave impact before the other transduces. Except for this common thread, the p – signals and values are rather different for the 3 tested conditions and present features in line with the literature background.

- The surging breaker presents a sharp spike in the pressure variation, associated to the violent impact against the wall ($p_{max} \approx 2$ kPa). The impact is followed by a pressure trace that reproduce the typical "church spire" shape, where the quasi – hydrostatic pressure is clearly visible and the ratio $p_{max}/p_{h,q} > 2.5$. In case of P2, $p_{max}/p_{h,q} \approx 5$: this very high ratio value can be explained by considering that, in case of small scale tests, the pressure peaks might be significantly overestimated, if the Froude similarity law is adopted [27].
- The plunging breaker shows a pressure peak p_{max} that is at least 4 times lower than the peak associated to the surging case. The pressure signal after the impact in case show relatively slow and damped oscillations, which – according to Bullock et al. [12] – are due to a significant amount of air pockets entrapped in the plunging breaker and which induce alternative expansions and compressions of the air. The ratio $p_{max}/p_{h,q}$ is included between 1 and 2.5.

61

- The impact subsequent to a broken wave is significantly slower, with respect to the other cases, and presents a relatively modest pressure peak ($p_{max} \approx 250$ Pa). The impact is followed by slow and damped oscillations, revealing a huge amount of bubble entrapped. The ratio $p_{max}/p_{h,q}$ is definitely < 1.

In all the plots, sub – atmospheric values of p immediately after the impacts can be observed, similarly to the findings by Bullock et al. [12], during their large – scale tests at seawalls. The authors explained this phenomenon as a consequence of the air expansion phase subsequent to the wave impact.
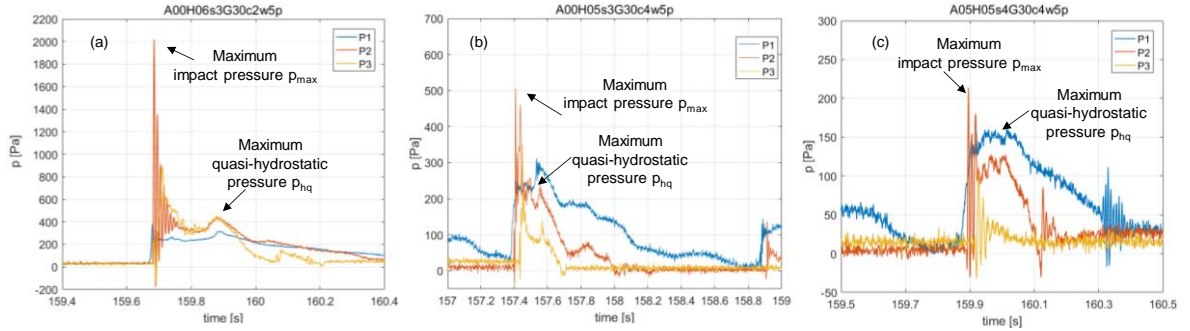
Figure 34. Time series of the pressures recorded at P1, P2 and P3 during 3 experiments with parapet relative to: surging breaker conditions (panel a, Test $A_c/H_s = 0.0$, $H_s = 0.06$ m, $s_{m-1,0} = 0.03$, $G_c = 0.30$ m, $cot(\alpha) = 2$, $h_w = 0.05$ m), plunging breaker conditions (panel b, Test $A_c/H_s = 0.0$, $H_s = 0.05$ m, $s_{m-1,0} = 0.03$, $G_c = 0.30$ m, $cot(\alpha) = 4$, $h_w = 0.05$ m) and broken wave conditions (panel c, Test $A_c/H_s = 0.5$, $H_s = 0.05$ m, $s_{m-1,0} = 0.04$, $G_c = 0.30$ m, $cot(\alpha) = 4$, $h_w = 0.05$ m).

The design forces can be calculated by integrating along the crown wall height the corresponding maximum and quasi – hydrostatic pressures, p_{max} and $p_{h,q}$. In the literature, the $p_{h,q}$ values are generally estimated through the p_{250} values [26]: this p_{250} estimator has to be evaluated as the average of the highest N/250 impact events, where N is the number of waves of the test time series.

Following the literature approach, the p_{250} values have been calculated for each test and for each pressure transducer. Table 6 collects the average p_{250} – values for the whole database (column "average") and for the datasets of tests at $cot(\alpha) = 2$ and $cot(\alpha) = 4$. The values have been made dimensionless through the group ($\rho g H_s$), where H_s is the significant wave height measured in channel. For each dataset, Table 6 also compares the p_{250} values to the corresponding average p_{max} values. Table 6 indicates that p_{max} can be 3 - 6 times p_{250}, i.e. significantly > 2.5. Generally, the higher differences between p_{max} and p_{250} are found at P2 and P3 and in case of c2. The high values of p_{max}/p_{250} can be explained by:

- the effects of small scale experiments, which induce overestimated maximum pressures [27];
- the presence of sub – atmospheric negative p – values, which were not discarded from the statistical analysis of the wave pressures and therefore affect the p_{250} estimators.

Table 6. Dimensionless average values of p_{250} and p_{max} at P1, P2 and P3.

Pressure transducer	$p_{250}/(\rho g H_s)$ [-]			$p_{max}/(\rho g H_s)$ [-]		
	average	$cot(\alpha)=2$	$cot(\alpha)=4$	average	$cot(\alpha)=2$	$cot(\alpha)=4$
P1	1.72	1.91	1.58	7.29	7.95	7.43
P2	2.06	2.37	1.83	10.11	11.24	9.99
P3	1.43	1.69	1.23	7.68	8.47	7.73

4.3.5 Parametric analysis of the results

Based on the statistics of p calculated at P1, P2 and P3 (see Section 4.3.4), the vertical profiles of the pressures along the walls have been reconstructed for each tested configuration. An example of the results is reported in Figure 35, which compares in each panel the vertical profiles of the dimensionless values $p_{250}/(\rho g H_s)$ calculated for a series of tests characterized by the same "basic" structure configuration c4 – w5. In each panel of Figure 35, the 4 graphs refer to the same wave attack and the same A_c/H_s, while they differ each other for G_c (0.15 and 0.30 m, respectively orange and green lines) and for the absence or presence of the parapet (continuous and dashed line, respectively). The 4 different panels are meant to be compared each other and present separately and in the order: the effects of A_c/H_s, which is increased from 0 (panel a) to 0.5 (panel b); the effects of the s_{m-10}, which increases from 0.03 (panel a) to 0.04 (panel c); the effects of H_s, which varies from 0.05 (panel a) to 0.06 (panel d).
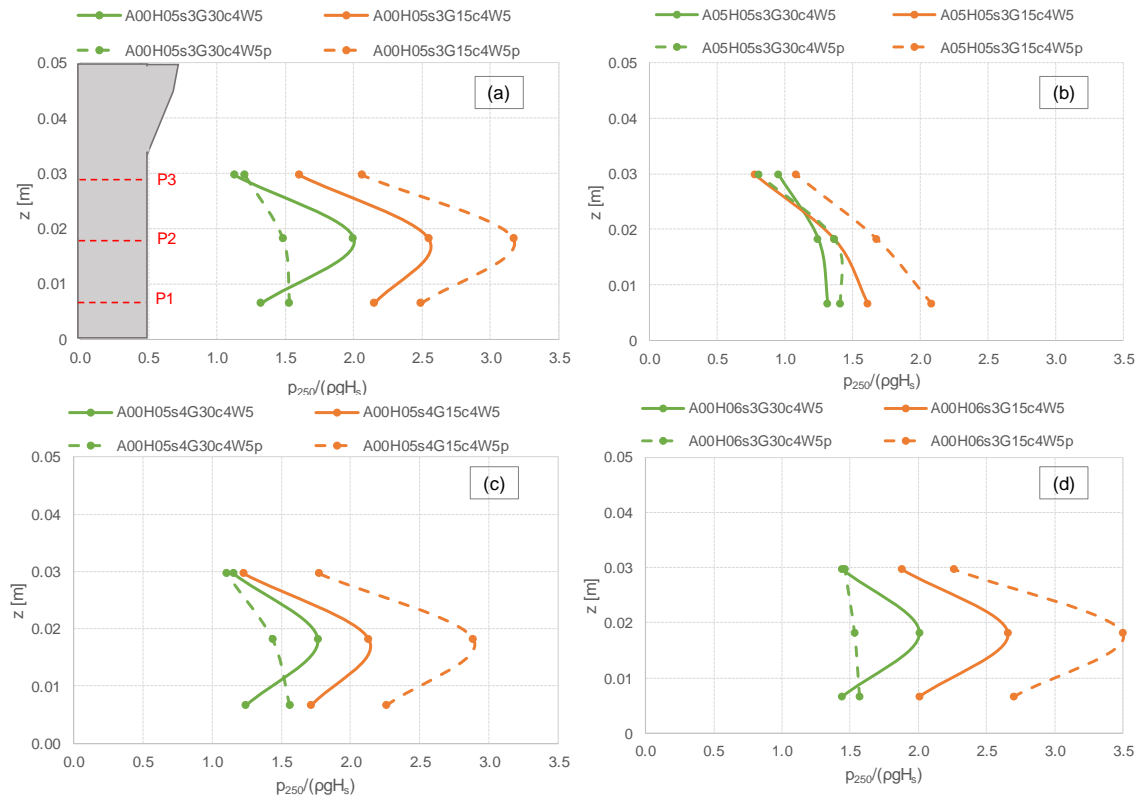
Figure 35. Vertical profiles of the dimensionless p_{250} values at P1, P2 and P3. Comparison between the same tests with and without parapet (same colour, continuous and dashed lines, respectively) and between the same tests with $G_c = 0.15$ and 0.30 m (orange and green colour, respectively). Panel a: structures at $A_c/H_s = 0$; panel b: structures at $A_c/H_s = 0.5$; panel c: tests with $s_{m-1,0}=0.04$; panel d: tests with $H_s = 0.06$. $cot(\alpha) = 4$, $h_w = 0.05$ m for all the plots.

The first evidence from Figure 35 is represented by the shape of the vertical distribution of the p values, which is strongly dependent on the crest freeboard conditions of the structure.

In case of structures at zero – freeboard ($A_c/H_s = 0$, see panels a, c and d of Figure 35), the peak of the wave loads is always found in correspondence of P2, i.e. in the mid – section of the vertical wall between the basis and the lower edge of the parapet. This result is quantitatively confirmed by the average values of $p_{250}/(\rho g H_s)$ and $p_{1000}/(\rho g H_s)$ reported in Table 6: in both cases, the statistical values of p are sensibly higher ($\approx + 20 - 40$ %) at P2 ($p_{250}/(\rho g H_s) = 2.06$, $p_{max}/(\rho g H_s) = 10.11$) than at P1 ($p_{250}/(\rho g H_s) = 1.72$, $p_{max}/(\rho g H_s) = 7.29$) and at P3 ($p_{250}/(\rho g H_s) = 1.43$, $p_{max}/(\rho g H_s)$

= 7.68). This result, which is evident also in the example p – signals of Figure 35, can be explained by considering the different dynamics of the wave overtopping and wave impact phenomena induced by the presence of the crest width. The frames of the overtopping and impact event reproduced in Figure 32 show that, after propagating along the dike crest (1st frame), the overtopping tongue impinges on the crown wall in correspondence of P2 (2nd frame). When the wave reaches P3 (3rd frame), it is already broken and has dissipated part of its energy, as it is evident by the relevant presence of air pockets due to the air entrainment.

In emerged conditions ($A_c/H_s = 0.5$, see panel b of Figure 35), the shape of the vertical distribution does not show the peak at P2 but presents a triangular distribution, with the maximum at the basis of the crown wall (P1) and the minimum in correspondence of the basis of the parapet. This shape may recall a hydrostatic – shape distribution, though the nature of the pressures is impulsive. Actually, the triangular shape is the result of the averaging of all the impacts during the test. Since the averaging is done considering the whole duration of the test, and since the number of wave impacts decreases from P1 to P3 due to the lowering number of waves reaching P2 and P3, the higher part of the wall is less frequently hit by the waves and more often unloaded, resulting in lower average p_{250} values.

The distribution of p_{max} is reported in Figure 36 for the same 4 tests of Figure 35b. Differently from p_{250}, p_{max} is not affected by the frequency of occurrence of the wave impacts and the vertical distribution of Figure 36 shows again the peak at P2, confirming that the mid – section of the crown wall is the most stressed. This phenomenon does not affect the statistics of p at $A_c/H_s = 0$ because in this case the run – up is significantly higher than at $A_c/H_s = 0.5$, and most of the incident waves reach all the 3 pressure transducers.
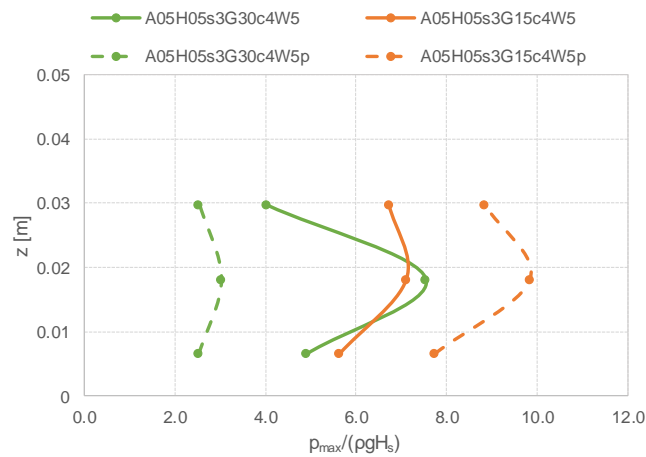
Figure 36. Vertical profiles of the dimensionless p_{max} values at P1, P2 and P3 for the same tests of Figure 35b.

Another technical aspect investigated during this laboratory campaign was the effect of structural and hydraulic parameters on the distribution of the wave pressures along the crown wall in case of breaking and non – breaking waves.

It has been verified that all the 64 tests carried – out with the dike slope c4 present breaking wave conditions, being $\xi_{m-1,0} = 1.23 – 1.94$. The vertical profiles of $p_{250}/(\rho g H_s)$ illustrated in Figure 35 are representative of most of the tests in breaking conditions, and are therefore used here as example cases for the analyses. Table 7 synthesizes the values of $p_{250}/(\rho g H_s)$ i) on the whole dataset (column "cot(α) = 4"); ii) by grouping the data into tests with and without parapet (columns "wall" – "wall + p"); iii) by grouping the test based on $G_c = 0.15$ or 0.30 m; iv) by grouping the tests according to $A_c/H_s = 0$ or 0.5.

Based on the example case of Figure 36 and on the results reported in Table 7, the following considerations can be drawn.

- The structure crest width determines a significant reducing effect of the wave pressures at any structure configuration and wave attack. The propagation of the overtopping flow along the crest width seems to be affected by a non – negligible friction effect. The reduction induced by $G_c = 0.30$ m with respect to the same test at $G_c = 0.15$ m (see Table 7) is almost constant along the crown wall height and on average $\approx 60 - 70\%$.

- All the plots in Figure 35 indicate that the reducing effect of G_c tends to be more pronounced if combined with the parapet (orange lines). In many cases (see panels a, c and d of Figure 35), the structures with $G_c = 0.30$ m and parapet (dashed green lines) show lower pressures than the same structures with $G_c = 0.30$ m without parapet (continuous green lines).

- The inclusion of the parapet does not induce a systematic effect on the pressure trend, neither at the basis of the parapet (P3) nor along the crown wall (P2, P1). By comparing the same structures under the same wave conditions, in some cases it is found that the wave loads are higher in presence of the parapet and in other cases without it. As it can be appreciated by the average values reported in Table 7, there are no substantial differences in the statistics of p_{250} in case of wall (1.53, 1.80 and 1.20 at P1, P2, P3, respectively) and wall with parapet (1.60, 1.78, 1.20). This result can be explained considering that the flow reaches the crown wall in fully – broken conditions (see Figure 32), i.e. far from the impulsive nature of the non-breaking flow determining huge impact loads in case of recurved walls [14, [5757].

- The values and the vertical distribution of the wave loads vary significantly between structures at zero – freeboard (panels a, c and d) and structures in emerged conditions (panel b). The discussion about the shape of the profile in case of $A_c/H_s = 0$ and 0.5 is already given in Figure 35. As for the entity of the wave loads, it can be appreciated from Figure 35 that in case of $A_c/H_s = 0.5$, the p_{250} values are reduced of $15 - 100\%$, according to the position of the pressure transducer (the higher the position, the higher the reduction) and the structure configuration. The values of Table 7 suggest that the average reduction varies from 15% at P1 to 50% at P3.

- The wave steepness and the wave height seem to play pure scale effects (compare Figure 35a to Figure 36c for $s_{m-1,0}$ and Figure 35a to Figure 36d for H_s) on the values and trends of p_{250}: the vertical profiles are simply translated towards lower and higher values for higher $s_{m-1,0}$ and H_s values, respectively.

Overall, the most affecting parameter seems to be G_c, even if the experiments have been carried – out against smooth structures. From a practical point of view, this result suggests that, in case of breaking waves, relatively modest enlargements of the structure crest widths could significantly reduce the wave loads acting on the crown walls.

Table 7. Dimensionless average values of p_{250} at P1, P2 and P3. Average values among the whole dataset of tests at $cot(\alpha) = 4$ (column "average – $cot(\alpha) = 4$") and comparisons between: structures with and without parapet (columns "wall" – "wall+p"); structures with $G_c = 0.15$ and 0.30 m; tests at $A_c/H_s = 0$ and 0.5.

Pressure transducer	$p_{250}/(\rho g H_s)$ [-], tests at cot(α) = 4 (broken waves)						
	average – cot(α)=4	*wall*	*wall+p*	G_c=0.15 m	G_c=0.30 m	A_c/H_s=0	A_c/H_s=0.5
P1	1.56	1.53	1.60	1.91	1.22	1.70	1.43
P2	1.79	1.80	1.78	2.19	1.38	2.18	1.40
P3	1.20	1.20	1.20	1.45	0.95	1.52	0.88

The tests characterized by the slope $cot(\alpha) = 2$ include non – breaking waves only, with values of $\xi_{m-1,0} = 2.38 - 4.03$. Figure 37 presents a few representative examples of the vertical profiles of $p_{250}/(\rho g H_s)$ for a selection of tests with the same basic structure configuration $cot(\alpha) = 2$, $h_w = 0.04$ m. Each panel presents the same wave attack (H_s, T_{m-10}) and the same value of A_c/H_s, while the graphs differ each other for G_c (0.15 and 0.30 m, respectively blue and grey lines) and for the absence or presence of the parapet (continuous and dashed line, respectively). The panels (a) and (b) are meant to show the effects of A_c/H_s, which is increased from 0 (panel a) to 0.5 (panel b). The effects of $s_{m-1,0}$ and H_s are not considered because there is no relevant difference with respect to the case of breaking waves (see Figure 35).

The average values of $p_{250}/(\rho g H_s)$ obtained on the whole dataset of tests at $cot(\alpha) = 2$ are reported in Table 8. The main difference between the breaking and non – breaking wave conditions is represented by the effect of parapet. Figure 37 and Table 8 (columns "wall" – "wall + p") clearly show that the parapet in case of non – breaking waves induces a systematic increase of the pressures along the whole vertical section of the crown wall. With respect to the same structure configuration and wave conditions, the entity of the increase of p due to the inclusion of the parapet ranges in average between 50 and 70%, reaching and exceeding in some cases the 100%.

The determination of higher impulsive pressures and forces along recurved seawalls, compared to vertical walls, is a well – known phenomenon [14, 57] and it is related to the impulsive nature of the impact. When the waves reach the dike crest and impinge on the crown wall in non – broken conditions, the parapet blocks the overtopping flow of the surging waves, causing a sudden stop of the water mass horizontal momentum and generating a pressure shock wave. This phenomenon is evident in the frames of the overtopping event in Figure 33. The increase of the wave pressures is modest in case of dikes (50 – 70%) with respect to seawalls (up to 2 times for breaking waves and even 10 times for surging non – breaking waves) due to the wave energy dissipation caused by the wave run – up and the wave propagation along the structure crest. These results may extend the literature experience of huge impulsive pressures acting on recurved walls to dike – type structures with crown walls under non – breaking waves.

A second important result is related to the effects of G_c. From the plots of Figure 37 and the values reported in Table 8, it is evident that the crest width does not play a systematic role in the reduction of the wave loads, differently from the cases of breaking waves. In some cases, the p – values are even higher in case of $G_c = 0.30$ m than $G_c = 0.15$, especially at P2 and P3. The marginal effect of G_c is again related to the non – breaking, energetic wave conditions characterizing the flow over the structure crest (see Figure 37). Furthermore, the higher run – up level associated to the non – breaking surging wave conditions determines thicker overtopping layers along the dike crest (compare Figure 33 to Figure 32) and the thicker the water layer, the less affecting the friction in the boundary layer along the structure crest and therefore the lower the wave energy dissipation.
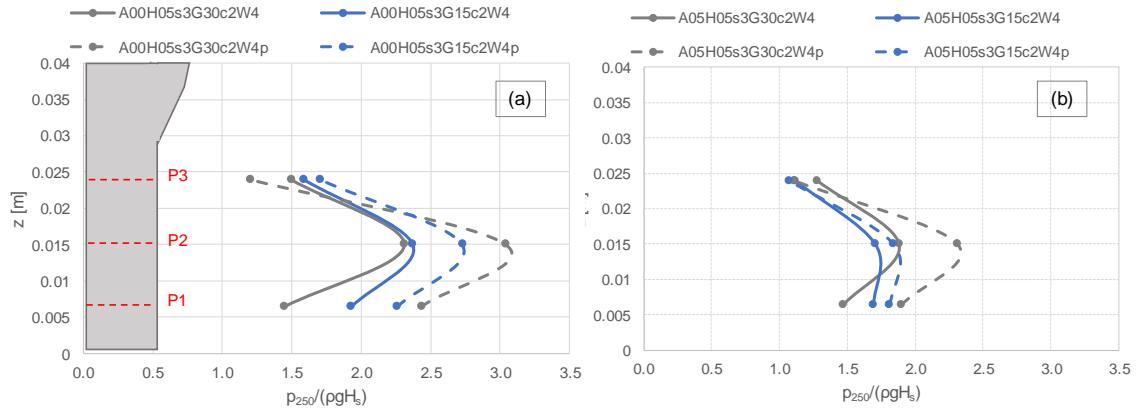
Figure 37. Vertical profiles of the dimensionless p_{250} values at P1, P2 and P3. Comparison between the same tests with and without parapet (same colour, continuous and dashed lines, respectively) and between the same tests with $G_c = 0.15$ and 0.30 m (blue and grey colour, respectively). Panel a: structures at $A_c/H_s = 0$; panel b: structures at $A_c/H_s = 0.5$. $cot(\alpha) = 2$, $h_w = 0.04$ m for all the plots.

Table 8. Dimensionless average values of p_{250} at P1, P2 and P3. Average values among the whole dataset of tests at $cot(\alpha) = 2$ (column "average – c4") and comparisons between: structures with and without parapet (columns "wall" – "wall + p"); structures with $G_c = 0.15$ and 0.30 m; tests at $A_c/H_s = 0$ and 0.5.

Pressure transducer	$p_{250}/(\rho g H_s)$ [-], tests at cot(α)=2 (non-breaking waves)						
	average – cot(α)=2	*wall*	*wall+p*	*G_c=0.15 m*	*G_c=0.30 m*	*A_c/H_s=0*	*A_c/H_s=0.5*
P1	1.91	1.79	2.00	2.01	1.76	2.03	1.78
P2	2.37	2.16	2.56	2.19	2.62	2.72	2.03
P3	1.69	1.47	1.87	1.49	1.95	1.95	1.43

To conclude, 128 new small scale experiments on wave overtopping and wave impacts at dikes with crown walls and parapet have been carried – out in the wave flume of the Hydraulic Laboratory of Bologna. The tested conditions consisted of irregular wave attacks and included both breaking non – breaking waves, with breaker types ranging from plunging ($\xi_{m-1,0} \approx 1.23 - 2$) to surging ($\xi_{m-1,0} \approx 2 - 4$). Different structure configurations were considered, by varying the dike slope, the crest width and freeboard, the crown wall height and the inclusion of not of the top parapet. Specific objective of the investigation was to carry out a systematic analysis of the effects of the structure geometrical parameters on the wave impacts acting on the crown walls.

A first analysis was carried – out to associate each tested configuration to a specific breaker type. In agreement with the literature [12, 83], it was verified that the nature and the magnitude of the impact loads and the shape of the pressure signal consequent to the wave impact are strongly dependent on the breaker type and the amount of air pockets entrapped. The maximum pressure peaks associated to the most violent impacts are associate to surging non – breaking waves and low air entrapment conditions.

The signals of the wave pressure of each test have been further analysed to calculate the statistical values of practical interest, p_{250} and p_{max} and reconstruct the vertical profiles of the wave pressures along the crown walls. By comparing the statistics resulting from the different configurations, the following main outcomes were found.

- The maximum pressures are localized around the mid – section of the crown wall, were most of the impacts are concentrated;
- A substantial difference occurs between the tests in breaking/broken and non – breaking wave conditions;

- In case of breaking/broken waves, the crest width G_c significantly contribute to reduce the magnitude of the impacts. For the same test conducted against the same structure, reductions of p_{250} up to $60 - 70\%$ were observed in case of larger G_c configurations. Increasing the crest width might represent an effective method to reduce the enhanced loads due to the introduction of the parapet on the crown wall;
- In case of non – breaking waves, the effect of G_c is negligible. On the contrary, the inclusion of the parapet induces a severe increase of the p_{250} values along the whole vertical section of the crown wall. The average rate of increase of $50 - 70\%$. From a practical point of view, it is suggested to avoid the inclusion of parapet in case the structure is expected to be subjected to surging waves.

These small – scale tests may be affected by side wall effects, viscous forces and surface tension. However, the good agreement of the measured and theoretical [115] demonstrates a modest effect of the walls, while the visual observation of the turbulent flow and of the air entrainment are a clear sign that the viscous forces and the surface tension are limited.

5. From laboratory to prototype scale: design optimization with IH – 2VOF

The numerical modelling of the OBREC device performed with the single – phase code IH – 2VOF [60, 63] was aimed to support and extend the results obtained during the laboratory campaigns [20, 48, 106] (summarized in Section 4.1), to define some fundamental guidelines for the design of the OBREC pilot plant, installed in the port of Naples (Italy).

Specifically, the model calibration was essentially based on both the configurations tested during the 2012 campaign [106], i.e. $d_{w,low}$ and $d_{w,high}$. It was carried – out by considering a sub – set of the most representative wave conditions, i.e. ordinary and extreme, reported Table 2, together with the main geometrical characteristics.

Then, the numerical investigations, based on the $d_{w,high}$ configuration, were aimed to assess the influence of some geometric parameters on the hydraulic and structural response of the device, extending the experimental database. All the geometries were tested under ordinary and extreme wave conditions.

5.1 Numerical model set – up

The setup of the numerical domain reproduces the model tests carried – out at Aalborg University in 1:30 scale [20, 48, 106]. Figure 38 shows the experimental flume that is 20 m long and is characterized by a horizontal bottom, followed by a 1:98 slope until the model.
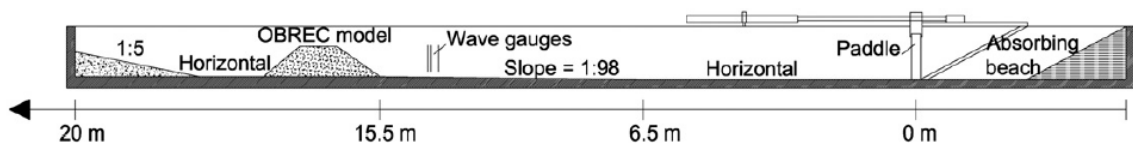
Figure 38. Layout of model test in 2D wave flume [106].

The wave flume and the structure were reproduced, at the laboratory scale in the numerical model, with the graphical tool CORAL. The length of the wave channel is equal to the experimental one, while the height was set equal to 1.05 m. The first 6 m of the domain were characterized by a 1:20 slope, followed by a horizontal bottom (Figure 39). Such a foreshore was introduced to have the same water depth at generation as in the laboratory tests, while minimizing the channel length.
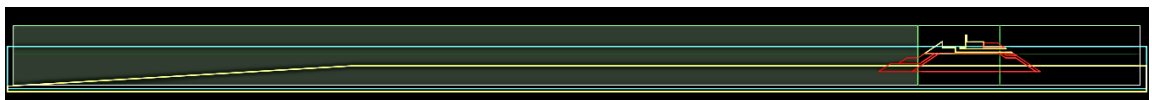
Figure 39. Layout of 2D model domain in CORAL software.

As shown in Figure 39, the domain mesh was divided in 3 zones along the flume (in the x direction) and 1 along the vertical (in the y direction), see Table 9. The definition of the extension and resolution of the zones depends on the position of the structure. The first zone corresponds to wave generation and transformation along the foreshore. The second zone falls around the central part of the structure, where the run – up and the overtopping phenomena occur. The third zone is inshore the structure. The second one was provided with a regular, very refined structured mesh to maximize the accuracy of the results useful to analyze the performance of the structure. The first and the third ones were characterized by a grading structured mesh, which was more refined

close to the structure, to reduce the number of cells and so the computational effort of the numerical model. In the y direction, a regular structured mesh was used with a minimum cell size, which depend on the wave characteristics.

Table 9 provides the information related to the mesh definition (Figure 40). For each sub – zone, the following parameters have to be defined:

- Center [m]: abscissa related to the end of the sub – zone;
- Division [m]: abscissa related to the beginning of the sub – zone;
- N° of cells to the left: number of the cells to the left with respect to the center;
- N° of cells to the right: number of the cells to the right with respect to the center;
- Maximum separation center [m]: minimum cell size of a specific sub – zone.

Table 9. CORAL mesh characteristics (x and y directions).

Sub – zones / Parameters	Subzones in x			Subzones in y
	Sub-zone 1	Sub-zone 2	Sub-zone 3	Sub-zone 1
Center [m]	16.04	16.06	17.50	0.50
Division [m]	0.00	16.05	17.49	0.00
N° of cells to the left	800	1	1	50
N° of cells to the right	1	143	100	55
Max. sep. center [m]	0.01	0.01	0.01	0.01
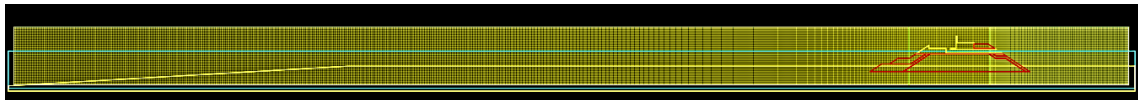
Figure 40. Layout of the CORAL mesh.

Figure 41 shows the mesh quality in the x direction, and in particular the cell size variation along the domain. The x axis provides the abscissa and the cell number inside the brackets, whereas the y axis the cell size. Therefore, the black line returns the cell dimension in a specific point of the domain, in the x direction. The cell size, initially equal to 0.3 m, then tends to decrease up to 0.01 m in correspondence of the first section of the second sub – zone, in which this value remain constant. This allows to obtain more accurate results in correspondence of the impermeable sloping plate and the reservoir. In the inshore part of the domain the cells size tends to increase up to 0.03 m, as in the wave generation zone.
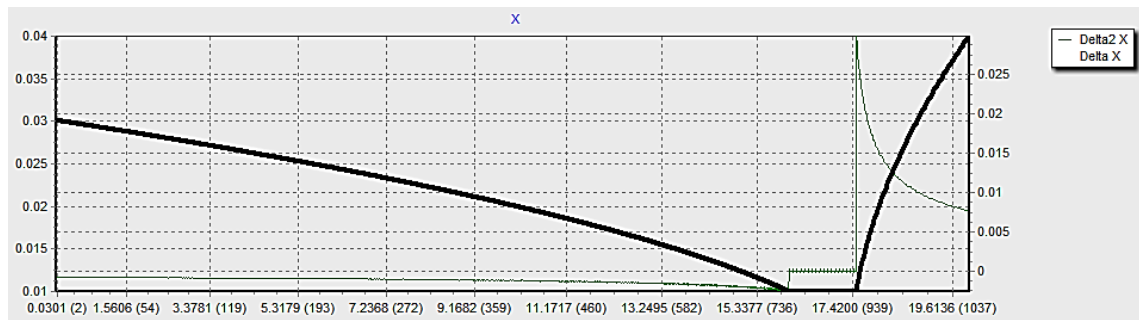
Figure 41. Quality of the CORAL mesh in the x and y directions.

Figure 42 shows the main OBREC geometric parameters. B_r is the reservoir width, B_s the horizontal extension of the sloping plate, α its inclination (equals to 34° in the physical model), d_w is the height of the sloping plate and R_r and R_c are the freeboard crests (with respect to the

70

mean sea water level) of the sloping plate and of the rear wall, respectively. Specifically, Figure 42a and b show the reference traditional breakwater and the physical OBREC model used in the 2012 experimental campaign, while Figure 42c the numerical model of the device in IH – 2VOF.
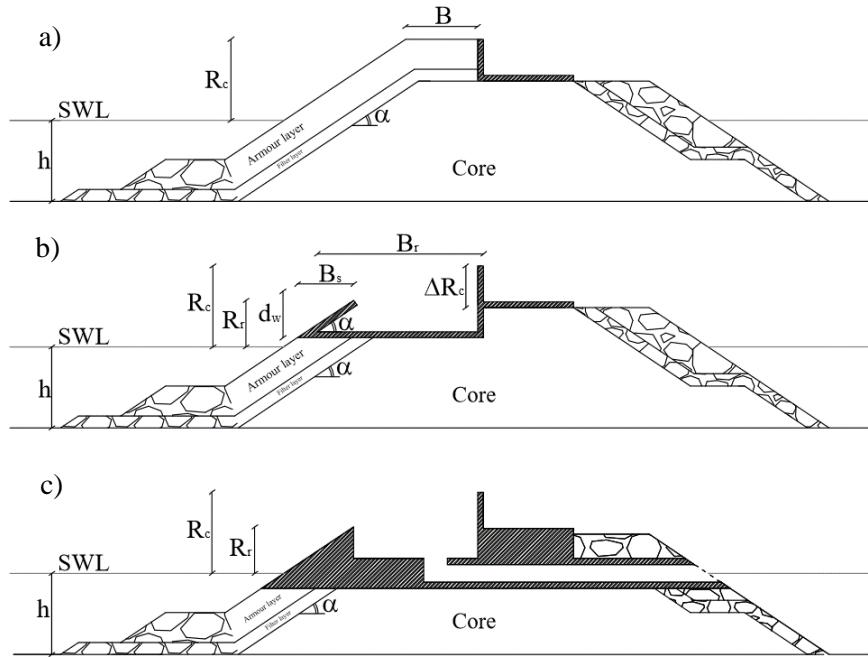
Figure 42. (a) The traditional rubble mound breakwater, (b) the OBREC physical model, and (c) the OBREC numerical model (adapted from Vicinanza 2014 [106], with permission from ELSEVIER, 2018). The main geometric parameters are: B_r the reservoir width, B_s the horizontal extension of the sloping plate, α its inclination, d_w the height of the sloping plate and R_r and R_c the freeboard crests of the sloping plate and of the rear wall, respectively.

To guarantee the numerical stability of the simulations and the correct representation of the physical processes, the cross section in the numerical model was slightly modified (Figure 42c). During the experiments, the water was pumped – out from the reservoir by means of external pipes, which were insufficient to avoid the saturation of the reservoir during the extreme tests (Section 4.1). The numerical cross section was modified by including an internal pipe from the reservoir bottom to the structure inshore slope to allow the water to freely flow out from the reservoir. The thickness of the OBREC slab foundation was slightly increased to avoid numerical instabilities induced by the limited thickness of the impermeable layer over the permeable structure in the run – up/down area, i.e. in an area characterized by very frequent changes of wet/dry conditions.

The breakwater used during the experiments is composed of a rock armour, a filter layer and a core. The average size of the rocks are $D_{n50} = 40$ mm for the armour layer, $D_{n50} = 20$ mm for the filter layer and $D_{n50} = 2$ mm for the core, which were set equal in the numerical model. Here, several values related to the porous media characteristics have to be defined such as the porosity itself n, the added mass coefficient c_A, the linear α and non – linear β friction coefficients. These last 2 parameters describe respectively the laminar and the turbulent flow properties in between the stones by means of the Forchheimer equation [34], already defined in Eq. (9).

5.2   Wave conditions and measurements

The irregular wave series, in the 2012 campaign, were generated based on the 3 JONSWAP spectrum parameters: the wave height H_{m0}, the peak frequency f_p and the so – called peak enhancement factor γ (3.3 in all the tests). The wave series considered at least 1000 waves. The numerical simulations were carried – out by defining H_{m0}, γ, the spectral wave period $T_{m-1,0}$, the water depth in the generation zone h and the duration of the simulation t. The simulation program was divided into 2 kind of test, i.e. "ordinary" (representing poor and mild wave climate) and "extreme" (representative of a severe storm condition) wave conditions. Table 10 contains the characteristics of both the ordinary and extreme wave conditions. Each numerical test considers at least 500 waves, which are sufficient to perform a statistical wave overtopping analysis as demonstrated by Romano [85].

Table 10. The characteristics of the ordinary and extreme wave conditions.

Tests	h (m)	H_{m0} (m)	$T_{m-1,0}$ (s)	R_c (m)	R_r (m)
Normal	0.27	0.077–0.149	1.327–2.090	0.155	0.27
Extreme	0.34	0.193	2.233	0.085	0.20

All the normal wave conditions – except for the one characterized by the smallest wave height H_{m0} (0.077 m) – are characterized by the same H_{m0} but different spectral wave periods $T_{m-1,0}$. Therefore, the tests chosen allowed the analysis of the hydraulic performance according to the wave steepness s_o.

Several wave gauges (WGs) were installed inside the numerical channel to evaluate:

- the reflection coefficient K_r, in normal conditions;
- the average overtopping discharge inside the reservoir $q_{reservoir}$, in normal conditions;
- the pressures p acting on the structure, under extreme conditions;
- the average overtopping discharge at the rear side of the crown wall q_{rear}, under extreme conditions.

A 3 – point method [65] was applied to derive the reflection coefficient K_r, by using WG1, WG2 and WG3 in Figure 43, located in front of the structure. The offshore wave gauge, WG0, was used to measure the generated wave height.
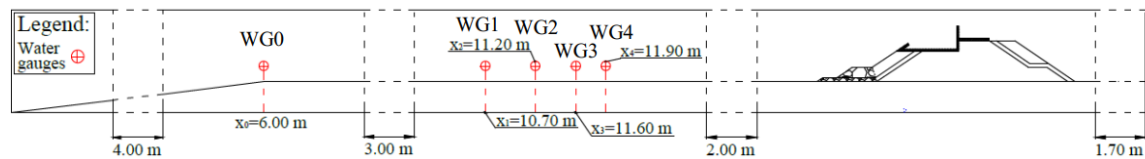
Figure 43. The positions of the wave gauges for the evaluation of K_r.

The numerical pressure transducers were placed along the structure in the same position as in the laboratory experiments (Figure 44). The sensors 13, 12, 11 and 10, during the experiments, were used to evaluate the uplift pressures, while in the numerical simulations, also the downward ones.
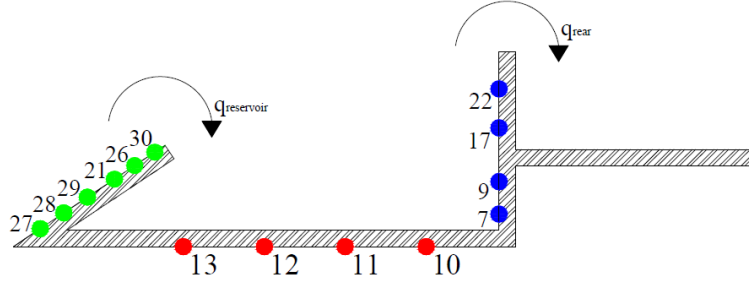
Figure 44. The positions of the water gauges to evaluate 1) the pressure acting on the device and 2) the $q_{reservoir}$ and q_{rear}.

The average overtopping discharges at the rear side of the OBREC (q_{rear}) was determined in the lab by using a ramp to guide the overtopping wave volumes into a box. A depth gauge was installed in the box to measure the overtopping discharge and to control the pump to empty the box at a given threshold level. Similarly, the overtopping discharge in the front reservoir ($q_{reservoir}$) was measured using depth gauges, which controlled several pumps. The 2D model was provided with a pipe to let the overtopping water flows towards the inshore edge, and 2 WGs were placed on the top of the sloping plate and at the rear side of the rear wall to estimate respectively the values of $q_{reservoir}$ and q_{rear} (Figure 44). The overtopping discharges were derived by integrating (along the vertical) cell by cell the horizontal velocity component multiplied by the cell height (i.e., z direction).

5.3 Calibration of the numerical model

Following Palma [77], the calibration of the 2D numerical model was aimed to reach the best representation of K_r and $q_{reservoir}$ under normal conditions, by varying the porosity values n and by keeping constant all the other parameters, wave attack included, to optimize the representation of the device hydraulic performance. Specifically, the coefficient β_F was set equal to 1000, while α_F to 1.1, 1.0 and 0.8 for the armour, the filter and the core layers, respectively. These values have been defined based on the literature [45, 64, 104].

Table 11 reports the values assigned to each layer together with the comparison between the experimental $q_{res,exp}$ and the numerical $q_{res,num}$ discharge flows. The final n was defined according to the best agreement, i.e., configuration 2 in Table 11.

Table 11. The experimental vs. numerical $q_{reservoir}$ obtained by varying the porosities n assigned to the layers of the breakwater, i.e., armour, filter and core.

Configuration	Armour	Filter	Core	$q_{res,exp}$ (l/m/s)	$q_{res,num}$ (l/m/s)
1	0.8	0.7	0.6	0.046	0.073
2	0.7	0.6	0.5	0.046	0.056
3	0.6	0.5	0.4	0.046	0.006
4	0.7	0.5	0.4	0.046	0.004

The 2D numerical model was tested then under all the normal wave conditions, already presented in Table 10, to determine K_r, $q_{reservoir}$ and therefore the reliability of the numerical model. In order to compare the numerical $q_{reservoir}$ with the experimental values and the theoretical formulations, they were non – dimensionalised. Furthermore, by following the definition proposed by Ahrens and Heimbaugh [1], in Eq. (17), it has been possible to take into account the difference between the wave spectra generated in the lab and in the numerical wave channel. The theoretical formulae considered to evaluate the overtopping discharge are reported in Eq.s (18)

and (19), and correspond to those adopted in the EurOtop [32] to assess the same phenomenon on the slopes such as dikes, levees and embankments. The values of α_{off} is the offshore slope angle, while γ_b is the berm influence factor, γ_f is the roughness influence factor, γ_β is the oblique wave action influence factor, γ_v is the influence factor for a vertical wall, $\xi_{m-1,0}$ is the breaker parameter and R_r is the freeboard crest of the sloping plate.

$$q^{*}_{reservoir} = \frac{q}{\sqrt{g \cdot H_{m0}{}^3}} \tag{17}$$

with a maximum of

$$\frac{q}{\sqrt{g \cdot H_{m0}{}^3}} = \frac{0.023}{\sqrt{\tan \alpha_{off}}} \cdot \gamma_b \cdot \xi_{m-1.0} \cdot \exp\left[-\left(2.7 \frac{R_r}{\xi_{m-1.0} \cdot H_{m0} \cdot \gamma_b \cdot \gamma_f \cdot \gamma_\beta \cdot \gamma_v}\right)^{1.3}\right] \tag{18}$$

$$\frac{q}{\sqrt{g \cdot H_{m0}{}^3}} = 0.09 \cdot \exp\left[-\left(1.5 \frac{R_r}{H_{m0} \cdot \gamma_f \cdot \gamma_\beta}\right)^{1.3}\right] \tag{19}$$

Figure 45 shows that the numerical model slightly and systematically overestimates the reflection coefficients. The deviation is on average equal to 15%, and it increases with the increasing of s_o. The differences between the experimental and the numerical cross sections affect the reflection phenomenon because in the latter case, the thickness of the impermeable part has been increased. However, such modification has no implication in the representation of the discharge flows inside the reservoir, i.e., $q_{reservoir}$. In fact, Figure 46 shows that the numerical $q^{*}_{reservoir}$ gives a better estimation of the laboratory results. The difference among the experimental, the numerical and the theoretical values obtained are statistically computed by means of 2 parameters, describing the error made, i.e., the root mean square error (RMSE) and the Willmott index (WI) [111], defined in Eq.s (20) and (21), respectively. The quantity "y" represents the dimensionless discharge rate, defined in Eq. (17). The subscripts "s" stands for the experimental data, while "mod" for the numerical and the theoretical ones are according to the analysis performed. Therefore, "$\bar{y}_s$" is the mean of the experimental discharge flows. A good representation of the experimental data is characterized by a RMSE value close to 0 and WI values close to 1. Indeed, the numerical RMSE and WI are equal to 0.005 and 0.75, while the theoretical ones to 0.007 and 0.59, respectively.

The difference between the experiments and the formulae was expected, as the formulae are essentially based on traditional structures and the calibration of the roughness factor is insufficient to allow greater accuracy [106].
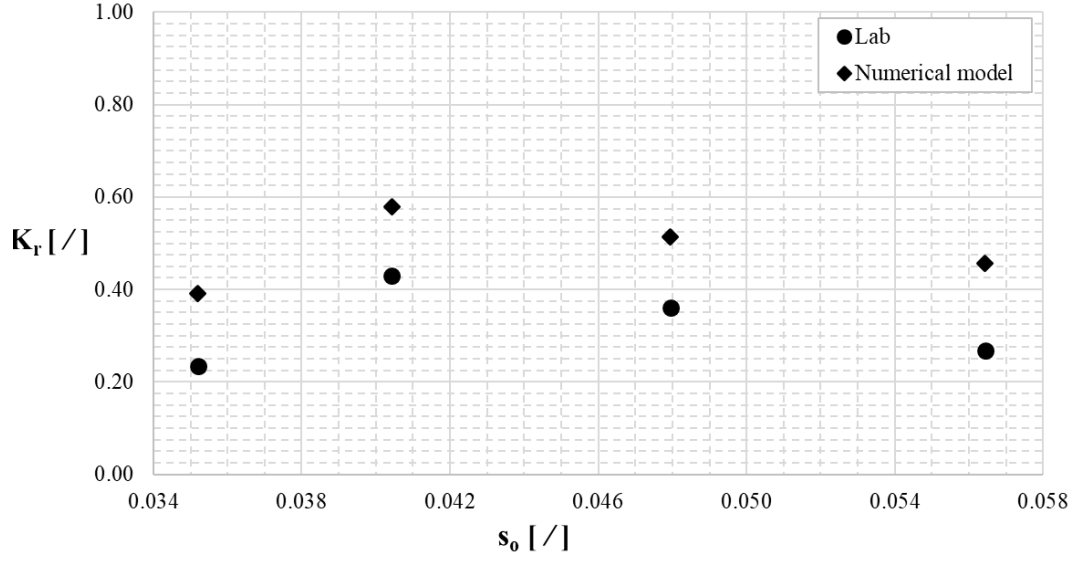
Figure 45. The laboratory vs. numerical model K_r for the normal wave conditions only.
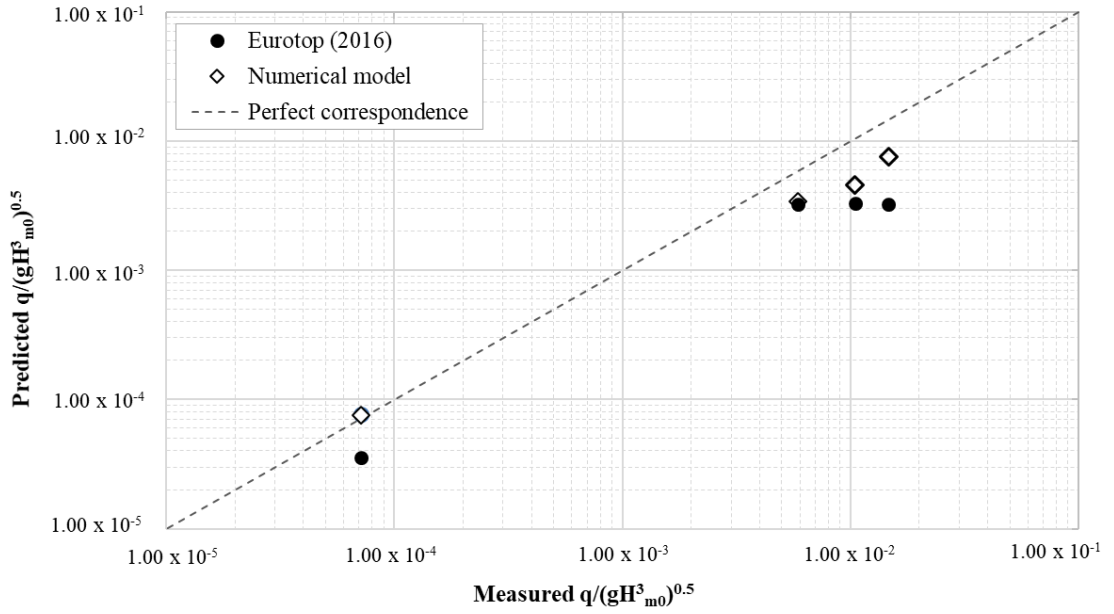
Figure 46. The numerical and theoretical vs. laboratory $q*_{reservoir}$ for the normal wave conditions.

$$RMSE = \sqrt{\frac{1}{N}\sum_{j=1}^{N}\left(y_{s,j} - y_{mod,j}\right)^2} \qquad (20)$$

$$WI = 1 - \frac{\sum_{j=1}^{N}\left(y_{s,j} - y_{mod,j}\right)^2}{\sum_{j=1}^{N}\left[\left|y_{s,j} - \bar{y}_s\right| + \left|y_{mod,j} - \bar{y}_s\right|\right]^2} \qquad (21)$$

5.4 Parametric analysis on the hydraulic and structural performance

Once the model calibration was performed, a sensitivity analysis has been carried – out by using 5 different geometries, which differ from the original one by changing one geometric parameter at once. The aim is to propose a design for the OBREC that maximizes the device exploitability, while obtaining the best compromise among energy production, harbour safety and easy installation.

5.4.1 Tested configurations

The hydraulic and the structural analysis were performed by varying the reservoir width B_r and the shape of the sloping plate (its inclination α); while keeping constant the sloping plate freeboard R_r (i.e. $d_{w,high}$ in Figure 16b) and its longitudinal dimension of B_s. Figure 47 shows all the tested configurations (named M1 – M5), whose main parameters are synthesized in Table 12.

M1 reproduces the 2012 laboratory $d_{w,high}$ configuration, as shown in Figure 47a. The differences between the laboratory and the numerical models were already discussed in the numerical set – up Section. This configuration represents a benchmark case in which it is possible to analyse the relevance of the berm in the wave – structure interactions. As a matter of fact, M2 corresponds to M1 except for the presence of this element (see Figure 47a and b).

To analyse properly all the parameters related to the OBREC device, M2 was chosen as the reference configuration. The compatibility of this kind of installations in breakwaters, not provided with a berm, was already analysed during the second laboratory campaign [48] and by means of preliminary numerical investigations [31]. Therefore, the other selected OBREC cross sections differ from M2 only for a geometric parameter at once, allowing the assessment of the effects of a specific element on the hydraulic and structural performance.

The configurations M3 and M4 were selected to analyse the change in the reservoir width B_r. The 2 cross sections imply a variation of B_r of the 25% with respect to the benchmark case. The aim of this analysis is to assess its relevance in the saturation of the reservoir, the maximization of the energy production, the limitation of the pressures along the crown wall and the values of q_{rear}.

The configuration M5 (Figure 47e) differs in the shape of the sloping plate. This section was designed according to the results obtained from the research aimed to optimize the WECs profile. Kofoed [54] proved that the adoption of a 30° inclined slope angle improve the hydraulic performance in terms of overtopping discharge. This result was then validated by Nam [70]. Such author considered also a double inclination for the ramp shape, with the submerged part having a vertical orientation, demonstrating its positive effects in increasing the run – up.

Table 12. Geometrical characteristics of the configurations analysed, shown in Figure 47.

Configuration	Berm	R_c [m]	R_r [m]	B_s [m]	B_r [m]	$\alpha_{off, plate}$ [°]
M1	√	0.27	0.155	0.3074	0.41	34°
M2	×	0.27	0.155	0.3074	0.41	34°
M3	×	0.27	0.155	0.3074	0.30	34°
M4	×	0.27	0.155	0.3074	0.50	34°
M5	×	0.27	0.155	0.3074	0.41	90°+30°
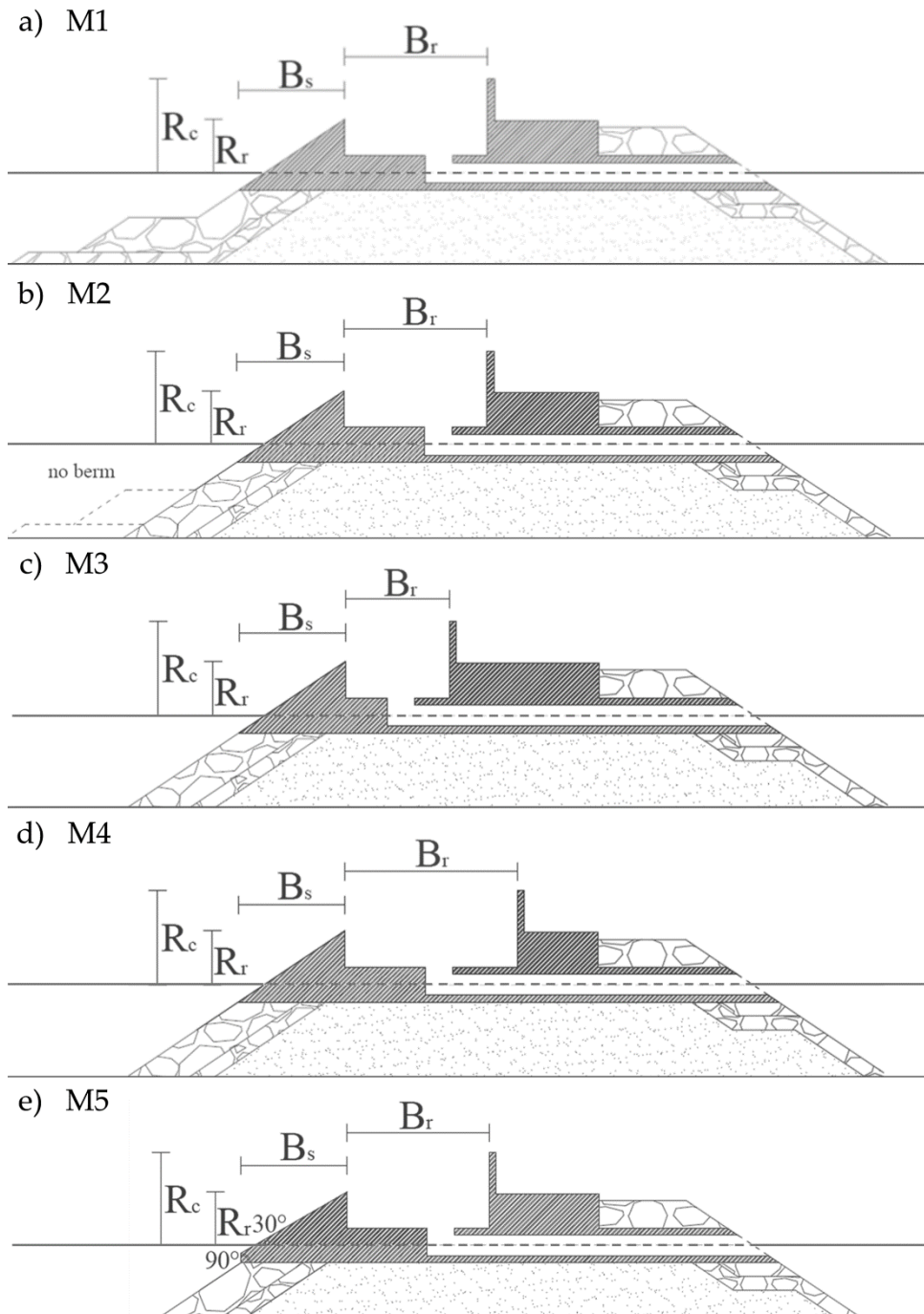
Figure 47. a) Original $d_{w,high}$ configuration (M1); b) Conf. without a berm (M2); c) $B_r = 0.3$ m (M3); d) $B_r = 0.5$ m (M4); e) Sloping plate 90°+30° (M5).

5.4.2 Effects of geometric changes on the hydraulic performance

The hydraulic performance of the OBREC device are here analysed in terms of K_r and non – dimensional overtopping at the rear of the structure, $q^*_{reservoir}$, under normal conditions.

Figure 48 shows the values of K_r versus the steepness s_o for all the configurations, under normal conditions. The laboratory results (already shown in Figure 45) is respected. The configuration M2 leads to greater values with respect to M1. This result was expected considering the work of Zanuttigh [118], who demonstrated that structures characterized by a submerged berm lead to a smaller K_r than those ones with a straight slope validated also by the study performed by

Formentin [35]. The design of a toe protection in case of an OBREC installation in a breakwater without berm should be taken into account.

The width of the reservoir B_r does not significantly affect the wave reflection, as it can be derived from the similar values of K_r for M2, M3 and M4. The value of B_r can therefore be selected based on the maximization of the energy production and on the minimization of the costs, while adapting the overall dimension of the device to the spatial constraints posed by the installation in existing breakwaters.

The shape of the sloping plate, instead, affects significantly the reflection phenomenon. The offshore angle of the ramp influences the wave run up, while the position of the change of the inclination with respect to the sea water level affects the dissipation induced by wave breaking. The configuration M5 shows similar results to M2, except for the first wave condition characterized by the smallest H_{m0}. As a matter of fact, the presence of a vertical element in the ramp shape has a greater influence on the smallest wave height. Therefore, it is important to consider the response of the structure with respect to the wave condition characterized by the greatest frequency in a typical wave climate.

In Figure 49 the values of $q^*_{reservoir}$ for M1 – M5 are compared with the results related to M2. The absence of the berm does not change the values of $q^*_{reservoir}$ with respect to M1, at least for the tests characterized by the greatest discharge rates and so the greater wave heights. Therefore, the higher reflection does not change in a significant way the potential power production.

The slightly lower values of $q^*_{reservoir}$ for M3 suggest that the reservoir is under – dimensioned. The greater reservoir size of M4 does not lead to a real improvement of the discharge rate. Therefore, it can be concluded that this parameter does not affect significantly the hydraulic performance of the device. Therefore, its design in existing breakwaters has to be focused on the height and the shape of the sloping plate that directly influence the overtopping phenomenon. The dynamic inside the reservoir is more connected to the position of the pipes, which lead the water to flow towards the turbines.

The configuration M5 shows the same result of M2. Therefore, the introduction of a vertical submerged part could be considered to generalize the OBREC cross section, without compromising its hydraulic performance.
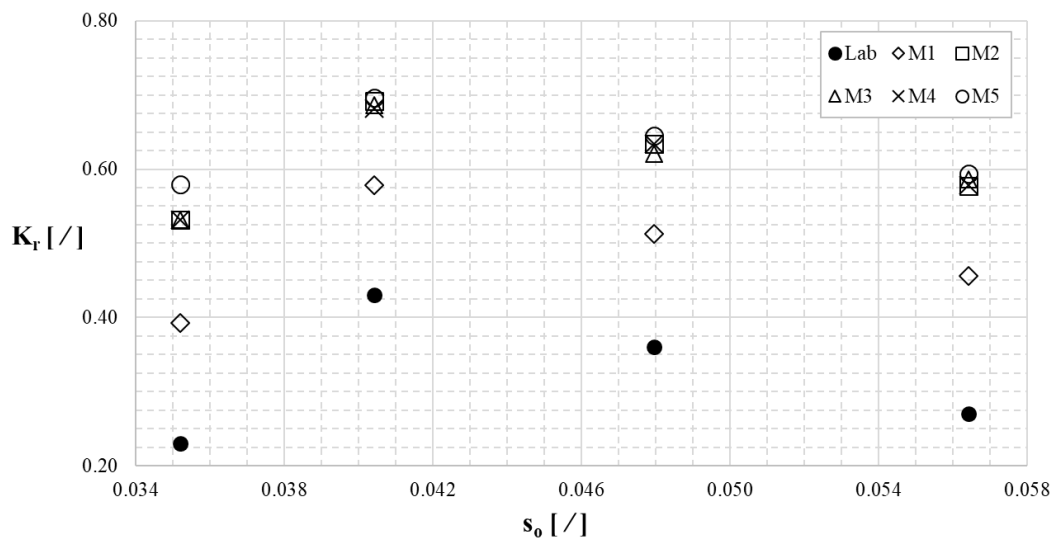
Figure 48. Comparison of the values of K_r for M1 – M5 configurations, under normal conditions only (Table 10).
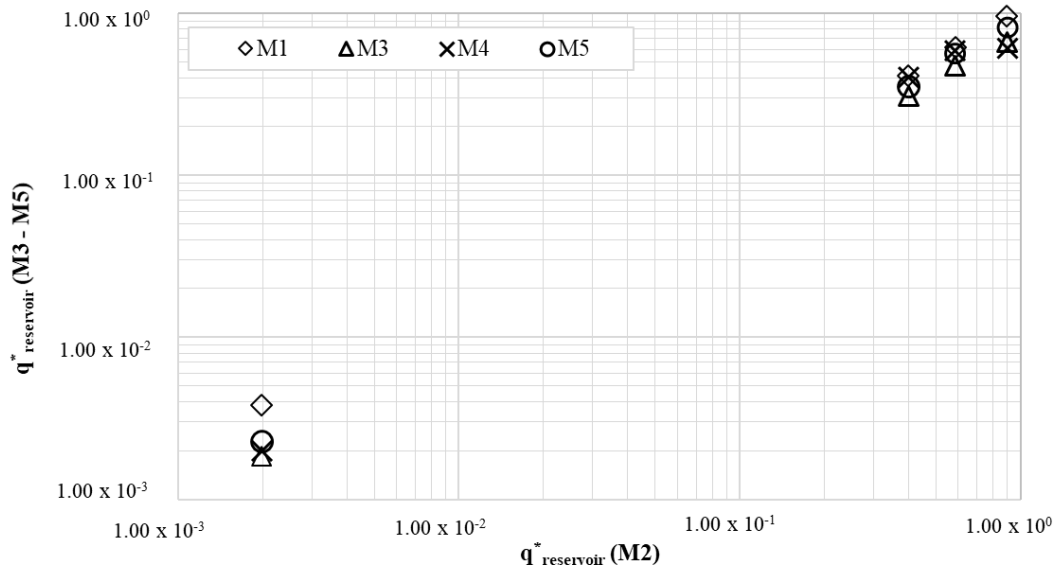
Figure 49. Non – overtopping flow rate at the rear of the structure, $q_{*reservoir}$, for M1 – M5 configurations compared with case M2 under normal conditions (Table 10).

5.4.3 Effects of geometric changes on the structural loads

The assessment of the loads across the structure was performed by using numerical pressure transducers, placed in the same position of the experimental ones (Figure 44) to perform a consistent analysis. The results discussed in this section are related to the extreme condition reported in Table 10. However, the modified geometry required some adaptation for a few cases. The configuration M3 includes 3 sensors along the reservoir, due to the reduced value of B_r. In M5 the sensors related to the sloping plate were shifted along the orthogonal direction that links the original inclination to the new ones.

The pressures are analysed in terms of p_{250}, which corresponds to the non – exceedance level of about 99.7%. Table 13 reports the values related to the sloping plate, the crown wall and the bottom part of the reservoir (uplift pressures).

The sample frequency adopted in the numerical model is lower than the laboratory one, to minimize the computational effort without compromising the accuracy of the results. A higher sample frequency in the numerical modelling would be required in case the model could reproduce the compressibility of the air, which usually leads to the highest impulsive peaks not so easy to be recorded. Therefore, the numerical results may underestimate the pressures acting on the elements exposed to wave breaking and to the water jet, such as the highest part of the sloping plate and the crown wall.

The configuration M1 reproduces well the experimental values along the sloping plate, with a small underestimation related to the upper part. The configurations M2 – M5 show values of p_{250} similar to M1.

The pressures related to the crown wall are very similar for all the configurations. The trend of the physical model is respected, but the discrepancy between the numerical and the experimental results increases from the bottom to the top of the crown wall. Only in the M4 case, all the discharge flows down in the wider reservoir, leading to an unstressed wall even in extreme conditions. This behaviour was found to be in agreement with the calculated pressure and physical model measurements on a 1.66 scale of a different overtopping device, named SSG (Seawave Slot – Cone Generators) [66, 107]. The authors attributed these differences to the absence of air in the numerical model. Therefore, some pressure peaks reduction (especially in the higher part of the crown wall) when compared to the physical model test could be experienced.

The uplift pressures are well estimated leading also to cautious values. This result is very useful considering that the uplift pressures represent the destabilizing force, which play a key role in the overall stability of the breakwaters top element [39].

The numerical model allows to obtain also the downward pressures (Table 14), where no direct comparison with the experimental data is possible. All the configurations show results very similar to each other, being the inshore corner, i.e. corresponding to the gauge 10_{in} (Figure 44), the most stressed part of the reservoir. This is not completely true for the configurations M4 and M5 due to the size of B_r and to the lower number of overtopping waves, respectively.

Table 13. p_{250} values acting on the sloping plate, the crown wall and the bottom part of the reservoir (uplift pressures) in kPa. See Figure 44 for the gauges location.

WG No.	Lab	M1	M2	M3	M4	M5
27	1.66	1.68	1.69	1.64	1.77	1.66
28	1.54	1.50	1.53	1.46	1.59	1.47
29	1.44	1.30	1.35	1.26	1.37	1.27
21	1.45	1.09	1.12	1.06	1.15	0.96
26	1.82	1.01	1.07	1.03	1.09	0.79
30	1.96	0.58	0.62	0.76	0.57	0.62
7	2.75	2.18	2.11	2.14	0	2.06
9	2.67	1.77	1.72	1.77	0	1.65
17	2.70	1.52	1.32	1.36	0	1.26
22	1.67	0.97	0.91	0.80	0	0.92
13	2.09	2.30	2.28	2.20	2.30	2.27
12	1.89	2.13	2.11	2.01	2.15	2.10
11	1.84	1.95	1.94	1.81	2.00	1.93
10	1.52	1.75	1.74	/	1.83	1.74

Table 14. Pressures acting inside the reservoir in kPa, with the same abscissa of the pressure transducers related to the uplift pressures.

WG No.	Lab	M1	M2	M3	M4	M5
13_{in}	/	1.71	1.73	1.84	1.75	1.77
12_{in}	/	1.60	1.60	1.75	1.54	1.62
11_{in}	/	1.80	1.83	2.06	1.64	1.82
10_{in}	/	2.06	2.07	/	1.83	2.01

5.4.4 Harbour safety

The harbour safety was evaluated in terms of q_{rear}, i.e. the average overtopping discharge at the rear side of the crown wall, in extreme conditions (see Table 10).

For these numerical simulations, the reservoir was closed to analyse the worst functioning condition, i.e. when the pipe is not capable of draining all the water that overtops the sloping plate.

In the 2012 experimental campaign, for the same wave condition, the values of q_{rear} measured for the OBREC case (Figure 42b) were higher compared to a traditional rubble mound breakwater with similar overall dimensions (Figure 42a) [106]. Therefore, a parapet (*nose*) was introduced on the top of the crown wall to increase the safety level of the area inshore the structure. The role

of the parapet is to redirect the up – rushing waves back into the front reservoir and towards the sea.

In this study case, the parapet was designed according to the work performed by Van Doorslaer [100], who investigated the effects of some geometrical parameters on q_{rear}, such as the crown wall height h_{wall}, the extension of the *nose* h_n and the inclination of the parapet ε (Figure 50).
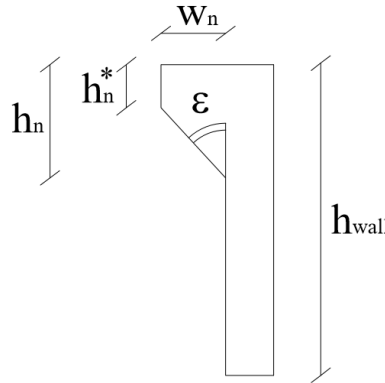
Figure 50. Scheme of a parapet, with all the geometrical parameters.

The larger the angle ε, the higher is the wave reflection inside the reservoir, resulting in smaller values of q_{rear}, as shown in Table 15. The optimal range for ε was found between 30° and 45°, which combines a good reduction of q_{rear} and a limited increase of the pressures on the wall in correspondence of the parapet, i.e. WG22, as shown in Table 16. Although the value of ε is the dominant geometric variable, q_{rear} also decreases with increasing h_n (Figure 50). The best reduction was achieved for $\lambda = h_n / h_{wall} \geq 0.3$. Based on these literature results, 2 parapet configurations have been considered, i.e. $\varepsilon = 30°$ and 45° and a fixed value of $\lambda = 0.3$. The resulting thickness of the *nose* w_n is equal to 0.027 m and 0.046 m, for $\varepsilon = 30°$ and 45°, respectively.

Table 15 reports the results of q_{rear} for the OBREC sections with and without the parapet. In case of the straight crown wall, the greater the reservoir width the lower the overtopping at the rear side of the structure. The presence of the nose reduces the values of q_{rear} by 34% and by 41%, on average, for $\varepsilon = 30°$ and 45°, respectively. For both inclinations, the configuration M3 shows the maximum reduction, i.e. the 70% and the 80% for $\varepsilon = 30°$ and $\varepsilon = 45°$, respectively. Therefore, the inclusion of the nose leads to a safe harbour area even in case of a constrained reservoir width.

Table 15. Average overtopping discharge at the rear side of the crown wall (q_{rear} [l/s/m]) for cases without parapet and with parapet ($\varepsilon = 30°$ and 45° respectively).

Configurations	M1	M2	M3	M4	M5
Crown wall	0.47	0.45	0.63	0.00	0.44
Crown wall and parapet (ε=30°)	0.28	0.30	0.19	0.00	0.31
Crown wall and parapet (ε=45°)	0.26	0.25	0.13	0.00	0.28

Table 16 shows the values of p_{250} inside the reservoir and along the crown wall to understand the effects, in terms of pressures, of the presence of the nose. Due to the absence of overtopping at the rear side of the structure, the configuration M4 was not analysed. Results of non – dimensional pressures acting on crown wall and inside the reservoir are graphically represented in Figure 51 and Figure 52, respectively. In order to provide general results, the relative positions of pressure transducer were considered non – dimensional. In particular, in Figure 51 the vertical distances from the bottom (z) rather than the wave height (H_{m0}) are shown. In Figure 52, the

relative abscissa (x) of pressure transducers from the seaward border of the reservoir has been non – dimensionalised respect to the reservoir width (B_r).

The presence of the parapet leads to higher pressures on the crown wall, which increase with the increasing of ε. The downward pressures are almost constant for all the configurations due to the load dampening caused by the presence of the water inside the reservoir, which is always saturated. Only for M3 the computed statistical values are slightly higher, due to the reduced value of B_r.

Therefore, the OBREC design has to consider the introduction of a parapet to reduce the overtopping at the rear side of the structure. The best configuration which optimizes the values of q_{rear} implied the parapet inclined of 45°, without increasing the pressures. The other geometric parameters, i.e. the berm and the reservoir width, do not affect q_{rear} and p_{250}.

Table 16. p_{250} values inside the reservoir and on the crown wall [kPa], for $\varepsilon = 0°$ (no parapet) $\varepsilon = 30°$ and $\varepsilon = 45°$. Position of the water gauges (WG) shown in Figure 44.

Wg	M1	M2	M3	M5
		$\varepsilon = 0°$		
7	2.18	2.11	2.14	2.06
9	1.77	1.72	1.77	1.65
17	1.52	1.32	1.36	1.26
22	0.97	0.91	0.8	0.92
13$_{in}$	1.71	1.73	1.84	1.77
12$_{in}$	1.6	1.6	1.75	1.62
11$_{in}$	1.8	1.83	2.06	1.82
10$_{in}$	2.06	2.07	/	2.01
		$\varepsilon = 30°$		
7	2.13	2.14	2.32	2.17
9	1.76	1.75	1.93	1.76
17	1.43	1.4	1.56	1.41
22	1.49	1.58	1.28	1.52
13$_{in}$	1.72	1.73	1.95	1.73
12$_{in}$	1.59	1.6	1.91	1.62
11$_{in}$	1.8	1.8	2.22	1.83
10$_{in}$	2.07	2.08	/	2.08
		$\varepsilon = 45°$		
7	2.39	2.18	2.4	2.23
9	2.05	1.8	2.01	1.85
17	1.88	1.44	1.64	1.57
22	2.38	1.54	1.57	1.83
13$_{in}$	1.76	1.74	2	1.76
12$_{in}$	1.69	1.62	1.92	1.67
11$_{in}$	1.91	1.84	2.27	1.89
10$_{in}$	2.26	2.12	/	2.15
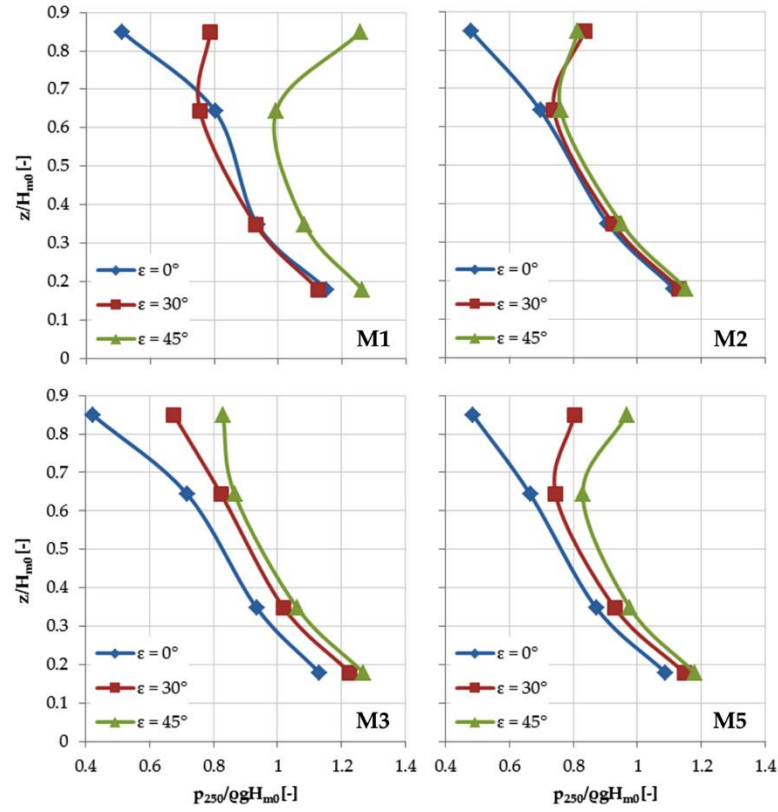
Figure 51. Non – dimensional pressures values along the crown wall.
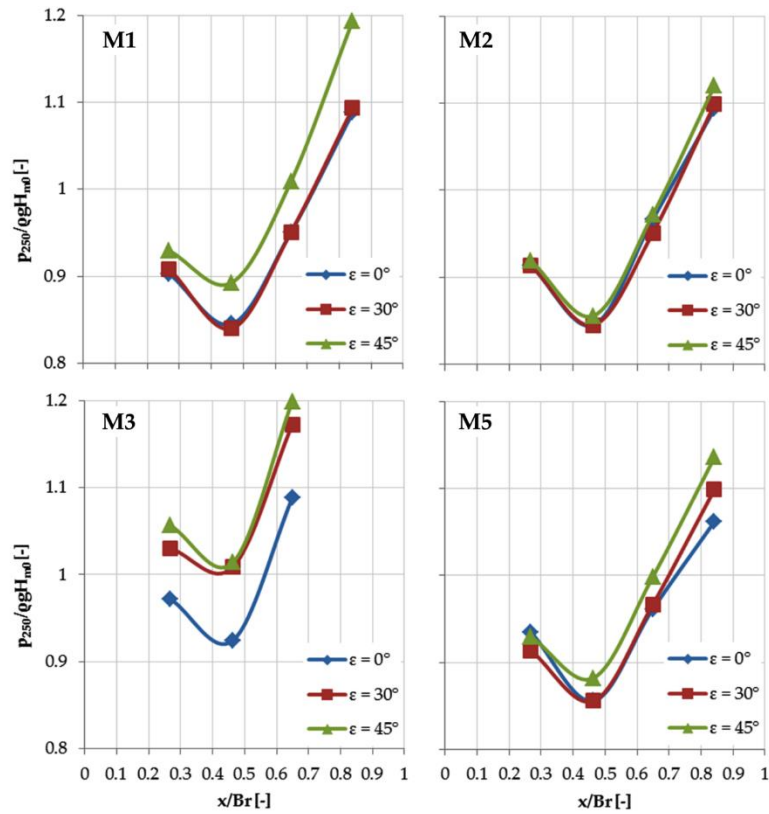
Figure 52. Non – dimensional pressures inside the reservoir.

5.5   Design of the OBREC pilot plant

The test campaigns performed during 2012 and 2014 were aimed to understand the general behaviour of the OBREC device and the relevance of its elements on the hydraulic and structural performances. However, to establish the fraction of extractable resource and safety performance, more detailed considerations were required. In principle, there is not "the best" OBREC cross section that may be used everywhere. It is expected that, depending on the selected site characteristics, some shape of the sloping plate could be more efficiently used than others. In any case, the selection of the optimal OBREC configuration is a complex matter, which cannot be done in a brief overview. For a site – specific installation, in fact, the design considerations have to be tuned based on the operating (normal) and extreme wave climate at the site. The design has to also account for the spatial constraints due to the harbour layout and the configuration of the existing breakwaters.

The main result observed from the numerical simulations here reported that the enhancement of $q^*_{reservoir}$ could increase the values of q_{rear}. In particular, assuming that the water jets follow the tangent of the ramp crest, which works as a deflector, the greater the hydraulic performances of the frontal sloping ramp, the greater the value of up – rushing water driven directly on the upper part of the crown wall is. This means a potential higher overtopping discharge at the rear of the structure and a higher pressure on the parapet.

Looking to the tested configurations, one of the best compromises is represented by the double shaped sloping plate (configuration M5). This kind of cross section does not affect significantly the wave overtopping inside the reservoir and is able to reduce the overtopping at the rear of the structure and also if a crown wall without a nose is considered. Then, not so high values of wave loading are measured. Furthermore, the idea behind M5 is to define a more general cross section, which can be easily placed on top of existing breakwaters independently from its off – shore slope. Therefore, the double plates configuration was considered for the first OBREC pilot plant (Figure 53). The prototype was installed in the San Vincenzo breakwater, located in the port of Naples [21]. The prototype cross section includes two configurations, i.e., NW – LAB (Natural Waves LABoratory) and RS – LAB (Real Scale LABoratory) shown in Figure 54.

Figure 53. The OBREC prototype installed in the San Vincenzo breakwater, port of Naples.
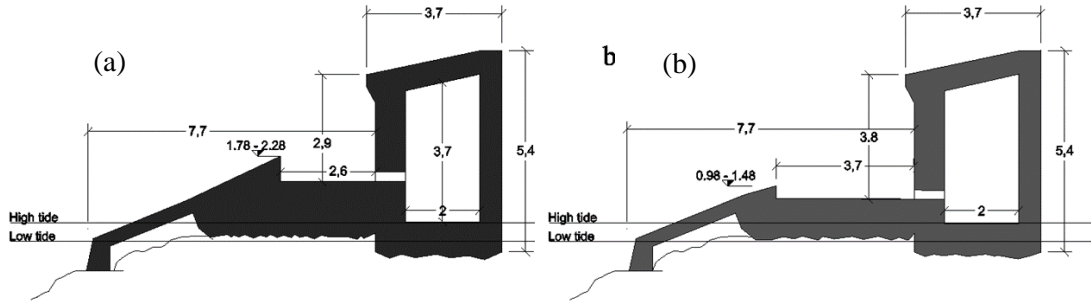
Figure 54. The cross sections of the OBREC prototype installed in the Naples harbour: (a) the RS – LAB (Real Scale Laboratory) configuration and (b) the NW – LAB (Natural Waves Laboratory) configuration.

They are characterized by the same longitudinal dimension, having in common the rear wall and the room for the turbines (Figure 53). This leads to the main geometric differences in the frontal part of the device. Indeed, they differ mainly in the height of the sloping plate R_r, and to meet the same spatial constraints, they have different dimensions of the reservoir width B_r. The two values of R_r have been selected according to the analysis of the typical wave climate of the site and to take into account the different turbine technologies, working with a different nominal head. The intention is not only to provide results for the sea climate at the study site but also to gather useful data easily exportable for more energetic sites. According to the analysis of the typical wave climate, the selected values of R_r for NW – LAB and RS – LAB are 1.2 m and 2.0 m respectively (values referred to the mean tide level). The corresponding values of the reservoir width are 2.6 m and 3.7 m. The lower value of R_r was selected according to the mean run – up of the most frequent wave (i.e., $H_s = 0.8$ m). The upper value of R_r was intended to capture the higher power generated by the higher waves. Its definition, however, followed a different approach. If one look at the maximum value of the power was multiplied by the wave frequency of occurrence (F), the prevalent wave height is associated to $H_{m0} = 2.2$ m, $T_p = 6.8$ s. In this case, however, the yearly average frequency of occurrence is too low ($F = 1.4\%$) corresponding to just five days per year. Therefore, considering that the lowest nominal hydraulic head of the greatest low head Kaplan turbine [109] is 1.5 m, a ramp crest of about 2 m (1.78 ÷ 2.28 m for low – and high – water levels respectively) has been selected. This value can guarantee an average of about 30 equivalent working days per year of the RS – LAB (the name Real Scale, hence, indicates the site – specific considerations made for that ramp crest).

Figure 54 shows, separately, the actual 2D OBREC cross sections, resulting from some modifications on the original project presented in Contestabile et al. [22]. It is possible to recognize some geometrical details derived from the results obtained from the experiments and the numerical simulations here presented. For instance, the submerged quasi – vertical part of the ramp has been introduced to improve the ramp resistance to bending and to fatigue. Furthermore, the interlocking between the rocks of the armour layer and the device is also enhanced.

As shown in Figure 54, the smaller reservoir is associated to the higher sloping plate and vice versa. In the first case, the number of overtopped waves is lower and can be handled by a reduced dimension of B_r. The wider reservoir is more appropriate for the lower sloping plate, which is overtopped more frequently. The sensitivity of this parameter with respect to the hydraulic and structural performance, as it has been demonstrated during the experimental and numerical analysis, can be neglected. Therefore, the selection of B_r can be done after the design of R_r.

To guarantee the harbour safety at the inshore area of the structure, a parapet has been placed on the crown wall. The effectiveness of this element increases as the dimension of the reservoir width decreases, ensuring an adequate safety level for both the configurations.

Differently from the laboratory and the numerical models, the prototype cross sections (Figure 54) are provided with a wave chamber where a new set of turbines is going to be installed to produce electricity. The bottom elevation of the chamber maximizes its difference with respect to the sea water level. The chamber is linked with the reservoirs by means of holes (Figure 53) and five pipes (Figure 54). The lowest hole along the wall aims to collect as much water as possible, maximizing the energy exploitation. The position and the size of the holes and the pipes have not been yet investigated due to the limitations of testing in 2D conditions. For this reason, a 3D investigation, capable of reproducing the dynamics between the reservoir and the wave chamber, is needed. The 3D numerical modelling of the OBREC pilot plant, which is composed by the two configurations here analysed, could improve the representation of the discharge rates. The realistic representation of the pipes can be the key to defining the design criteria to maximize the energy production.

To conclude, this work was focus on the development of a 2D numerical model of the OBREC device, calibrated in order:

- to extend the experimental database of the laboratory tests performed in 2012 and in 2014; and
- to perform a sensitivity analysis related to the elements composing its cross section.

The elements examined during the sensitivity analysis were:

(a) the presence of the berm;

(b) the shape of the sloping plate and the introduction of a parapet on the rear wall; and

(c) the reservoir width.

The inclusion of the berm did not change significantly the $q_{reservoir}$ or the pressure distribution along the structure. However, it slightly increased K_r as expected, suggesting the design of a toe protection.

The investigation of a double inclination in the ramp shape was aimed to generalize the OBREC cross section. However, the analysis performed showed that the position of the inclination change is more sensitive than the values of the slope angles. Therefore, it is suggested to locate the slope change point under the still water level in order to minimize the energy losses due to the wave breaking. The benefits of the double – shaped frontal ramp are emphasized considering the effective sloping ramp configuration of the OBREC full – scale prototype. In fact, for the OBREC installation above an existing breakwater, the use of prefabricated structures is strongly recommended. In such conditions, a single slope plate is quite difficult to build due to construction requirements. Therefore, the prefabricated ramps cross section can be conveniently constituted by 2 elements:

1. an auxiliary submerged part with a subvertical face (aimed to improve the ramp resistance to bending and to fatigue) and;

2. an emerged plate with the slope angle designed to improve the overtopping of a specific range of wave amplitude and wave frequency.

The reservoir width does not significantly affect the values of K_r and p_{250}, except for the wider reservoir that leads to an unstressed rear wall. Therefore, B_r can be selected after the design of the sloping plate, which appeared to be the most sensitive element.

To ensure the harbour safety of the inshore area of the structure, 2 parapets configurations have been analysed. In extreme conditions, the parapet inclined of 30° reduces the values of q_{rear} by 34%, while the one inclined at 45° was reduced by 41%, on average. The maximum reduction has been measured for the configuration characterized by the smallest reservoir width, i.e. 70% and

80% for $\varepsilon = 30°$ and $\varepsilon = 45°$, respectively. Therefore, the inclusion of the inclined parapet leads to a safer harbour area even in case of constrained values of B_r. The best results have been obtained for the parapet inclined of 45°, which optimizes the values of q_{rear} without increasing the pressures.

6. Numerical modelling with incompressible openFOAM

This Chapter presents the multi – phase numerical modelling of the OBREC prototype installed in the port of Naples. Specifically, it describes the numerical model and set – up and the wave conditions and measurements. Eventually, a discussion on the hydraulic and structural performance of the device, under a real storm event and the typical wave climate of the Gulf of Naples, was presented.

6.1 Numerical model and set – up

The 2D numerical simulations have been performed with the free, open source CFD software openFoam (www.openfoam.org). Specifically, the toolbox *waves2Foam*, originally developed at the Technical University of Denmark by Jacobsen et al. [50] and capable of generating/absorbing the waves, has been used.

The principal direction of the waves in the installation site is mainly perpendicular to the OBREC device all over the year. Therefore, this reduces the error due to simulating the wave – structure interactions of the real site by means of a 2DV representation. The model is based on the Volume Average Reynolds Average Navier Stokes equations (VARANS), implemented using the Volume of Fluid (VOF hereafter) method. The library *waves2foam* is a modification of the native one, i.e. *interFoam*. It is capable of solving 2 incompressible, isothermal immiscible fluids, i.e. air and water, simultaneously tracked using a scalar field (equal to 0 for air and 1 for water, and any intermediate value is a mixture of the 2 fluids), considering the wave generation/absorption by means of the relaxation zone technique In the momentum balance equation, an extra term is included to take into account of the surface tension between the 2 phases. The generation/absorption of free surface water waves is based on the application of the relaxation zone technique (active sponge layers), and includes a large range of wave theories for regular and irregular waves. The turbulence LES model [16] has been introduced for this study case.

The geometries, the numerical domain and the mesh have been defined, at prototype scale, by means of Gmsh [38], a free 3D finite element mesh generator with a built – in CAD engine and post – processor.

An open – flow condition, together with an absorption relaxation zone (Figure 55), has been implemented as the outlet boundary, to support the free outflow of the water. The porous layers, composing the San Vincenzo breakwater, are characterized by a cell size equivalent to the nominal diameter of the rocks. In *waves2foam,* the flow through the porous media is modelled by means of the extended Darcy – Forchheimer equation (9). The term related to the turbulent flow follows the expression developed by van Gent [104], already presented in Eq. (11) and reported in Eq. (22), representing the effect of the oscillatory flows through the Keulegan – Carpenter (KC) number.

$$b = \beta \left(1 + \frac{7.5}{KC} \right) \frac{1-n}{n^3} \frac{1}{gD_{50}} \tag{22}$$

The parameters needed to characterize a specific layer are: porosity n [32]; added mass coefficient c_A [104]; KC number, linear and non – linear friction coefficients α_F and β_F, set according to the study performed by Jensen et al. [51] on a traditional rubble – mound breakwater, see Table 17.

The off – shore slope, composed by Antifers, has been represented as a straight line (Figure 55). In the reality, the random placement of the concrete blocks produced a curved edge, which acts like a berm. This simplification has to be taken into account during the analysis of the numerical results.

Table 17. Characteristics of the porous layers composing the San Vincenzo breakwater.

	n	KC	c_A	D_{50} [m]	α_F	β_F
Antifer	0.50	128	0.34	2	500	2.0
Armour	0.45	128	0.34	1.4	500	2.0
Filter	0.45	128	0.34	0.75	500	2.0
Core	0.45	128	0.34	0.50	500	2.0

To analyze the OBREC behavior under the typical wave climate, the 2 configurations have been provided with a pipe, reproducing the prototype functioning. For the analysis of the selected storm event, an additional case have been proposed, by closing the pipe (i.e. closed configuration), to represent the most severe conditions, corresponding to the prototype observation that the reservoirs do usually work in saturated conditions during severe storms.

The numerical domain has been defined considering the extreme wave condition, i.e. Test 8 in Table 3. In this way it was possible to correctly represent the wave development for all the wave attacks. The length of the domain has been set equal to 334 m, which corresponds to three times the wavelength $L = 107.5$ m. The inlet relaxation zone, where the wave generation occurs, has been set equal to 0.5L (54 m), while 2L (215 m) have been considered for the wave development before the wave – structure interactions (Figure 55). The breakwater footprint length is 65 m (see Figure 55), including the outlet relaxation zone is included (10 m).

The wave height affects the extension of the vertical dimension of the domain. To minimize the computational effort, i.e. the number of the cells, the domain has been divided in 2 parts, which differ for their vertical extension and for the mesh adopted. The first part is 31 m high, i.e. 26 m of water depth plus 5 m to allow the correct representation of the waveform. In the second part, where the wave – structure interaction occurs, the vertical dimension has been extended up to 35 m.
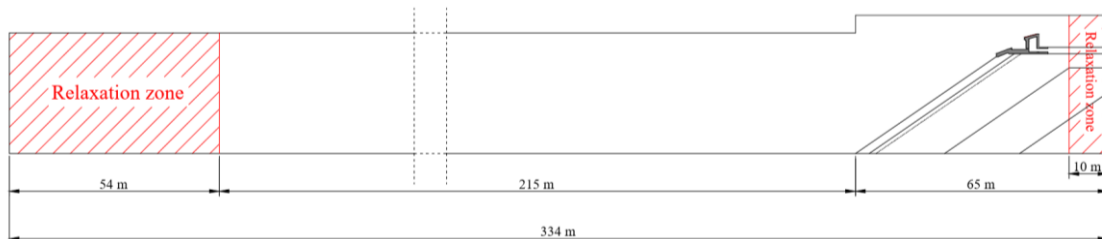
Figure 55. Scheme of the numerical domain.

The mesh characterizing the first part of the domain is structured and graded, both in the horizontal and vertical directions. In particular, the cell dimension decreases in correspondence of the still water level and going towards the structure. The second zone is characterized by an unstructured mesh, more flexible and suitable for peculiar geometries, i.e. the OBREC device installed in a traditional breakwater. The grid reaches its minimum dimension, i.e. 0.02 m, in correspondence of the reservoir and the pipe inside the OBREC, where a high accuracy of the results is required (Figure 56).

The bottom edge of the numerical domain has been set as impermeable. The left and the right edges are combined with the inlet and outlet relaxation zones. The former is responsible of

generating the wave trains, while the latest allows the free outflow of incoming water, taking into account also of the presence of the porous media. The atmosphere patch characterize the top edge and the end of the pipe, to let the fluids to freely flow out of the domain.
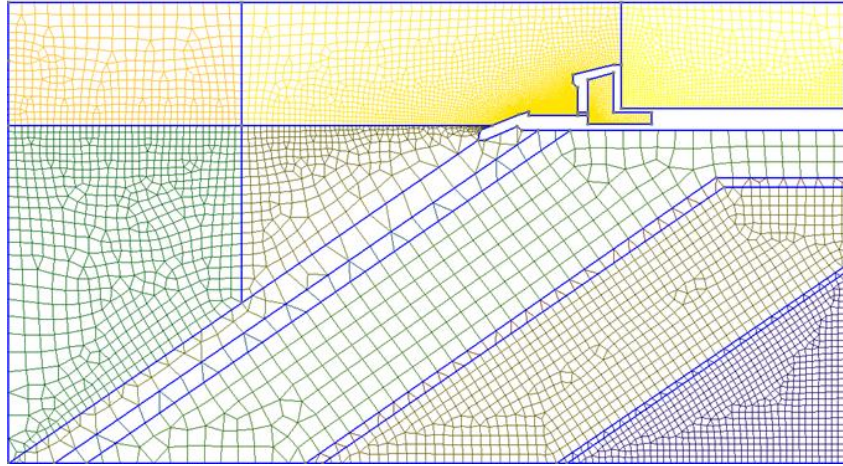
Figure 56. Unstructured mesh characterizing the second part of the domain, occupied by the breakwater**.**

6.2   Wave conditions and measurements

The OBREC cross sections have been tested under several wave conditions. The analysis reported in this work are aimed to assess the OBREC behavior i) during a monitored storm event, and ii) under the typical wave climate of Naples.

The selected storm event, occurred the 6th of January 2018 and lasted for 5 days (see sub – Section 4.2.3). During the first 2 days there was the rising phase, followed by the peak one and finally by the decay phase that lasted up to the 10th of January. The field data, related to 6 hours of the peak phase, have been compared with the numerical results. The selected temporal window is characterized by $H_s = 2.13$ m and $T_p = 8.37$ s, which were used as input parameters to describe the wave attack in the numerical simulations.

A sub – set of wave conditions was used to assess the hydraulic and structural performance of the OBREC under the typical wave climate (Table 3). Each wave attack lasted in this case for or about 600 waves.

In the numerical model, the wave attacks were reproduced by implementing a Jonswap wave spectrum characterized by a peak enhancement factor $\gamma = 3.3$.

Several wave gauges and probes are placed, inside the numerical channel and along the structure, to analyze the surface elevations, the pressures and the velocities profiles. To track the free surface location, 35 wave gauges are set every 10 m from the beginning of the domain until the structure toe. The wave reflection coefficient K_r is evaluated, applying a 3 – point method [65] to the 3 gauges positioned at 155, 156.1 and 157.8 m, quasi 2 wavelengths L far from the structure.

The average overtopping discharge rates inside the reservoir Q_{in}, flowing through the pipe Q_{pipe} and overtopping the rear side of the structure Q_{rear} (Figure 57) have been computed by integrating the horizontal water velocity components along the vertical direction. The velocity output is given every 0.005 m inside the pipe, while is discretized every 0.01 m at the rear side of the structure and inside the reservoir. The different accuracy is to achieve the best representation of the different dynamics related to these 3 parts of the structure.

In order to have a more comprehensive understanding of the OBREC functioning under the typical wave climate, an additional parameter has been computed, i.e. $T_{\%full}$. It represents the

average percentage of the pipe section filled by water, during the entire simulation. Figure 57 shows the location of the pressure measurement points along the OBREC profile. A linear pressure distribution between two consecutive transducers has been assumed along the structure, considering the short distance between the probes, i.e. 0.02 m along the entire profile, with the exception of the probes related to the uplift pressures.
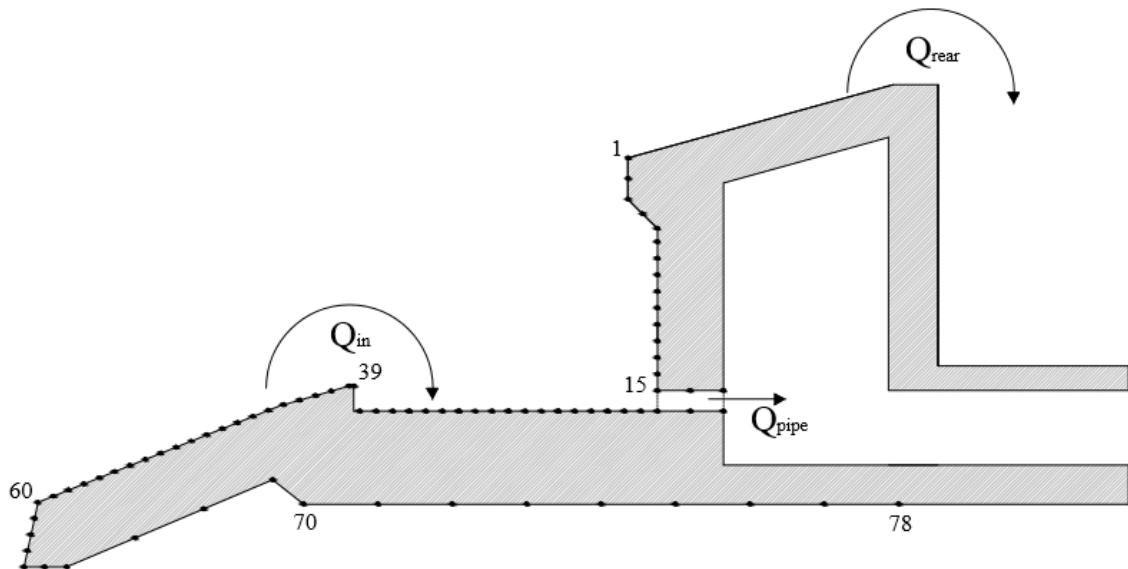
Figure 57. Example of the measuring points for the NW – LAB configuration, i.e. pressure probes and discharge rate inside the reservoir Q_{in}, through the pipe Q_{pipe} and at the rear side of the structure Q_{rear}.

6.3   Hydraulic and structural response of the OBREC device

This Section analyses both qualitatively and quantitatively the pressures acting along the OBREC prototype under a real storm event, by comparing the multi – phase numerical model results with the monitoring data. The numerical prototype is tested also under the typical wave climate of the Gulf of Naples, in order to preliminarily assess the energy production and the most relevant design parameters.

6.3.1 Description of the wave – structure interaction and pressure dynamics

The structural response is affected by the hydrodynamic of the wave – structure interactions, characterizing the OBREC device. The water goes inside the reservoir by overtopping the frontal part of the structure, running – up the sloping plate. During a severe storm event, the pipe is not capable of absorbing all the water, creating a "water bag" that attenuates the loads both on the reservoir and on the lower part of the crown wall. Therefore, the highest impacts occur against the central part of the crown wall and the parapet, during the extreme events. However, a qualitative analysis of the field measurements highlights an impulsive nature of the loads also for the sloping plate. Furthermore, all the signals recorded are characterized by a strong noise due to the complex interactions occurring between the waves and the device under a real sea state, including a significant number of negative values. The latter ones are due to the high – aeration occurring during the wave – structure interactions, which produces sub – atmospheric pressures after the impact takes place, as already observed in large – scale experiments [74]. According to Kortenhaus and Oumeraci [56], the loads can be classified in quasi – static, slightly breaking,

91

impulsive and broken. This classification depends on the characteristics of the structure and on the wave conditions. During the small – scale OBREC experiments [20], the sloping plate was characterized by a quasi – static loading time history, while the crown wall was affected by signals showing evident rapid variations in time, with a high force peak typically described as impact wave loads. For the full – scale prototype this was not completely true, at least for the sloping plate. In this latter case, the monitored pressure signals can be classified as slightly breaking and broken wave loads, due to the presence of the berm that anticipates the breaking process. The differences between the small and full – scale dynamics points out the importance of a prototype installation to better understand the behaviour of the device under a real sea state.

6.3.2 Verification of the numerical model during storm A

The numerical results for the 2 numerical OBREC configurations have been directly compared with the pressures measured during the peak phase of the *storm* event A (see Table 18), by the transducers installed on the OBREC prototype (see Figure 28, in sub – Section 4.2.1). The results are here proposed in terms of maximum and statistical values, p_{max} and p_{250} in Table 18. The latter one corresponds to the non – exceedance level of about 99.7% (i.e. the average of the highest 4% of values).

Table 18 shows that the numerical model tends to generally overestimate the field data, except for the upper part of crown wall of the open configuration, i.e. C and N. This is due to the presence of the pipe, which absorbs part of the overtopping waves that in the 2D simulations is represented like a rectangular section that covers entirely the width of the domain. Therefore, the monitored p_{max} are expected to fall in the middle of these 2 cases, i.e. open and closed reservoirs. It is clear that the right dynamic may be represented only with a fully 3D simulation. The numerical values of p_{250} show a good agreement with the field measurements at the wall, while they result in a cautious estimation along the OBREC profile even if the solver does not take into account of the compressibility of the fluids.

The numerical values of p_{max} and p_{250} on the sloping plate are about 4 times higher than the monitored ones (Table 18). These differences could be related to the following main simplifications:

- the offshore slope of the external layer is represented as a straight line. In the reality, the random placement of the blocs created a curved edge (see Figure 1), which acts like a berm, anticipating the local breaking process;

- the sloping plate is numerically represented as completely in-built on the breakwater, while in reality it is placed on the Antifers blocks (Figure 58), leading to significant change in the representation of the flow under the plate and of the resulting lift force on the device;

- numerical simulations are observed to generate lower level of run-down and more noisy pressure signal, with higher spikes compared to the physical tests, according to a previous study on the Seawave Slot – cone Generator [11];

- the effect of air, not modeled in the numerical model, have some influence on the correct representation of impact waves series, as also found by Di Lauro et al. [29]. In particular, the oscillatory nature of the pressure signals is influenced by the compression of the air – pocked trapped between the wave and the parapet, leading to a general overestimation in numerical model.

Table 18. Maximum and statistical pressure values p_{max} and p_{250} in kPa, measured during the monitoring compared with the numerical results related to both the open and closed OBREC configurations.

Probes	F	G	H	A	B	C	N
p_{max} [kPa]							
Prototype	9.0	8.8	8.8	31.8	37.9	45.6	38.4
Open Conf.	20.1	21.2	29.5	71.5	47.2	30.5	36.2
Closed Conf.	25.6	27.1	30.8	78.1	85.6	70.7	62.7
p_{250} [kPa]							
Prototype	5.0	4.8	4.8	17.9	21.3	25.6	21.7
Open Conf.	19.6	20.7	22.7	35.2	28.7	27.8	32.2
Closed Conf.	24.4	25.5	28.9	37.3	39.6	38.9	38.6

Figure 58. Construction of the bottom slap and positioning of the prefabricated sloping plates [21].

The numerical model allows also a direct comparison between i) the NW – Lab and the RS – Lab configurations, and ii) the closed and the open cases. Figure 59 and Figure 60 show qualitatively the pressures, i.e. p_{max} and p_{250}, acting along the open and closed cross sections during the storm A, for the NW – LAB and RS – LAB cases, respectively. The values of p_{250} have a similar qualitative distribution of p_{max} along the OBREC profile both in Figure 59 and Figure 60.

The NW – LAB results to be more stressed with respect to the RS – LAB configuration, because of the lower sloping plate that leads to a greater overtopping.

For both the configurations, the closed cross sections show higher pressures, with respect to the open ones, in the upper part of the crown wall. The lower part and the reservoir are more stressed in the open case, because of the presence of the pipe that limits the run – up along the crown wall towards the bullnose, by absorbing part of the overtopping waves.

The pressure distribution along the sloping plate and the bottom edge of the device does not shown a strong impulsive component as for the crown wall and the reservoir. This observation is supported also by the similarity between the maximum and the statistical values along these 2 parts of the structure. For the uplift pressures, the presence of contiguous porous layers, characterized by smaller diameters, going towards the inshore edge of the breakwater, damps the loads.
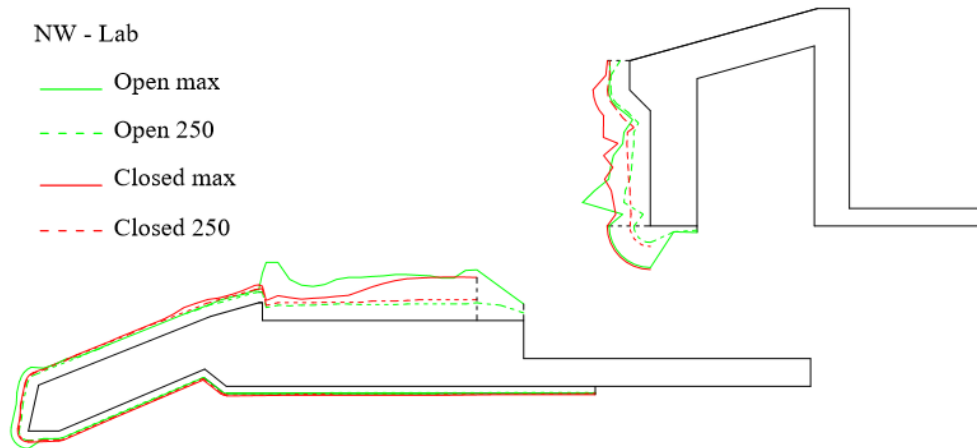
Figure 59. Qualitative representation of the maximum and statistical pressures acting along the OBREC profile, during the numerically simulated storm event A, for NW – LAB configuration (open and closed cases).
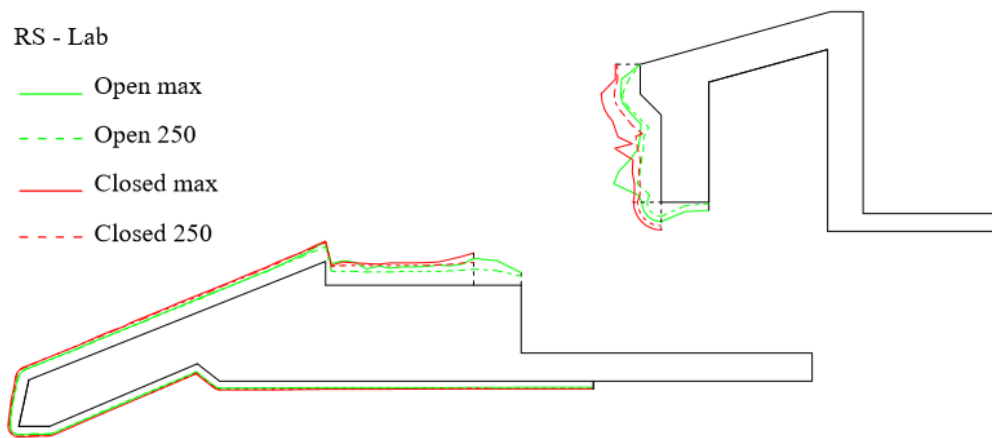
Figure 60. Qualitative representation of the maximum and statistical pressures acting along the OBREC profile, during the numerically simulated storm event A, for RS – LAB configuration (open and closed cases).

6.3.3 Analysis of the OBREC performance under the typical wave climate

The hydraulic and structural performance of the OBREC under the typical wave climate are analysed to improve the OBREC design. These 2 technical aspects are fundamental in terms of energy production, but also of structural reliability. Indeed, the tested wave conditions were selected considering that the ratio H_s/R_c had to be bigger than 1, i.e. sea state 3-8 for the NW – LAB and 4 – 8 for the RS – LAB configurations (Table 3). The purpose is to obtain interesting information in terms of overtopping and loads.

Table 19 reports the discharge rates flowing inside the reservoir Q_{in}, through the Q_{pipe} and at the rear side of the structure Q_{rear}. Furthermore, the values of K_r and $T_{\%full}$, which represent the wave reflection coefficient and the percentage of time in which the pipe works in saturated condition, are presented. The values of Q_{in}, Q_{pipe} and $T_{\%full}$ are strictly related to each other. By analysing the general trend, all these values increase with the increasing of H_s (see Table 19 and Figure 61). Indeed, for the highest waves the pipe lose its capacity of absorbing all the water that goes inside the reservoir. However, the analysis of the values of $T_{\%full}$ shows that the average percentage of

filling of the pipe section, for the most severe wave condition here analysed, is the 62% and 48% for the NW – LAB and the RS – LAB case, respectively.

By comparing the 2 configurations the NW – LAB case shows, for all the sea states, higher values of Q_{in}, Q_{pipe} and $T_{\%,full}$ due to then lower sloping plate, which allows more overtopping with respect to the RS – LAB. However, further considerations are needed to define which is the most promising configuration. Indeed, the characteristics of the NW – LAB cross section (see Figure 25d) minimize the distance between the still water level and the theoretical position of the rotor of the turbine the theoretical position of the rotor of the turbine, at the expense of the theoretical energy production.

The values obtained of Q_{rear} in Table 19 respect the limits for wave overtopping for structural design of breakwaters, seawalls, dikes and dams suggested by the EurOtop [32]. Indeed, the presence of the parapet, on top of the crown wall, allows the minimization of the overtopping rate at the rear side of the structure, as already demonstrated during the preliminary experimental and numerical investigations [77, 106].

The basic principle of the wave energy absorption, on which the OBREC has been designed, avoids the increasing of the values of K_r, with respect to traditional rubble mound breakwater, as already experience during the laboratory experiments performed by Vicinanza et al. [106].

Table 19. Discharge rate inside the pipe Q_{pipe} and at the rear side of the structure Q_{rear}, percentage of the time in which the pipe works as a full section and the reflection coefficient K_r for both the configurations.

H_s [m]	NW_LAB					RS_LAB				
	Q_{in} [m³/s]	Q_{pipe} [m³/s]	$T_{\%,full}$ [/]	Q_{rear} [m³/s]	K_r [/]	Q_{in} [m³/s]	Q_{pipe} [m³/s]	$T_{\%,full}$ [/]	Q_{rear} [m³/s]	K_r [/]
1.25	0.029	0.029	0.11	0	0.46	/	/	/	/	/
1.75	0.105	0.102	0.25	0	0.50	0.024	0.0226	0.07	0	0.51
2.25	0.221	0.170	0.35	0	0.46	0.107	0.09	0.19	0	0.46
2.75	0.411	0.296	0.57	0	0.47	0.238	0.193	0.35	0	0.50
3.25	0.629	0.364	0.59	0.0047	0.45	0.346	0.214	0.33	0.02	0.47
3.75	0.757	0.415	0.62	0.0053	0.48	0.484	0.324	0.48	0.0188	0.54
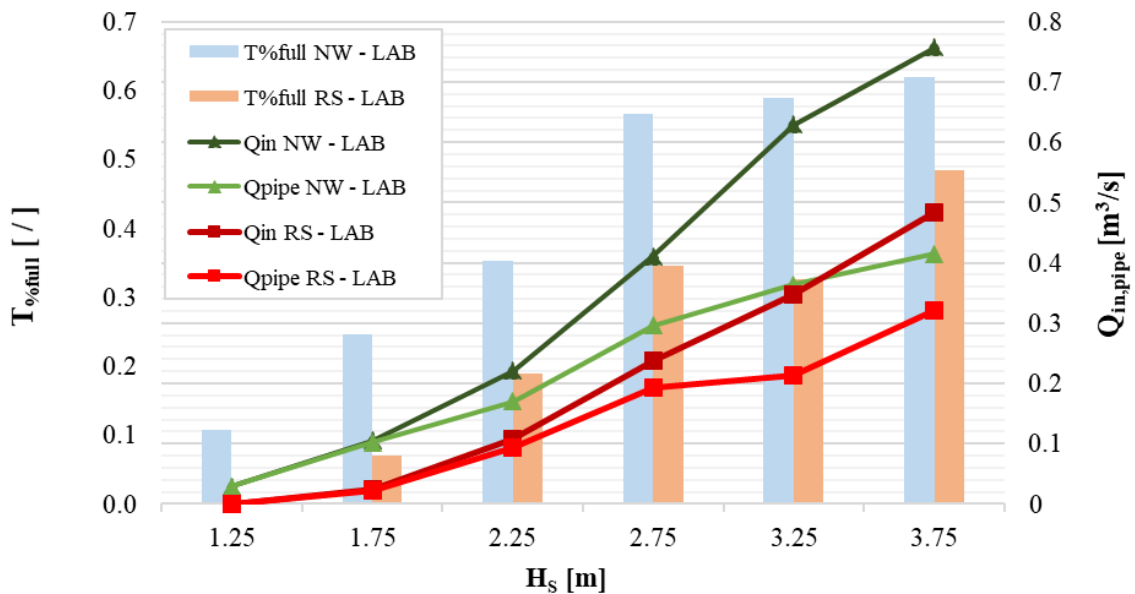
Figure 61. Comparison between the discharge rate inside the reservoir Q_{in} and inside Q_{pipe} for both the configuration.

Figure 62 shows the pressures acting on the OBREC cross sections. For both the configurations, the loads do increase with increasing H_s. The crown walls and the reservoirs are affected by impulsive impacts, while the sloping plate and the bottom edge of the device to the quasi – static ones. For both the NW – LAB and the RS – LAB configurations, the most stressed part of the structure is the crown wall. Specifically, for the former the impacts are concentrated just above the pipe, while for the latter just below the bullnose. The higher sloping plate and the smaller reservoir generally increase the magnitude of the pressures against the crown wall, leading to a more stressed bullnose with respect to the NW – LAB cross section.

An integrated perspective shows a strong connection between the hydraulic and the structural performance. The highest waves overtop the sloping plate with more energy, which is partially dissipated in the direct impact against the crown wall. This dynamic does not allow a significant increase of Q_{pipe} for the most severe sea states. The smallest waves, characterized by less energy, tend to follow the OBREC geometry flowing through the pipe without any loss (Figure 62). Indeed, they have been selected considering that the ratio between H_s and the height of the sloping plate had to be bigger than 1, i.e. sea state 3 for the NW – LAB and 4 for the RS – LAB configurations (Table 3). This criterion allowed to obtain a significant overtopping, in terms of hydraulic performance, even if smaller.
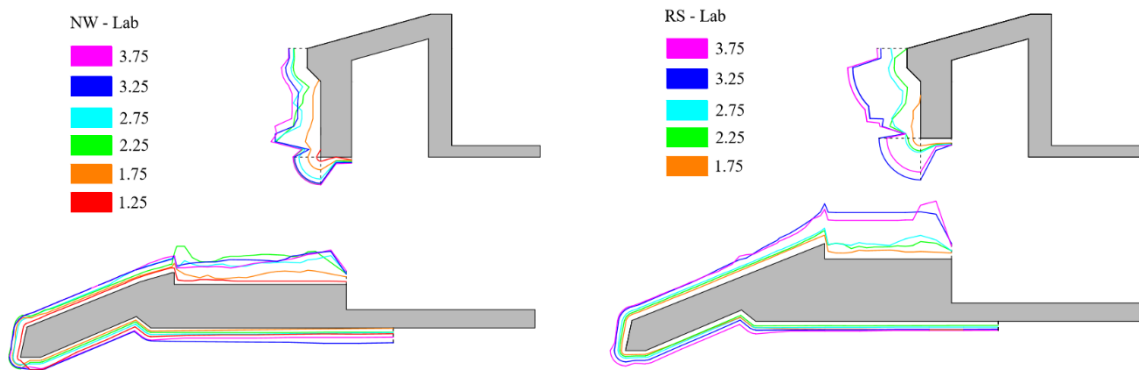
Figure 62. Maximum values of pressures along the OBREC device: a) NW – LAB and b) RS – LAB configurations.

6.3.4 Scale effects on wave loads

During the small – scale OBREC experiments [20], the sloping plate was characterized by a quasi-static loading time history, while the crown wall was affected by signals showing evident rapid variations in time, with a high force peaks typically described as impact wave loads [20]. For the full – scale prototype, this is not completely true, at least for the sloping plate. In this latter case, the monitored pressure signals can be classified as slightly breaking and broken wave loads, due to the presence of the berm that anticipates the breaking process. The differences between the small and full – scale dynamics point out the strong non-linear interaction between the fluid and the sloping plate, in contrast with the quasi – static conditions measured during the laboratory campaigns [20, 106]. In particular, in correspondence of drastic changes of roughness and permeability, the air-water interface give some numerical disturbance leading to misleading results.

Furthermore, the qualitative analysis of the field measurements highlights that all the recorded signals are characterized by a strong noise including a significant number of negative values. The latter ones are due to the high – aeration occurring during the wave – structure interactions, which

produces sub – atmospheric pressures after the impact takes place, as already observed in large-scale experiments [74].

However, the general hydrodynamic at prototype during extreme wave conditions was already well represented during the small-scale experiments [106]. In the laboratory, the creation of a "water bag" that attenuates the loads both on the reservoir and on the lower part of the crown wall was observed. At prototype scale, this process is confirmed by the pipe saturation occurred during the extreme events. Furthermore, the laboratory, the field and the numerical results highlight that the main difference between the RS – LAB and NW – LAB configurations is the point where the wave impact occurs. In case of the higher sloping plate the highest waves are conveyed directly towards the upper part of the crown wall, while in the lower one, the wave falls inside the reservoir and then run-up along the crown wall.

6.3.5 Theoretical power production

The purpose of this Section is to provide a preliminary assessment of the theoretical power flux available at prototype scale. The assessment is based on hydraulic considerations disregarding the energy conversion method and the power losses. The theoretical power production is obtained by combining the overtopping rates flowing inside the shunt tank Q_{pipe} and the total hydraulic head h_{tot}, for each tested wave condition.

The hydrodynamics observed at the OBREC prototype, supported by the numerical modelling, showed that the overtopping waves are firstly collected inside the reservoir and then conveyed, by means of the pipe, in the machine room. Here, a shunt tank stabilizes the hydraulic head available for the hypothetical PTO system (Figure 63a). The size of the tank installed in the OBREC prototype, i.e. 0.45 m (width) x 0.45 m (height) x 1 m (longitudinal extension), is showed in Figure 63b. The most important parameter is the diameter of the hole on the bottom of the shunt tank, acting as intake for the turbine. As aforementioned, due to the limitation of the 2D model, the pipe toward the crown wall has been modeled as a rectangular hole covering the whole width of the domain. Therefore, the hydrodynamics inside the reservoir and the power efficiency parameters are computed by means of another specifically – designed numerical model, called OBRECsim [23]. OBRECsim solves the full, dynamic, 1 – D Saint Venant equation using an implicit, finite difference method. The code is based on the continuity equation (23):

$$Q^*_{reservoir} = Q^*_{in} - Q^*_{rear} - Q^*_{overflow} \tag{23}$$

where: $Q^*_{reservoir}$ is the flow through the turbines; Q^*_{in} is the total overtopping flow rate, derived from the overtopping discharge formula fitted by Iuppa et al. [48] on the OBREC small – scale laboratory tests; Q^*_{rear} is the overtopping flow rate at the rear side of the structure; $Q^*_{overflow}$ is the outgoing reflected flow when the reservoir is saturated.
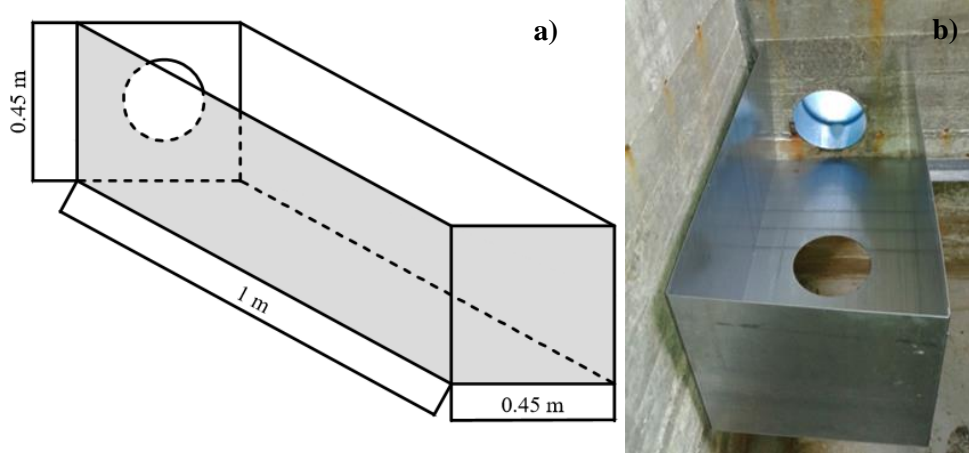
Figure 63. Shunt tank: a) CAD scheme; b) installed in the prototype of the port of Naples.

The total hydraulic head h_{tot} is composed by 2 contributions (Eq. 3), i.e. the difference between the still water level and the bottom edge of the reservoir h and the average hydraulic head dh established in the shunt tank (Figure 63), dependent on Q_{pipe}:

$$h_{tot} = h + dh \tag{24}$$

where h is equal to 0.7 m and 1.25 m for the NW – LAB and RS – LAB sections, respectively. It is worthy to highlight that the value of dh represents only the static contribution, even if the observations pointed out the importance to consider also the kinetic one. Therefore, it represents a cautious assumption for the evaluation here performed.

The theoretical input power P_{in} to a generic Power Take Off (PTO) system, by neglecting the power losses, is given by:

$$P_{in,i} = \rho \cdot g \cdot Q_{pipe,i} \cdot h_{tot,i} \tag{25}$$

where ρ is the fluid density, g is the gravitational acceleration, h_{tot} is the total hydraulic head, Q_{pipe} is the overtopping discharge rate flowing through the pipe, and the subscript i is the sea state. The contribution given by each wave condition $P_{in,ws}$ (Table 20) is derived by multiplying the value obtained for a specific i for the frequency of occurrence Fr associated to i (in terms of hours/year). The sum of the values of $P_{in,ws}$ gives the theoretical available input power for the PTO system of each OBREC configuration during a year $P_{in,year}$.

Table 20 shows the values of dh, P_{in}, $P_{in,w}$ and the resultant $P_{in,year}$ for each OBREC configuration, according to the results obtained by the numerical modelling. Most of the sea states give values of dh (Table 20) greater than the height of the shunt tank, i.e. 0.45 m, and therefore the values of P_{in} is computed accounting for this upper limitation of dh. The shunt tank should be resized to allow a higher available hydraulic head and thus energy production.

For waves with $H_s < 1.25$ m, the NW – LAB configuration produces higher values of Q_{pipe} than the RS – LAB configuration (Table 19). The values of P_{in} for $H_s = 1.25$ m are similar between the two configurations. For higher wave heights, P_{in} grows more and more for the RS – LAB cross section, highlighting that the smaller values of Q_{pipe} are effectively compensated by the higher values of h_{tot}, essentially due to the higher value of the constant contribution h.

It is worthy to remark that these results were derived in case of one hole and one corresponding 0.25 diameter pipe. The optimization of the design and location of the holes for the pipes requires a fully 3D modelling that is out of the scope of this contribution.

Table 20. Hydraulic head established in the shunt tank dh and power produced by the turbine P_{in}, for each sea state characterized by a certain frequency Fr and available theoretical power P_{year}. Values derived in case of one 0.25 m diameter hole.

Sea states			NW-LAB			RS-LAB		
H_s	Fr	P_{year}	dh	P_{in}	$P_{in,ws}$	dh	P_{in}	$P_{in,ws}$
[m]	[/]	[kW/m]	[m]	[kW]	[kWh]	[m]	[kW]	[kWh]
0.25	0.1498	0.01	0.00	0.00	0.02	0.00	0.00	0.04
0.75	0.5912	0.60	0.01	0.16	842.02	0.00	0.08	427.74
1.25	0.2083	0.75	0.10	1.03	1886.72	0.05	1.00	1845.69
1.75	0.0409	0.34	0.20	2.09	751.62	0.16	2.74	983.72
2.25	0.0083	0.13	0.27	2.66	203.56	0.30	4.26	325.79
2.75	0.0012	0.03	0.31	2.93	25.63	0.40	5.13	44.96
3.25	0.0003	0.01	0.36	3.16	5.53	0.51	5.96	10.44
3.75	0.0001	0.00	0.37	3.12	2.19	0.54	5.82	4.08
Total	**1.00**	**1.87**			$P_{in,year}$ **3717.27**			$P_{in,year}$ **3642.46**

A coherent comparison between the two configurations can be performed by considering the values of $P_{in,year}$, which results to be 3717 kWh and 3642 kWh for the NW – LAB and RS – LAB cases, respectively. The lower sloping plate of NW-LAB captures a wider set of wave conditions, maximizing the OBREC operational window $T_{o.w.}$ with respect to the typical wave climate and P_{year} given the higher frequency of occurrence Fr of the less energetic sea states. The NW – LAB is characterised by an operational window $T_{o.w.}$ $(\sum Fr) > 32\%$ (Table 21), while the RS – LAB is able to operate just 10.3 % of the year.

The parameters $P_{in,year}$ and $T_{o.w}$ can be assumed as the reference parameters for the design optimisation of the sloping plate. However, appropriate site-specific threshold values for these parameters should be selected to derive the optimal value of R_c, while considering the design procedure and the technical considerations here reported of general validity.

The theoretical results of the power production have finally to cope with the technical characteristics of the selected PTO. The very low head turbines tested for OBREC can exploit minimum head differences ≥ 1.5m, and therefore the NW – LAB configuration would not produce energy, while the RS – LAB configuration would produce energy only for the highest waves (see Table 21). Therefore, the final design of the device has to account for the limitations of the PTO system, which in this specific case does not allow the selection of the NW – LAB configuration. These considerations point out, once more, that the very low head turbine is still a challenge to be overcome [18], and that improved technological solutions have to be developed to make feasible the systematic production of marine renewable energy.

Table 21. Yearly operating time, in terms of percentage per year, and total average hydraulic heads $dh_{tot,real}$ computed for each sea state.

#	H_{m0} [m]	NW – LAB		RS – LAB	
		$T_{o.w.}$ [%]	$h_{tot,real}$ [m]	$T_{o.w.}$ [%]	$h_{tot,real}$ [m]
1	0.25	0.00	0.70	0.00	1.25
2	0.75	12.92	0.71	1.71	1.25
3	1.25	14.63	0.80	5.50	1.30
4	1.75	3.79	0.90	2.33	1.41
5	2.25	0.85	0.97	0.67	1.55
6	2.75	0.10	1.01	0.09	1.65
7	3.25	0.02	1.06	0.02	1.76
8	3.75	0.01	1.07	0.01	1.79
Total		32.32	/	10.34	/

6.3.6 Cross section optimization for energy production

The results obtained from the analysis reported in sub – Section 6.3.5 could be useful to give some indications about the optimal design of the OBREC device, in order to maximize the energy production.

According to its principle of operation, the main design parameter is the height of the sloping plate R_c, which determines the run – up process, and therefore the overtopping rate. Its definition can be independent from the reservoir width, which has to primarily satisfy the site specific constraints related to i) the available space for the overall structure, and consequently ii) the construction and the installation costs. An undersized reservoir, with respect to the highest overtopping volumes, allows the dissipation of part of the wave energy during the wave – crown wall impact, protecting the machine room that contains sensitive instruments. Therefore, the selection of the reservoir width has to be subordinated to the value of R_c and to the related estimate of the overtopping volumes.

For the specific case of the prototype installation, the lower sloping plate maximizes the theoretical power available to the system, being capable of exploiting a wider range of wave conditions with respect to the higher sloping plate. However, the selection of the proper value of R_c, during the design procedure, cannot be independent from the minimum hydraulic head needed for the selected PTO system to produce energy.

6.4   Discussion

The OBREC cross sections were tested in 2D conditions, considering that the principal direction of the wave propagation, in the Gulf of Naples, is orthogonal to the device. Under extreme events, 2 cross section profiles were modelled for both NW – LAB and RS – LAB: an "open" and a "closed" profile, which include (real case) or not the presence of the pipe, respectively, to represent the case of pipe saturation observed.

The numerical model tends to generally overestimate the field data, except for the upper part of the crown wall of the open configuration, probably due to the presence of the rectangular section covering the width. Therefore, the monitored maximum pressures fall in the middle of these 2 cases, i.e. open and closed reservoirs. The numerical values of p_{250} (non – exceedance level of 99.7%) show a good agreement with the field measurements at the wall, while strongly overestimate the stresses along the sloping plate. This could be due to the curved offshore profile of the real breakwater that slightly anticipates the breaking process, which is not reproduced in

the virtual domain. Furthermore, some numerical mesh limitations lead to a different air – water interface under the sloping plate element.

The numerical model is then adopted to test the prototype under the typical wave climate of Naples. The results obtained show that OBREC is capable of minimizing the overtopping discharge at the rear side of the structure, without increasing the wave reflection.

The theoretical power available to the PTO system in a year, i.e. $P_{in,year}$, is derived by combining the overtopping rates flowing inside the shunt tank Q_{pipe} and the total hydraulic head h_{tot}, for each tested wave condition, accounting for the frequency of occurrence Fr associated to each sea state. The values of $P_{in,year}$ are equal to 3717.27 kWh and 3642.46 kWh for the NW – LAB and RS – LAB, respectively.

Indeed, the lower sloping plate captures a wider set of wave conditions characterized by an operational window $T_{o.w.} > 32\%$, while for the RS – LAB the values of $T_{o.w.}$ resulted to be $> 10\%$. These 2 parameters are crucial for the design optimisation of the sloping plate, even if site – specific threshold values should be selected. The hydraulic optimization has finally to be combined with the technical characteristics, and sometimes the limitations, of the available PTO systems. For the case of OBREC, the selection of commercial low – head turbines implies that the NW – LAB configuration cannot be selected because of the insufficient hydraulic head for turbine operation.

7. Development of a plug – in compressible solver in the openFOAM environment

This Chapter is devoted to the development of 2 new plug – in solvers, in the openFOAM environment, aimed to improve the knowledge related to the role of the fluid compressibility during the wave impact. Specific objective were:

- the codes compilation, paying attention to the compatibility issues for the functions and the correct statement of the new variables;
- the implementation of the proper initial conditions, updating the resolution schemes in the system files, i.e. *fvSchemes* and *fvSolution*, to run the benchmark cases;
- the stabilization of the solver by working on the optimal mesh, the right boundary and initial conditions, but improving also the resolution schemes for the variables.

7.1 Background and codes development

In Section 2.4.2, it was highlighted the importance of the compressibility of the fluids during the wave impact, moreover when the front of the breaker is almost parallel to the wall at that particular moment. If the wave overturns as it strikes the wall, it can trap an air pocket, whereas, if the wave has already broken, large quantities of air can be entrained so that a turbulent air – water mixture strikes the wall. In either case, the compressibility of the trapped or entrained air will affect the dynamics and is often thought to reduce the maximum pressure due to cushioning effect. However, a trapped air pocket will also tend to distribute the impact pressure more widely so that the overall force on the wall may not be reduced [82] and the impulse may be increased due to rebound [114]. Therefore, the development of this new tool can improve the analysis of the structural response of traditional and innovative coastal structures, such as the OBREC device.

As for *waves2foam* [50], the new toolbox *IsoCompressibleWaves2Foam* is composed by 2 solvers capable of 2D/3D numerically simulating the wave – impermeable/permeable structure interactions, i.e. *IsoCompressibleWaveFoam* (hereafter *ICWF*) and *IsoPorousCompressibleWaveFoam* (hereafter *IPCWF*), respectively), but considering the fluid compressibility during the problem resolution. They are substantially a modification of the openFOAM native solver *compressibleInterFoam*, which solves 2 compressible, non – isothermal immiscible fluids. The code modifications are similar to the ones made to *interFoam* to compile *waves2foam* [50], and are available in the appendices A and B for ICWF and IPCWF, respectively. Therefore, the wave generation/absorption and the porosity *modules* were introduced in the main. The term *module* stays for all the header files (where the variable are stated) and the libraries needed to account for the presence of waves and/or porous media in the numerical domain. Table 22 reports the openFOAM native libraries together with the corresponding ones, provided with the wave generation/absorption and the porosity features.

Therefore, the compilation procedure performed in this thesis can be split in 2 steps:

- introduction of the wave module in the native solver *compressibleInterFoam*, obtaining *IsoCompressibleWaveFoam* (Appendix A) → capable of solving 2 compressible, isothermal immiscible fluids by generating/absorbing free water surface in presence of impermeable structures;
- introduction of the porosity module in the new plug – in solver *ICWF*, obtaining *IsoPorousCompressibleWaveFoam* (Appendix B) → capable of solving 2 compressible, isothermal immiscible fluids by generating/absorbing free water surface in presence of permeable/complex structures.

Table 22. Native openFOAM solvers and corresponding plug – in solvers, which take into account the wave generation/absorption. *IsoCompressibleWaves2foam* is the one developed in the present thesis.

Native solver	**Plug – in solver**
interFoam. Solver for 2 incompressible, isothermal immiscible fluids using a VOF, no wave generation and related wave absorption.	**waves2foam.** Solvers for 2 incompressible, isothermal immiscible fluids using a VOF, aimed to generate and absorb free surface waves (waveFoam), in presence of porous / complex structures (porousWaveFoam).
compressibleInterFoam. Solver for 2 compressible, non – isothermal immiscible fluids using a VOF phase – fraction, no wave generation and related wave absorption.	**IsoCompressibleWaves2foam.** Solvers for 2 compressible, isothermal immiscible fluids using a VOF phase – fraction, aimed to generate and absorb free surface waves (ICWF), in presence of porous / complex structures (IPCWF).

The toolbox *waves2foam* represents an *application* in the openFOAM environment. Therefore, it is provided with the solver codes, i.e. *waveFoam* and *porousWaveFoam*, updated for each openFOAM version developed up to that moment. Indeed, different OF versions imply different rearrangement of the libraries, the links and the available functions with the aim to improve the robustness and to speed – up the problem solving procedure. In this thesis, the compilation of the new toolbox was performed for the OF version 3.0.0.

The OF library is written in the C++ language, supporting the object – oriented programming. Indeed, it is based on *objects*, which can contain data in the form of fields, while the *codes* in the form of procedures. It provides the mechanism, known as *classes*, to declare types and associated operations that are part of the verbal and mathematical languages used in science and engineering. The solver applications, written using the OF *classes*, have a syntax that closely resembles the partial differential equations being solved (see Chapter 3). Solver codes are largely procedural since they are a close representation of solution algorithms and equations, which are themselves procedural in nature. To compile a solver it is not required a deep knowledge of object – orientation and C++ programming, but it sufficient to manage carefully every piece of code that requires its own set instructions to access dependent components of the OF library. The compilation can be easily performed thanks to the *wmake* script, provided by OF itself. Figure 64 shows the file structure to better understand the compilation process. A *class* is defined through a set of instructions such as object construction, data storage and class member functions. The file containing the *class* definition takes a *.C* extension, e.g. a *class nc* would be written in the file *nc.C*. This file can be compiled independently of other code into a binary executable library file known as a shared object library with the *.so* file extension, i.e.*nc.so*. When compiling a piece of code, say *newApp.C*, that uses the *nc* class, *nc.C* need not be recompiled, rather *newApp.C* calls *nc.so* at runtime. This is known as dynamic linking [40].
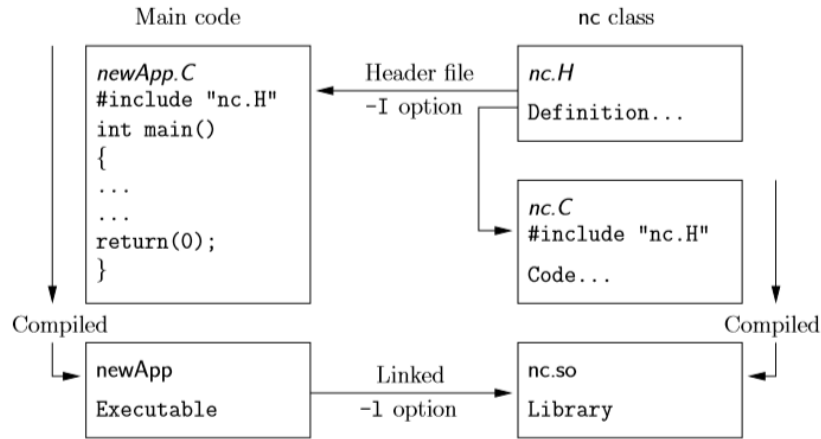
Figure 64. Header files, source files, compilation and linking [40].

7.1.1. Compilation issues

The main compatibility issues, faced during the compilation phase, were related to the continuity equation written in the *UEqn.H* for the solver *IPCWF*. The expression, introduced in the above mentioned header file to account for the presence of the porous media, was analysed from an older version of the porous incompressible solver (because *porousWaveFoam* was not updated for the version 3.0.0), where the shear – rate tensor is defined explicitly (Figure 65). However, the porous compressible solver has been developed starting from the impermeable compressible one (version 3.0.0), where the diffusive term of the momentum equation is written by means of a new function (Figure 66). Specifically, the shear – rate tensor is calculated by calling the functions *divDevReff* or *divDevRhoReff*, in case incompressible or compressible fluids, respectively.

```
     ≡    Code Writer

1        surfaceScalarField muEff
2        (
3            "muEff",
4            twoPhaseProperties.muf()
5          + fvc::interpolate(rho*turbulence->nut())
6        );
7
8        // Calculate and cache mu for the porous media
9        volScalarField mu(twoPhaseProperties.mu());
10
11           fvVectorMatrix UEqn
12        (
13             pm->ddt(rho, U)
14           + 1.0/porosity*fvm::div(rhoPhi/(porosityFace), U)
15           - fvm::laplacian(muEff/porosityFace, U)
16           - (fvc::grad(U) & (1.0/porosity*fvc::grad(muEff)))
17        );
18
19        UEqn.relax();
20
21        pm->addResistance(UEqn);
22
23        if (pimple.momentumPredictor())
24        {
25            solve
26            (
27                UEqn
28             ==
29                fvc::reconstruct
30                (
31                    (
32                        fvc::interpolate(interface.sigmaK())*fvc::snGrad(alpha1)
33                      - ghf*fvc::snGrad(rho)
34                      - fvc::snGrad(p_rgh)
35                    )*mesh.magSf()
36                )
37            );
38        }
39
```

Figure 65. *UEqn.H* for the incompressible porous solver, i.e. *porousWaveFoam* version 2.4.0.

104

```
≡     Code Writer

1     fvVectorMatrix UEqn
2     (
3         fvm::ddt(rho, U)
4       + fvm::div(rhoPhi, U)
5       + turbulence->divDevRhoReff(U)
6     );
7
8     UEqn.relax();
9
10    if (pimple.momentumPredictor())
11    {
12        solve
13        (
14            UEqn
15          ==
16            fvc::reconstruct
17            (
18                (
19                    interface.surfaceTensionForce()
20                  - ghf*fvc::snGrad(rho)
21                  - fvc::snGrad(p_rgh)
22                ) * mesh.magSf()
23            )
24        );
25
26        K = 0.5*magSqr(U);
27    }
28
```

Figure 66. *UEqn.H* for the compressible impermeable solver, i.e. *ICWF* derived from *waveFoam* version 3.0.0.

Therefore, by analysing the *ICWF* code (Figure 66), the first line corresponds to the time derivation, the second one to convective term, while the last one is related to the diffusive component, which result in the shear – rate tensor. The name of the function includes the term *rho* because it is calculated based on the theory for compressible fluids. Thus, the dilatation term is included due to expansion and compression phenomena, which can be related to the no – constant density. Therefore, the shear rate tensor, for the new OF versions, is calculated by calling the *divdevRhoReff* function, defined in the snippet code shown here below:

```
tmp < fvVectorMatrix > laminar::divDevRhoReff (volVectorField & U) const


{
        return

        (
        - fvm :: laplacian ( muEff(), U )

        - fvc :: div ( muEff() * dev2 ( T ( fvc::grad(U) ) ) )
        );
}
```

Here, it is possible to note the function *dev2*, which somehow calculates the deviatoric part of a tensor but subtracting twice the hydrostatic part instead of once. The snippet code showing the dev2 function is reported mathematically in Eq. (26), where A stands for $(\nabla U)^T$:

```
template < class Cmpt >

inline Tensor  < Cmpt > dev2 ( const Tensor < Cmpt > & t)

{
```

```
        return t - SphericalTensor < Cmpt > :: twoThirdsI * tr (t) ;
}
```

$$A^{dev} = A - 2A^{hyd} = A - \frac{2}{3}tr(A)I \tag{26}$$

By simply analysing the 2 different expressions for the *UEqn.H* in Figure 65 and in Figure 66, it is possible to note that the first 2 lines of the momentum equation codes are equals, except for the presence of the variables *porosity* and *porosityFace*. Therefore, the function *diveDevRhoReff* is here analysed, which is composed by 2 terms in Eq. (27) and (28), respectively:

$$- fvm :: laplacian (\mu_{eff}, U) = -\nabla\cdot(\mu_{eff}(\nabla U)) \tag{27}$$

$$- fvc :: div (\mu_{eff} \cdot dev2 (T (fvc::grad(U)))) = -\nabla\cdot(\mu_{eff} \cdot dev2(\nabla U)^T) \tag{28}$$

Following Eq. (26):

$$dev2((\nabla U)^T) = (\nabla U)^T - \frac{2}{3}tr(\nabla U)^T I \tag{29}$$

After combining these terms, it follows that the shear rate tensor τ_{eff}:

$$-\nabla\cdot\tau_{eff} = -\nabla\cdot(\mu_{eff}\nabla U + \mu_{eff}(\nabla U)^T - \frac{2}{3}\mu_{eff}tr(\nabla U)^T I) \tag{30}$$

Therefore, the new expression of the shear – rate tensor is equivalent to the older statements of the continuity equation, and in line with the new OF version rearrangement. Hence, for the new porous compressible solver the code has been modified as in Figure 67.

The other main issue, which was taken into account for the compilation of the IPCWF is related to the presence of the add resistance term in the *UEqn.C* (Figure 67), which is not need in case of compressible solvers:

pm → addResistance(UEqn);

It recalls the variable *mu* (the molecular viscosity) that is stated in the porosity model source code, and specifically in the *jjc2014Zone.C* developed by Jensen et al. [51], used for this kind of applications. In case of compressible fluids this variable *mu* has to be replaced with the *thermo:mu*.

```
≡    Code Writer
1   /*  surfaceScalarField muEff //add
2     (
3         "muEff",
4         mixture.muf()
5       + fvc::interpolate(rho*turbulence->nut())
6     ); //add */
7
8     volScalarField mu(mixture.mu()); //add
9
10    fvVectorMatrix UEqn
11
12 (
13       pm->ddt(rho, U) //add
14     + 1.0/porosity*fvm::div(rhoPhi/(porosityFace), U)
15     + (1.0/porosity) * turbulence->divDevRhoReff(U)
16
17 );
18
19    UEqn.relax();
20
21    pm->addResistance(UEqn); //add
22
23    if (pimple.momentumPredictor())
24    {
25        solve
26        (
27            UEqn
28          ==
29            fvc::reconstruct
30            (
31                (
32                    interface.surfaceTensionForce()
33                  - ghf*fvc::snGrad(rho)
34                  - fvc::snGrad(p_rgh)
35                ) * mesh.magSf()
36            )
37        );
38
39        K = 0.5*magSqr(U);
40
41 //       fvOptions.correct(U);//add
42    }
43
```

Figure 67. New expression for the *UEqn.H* for *the new* solver *IPCWF*.

7.2 Running the benchmark cases with both the new plug – in solvers

The compilation of the new solver implies some modifications to the native source codes (see Section 7.1), which however are not sufficient to run the solvers. By introducing the compressibility of the fluids, new equations and new variables have been stated. Therefore, the simulation folders (see sub – Section 3.2.2) have to be updated. A benchmark case, for both the *ICWF* and *IPCWF* solvers were developed to account for the presence of a completely impermeable and partially porous structure inside the domain, respectively. In Table 23, the input files strictly necessary to run both the native and the new plug – in solvers are reported.
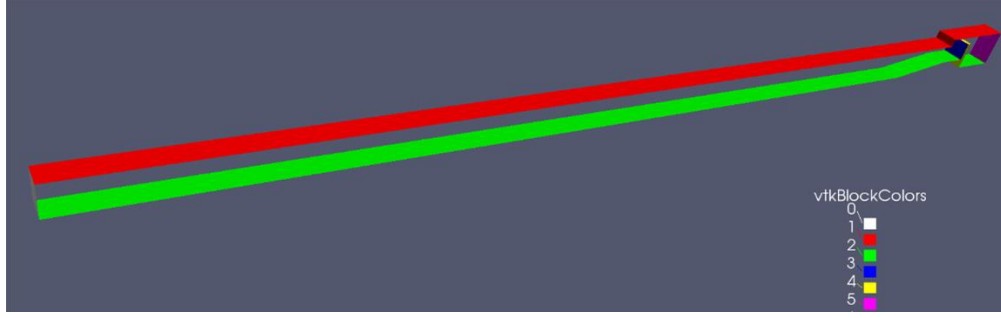
Figure 68. Qualitative view of the benchmark case (in Paraview). Impermeable wall in case of *ICWF* and porous wall for *IPCWF*. Different colours represent the patches in which the numerical domain is broken.

Table 23. Input file needed to run *waveFoam* (*WF*), *porousWaveFoam* (*PWF*), *IsoCompressibleWaveFoam* (*ICWF*), *IsoPorousCompressibleWaveFoam* (*IPCWF*).

Folder	Input files	Native solver		Plug – in solver	
		WF	**PWF**	**ICWF**	**IPCWF**
0	alpha.water	√	√	√	√
	p_rgh	√	√	√	√
	U	√	√	√	√
	p			√	√
	T			√	√
constant	environmentalProperties	√	√	√	√
	g	√	√	√	√
	thermophysicalProperties			√	√
	thermophysicalProperties.water			√	√
	thermophysicalProperties.air			√	√
	transportProperties	√	√	√	√
	turbulenceProperties	√	√	√	√
	waveProperties.input	√	√	√	√
system	controlDict	√	√	√	√
	fvSchemes	√	√	√	√
	fvSolution	√	√	√	√

As shown in Table 23, to run the compressible solvers, it is necessary to initialize both the temperature and the total pressure *p* in addition to the dynamic one *p_rgh*. Furthermore, to properly run the compressible solvers, the whole pressure field has to bet initially set equal to the atmospheric pressure $p_{atm} = $ 1e5 Pa, due to the presence of the thermo – physical laws. Indeed, the native compressible solvers, such as *compressibleInterFoam*, solves for the absolute pressure, while the incompressible ones, as *interFoam*, for the gauge pressure.

Furthermore, the compressible solvers have to be provided with the input files related to the thermos – physical properties characterizing the *species* involved in the problem resolution, i.e. air and water in this case.

7.3   Stabilization of the solvers

A compressible solver, developed by coupling the native openFOAM solver *compressibleInterFoam* with the wave generation/absorption developed in *waves2foam* by Jacobsen et al. [50], has been already developed by Seiffert [87] and Simonetti [89], for different purposes. They performed several numerical investigations, to study the effect of the air compressibility during the wave impact against a bridge deck tested under solitary and cnoidal

waves and to optimize an Oscillating Water Column device by analysing it behaviour under regular waves, respectively. However, the number of the waves considered in these studies varied between 1 to 10, while a long statistic for this kind of phenomena is needed.

Indeed, this Section deals with the stabilization of the new compressible solvers, which are usually used, also in their native OF version, only for short simulations. It is worthy to remark that to analyse the role of the compressibility during the wave impacts, and so the pressures/forces associated to them, it is necessary to take into account of the deterministic nature of the phenomenon.

Indeed, the coastal structures are subjected to highly variable wave loads in the marine environment. Moreover, the analysis of the impact loads (see Section 2.4.2) became necessary to assess the stability of massive structures [74]. Therefore, it is necessary to recognise the wide variation in force type and magnitude, and to incorporate a measure of their probability of occurrence, in order to develop improved design methods [69]. The work performed during the MAST III – PROVERBS was aimed to identify the suitable statistical distribution for wave forces, moreover on vertical wall structures, to develop probabilistic design tools. Previous works on the statistics of wave forces were concentrated on the establishment of the extreme distribution of a series of (theoretically) regular waves [52], that cannot be applied to real (random) seas. Allsop et al [3] showed that the onset wave impacts can be defined as a change in gradient of the probability plot, where wave forces start to increase rapidly above those predicted by the simple Weibull distribution, usually used to describe pulsating wave loads. Therefore, the design load should be based on the analysis of the wave impact forces rather than waves characterized by a $\xi_{m-1,0} < 2$, i.e. where the breaking process occurs before the impact against the structure (see sub – Section 2.4.2). Furthermore, it is important to account for the statistical distribution of wave impact forces, and to know the relative proportions of pulsating and impact forces for a given structural configuration [69].

The structural response has to be always combined with the hydraulic performance, which in this work are analysed moreover in terms of reduction of the overtopping discharge rate at the rear side of the structure. This process has been numerically investigated, according also to the role of the length of the tested wave sequence by Romano et al. [85]. A sensitivity analysis carried – out on the partial overtopping time series has pointed out that shorter time series (at least 500 waves) can be used for overtopping tests, by obtaining a comparable accuracy in average overtopping discharge with respect to the recommended 1000 waves series. Van Dooslaer et al. [102] obtained reliable forces estimation, by testing similar structures (as the ones here analysed) under smaller number of non – breaking waves.

Therefore, the compressible solver has been stabilized to correctly represent irregular wave series, containing at least 400 – 500 waves. This procedure implied a combination of actions, which include i) the improvement of the mesh adopted, ii) the adjustment of the boundary conditions associated to the variable fields and iii) the definition of the most robust resolution schemes.

7.3.1 Mesh problem

An unstructured mesh, performed with the Gmsh software [38], was adopted for the numerical domain of the test benchmark case. The simulation experienced problems (as the low convergence of the U field) in correspondence of particular corners of the numerical domain, where the grid is not regular, i.e. where the mesh provides triangular and not regular rectangles cells. Therefore, the robustness of the mesh has to be checked to assess if it is a crucial element for the stability of the simulation. Therefore, the domain has been forced to be a regular rectangle, avoiding any discontinuities both in the height and longitudinal dimension of the domain. Furthermore, a

structured grid has been preferred, instead of an unstructured one. As for the present case, i.e. a 2D numerical domain, a structured mesh has a series of nodes, all characterized by an integer index, i.e. i and j indices value which is unique and specify its location inside the domain. In the CFD code, a structured mesh simplify the loop iterations through neighbours and results to be more efficient in terms of memory, with respect to an unstructured mesh. Indeed, it is commonly argued that unstructured meshes offer more geometrical flexibility, but for the price of being more expensive per degree of freedom than their structured mesh counterparts.

The structured mesh has been developed by combining the *blockMesh* and the *snappyHexMesh* utilities supplied by OF (see sub – Section 3.2.2). The former creates parametric meshes with grading and curved edges. The principle behind it is to decompose the domain geometry into a set of 1 or more 3 dimensional, hexahedral blocks. Edges of the blocks can be straight lines, arcs or splines. The mesh is ostensibly specified as a number of cells in each direction of the block, sufficient information for *blockMesh* to generate the mesh data, by using the input file *blockMeshDict*. The *snappyHexMesh* utility generates 3D containing hexahedra (hex) and split – hexahedra (split – hex) automatically from triangulated surface geometries, or tri – surfaces, in Stereolithography (STL) or Wavefront Object (OBJ) format. The mesh approximately conforms to the surface by iteratively refining a starting mesh and morphing the resulting split – hex mesh to the surface. An optional phase will shrink back the resulting mesh and insert cell layers. The specification of mesh refinement level is very flexible and the surface handling is robust with a pre – specified final mesh quality. The structure has been designed with the support of the software cad AutoCAD, provided with the capability of producing STL files that can be red by the *snappyHexMesh* utility.

To minimize the computational effort, it has been decided to adopted a graded structured mesh, which shrink the cell dimension in correspondence of the still water level (SWL) and the structure, to correctly represent the wave development and the wave – structure interactions, respectively. In the *blockMeshDict* file (Appendix C), the numerical domain was divided in 2 blocks, which have as a common edge the interface between the SWL and the air. Each block is characterized by a specific expansion ratio, i.e. the ratio between the longest and the shortest cell dimension in a certain dimension, both in the x (structure refinement) and z directions (SWL refinement). Considering that the cells characterized by the smallest dimensions are in correspondence of the structure, the *snappyHexMeshDict* file (Appendix C), and specifically the level refinement n in correspondence of the region (i.e. *refinimentSurface*) can be set equal to 0. The effect of the refinement level n on the new cell dimension x_1, starting from old one x_0, set in correspondence of the entry *refinementSurfaces* in *snappyHexMeshDict*, is explained in Eq. (31) and shown in Figure 69:

$$x_1 = \frac{x_0}{2^n} \tag{31}$$
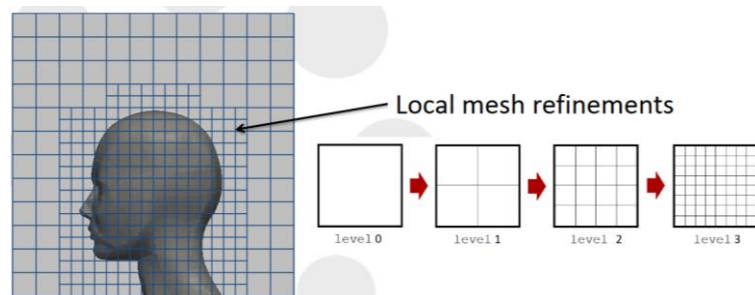
Figure 69. Effect on the mesh refinement on level set for the *refinementSurfaces* entry in *snappyHexMeshDict*.

7.3.2 Boundary conditions

In openFOAM the numerical domain is broken in patches, which can be composed by several blocks. Figure 68 shows the qualitative view of the benchmark case, where the colours represent the patches composing the numerical domain. The front and the back edge of the domain are *empty*, because a 2D case does not requires any solution along the width of the domain and it is therefore represented by one cell (as explained in the previous sub – Section). Each patch has to be characterized by a boundary condition (BC hereafter), containing a list of keyword entries. The compulsory entry, *type*, describes the patch field condition specified for the field. The remaining entries correspond to the type of patch field condition selected and can typically include field data specifying initial conditions on patch faces. openFOAM supplies more than 70 boundary conditions. Figure 70 shows a sub – set of the BC, supplied by openFOAM and waves2foam (where indicated), for a generic field φ.

Table 24 reports the BC adopted for the new compressible solvers. As anticipated in the previous sub – Section, despite of the incompressible solver, here the field p and T have to be initialized.

Boundary condition	Definition for patch field ϕ
waveAlpha	Input wave surface elevation determined by waves2Foam
waveVelocity	Input wave velocity determined by waves2Foam
zeroGradient	Normal gradient of ϕ is zero
fixedGradient	Normal gradient of ϕ is specified
inletOutlet	Switches **U** and p between *fixedValue* and *zeroGradient*
fixedValue	Value of ϕ is specified
buoyantPressure	Sets fixedGradient pressure based on the atmospheric pressure gradient
slip	zeroGradient if ϕ is a scalar; if ϕ is a vector, normal component is fixedValue zero, tangential components are zeroGradient
totalPressure	Total pressure $p_0 = p + \frac{1}{2}\rho\,|\mathbf{U}|^2$ is fixed; when **U** changes, p is adjusted accordingly
pressureInletOutletVelocity	Combination of pressureInletVelocity and inletOutlet
pressureInletVelocity	When p is known at inlet, **U** is evaluated from the flux, normal to the patch
empty	Instructs OpenFOAM to solve in two dimensions

Figure 70. Sub – set of the available boundary conditions supplied both by openFOAM and *waves2foam*, for the wave – structure problem cases.

Table 24. Boundary condition adopted for *ICWF* and *IPCWF* to stabilize the solvers.

Boundary	α	p	p_rgh	U	T
Inlet	waveAlpha	calculated	fixedFluxPressure	waveVelocity	fixedValue
Outlet	zeroGradient	calculated	fixedFluxPressure	fixedValue(0,0,0)	fixedValue
Bottom	zeroGradient	calculated	fixedFluxPressure	slip	fixedValue
Atmsphere	inletOutlet	calculated	totalPressure	slip	inletOutlet
Body	zeroGradient	zeroGradient	zeroGradient	slip	fixedValue
FrontBack	empty	empty	empty	empty	empty

7.3.3 System files

The *fvScheme* and *fvSolution* dictionaries (reported in Appendix D), located in the *system* directory, sets the numerical schemes for terms that appear in applications being run (such as derivatives in equations), and the equation solvers, tolerances and algorithms, respectively.

To run the compressible solvers the new variables stated have to be take into account in the abovementioned dictionaries. The introduction of both the numerical schemes and the algorithms have been performed by analysing the files related to both *waves2foam* and *compressibleInterFoam*.

The main modification has been done in the *fvSolution*. The new solvers, as *waves2foam*, solve equations for velocity U and pressure p. however, for the former a preconditioned bi – conjugate gradient PBiCG is adopted, while the generalised method of geometric – algebraic multi – grid (GAMG) here was preferred. The GAMG method uses the principle of generating a quick solution on a mesh with a small number of cells; mapping this solution onto a finer mesh; using it as an initial guess to obtain an accurate solution on the fine mesh. GAMG is faster than standard methods when the increase in speed by solving first on coarser meshes outweighs the additional costs of mesh refinement and mapping of field data.

Furthermore the computational time step, defined in the *controlDict* file in the system folder, has been reduced to the value of 10^{-4}, to improve the convergence of the solution. Here below, the system files adopted for the new solvers, are reported.

7.4 Comparison of numerical and experimental data

This Section is devoted to the comparison of the results, obtained during the laboratory campaign (presented in Section 4.3) and the 2D numerical simulations performed with both the incompressible solver *waveFoam* and the new compressible one *IsoCompressibleWaveFoam*, developed in this PhD thesis.

7.4.1 Numerical set – up and measurements

The sub – set of the physical tests selected for this comparison, is focused on the dike configuration with the offshore slope characterized by $cot(\alpha) = 4$, the crest width G_c of 0.3 m and a wall height h_{wall} of 0.04 m. As anticipated in Figure 34 panel c (sub – Section 4.3.4), the oscillations in the pressure signals related to breaking waves ($\xi_{m-1,0} < 2$) are due to the presence of air bubbles generated in the wave front during the breaking process occurring along the offshore slope. Table 25 shows the tested wave conditions. The technical considerations made in Section 4.3 about the effects of the of the wave height H_s, the wave peak period T_p (and so the wave steepness s_{op}) and the freeboard H_s/R_c on the pressures remain valid for the numerical models results. Here, the focus is the comparison of the results obtained with the 2 solvers, and where it was possible, with the laboratory measurements.

Table 25. Wave parameters for the test cases performed both the incompressible and compressible solvers.

Test case	1	2	3	4
H_s [m]	0.05	0.05	0.06	0.05
H_s/R_c [/]	0	0	0	0.5
T_p [s]	1.21	1.08	1.21	1.21
ID	R00H05s3G30c4W4	R00H05s3G30c4W4	R00H05s3G30c4W4	R00H05s3G30c4W4

The simulated wave conditions were generated based on the JONSWAP spectrum, by defining the values of H_s, T_p and the peak enhancement factor γ ($= 3.3$ for all the tests). Each test contains 400/500 of waves to obtain a reliable assessment of both the hydraulic and structural performance [85, 102]. Indeed, as anticipated in Section 7.3, the stabilization of the new solver was aimed to reach a correct representation of the wave train for numerical simulations characterized by long durations, to allow a reliable analysis of the overtopping discharge rates at the rear side of the structure and of the pressures.

The numerical set – up and measurements are completely equivalent for the incompressible and the compressible cases. The numerical domain reproduces as much as possible the physical wave channel. Its length (11.2 m) and height (1.5 m) were slightly extended, with respect to the physical one, to introduce the outlet relaxation zone and to avoid numerical instabilities during the wave structure interactions, respectively.

The mesh characteristics are specified in the *blockMeshDict* and *snappyHexMeshDict* reported in sub – Section 7.3.1. A graded mesh was adopted to minimize the cell size in correspondence of the SWL and the structure, avoiding a local refinement usually performed with the *snappyHexMesh* utility that forces the test case to be simulated in 3D.

Several measurements were performed during the tests, i.e. the wave reflection K_r, the overtopping discharge rate $q_{overtopping}$ and the pressures p acting on the structures. Figure 71 shows the position of the 3 virtual gauges used to assess the values of K_r, and the one defined just after the crown wall (in red) to measure the values of $q_{overtopping}$. The latter was computed by integrating along the vertical direction the horizontal velocity components, combined with the VOF values to isolate the water contribution. Figure 72 shows the location of the numerical probes along the crest width and the crown wall. Indeed, in the numerical model was possible to increase the number of the measurements points, with respect to the laboratory campaign, to extend the information related to the wave – structure interactions.
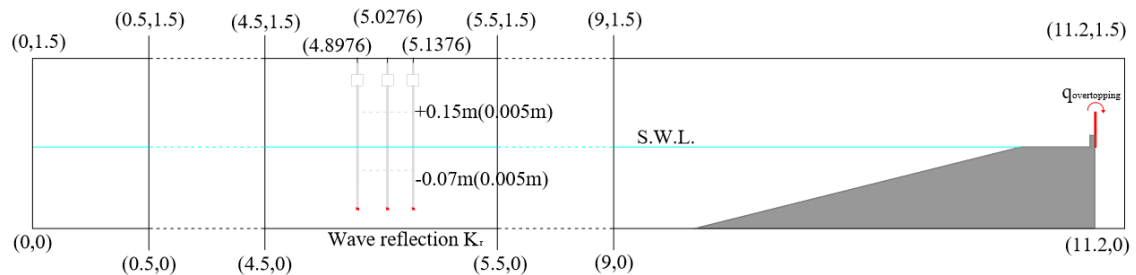
Figure 71. Scheme of the numerical domain, with the specific definition of the virtual wave gauges to evaluate the wave reflection and the wave overtopping.
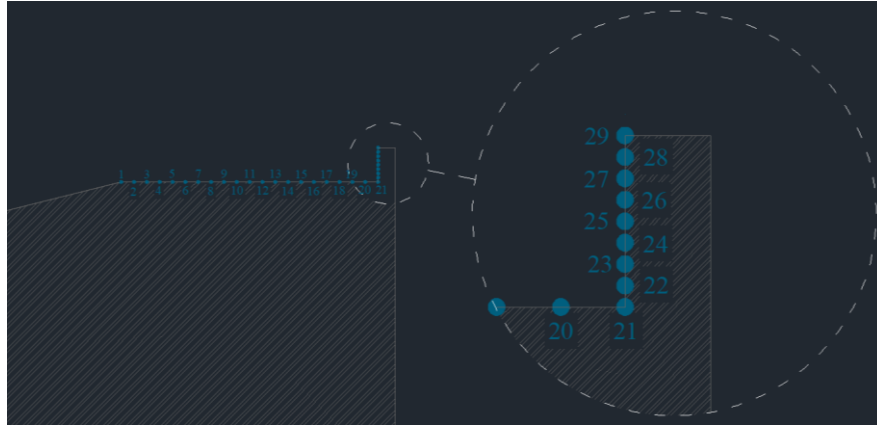
Figure 72. Location of the numerical probes along the crest width and in correspondence of the crown wall.

7.4.2 Laboratory vs. numerical overtopping discharge rates

This sub – Section presents the comparison between the laboratory and the numerical models results, both in terms of wave reflection coefficient K_r and overtopping discharge rates at the rear side of the structure $q_{overtopping}$. Figure 73 shows that, except for one case, the numerical models generally to slightly overestimate the laboratory values of K_r, moreover in the case of the compressible solver. This result is compensated by the obtained values of $q_{overtopping}$ shown in Figure 74. The overestimation with respect to the incompressible solver in on average the 15%. A more accurate sensitivity study on the mesh specifications is needed. The convergence of the compressible solver is slower and strictly related to the Co number, defined as follows:

$$\mathrm{Co} = \frac{U \cdot \Delta t}{\Delta x} \tag{32}$$

Where U is flux velocity, Δt is the computational step and Δx the spatial interval. A strong reduction of the value Δt, to improve the solver convergence, could increase enormously the computational cost of the simulation. Therefore, at this stage, the slight overestimation of the values of $q_{overtopping}$ was accepted to speed – up the simulation time, which is quite longer with respect to the incompressible solver due to the problem complexity. However, according to the main objective of this Chapter, the small error obtained in the hydraulic performance was subordinated to the main objective, i.e. to assess the reliability of the new compressible solver in evaluating the wave loads in presence of compressible fluids.
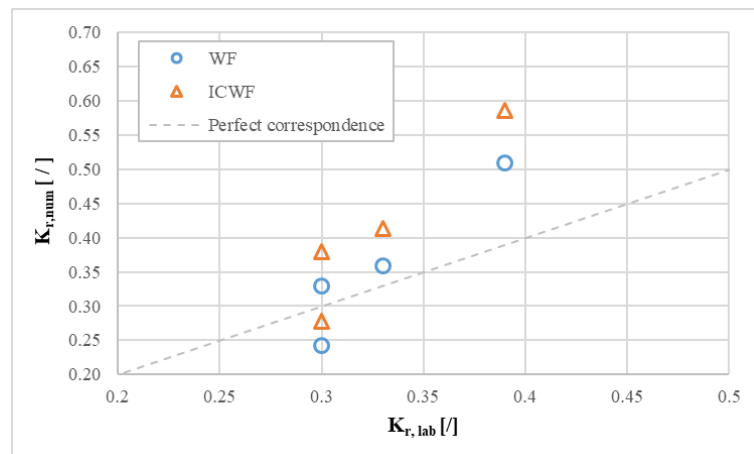
Figure 73. Laboratory vs. numerical (*WF* and *ICWF*) wave reflection coefficients K_r.

114
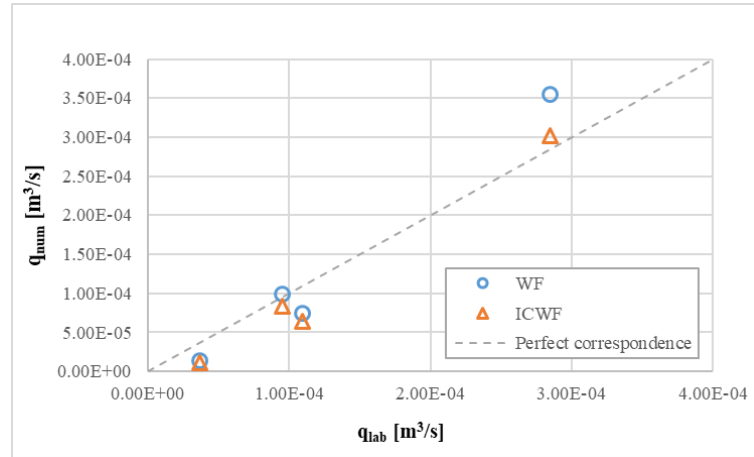
Figure 74. Laboratory vs. numerical (*WF* and *ICWF*) overtopping discharge rates at the rear side of the structure $q_{overtopping}$.

7.4.3 Preliminary pressure sensitivity analysis

To minimize the computational cost of the simulations, a preliminary sensitivity analysis on the output frequency f_{output} and the number of the wave components N was performed on the benchmark case. The main objective was to understand the effect of these 2 parameters on the computational cost, to minimize it without losing the accuracy of the results.

To generate an irregular sea state based to a wave spectrum, the incident wave spectrum must be discretised into a number of discrete frequencies. Each of them represents a regular wave component, and their superposition forms the irregular sea state. In the laboratories, the spectral discretization is defined as $\Delta f = 1/T_e$, where f is the frequency and T_e is the duration of the experiment. In the numerical modelling, for practical considerations, a discrete number of wave components, i.e. 100, is usually preferred.

Therefore, in this sub – Section, the benchmark case was tested by varying the values of f_{output} and N, using the incompressible solver *waveFoam*, as shown in Table 26. The pressures acting along the crest width and in correspondence of the crown wall were analysed. The results are shown in terms of maximum pressures p_{max} and statistical values, i.e. p_{250} and p_{100}, which represent the non – exceedance level of 99.7 % and 90%, respectively. Specifically, the pressures acting along the crest width are shown in Figure 75, Figure 76 and Figure 77, while the ones against the crown wall in Figure 78, Figure 79 and Figure 80.

Table 26. Number of wave components and output frequency assigned for each test case.

Test case	Solver	Wave components [/]	Output frequency [Hz]
1	*waveFoam*	20	20
2	*waveFoam*	100	20
3	*waveFoam*	100	250

By performing the numerical simulations, it was possible to note that the computational cost is strongly more affected by the values of f_{output}, instead of N. To summarize the results shown in the graphs below (from Figure 75 to Figure 80), 2 general considerations can be made:

- by comparing the test case 1 and 2, i.e. 20 to 100 N, the values of p_{max} increase on average of the 24%, while the statistical ones of the 16%;
- by comparing the test case 2 and 3, i.e. 100 to 250 Hz, the values of p_{max} increase on average of the 20%, while the statistical ones of the 10%.

115
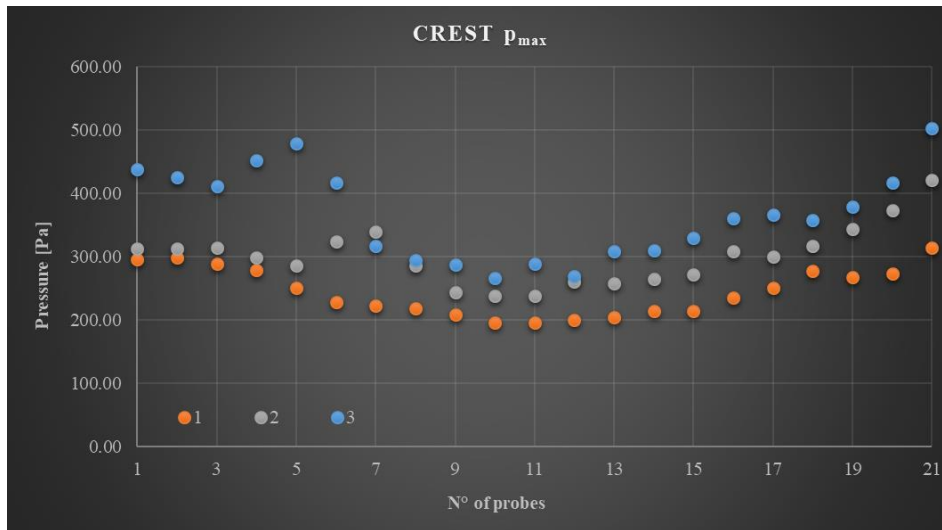
Figure 75. Maximum pressures p_{max} along the crest width, for the test cases reported in Table 26.
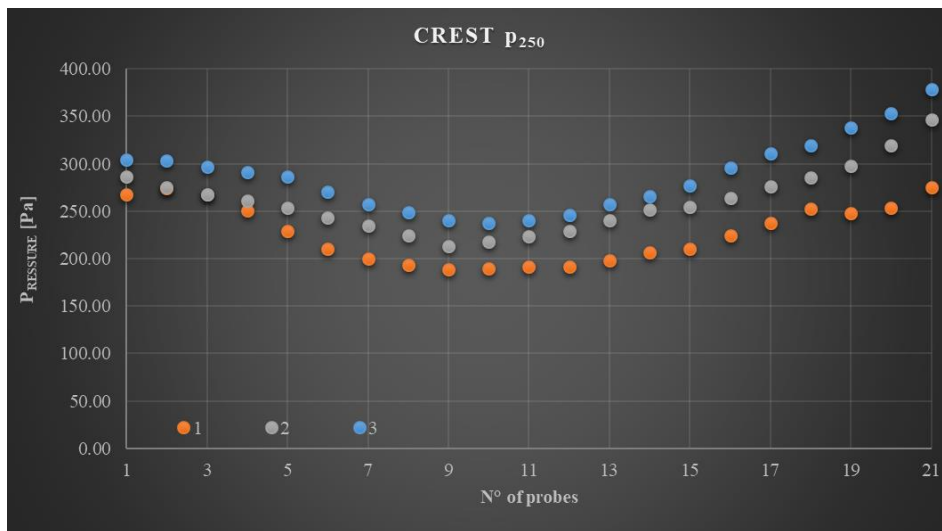
Figure 76. Statistical pressures in terms of p_{250} along the crest width, for the test cases reported in Table 26.
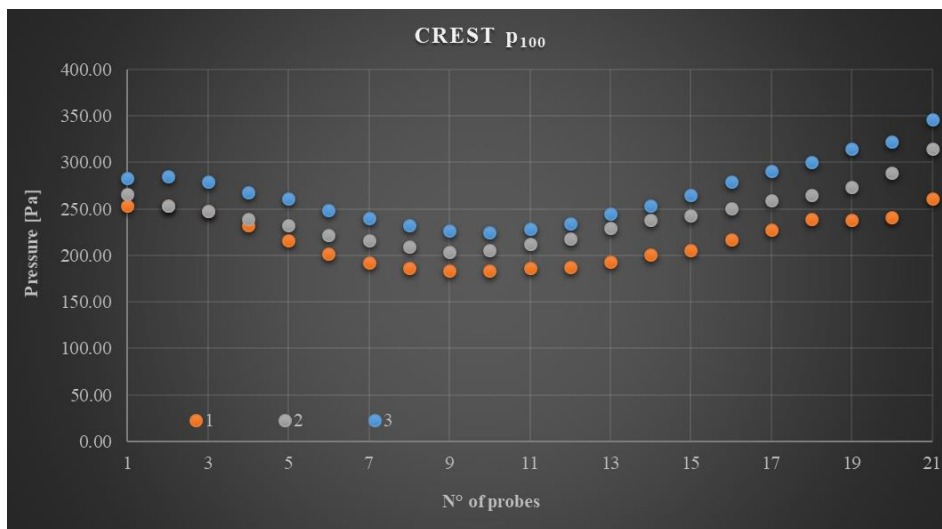
Figure 77. Statistical pressures in terms p_{100} along the crest width, for the test cases reported in Table 26.
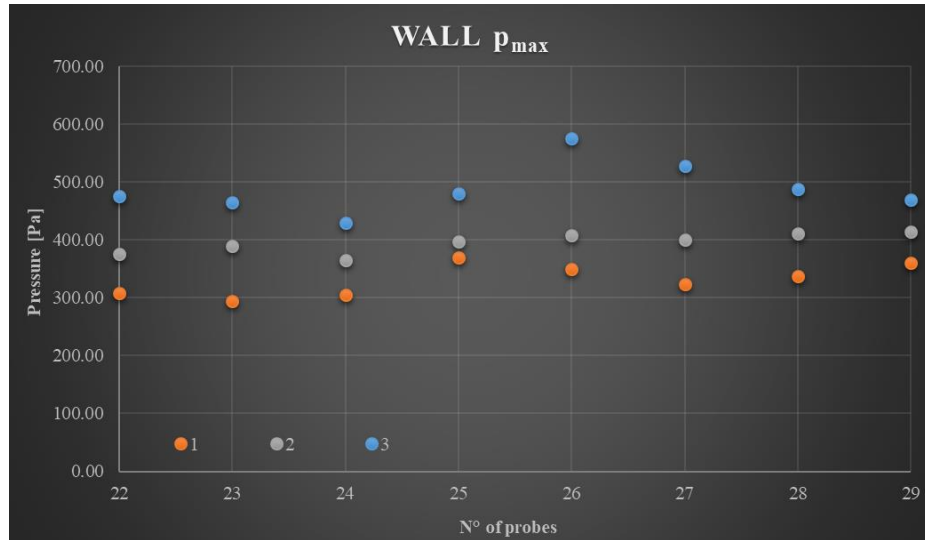
Figure 78. Maximum pressures p_{max} along the crown wall, for the test cases reported in Table 26.
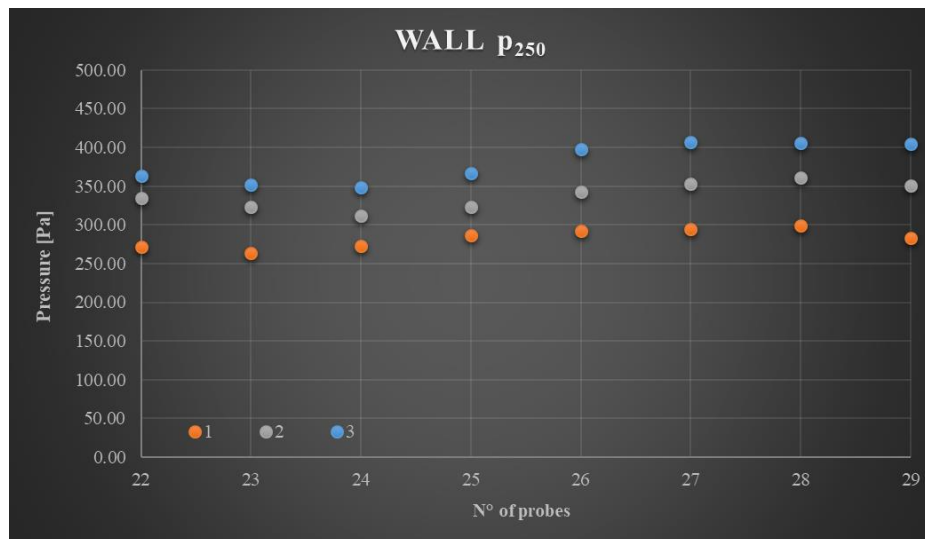
Figure 79. Statistical pressures in terms of p_{250} along the crown wall, for the test cases reported in Table 26.
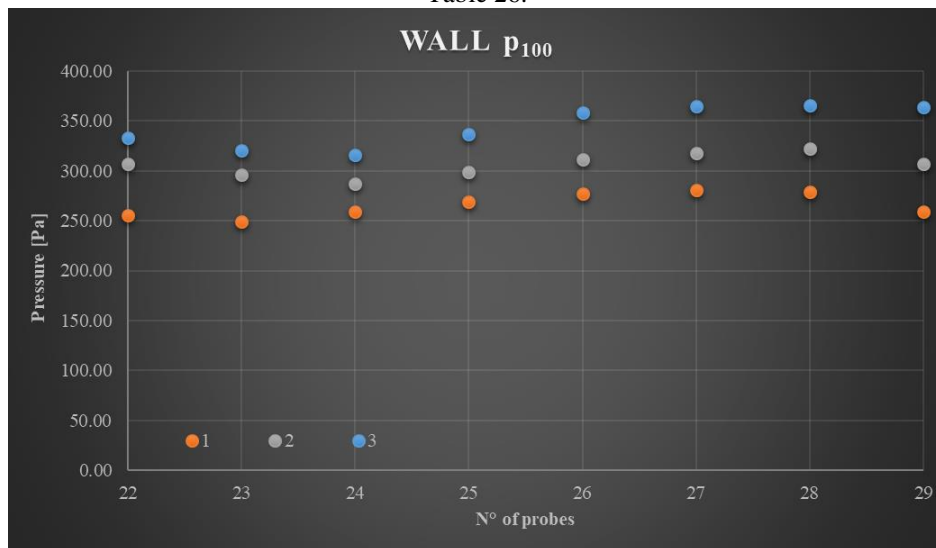
Figure 80. Statistical pressures in terms p_{100} along the crown wall, for the test cases reported in Table 26.

7.4.4 Pressure analysis

This sub – Section presents the comparison between the laboratory and the numerical results, obtained with both the incompressible *waveFoam* (*WF*) and the compressible *IsoCompressibleWaveFoam* (*ICWF*) solvers. As for the sensitive analysis shown in the previous sub – Section, the pressures acting along the structure were analysed in terms of maximum and statistical values (i.e. p_{max}, p_{250} and p_{100}), for a sub – set of the test cases, presented in Table 25 (in sub – Section 7.4.1), which are a part of the laboratory campaign discussed in Section 4.3.

It is important to highlight that a direct comparison between the physical and the numerical pressures can be performed only for the crown wall element. In the laboratory set – up, 3 pressure transducers were installed in correspondence of the crown wall, while in the numerical wall the measurement points were increased to reconstruct the pressure profiles along the whole wall height (see Figure 72). For this reason, to assess the reliability of the new solver *ICWF*, firstly the results related to the crown wall are presented and commented. Once the behaviour of *ICWF* has been checked according to the laboratory measurements, it was then used to extend the analysis on the crest width. The results related to the test case 1 (Table 25) are shown this sub – Section, while the ones related to the tests cases 2, 3, and 4 are available in the Appendix E. Table 27 indicates the Figures showing the results for a specific structural element, for each wave condition. For each of them, the pressures are provided in terms of p_{max}, p_{250} and p_{100}, in this order. The location of the probes is shown in Figure 72 (sub – Section 7.4.1).

Table 27. Summary of the Figures showing the laboratory and the numerical results, for the tests cases reported in Table 25. Test case 1 is shown in this sub – Section, while tests cases 2, 3 and 4 in Appendix E.

Test Case	ID	Crown wall	Crest width
1	**R00H05s3G30c4W4**	Figure 81 to Figure 83	Figure 84 to Figure 86
2	**R00H05s4G30c4W4**	Figure 89 to Figure 91	Figure 92 to Figure 94
3	**R00H06s3G30c4W4**	Figure 95 to Figure 97	Figure 98 to Figure 100
4	**R05H05s3G30c4W4**	Figure 101 to Figure 103	Figure 104 to Figure 106

To summarize the results obtained, some general considerations can be drawn, starting from the analysis related to the crown wall results. The solver *ICWF* gives higher values of pressures with respect to *WF*, for all the tested wave conditions. The overestimation of the values of p_{max}, p_{250} and p_{100} is on average the 97%, the 48% and the 41%, respectively. This demonstrates that the fluid compressibility plays a key role in the wave – structure interactions, moreover in terms of the magnitude of the loads. Indeed, the compressibility of the trapped or entrained air affect the dynamics and is often thought to reduce the maximum pressures due to cushioning effect. However, a trapped air pocket will also tend to distribute the impact pressures more widely so that the overall force on the wall may not be reduced [82] and the impulse may be increased due to rebound [114].

The results obtained for the crown wall profiles show that both the numerical models tend to generally underestimate both the maximum and the statistical values obtained from the laboratory measurements. However, the discrepancy characterizing the incompressible solver *WF* is much bigger than the one related to *ICWF*. The underestimation of the values of p_{max} is on average the 62% and the 26% for *WF* and *ICWF*, respectively. Comparison of new data – sets with previous experiments and prediction formulae proved that the impact pressures in the field are generally lower then those measured during laboratory tests, mainly due to high percentage of air entrained [26]. Indeed, the amount of air bubbles in the overtopping flow might be smaller in small – scale tests leading to higher impacts [102].

The analysis of the statistical pressures show that the differences between the numerical and the laboratory are reduced, i.e. the underestimation is on average the 34% in case of *WF* and the 4% in case of *ICWF*. Therefore, the new compressible solver behaves better with respect to the incompressible one, to estimate the wave loads acting on crown walls. It shows a good agreement moreover in case of the statistical values, i.e. of p_{250} and p_{100}, which are more representative with respect to the maximum ones. Indeed, several studies [101, 102] demonstrated that the latters are statistically less stable and show greater scatter with respect to laboratory measurements. Furthermore, the time duration to reach maximum pressure is very short (narrow peak in the churchroof time signal) in relation to the response time of the structure, leading the structure to not always "feel" this highest impact. Therefore, the p_{250} represents usually a good compromise, still used to evaluate the design forces proposed by Goda [39] and used in the Coastal Engineering Manual.

The results obtained for the crown wall, are confirmed by the analysis extended to the crest width element. Here, the overestimation given by *ICWF* for the values of p_{max}, p_{250} and p_{100} is on average the 197%, the 72% and the 58%, respectively. The higher overestimation could be explained by the fact that the breaking point for the configuration analysed ($cot(\alpha) = 4$) between the offshore slope and the crest. Therefore, the wavefront propagates along the crest is already characterized by the presence of water – air mixture that distributes the impact pressures more widely, increasing its magnitude due to rebound effects.

According to the results obtained, it is possible to conclude that the new solver *ICWF* could represents valuable tool for the analysis of the structural response of traditional, but even more complicated coastal structures.
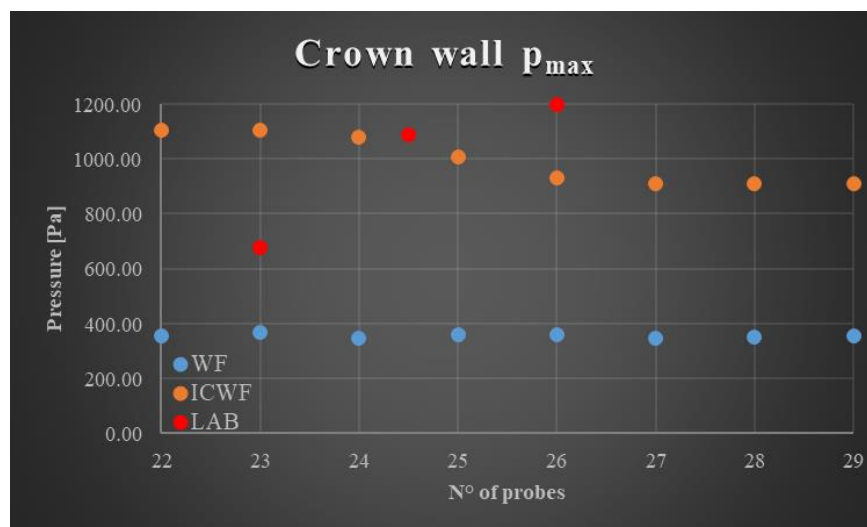
Figure 81. Comparison between the values of p_{max}, acting against the crown wall, in case of *waveFoam and IsoCompressibleWaveFoam*, for the test case 1 in Table 25, i.e. R00H05s3G30c4W4.
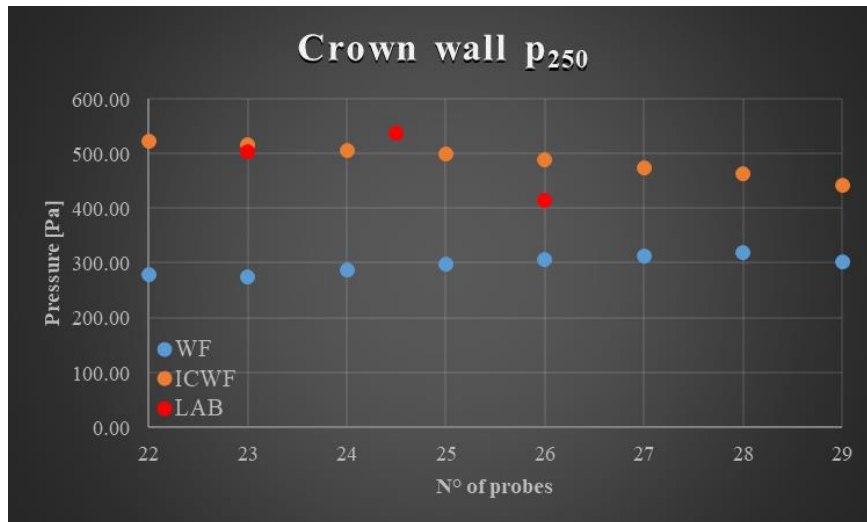
Figure 82. Comparison between the values of p_{250}, acting against the crown wall, in case of *waveFoam* and *IsoCompressibleWaveFoam*, for the test case 1 Table 25, i.e. R00H05s3G30c4W4.
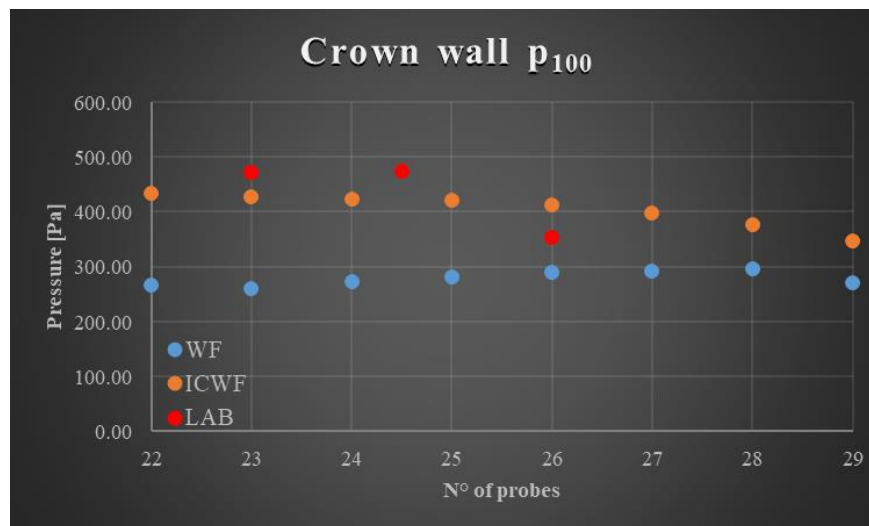
Figure 83. Comparison between the values of p_{100}, acting against the crown wall, in case of *waveFoam* and *IsoCompressibleWaveFoam*, for the test case 1 in Table 25, i.e. R00H05s3G30c4W4.
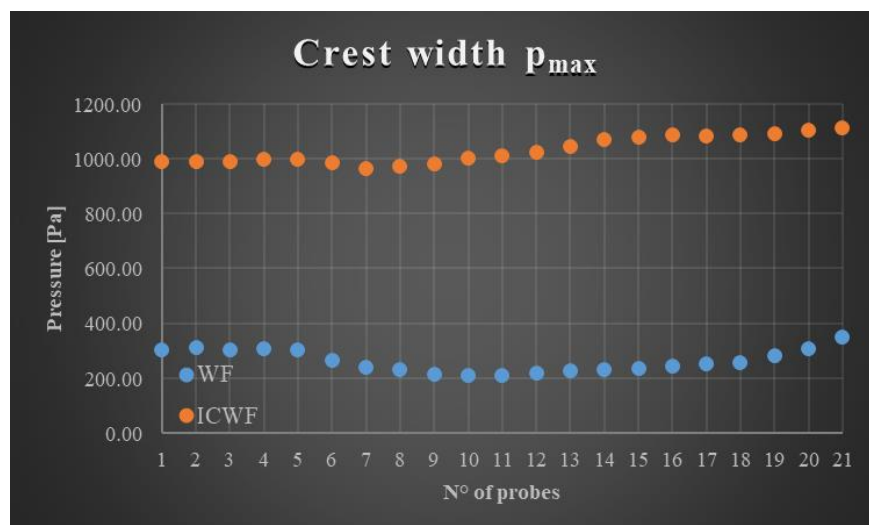
Figure 84. Comparison between the values of p_{max}, acting along the crest width, in case of *waveFoam* and *IsoCompressibleWaveFoam*, for the test case 1 in Table 25, i.e. R00H05s3G30c4W4.
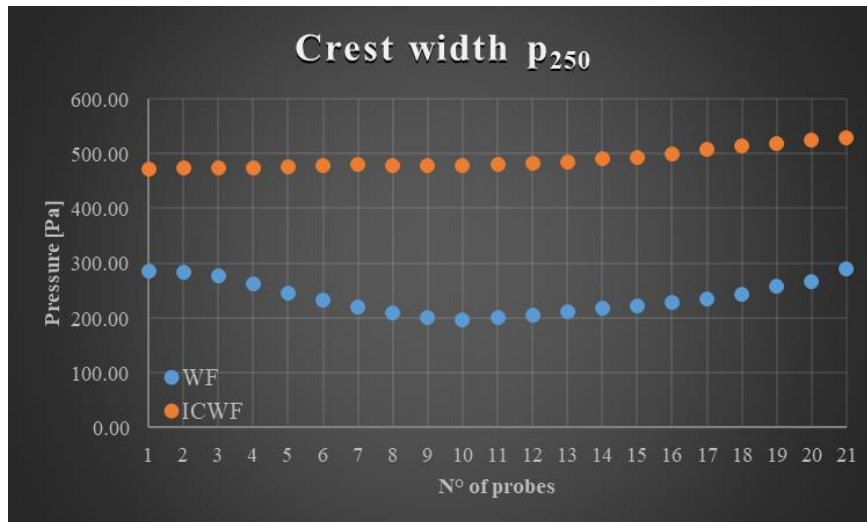
Figure 85. Comparison between the values of p_{250}, acting along the crest width, in case of *waveFoam and IsoCompressibleWaveFoam*, for the test case 1 in Table 25, i.e. R00H05s3G30c4W4.
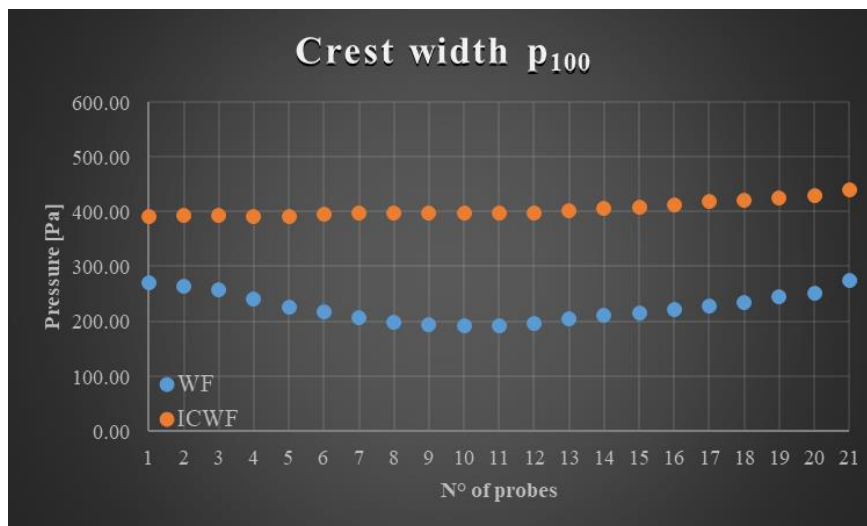
Figure 86. Comparison between the values of p_{100}, acting along the crest width, in case of *waveFoam and IsoCompressibleWaveFoam*, for the test case 1 in Table 25, i.e. R00H05s3G30c4W4.

8. Conclusions

The aim of this thesis was the optimization of the hydraulic and structural performance of multifunctional maritime structures aimed to protect harbours and produce energy. The reference study case is represented by the Overtopping Breakwater for the Energy Conversion, named OBREC, developed by the team of the University of Campania.

Specifically, the present work was conducted to close the gaps related to the relevance of some geometric parameters of the structure cross section and of the role of the fluid compressibility in their response. To achieve a more comprehensive understanding of the wave – interaction processes, several methodologies were adopted and combined. Being the numerical modelling the driver tool of this research, small – scale laboratory tests and prototype – scale investigations of the OBREC device, together with a new laboratory campaign focused on the air entrainment effects during the wave impact, were also considered.

The numerical modelling of the OBREC cross section with the single – phase code IH – 2VOF allowed to draw some conclusions about key geometric parameters such as the plate off-shore slope, the reservoir width and the crown wall.

A submerged quasi – vertical part can be introduced in the frontal part of the sloping plate, without compromising its hydraulic performance in terms of the overtopping discharge rates inside the reservoir. The consequent double inclination of the sloping plate improves also the ramp resistance to bending and to fatigue, enhancing the interlocking between the rocks of the armour layer and the device. Such modification results also in a more general cross section, which can be easily placed on top of existing breakwaters independently from their off – shore slopes.

The reservoir width is not affecting the OBREC performance and therefore its selection can be subordinated to the height of the sloping plate, which has to be tuned on the site – specific typical wave climate.

To guarantee the harbour safety, a parapet characterized by an angle of 45° has to be placed on the crown wall. The effectiveness of this element increases as the dimension of the reservoir width decreases, ensuring an adequate safety level even in case the site – specific spatial constraints does not allow the implementation of a wide reservoir.

The analysis of the prototype monitoring data and the numerical modelling with the multi – phase code openFOAM of the prototype cross sections assessed that the lower sloping plate maximizes the theoretical power available to the system, being capable of exploiting a wider range of wave conditions with respect to the higher sloping plate (operational window $T_{o.w.} > 32\%$ instead of $> 10\%$). However, the hydraulic optimization has finally to be combined with the technical characteristics, and sometimes the limitations, of the available PTO systems.

The new laboratory campaign performed at the Hydraulic Laboratory of the University of Bologna allowed to analyze the effects induced by the inclusion of a sloping parapet on the top of dikes with different offshore slopes, crest widths, crown wall heights and crest freeboards under breaking and non – breaking irregular wave conditions.

The qualitative analysis of the pressure distribution along the crown walls showed that the nature and the magnitude of the impact loads and the shape of the pressure signals consequent to the wave impacts are strongly dependent on the breaker type and on the amount of air pockets entrapped. The maximum pressure peaks associated to the most violent impacts are associate to surging non – breaking waves and to low air entrapment conditions.

In case of non – breaking waves, the effect of the crest width is indeed negligible, while in case of breaking/broken waves, the magnitude of the impacts decreases with increasing the crest width with reductions of p_{250} up to $60 - 70\%$ in case of the wider crest.

The inclusion of the parapet induces a severe increase (on average of $50 - 70\%$) of the p_{250} values along the whole vertical section of the crown wall. Therefore, the inclusion of the parapet has to be carefully considered.

A new toolbox was developed in the openFOAM environment for solving wave – impermeable/permeable structures interactions, accounting for the fluid compressibility. The new plug – in Isothermal Compressible WaveFoam *ICWF* solver was validated based on a sub – set of the tests of the new laboratory campaign on dikes with crown walls and parapets.

The new compressible solver *ICWF* shows higher values of pressures with respect to the incompressible Wave Foam solver *WF*, being the values of p_{max}, p_{250} and p_{100} on average the 97%, the 48% and the 41%, respectively greater for *ICWF* than for *WF*.

The numerical results tend to generally underestimate both the maximum and the statistical values of the pressures obtained from the laboratory measurements. However, the discrepancy derived from the incompressible solver *IWF* is much bigger than the one associated to the *ICWF* solver. The underestimation of the values of p_{max} is on average the 62% and the 26% for *WF* and *ICWF*, respectively; while the differences are reduced up to the 34% for *WF* and the 4% for *ICWF* on average when the statistical pressures are considered.

9. Further research

To improve the optimization process of the OBREC device, a 3D model of the pilot plant installed in the port of Naples has been developed in the openFOAM environment.

The 3D simulation of the OBREC prototype (shown in Figure 87) will allow for a direct comparison of the numerical results with the field data, avoiding any simplification of the geometries and therefore of the processes, under ordinary and extreme conditions.

A parametric study will be carried out to optimize the number, the location and the size of the pipes (characterized by a strong 3D nature) to maximize the energy production and to drive the selection of a suitable PTO system. The analysis of the power production will be improved by introducing the shunt tank in the numerical model, to estimate the hydraulic head established, available for the PTO system. Furthermore, the effects of the 2 configurations to each other will be assessed, from both the hydraulic and the structural points of view.

The breakwater, and specifically the offshore slope characterizing the tetrapods layer, has been reproduced according to the real characteristics of the structure. The cell sizes of the mesh characterizing the porous layers correspond to the nominal size of rocks. Furthermore, the mesh has been refined in correspondence of the still water level, to better represent the wave development along the domain; and in correspondence of the OBREC device, to improve the analysis of the wave – structure interactions (Figure 87).

Figure 88 shows the 3D nature of the numerical model, focusing the attention on what happens inside the OBREC device. Indeed, part of the overtopping flow goes through the pipes, here characterized by their real cylindrical shape, to then flow out from the device thanks to a rectangular opening located at the rear of the wave chamber. The other component of the overtopping flow hits the crown wall to be then reflected towards the sea. As expected, the wave impact produces high dynamic pressures p_rgh along the OBREC profile, as highlighted in Figure 88 (red colour).

The hydraulic and the structural performance will be assessed by measuring:

- the wave reflection by means of 3 virtual wave gauges placed along the numerical domain, more than one wavelength far from the structure;
- the water flowing through the pipes, towards the turbines, thanks to 2 gauges (one for each pipe), which measure the positive flow velocity, by isolating the water contribution;
- the overtopping flows at the rear side of the structure that is quantified as for the previous case. A wave gauge is set in the middle section of each configuration to highlight the different behaviour of the two, in terms of overtopping reduction;
- the wave loads acting along the OBREC configurations by means of numerical probes located in the same position of the physical ones installed at the pilot plant. Furthermore, the numerical model allows to extend to available information, by increasing the measuring points along the whole structure.

a)   b)

c)   d)
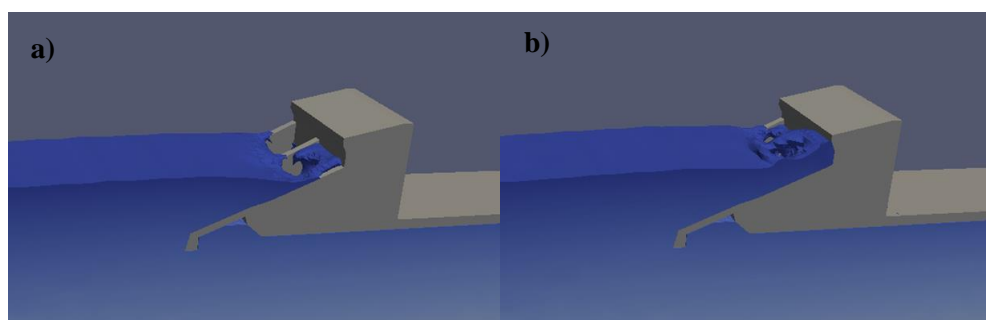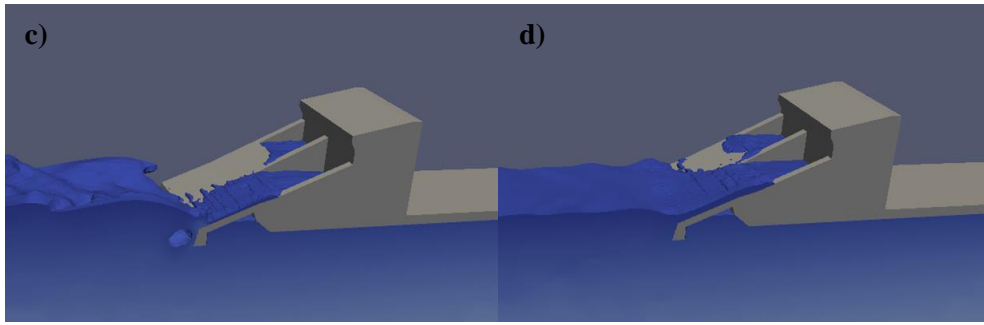
Figure 87. Screenshots of the 3D simulation.
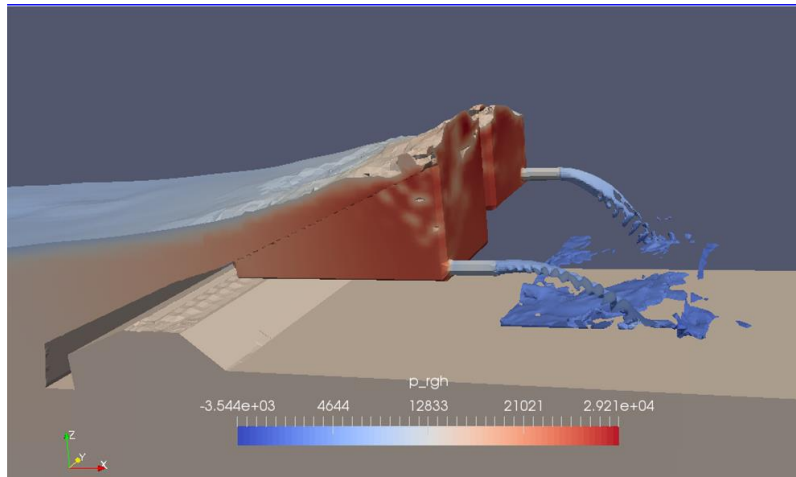
Figure 88. Screenshot of the overtopping flow passing through the pipes.

Appendix A → *IsoCompressibleWaveFoam*

- **IsoCompressibleWaveFoam.C**

```
#include "fvCFD.H"
#include "MULES.H"
#include "subCycle.H"
#include "rhoThermo.H"
#include "interfaceProperties.H"
#include "twoPhaseMixture.H"
#include "twoPhaseMixtureThermo.H"
#include "turbulentFluidThermoModel.H"
#include "pimpleControl.H"
#include "fixedFluxPressureFvPatchScalarField.H"

#include "relaxationZone.H"
#include "externalWaveForcing.H"

// * * * * * * * * * * * * * * * * * * * * * * * * * * * * * * * * * * //

int main(int argc, char *argv[])
{
    #include "setRootCase.H"
    #include "createTime.H"
    #include "createMesh.H"

    pimpleControl pimple(mesh);

    #include "createTimeControls.H"

    #include "readGravitationalAcceleration.H" //add
     #include "readWaveProperties.H" //add
    #include "createExternalWaveForcing.H" //add


  #include "createFields.H"
  #include "CourantNo.H"
  #include "setInitialDeltaT.H"
  // * * * * * * * * * * * * * * * * * * * * * * * * * * * * * * * * //

  Info<< "\nStarting time loop\n" << endl;

  while (runTime.run())
  {
     #include "createTimeControls.H"
     #include "CourantNo.H"
     #include "setDeltaT.H"

     runTime++;

     Info<< "Time = " << runTime.timeName() << nl << endl;
```

```cpp
        externalWave->step(); //add

        // --- Pressure-velocity PIMPLE corrector loop
        while (pimple.loop())
        {
            #include "alphaEqnsSubCycle.H"

            relaxing.correct(); //add

            // correct interface on first PIMPLE corrector
            if (pimple.corr() == 1)
            {
                interface.correct();
            }

            solve(fvm::ddt(rho) + fvc::div(rhoPhi));

            #include "UEqn.H"


            // --- Pressure corrector loop
            while (pimple.correct())
            {
                #include "pEqn.H"
            }

            if (pimple.turbCorr())
            {
                turbulence->correct();
            }
        }

        runTime.write();

        Info<< "ExecutionTime = "
            << runTime.elapsedCpuTime()
            << " s\n\n" << endl;
    }

 // Close down the external wave forcing in a nice manner

    externalWave->close(); //add

    Info<< "End\n" << endl;

    return 0;
}
```

- **alphaControls.H**

```cpp
const dictionary& alphaControls = mesh.solverDict(alpha1.name());
```

127

```
label nAlphaCorr(readLabel(alphaControls.lookup("nAlphaCorr")));

label nAlphaSubCycles(readLabel(alphaControls.lookup("nAlphaSubCycles")));
```

- **alphaEqns.H**

```
{
    word alphaScheme("div(phi,alpha)");
    word alpharScheme("div(phirb,alpha)");

    surfaceScalarField phir(phic*interface.nHatf());

    for (int gCorr=0; gCorr<nAlphaCorr; gCorr++)
    {
        volScalarField::DimensionedInternalField Sp
        (
            IOobject
            (
                "Sp",
                runTime.timeName(),
                mesh
            ),
            mesh,
            dimensionedScalar("Sp", dgdt.dimensions(), 0.0)
        );

        volScalarField::DimensionedInternalField Su
        (
            IOobject
            (
                "Su",
                runTime.timeName(),
                mesh
            ),
            // Divergence term is handled explicitly to be
            // consistent with the explicit transport solution
            divU*min(alpha1, scalar(1))
        );

        forAll(dgdt, celli)
        {
            if (dgdt[celli] > 0.0 && alpha1[celli] > 0.0)
            {
                Sp[celli] -= dgdt[celli]*alpha1[celli];
                Su[celli] += dgdt[celli]*alpha1[celli];
            }
            else if (dgdt[celli] < 0.0 && alpha1[celli] < 1.0)
            {
                Sp[celli] += dgdt[celli]*(1.0 - alpha1[celli]);
            }
        }
```

```
    surfaceScalarField alphaPhi1
    (
        fvc::flux
        (
            phi,
            alpha1,
            alphaScheme
        )
      + fvc::flux
        (
            -fvc::flux(-phir, alpha2, alpharScheme),
            alpha1,
            alpharScheme
        )
    );

    MULES::explicitSolve
    (
        geometricOneField(),
        alpha1,
        phi,
        alphaPhi1,
        Sp,
        Su,
        1,
        0
    );

    surfaceScalarField rho1f(fvc::interpolate(rho1));
    surfaceScalarField rho2f(fvc::interpolate(rho2));
    rhoPhi = alphaPhi1*(rho1f - rho2f) + phi*rho2f;

    alpha2 = scalar(1) - alpha1;
    }

    Info<< "Liquid phase volume fraction = "
        << alpha1.weightedAverage(mesh.V()).value()
        << "  Min(" << alpha1.name() << ") = " << min(alpha1).value()
        << "  Min(" << alpha2.name() << ") = " << min(alpha2).value()
        << endl;
}
```

- **alphaEqnsSubCycle.H**

```
{
    #include "alphaControls.H"

    surfaceScalarField phic(mag(phi/mesh.magSf()));
    phic = min(interface.cAlpha()*phic, max(phic));

    volScalarField divU(fvc::div(fvc::absolute(phi, U)));
```

```
    if (nAlphaSubCycles > 1)
    {
        dimensionedScalar totalDeltaT = runTime.deltaT();
        surfaceScalarField rhoPhiSum
        (
            IOobject
            (
                "rhoPhiSum",
                runTime.timeName(),
                mesh
            ),
            mesh,
            dimensionedScalar("0", rhoPhi.dimensions(), 0)
        );

        for
        (
            subCycle<volScalarField> alphaSubCycle(alpha1, nAlphaSubCycles);
            !(++alphaSubCycle).end();
        )
        {
            #include "alphaEqns.H"
            rhoPhiSum += (runTime.deltaT()/totalDeltaT)*rhoPhi;
        }

        rhoPhi = rhoPhiSum;
    }
    else
    {
        #include "alphaEqns.H"
    }
}
```

- **createFields.H**

```
Info<< "Reading field p_rgh\n" << endl;
volScalarField p_rgh
(
    IOobject
    (
        "p_rgh",
        runTime.timeName(),
        mesh,
        IOobject::MUST_READ,
        IOobject::AUTO_WRITE
    ),
    mesh
);

Info<< "Reading field U\n" << endl;
volVectorField U
```

```
(
    IOobject
    (
        "U",
        runTime.timeName(),
        mesh,
        IOobject::MUST_READ,
        IOobject::AUTO_WRITE
    ),
    mesh
);

#include "createPhi.H"

Info<< "Constructing twoPhaseMixtureThermo\n" << endl;
twoPhaseMixtureThermo mixture(mesh);

volScalarField& alpha1(mixture.alpha1());
volScalarField& alpha2(mixture.alpha2());

Info<< "Reading thermophysical properties\n" << endl;

volScalarField& p = mixture.p();
volScalarField& rho1 = mixture.thermo1().rho();
const volScalarField& psi1 = mixture.thermo1().psi();
volScalarField& rho2 = mixture.thermo2().rho();
const volScalarField& psi2 = mixture.thermo2().psi();

volScalarField rho
(
    IOobject
    (
        "rho",
        runTime.timeName(),
        mesh,
        IOobject::READ_IF_PRESENT,
        IOobject::AUTO_WRITE
    ),
    alpha1*rho1 + alpha2*rho2
);

dimensionedScalar pMin
(
    "pMin",
    dimPressure,
    mixture
);

mesh.setFluxRequired(p_rgh.name());


volScalarField gh("gh", g & (mesh.C() - referencePoint)); //add
surfaceScalarField ghf("ghf", g & (mesh.Cf() - referencePoint));//add
```

131

```
// Mass flux
// Initialisation does not matter because rhoPhi is reset after the
// alpha1 solution before it is used in the U equation.
surfaceScalarField rhoPhi
(
    IOobject
    (
        "rhoPhi",
        runTime.timeName(),
        mesh,
        IOobject::NO_READ,
        IOobject::NO_WRITE
    ),
    fvc::interpolate(rho)*phi
);

volScalarField dgdt
(
    pos(alpha2)*fvc::div(phi)/max(alpha2, scalar(0.0001))
);

// Construct interface from alpha1 distribution
interfaceProperties interface(alpha1, U, mixture);

// Construct compressible turbulence model
autoPtr<compressible::turbulenceModel> turbulence
(
    compressible::turbulenceModel::New(rho, U, rhoPhi, mixture)
);

Info<< "Creating field kinetic energy K\n" << endl;
volScalarField K("K", 0.5*magSqr(U));

relaxationZone relaxing(mesh, U, alpha1); //add
```

- **pEqn.H**

```
{
    volScalarField rAU("rAU", 1.0/UEqn.A());
    surfaceScalarField rAUf("rAUf", fvc::interpolate(rAU));

    volVectorField HbyA("HbyA", U);
    HbyA = rAU*UEqn.H();

    surfaceScalarField phiHbyA
    (
        "phiHbyA",
        (fvc::interpolate(HbyA) & mesh.Sf())
      + fvc::interpolate(rho*rAU)*fvc::ddtCorr(U, phi)
    );
```

132

```
surfaceScalarField phig
(
    (
        interface.surfaceTensionForce()
      - ghf*fvc::snGrad(rho)
    )*rAUf*mesh.magSf()
);

phiHbyA += phig;

// Update the fixedFluxPressure BCs to ensure flux consistency
setSnGrad<fixedFluxPressureFvPatchScalarField>
(
    p_rgh.boundaryField(),
    (
        phiHbyA.boundaryField()
      - (mesh.Sf().boundaryField() & U.boundaryField())
    )/(mesh.magSf().boundaryField()*rAUf.boundaryField())
);

tmp<fvScalarMatrix> p_rghEqnComp1;
tmp<fvScalarMatrix> p_rghEqnComp2;

if (pimple.transonic())
{
    surfaceScalarField phid1("phid1", fvc::interpolate(psi1)*phi);
    surfaceScalarField phid2("phid2", fvc::interpolate(psi2)*phi);

    p_rghEqnComp1 =
        fvc::ddt(rho1) + fvc::div(phi, rho1) - fvc::Sp(fvc::div(phi), rho1)
      + correction
        (
            psi1*fvm::ddt(p_rgh)
          + fvm::div(phid1, p_rgh) - fvm::Sp(fvc::div(phid1), p_rgh)
        );
    deleteDemandDrivenData(p_rghEqnComp1().faceFluxCorrectionPtr());
    p_rghEqnComp1().relax();

    p_rghEqnComp2 =
        fvc::ddt(rho2) + fvc::div(phi, rho2) - fvc::Sp(fvc::div(phi), rho2)
      + correction
        (
            psi2*fvm::ddt(p_rgh)
          + fvm::div(phid2, p_rgh) - fvm::Sp(fvc::div(phid2), p_rgh)
        );
    deleteDemandDrivenData(p_rghEqnComp2().faceFluxCorrectionPtr());
    p_rghEqnComp2().relax();
}
else
{
    p_rghEqnComp1 =
        fvc::ddt(rho1) + psi1*correction(fvm::ddt(p_rgh))
      + fvc::div(phi, rho1) - fvc::Sp(fvc::div(phi), rho1);
```

```
    p_rghEqnComp2 =
        fvc::ddt(rho2) + psi2*correction(fvm::ddt(p_rgh))
      + fvc::div(phi, rho2) - fvc::Sp(fvc::div(phi), rho2);
}

// Cache p_rgh prior to solve for density update
volScalarField p_rgh_0(p_rgh);

while (pimple.correctNonOrthogonal())
{
    fvScalarMatrix p_rghEqnIncomp
    (
        fvc::div(phiHbyA)
      - fvm::laplacian(rAUf, p_rgh)
    );

    solve
    (
        (
            (max(alpha1, scalar(0))/rho1*p_rghEqnComp1()
          + (max(alpha2, scalar(0))/rho2*p_rghEqnComp2()
        )
      + p_rghEqnIncomp,
        mesh.solver(p_rgh.select(pimple.finalInnerIter()))
    );

    if (pimple.finalNonOrthogonalIter())
    {
        p = max(p_rgh + (alpha1*rho1 + alpha2*rho2)*gh, pMin);
        p_rgh = p - (alpha1*rho1 + alpha2*rho2)*gh;

        dgdt =
        (
            pos(alpha2)*(p_rghEqnComp2 & p_rgh)/rho2
          - pos(alpha1)*(p_rghEqnComp1 & p_rgh)/rho1
        );

        phi = phiHbyA + p_rghEqnIncomp.flux();

        U = HbyA
          + rAU*fvc::reconstruct((phig + p_rghEqnIncomp.flux())/rAUf);
        U.correctBoundaryConditions();
    }
}

// p = max(p_rgh + (alpha1*rho1 + alpha2*rho2)*gh, pMin);

// Update densities from change in p_rgh
rho1 += psi1*(p_rgh - p_rgh_0);
rho2 += psi2*(p_rgh - p_rgh_0);

rho = alpha1*rho1 + alpha2*rho2;
```

```
  K = 0.5*magSqr(U);

  Info<< "max(U) " << max(mag(U)).value() << endl;
  Info<< "min(p_rgh) " << min(p_rgh).value() << endl;
}
```

- **Ueqn.H**

```
fvVectorMatrix UEqn
(
    fvm::ddt(rho, U)
  + fvm::div(rhoPhi, U)
  + turbulence->divDevRhoReff(U)
);

UEqn.relax();

if (pimple.momentumPredictor())
{
    solve
    (
      UEqn
     ==
      fvc::reconstruct
      (
        (
            interface.surfaceTensionForce()
          - ghf*fvc::snGrad(rho)
          - fvc::snGrad(p_rgh)
        ) * mesh.magSf()
      )
    );

    K = 0.5*magSqr(U);
}
```

Appendix B → *IsoPorousCompressibleWaveFoam*

- *IsoPorousCompressibleWaveFoam*

```
#include "fvCFD.H"
#include "MULES.H"
#include "subCycle.H"
#include "rhoThermo.H"
#include "interfaceProperties.H"
#include "twoPhaseMixture.H"
#include "twoPhaseMixtureThermo.H"
#include "turbulentFluidThermoModel.H"
#include "pimpleControl.H"
#include "fixedFluxPressureFvPatchScalarField.H"

#include "relaxationZone.H"
#include "externalWaveForcing.H"

#include "wavesPorosityModel.H"

// * * * * * * * * * * * * * * * * * * * * * * * * * * * * * * * * //

int main(int argc, char *argv[])
{
    #include "setRootCase.H"
    #include "createTime.H"
    #include "createMesh.H"

    pimpleControl pimple(mesh);

    #include "createTimeControls.H"
    #include "readGravitationalAcceleration.H"

    #include "readWaveProperties.H" //add
    #include "createExternalWaveForcing.H"

    #include "createPorosityFields.H" //add

   #include "createFields.H"
   #include "CourantNo.H"
   #include "setInitialDeltaT.H"
    // * * * * * * * * * * * * * * * * * * * * * * * * * * * * * * * //

    Info<< "\nStarting time loop\n" << endl;

    while (runTime.run())
    {
        #include "createTimeControls.H"
        #include "CourantNo.H"
        #include "setDeltaT.H"

        runTime++;
```

```cpp
        Info<< "Time = " << runTime.timeName() << nl << endl;

        externalWave->step();

        #include "calcPorosity.H" //add

        // --- Pressure-velocity PIMPLE corrector loop
        while (pimple.loop())
        {
            #include "alphaEqnsSubCycle.H"

            relaxing.correct(); // try here

            // correct interface on first PIMPLE corrector
            if (pimple.corr() == 1)
            {
                interface.correct();
            }

            solve(fvm::ddt(rho) + fvc::div(rhoPhi));

            #include "UEqn.H"


            // --- Pressure corrector loop
            while (pimple.correct())
            {
                #include "pEqn.H"
            }

            if (pimple.turbCorr())
            {
                turbulence->correct();
            }
        }

        runTime.write();

        Info<< "ExecutionTime = "
            << runTime.elapsedCpuTime()
            << " s\n\n" << endl;
    }

    // Close down the external wave forcing in a nice manner
    externalWave->close(); //add

    Info<< "End\n" << endl;

    return 0;
}
```

- **alphaControls.H**

```
const dictionary& alphaControls = mesh.solverDict(alpha1.name());

label nAlphaCorr(readLabel(alphaControls.lookup("nAlphaCorr")));

label nAlphaSubCycles(readLabel(alphaControls.lookup("nAlphaSubCycles")));
```

- **alphaEqns.H**

```
{
   word alphaScheme("div(phi,alpha)");
   word alpharScheme("div(phirb,alpha)");

   surfaceScalarField phir(phic*interface.nHatf());

   for (int gCorr=0; gCorr<nAlphaCorr; gCorr++)
   {
      volScalarField::DimensionedInternalField Sp
      (
         IOobject
         (
            "Sp",
            runTime.timeName(),
            mesh
         ),
         mesh,
         dimensionedScalar("Sp", dgdt.dimensions(), 0.0)
      );

      volScalarField::DimensionedInternalField Su
      (
         IOobject
         (
            "Su",
            runTime.timeName(),
            mesh
         ),
         // Divergence term is handled explicitly to be
         // consistent with the explicit transport solution
         divU*min(alpha1, scalar(1))
      );

      forAll(dgdt, celli)
      {
         if (dgdt[celli] > 0.0 && alpha1[celli] > 0.0)
         {
            Sp[celli] -= dgdt[celli]*alpha1[celli];
            Su[celli] += dgdt[celli]*alpha1[celli];
         }
         else if (dgdt[celli] < 0.0 && alpha1[celli] < 1.0)
         {
```

```
                Sp[celli] += dgdt[celli]*(1.0 - alpha1[celli]);
            }
        }

        surfaceScalarField alphaPhi1
        (
            fvc::flux
            (
                phi,
                alpha1,
                alphaScheme
            )
          + fvc::flux
            (
                -fvc::flux(-phir, alpha2, alpharScheme),
                alpha1,
                alpharScheme
            )
        );

        MULES::explicitSolve
        (

            porosity,
            alpha1,
            phi,
            alphaPhi1,
            Sp,
            Su,
            1,
            0
        );

        surfaceScalarField rho1f(fvc::interpolate(rho1));
        surfaceScalarField rho2f(fvc::interpolate(rho2));
        rhoPhi = alphaPhi1*(rho1f - rho2f) + phi*rho2f;

        alpha2 = scalar(1) - alpha1;
    }

    Info<< "Liquid phase volume fraction = "
        << alpha1.weightedAverage(mesh.V()).value()
        << "  Min(" << alpha1.name() << ") = " << min(alpha1).value()
        << "  Min(" << alpha2.name() << ") = " << min(alpha2).value()
        << endl;
}
```

- **alphaEqnsSubCycle.H**

```
{
    #include "alphaControls.H"
```

139

```
surfaceScalarField phic(mag(phi/mesh.magSf()));
phic = min(interface.cAlpha()*phic, max(phic));

volScalarField divU(fvc::div(fvc::absolute(phi, U)));

if (nAlphaSubCycles > 1)
{
    dimensionedScalar totalDeltaT = runTime.deltaT();
    surfaceScalarField rhoPhiSum
    (
        IOobject
        (
            "rhoPhiSum",
            runTime.timeName(),
            mesh
        ),
        mesh,
        dimensionedScalar("0", rhoPhi.dimensions(), 0)
    );

    for
    (
        subCycle<volScalarField> alphaSubCycle(alpha1, nAlphaSubCycles);
        !(++alphaSubCycle).end();
    )
    {
        #include "alphaEqns.H"
        rhoPhiSum += (runTime.deltaT()/totalDeltaT)*rhoPhi;
    }

    rhoPhi = rhoPhiSum;
}
else
{
    #include "alphaEqns.H"
}
}
```

- **createFields.H**

```
Info<< "Reading field p_rgh\n" << endl;
volScalarField p_rgh
(
    IOobject
    (
        "p_rgh",
        runTime.timeName(),
        mesh,
        IOobject::MUST_READ,
        IOobject::AUTO_WRITE
    ),
```

```
      mesh
);

Info<< "Reading field U\n" << endl;
volVectorField U
(
    IOobject
    (
        "U",
        runTime.timeName(),
        mesh,
        IOobject::MUST_READ,
        IOobject::AUTO_WRITE
    ),
    mesh
);

#include "createPhi.H"

Info<< "Constructing twoPhaseMixtureThermo\n" << endl;
twoPhaseMixtureThermo mixture(mesh);

volScalarField& alpha1(mixture.alpha1());
volScalarField& alpha2(mixture.alpha2());

Info<< "Reading thermophysical properties\n" << endl;

volScalarField& p = mixture.p();


volScalarField& rho1 = mixture.thermo1().rho();
const volScalarField& psi1 = mixture.thermo1().psi();
volScalarField& rho2 = mixture.thermo2().rho();
const volScalarField& psi2 = mixture.thermo2().psi();

volScalarField rho
(
    IOobject
    (
        "rho",
        runTime.timeName(),
        mesh,
        IOobject::READ_IF_PRESENT,
        IOobject::AUTO_WRITE
    ),
    alpha1*rho1 + alpha2*rho2
);

dimensionedScalar pMin
(
    "pMin",
    dimPressure,
    mixture
```

```
);

mesh.setFluxRequired(p_rgh.name());

volScalarField gh("gh", g & (mesh.C() - referencePoint)); //add
surfaceScalarField ghf("ghf", g & (mesh.Cf() - referencePoint));//add

// Mass flux
// Initialisation does not matter because rhoPhi is reset after the
// alpha1 solution before it is used in the U equation.
surfaceScalarField rhoPhi
(
    IOobject
    (
        "rhoPhi",
        runTime.timeName(),
        mesh,
        IOobject::NO_READ,
        IOobject::NO_WRITE
    ),
    fvc::interpolate(rho)*phi
);

volScalarField dgdt
(
    pos(alpha2)*fvc::div(phi)/max(alpha2, scalar(0.0001))
);

// Construct interface from alpha1 distribution
interfaceProperties interface(alpha1, U, mixture);

// Construct compressible turbulence model
autoPtr<compressible::turbulenceModel> turbulence
(
    compressible::turbulenceModel::New(rho, U, rhoPhi, mixture)
);

Info<< "Creating field kinetic energy K\n" << endl;
volScalarField K("K", 0.5*magSqr(U));

relaxationZone relaxing(mesh, U, alpha1);
```

- **pEqn.H**

```
{
    volScalarField rAU("rAU", 1.0/UEqn.A());
    surfaceScalarField rAUf("rAUf", fvc::interpolate(rAU));

    volVectorField HbyA("HbyA", U);
    HbyA = rAU*UEqn.H();

    surfaceScalarField phiHbyA
```

```
(
    "phiHbyA",
    (fvc::interpolate(HbyA) & mesh.Sf())
  + fvc::interpolate(rho*rAU)*fvc::ddtCorr(U, phi)
);

surfaceScalarField phig
(
    (
        interface.surfaceTensionForce()
      - ghf*fvc::snGrad(rho)
    )*rAUf*mesh.magSf()
);

phiHbyA += phig;

// Update the fixedFluxPressure BCs to ensure flux consistency
setSnGrad<fixedFluxPressureFvPatchScalarField>
(
    p_rgh.boundaryField(),
    (
        phiHbyA.boundaryField()
      - (mesh.Sf().boundaryField() & U.boundaryField())
    )/(mesh.magSf().boundaryField()*rAUf.boundaryField())
);

tmp<fvScalarMatrix> p_rghEqnComp1;
tmp<fvScalarMatrix> p_rghEqnComp2;

if (pimple.transonic())
{
    surfaceScalarField phid1("phid1", fvc::interpolate(psi1)*phi);
    surfaceScalarField phid2("phid2", fvc::interpolate(psi2)*phi);

    p_rghEqnComp1 =
        fvc::ddt(rho1) + fvc::div(phi, rho1) - fvc::Sp(fvc::div(phi), rho1)
      + correction
        (
            psi1*fvm::ddt(p_rgh)
          + fvm::div(phid1, p_rgh) - fvm::Sp(fvc::div(phid1), p_rgh)
        );
    deleteDemandDrivenData(p_rghEqnComp1().faceFluxCorrectionPtr());
    p_rghEqnComp1().relax();

    p_rghEqnComp2 =
        fvc::ddt(rho2) + fvc::div(phi, rho2) - fvc::Sp(fvc::div(phi), rho2)
      + correction
        (
            psi2*fvm::ddt(p_rgh)
          + fvm::div(phid2, p_rgh) - fvm::Sp(fvc::div(phid2), p_rgh)
        );
    deleteDemandDrivenData(p_rghEqnComp2().faceFluxCorrectionPtr());
    p_rghEqnComp2().relax();
```

```
}
else
{
    p_rghEqnComp1 =
        fvc::ddt(rho1) + psi1*correction(fvm::ddt(p_rgh))
      + fvc::div(phi, rho1) - fvc::Sp(fvc::div(phi), rho1);

    p_rghEqnComp2 =
        fvc::ddt(rho2) + psi2*correction(fvm::ddt(p_rgh))
      + fvc::div(phi, rho2) - fvc::Sp(fvc::div(phi), rho2);
}

// Cache p_rgh prior to solve for density update
volScalarField p_rgh_0(p_rgh);

while (pimple.correctNonOrthogonal())
{
    fvScalarMatrix p_rghEqnIncomp
    (
        fvc::div(phiHbyA)
      - fvm::laplacian(rAUf, p_rgh)
    );

    solve
    (
        (
            (max(alpha1, scalar(0))/rho1)*p_rghEqnComp1()
          + (max(alpha2, scalar(0))/rho2)*p_rghEqnComp2()
        )
      + p_rghEqnIncomp,
        mesh.solver(p_rgh.select(pimple.finalInnerIter()))
    );

    if (pimple.finalNonOrthogonalIter())
    {
        p = max(p_rgh + (alpha1*rho1 + alpha2*rho2)*gh, pMin);
        p_rgh = p - (alpha1*rho1 + alpha2*rho2)*gh;

        dgdt =
        (
            pos(alpha2)*(p_rghEqnComp2 & p_rgh)/rho2
          - pos(alpha1)*(p_rghEqnComp1 & p_rgh)/rho1
        );

        phi = phiHbyA + p_rghEqnIncomp.flux();

        U = HbyA
          + rAU*fvc::reconstruct((phig + p_rghEqnIncomp.flux())/rAUf);
        U.correctBoundaryConditions();
    }
}

// p = max(p_rgh + (alpha1*rho1 + alpha2*rho2)*gh, pMin);
```

```
// Update densities from change in p_rgh
rho1 += psi1*(p_rgh - p_rgh_0);
rho2 += psi2*(p_rgh - p_rgh_0);

rho = alpha1*rho1 + alpha2*rho2;

K = 0.5*magSqr(U);

Info<< "max(U) " << max(mag(U)).value() << endl;
Info<< "min(p_rgh) " << min(p_rgh).value() << endl;
}
```

- **Ueqn.H**

```
volScalarField mu(mixture.mu()); //add

fvVectorMatrix UEqn
(


    pm->ddt(rho, U) //add
  + 1.0/porosity*fvm::div(rhoPhi/(porosityFace), U)
  + (1.0/porosity) * turbulence->divDevRhoReff(U)

);

UEqn.relax();

pm->addResistance(UEqn); //add

if (pimple.momentumPredictor())
{
   solve
   (
     UEqn
   ==
     fvc::reconstruct
     (
        (
          interface.surfaceTensionForce()
        - ghf*fvc::snGrad(rho)
        - fvc::snGrad(p_rgh)
        ) * mesh.magSf()
     )
   );

   K = 0.5*magSqr(U);
}
```

Appendix C → Mesh files

- *blockMeshDict*

```
/*--------------------------------*- C++ -*----------------------------------*\
| =========                 |
|
| \\      /  F ield          | OpenFOAM: The Open Source CFD Toolbox
|
|  \\    /   O peration      | Version:  1.5
|
|   \\  /    A nd            | Web:      http://www.OpenFOAM.org
|
|    \\/     M anipulation   |
|
\*---------------------------------------------------------------------------*/
FoamFile
{
    version     2.0;
    format      ascii;
    class       dictionary;
    object      blockMeshDict;
}
// * * * * * * * * * * * * * * * * * * * * * * * * * * * * * * * * * * * //

convertToMeters 1;

vertices
(
    ( 0    0   -0.35 ) //0
    (11.2 0   -0.35 ) //1
    ( 0    0.5 -0.35)  //2
    (11.2 0.5 -0.35)  //3

    ( 0    0    0 ) //4
    (11.2 0    0 ) //5
    ( 0    0.5 0 ) //6
    (11.2 0.5 0 ) //7

    ( 0    0   1.15 ) //8
    (11.2 0   1.15 ) //9
    ( 0    0.5 1.15 ) //10
    (11.2 0.5 1.15 ) //11
);

blocks
(
    hex (0 1 3 2 4 5 7 6) ( 300 1 58 )  simpleGrading (0.0100616169 1
0.4911375953)
    hex (4 5 7 6 8 9 11 10) ( 300 1 80 ) simpleGrading (0.0100616169 1
9.620062962)
);

edges
(
);
```

```
patches
(
    patch inlet
    (
        (0 4 6 2)
      (4 8 10 6)
    )
    wall bottom
    (
        (0 1 3 2)
    )
    patch outlet
    (
        (1 5 7 3)
      (5 7 11 9)
    )

    patch atmosphere
    (
      (8 9 11 10)

    )

    empty frontBack
    (
      (0 1 5 4)
      (4 5 9 8)
        (2 3 7 6)
      (6 7 11 10)
    )
);

mergePatchPairs
(
);

//
************************************************************************
*** //
```

- *snappyHexMeshDict*

```
/*--------------------------------*- C++ -*----------------------------
-------*\
| =========                 |
|
| \\      /  F ield         | OpenFOAM: The Open Source CFD Toolbox
|
|  \\    /   O peration     | Version:  2.1.1
|
|   \\  /    A nd           | Web:      www.OpenFOAM.org
|
|    \\/     M anipulation  |
|
\*---------------------------------------------------------------------
-------*/
FoamFile
{
```

```
    version     2.0;
    format      ascii;
    class       dictionary;
    object      snappyHexMeshDict;
}
// * * * * * * * * * * * * * * * * * * * * * * * * * * * * * * * * *
* * * //

// Which of the steps to run
castellatedMesh true;
snap            true;
addLayers       false;


// Geometry. Definition of all surfaces. All surfaces are of class
// searchableSurface.
// Surfaces are used
// - to specify refinement for any mesh cell intersecting it
// - to specify refinement for any mesh cell inside/outside/near
// - to 'snap' the mesh boundary to the surface
geometry
{
    G30c4W4.stl
    {
        type triSurfaceMesh;
        name imp;
    }

};


// Settings for the castellatedMesh generation.
castellatedMeshControls
{

    // Refinement parameters
    // ~~~~~~~~~~~~~~~~~~~~~~

    // If local number of cells is >= maxLocalCells on any processor
    // switches from from refinement followed by balancing
    // (current method) to (weighted) balancing before refinement.
    maxLocalCells 100000;

    // Overall cell limit (approximately). Refinement will stop
immediately
    // upon reaching this number so a refinement level might not
complete.
    // Note that this is the number of cells before removing the part
which
    // is not 'visible' from the keepPoint. The final number of cells
might
    // actually be a lot less.
    maxGlobalCells 2000000;

    // The surface refinement loop might spend lots of iterations
refining just
    // a few cells. This setting will cause refinement to stop if <=
    // minimumRefine are selected for refinement. Note: it will at
least do one
    // iteration (unless the number of cells to refine is 0)
    minRefinementCells 10;
```

```
    maxLoadUnbalance 0.10; //add
    // Number of buffer layers between different levels.
    // 1 means normal 2:1 refinement restriction, larger means slower
    // refinement.
    nCellsBetweenLevels 2;

    // Explicit feature edge refinement
    // ~~~~~~~~~~~~~~~~~~~~~~~~~~~~~~~~~~

    // Specifies a level for any cell intersected by its edges.
    // This is a featureEdgeMesh, read from constant/triSurface for
now.
    features ();



    // Surface based refinement
    // ~~~~~~~~~~~~~~~~~~~~~~~~~~

    // Specifies two levels for every surface. The first is the
minimum level,
    // every cell intersecting a surface gets refined up to the
minimum level.
    // The second level is the maximum level. Cells that 'see'
multiple
    // intersections where the intersections make an
    // angle > resolveFeatureAngle get refined up to the maximum
level.

    refinementSurfaces
    {
        imp
        {
            // Surface-wise min and max refinement level
            level (0 0);
        }
    }

    // Resolve sharp angles on fridges
    resolveFeatureAngle 60;


    // Region-wise refinement
    // ~~~~~~~~~~~~~~~~~~~~~~~~

    // Specifies refinement level for cells in relation to a surface.
One of
    // three modes
    // - distance. 'levels' specifies per distance to the surface the
    //   wanted refinement level. The distances need to be specified
in
    //   descending order.
    // - inside. 'levels' is only one entry and only the level is
used. All
    //   cells inside the surface get refined up to the level. The
surface
    //   needs to be closed for this to be possible.
    // - outside. Same but cells outside.

    refinementRegions
```

```
    {

     }


    // Mesh selection
    // ~~~~~~~~~~~~~~

    // After refinement patches get added for all refinementSurfaces
and
    // all cells intersecting the surfaces get put into these patches.
The
    // section reachable from the locationInMesh is kept.
    // NOTE: This point should never be on a face, always inside a
cell, even
    // after refinement.
    locationInMesh (0.01 0.01 0.59);


    // Whether any faceZones (as specified in the refinementSurfaces)
    // are only on the boundary of corresponding cellZones or also
allow
    // free-standing zone faces. Not used if there are no faceZones.
    allowFreeStandingZoneFaces false;
}



// Settings for the snapping.
snapControls
{
    //- Number of patch smoothing iterations before finding
correspondence
    //  to surface
    nSmoothPatch 3;

    //- Relative distance for points to be attracted by surface
feature point
    //  or edge. True distance is this factor times local
    //  maximum edge length.
    tolerance 4;

    //- Number of mesh displacement relaxation iterations.
    nSolveIter 3;

    //- Maximum number of snapping relaxation iterations. Should stop
    //  before upon reaching a correct mesh.
    nRelaxIter 5;
    nFeatureSnapIter 5;
}




// Settings for the layer addition.
addLayersControls
{
    // Are the thickness parameters below relative to the undistorted
    // size of the refined cell outside layer (true) or absolute sizes
(false).
    relativeSizes true;

    // Per final patch (so not geometry!) the layer information
```

```
    layers
    {
        imp
        {
            nSurfaceLayers 2;
        }
    }

    // Expansion factor for layer mesh
    expansionRatio 1;

    //- Wanted thickness of final added cell layer. If multiple layers
    //  is the
    //  thickness of the layer furthest away from the wall.
    //  Relative to undistorted size of cell outside layer.
    //  is the thickness of the layer furthest away from the wall.
    //  See relativeSizes parameter.
    finalLayerThickness 0.025;

    //- Minimum thickness of cell layer. If for any reason layer
    //  cannot be above minThickness do not add layer.
    //  Relative to undistorted size of cell outside layer.
    //  See relativeSizes parameter.
    minThickness 0.01;

    //- If points get not extruded do nGrow layers of connected faces
that are
    //  also not grown. This helps convergence of the layer addition
process
    //  close to features.
    // Note: changed(corrected) w.r.t 17x! (didn't do anything in 17x)
    nGrow 0;

    // Advanced settings

    //- When not to extrude surface. 0 is flat surface, 90 is when two
faces
    //  make straight angle.
    featureAngle 30;

    //- Maximum number of snapping relaxation iterations. Should stop
    //  before upon reaching a correct mesh.
    nRelaxIter 3;

    // Number of smoothing iterations of surface normals
    nSmoothSurfaceNormals 1;

    // Number of smoothing iterations of interior mesh movement
direction
    nSmoothNormals 3;

    // Smooth layer thickness over surface patches
    nSmoothThickness 10;

    // Stop layer growth on highly warped cells
    maxFaceThicknessRatio 0.5;

    // Reduce layer growth where ratio thickness to medial
    // distance is large
    maxThicknessToMedialRatio 0.3;
```

```
    // Angle used to pick up medial axis points
    // Note: changed(corrected) w.r.t 16x! 90 degrees corresponds to
130 in 16x.
    minMedianAxisAngle 90;

    // Create buffer region for new layer terminations
    nBufferCellsNoExtrude 0;


    // Overall max number of layer addition iterations. The mesher
will exit
    // if it reaches this number of iterations; possibly with an
illegal
    // mesh.
    nLayerIter 50;
}



// Generic mesh quality settings. At any undoable phase these
determine
// where to undo.
meshQualityControls
{
    //- Maximum non-orthogonality allowed. Set to 180 to disable.
    maxNonOrtho 65;

    //- Max skewness allowed. Set to <0 to disable.
    maxBoundarySkewness 20;
    maxInternalSkewness 4;

    //- Max concaveness allowed. Is angle (in degrees) below which
concavity
    //  is allowed. 0 is straight face, <0 would be convex face.
    //  Set to 180 to disable.
    maxConcave 80;

    //- Minimum pyramid volume. Is absolute volume of cell pyramid.
    //  Set to a sensible fraction of the smallest cell volume
expected.
    //  Set to very negative number (e.g. -1E30) to disable.
    minVol 1e-13;

    //- Minimum quality of the tet formed by the face-centre
    //  and variable base point minimum decomposition triangles and
    //  the cell centre.  Set to very negative number (e.g. -1E30) to
    //  disable.
    //      <0 = inside out tet,
    //       0 = flat tet
    //       1 = regular tet
    minTetQuality -1;

    //- Minimum face area. Set to <0 to disable.
    minArea -1;

    //- Minimum face twist. Set to <-1 to disable. dot product of face
normal
    //- and face centre triangles normal
    minTwist 0.01;

    //- minimum normalised cell determinant
```

```
    //- 1 = hex, <= 0 = folded or flattened illegal cell
    minDeterminant 0.001;

    //- minFaceWeight (0 -> 0.5)
    minFaceWeight 0.05;

    //- minVolRatio (0 -> 1)
    minVolRatio 0.01;

    //must be >0 for Fluent compatibility
    minTriangleTwist -1;


    // Advanced

    //- Number of error distribution iterations
    nSmoothScale 4;
    //- amount to scale back displacement at error points
    errorReduction 0.75;
    relaxed
    {
        maxNonOrtho 75;
    }
}


// Advanced

// Flags for optional output
// 0 : only write final meshes
// 1 : write intermediate meshes
// 2 : write volScalarField with cellLevel for postprocessing
// 4 : write current intersections as .obj files
debug 0;


// Merge tolerance. Is fraction of overall bounding box of initial
mesh.
// Note: the write tolerance needs to be higher than this.
mergeTolerance 1e-6;
// *********************************************************************
*** //
```

Appendix D → System files

- *fvScheme*

```
/*--------------------------------*- C++ -*----------------------------------*\
| =========                 |
| \\      /  F ield         | OpenFOAM: The Open Source CFD Toolbox
| \\    /   O peration      | Version:  1.5
|  \\  /    A nd            | Web:      http://www.OpenFOAM.org
|   \\/     M anipulation   |
\*---------------------------------------------------------------------------*/
FoamFile
{
    version     2.0;
    format      ascii;
    class       dictionary;
    object      fvSchemes;
}
// * * * * * * * * * * * * * * * * * * * * * * * * * * * * * * * * * * * * * //

ddtSchemes
{
    default Euler;
}

gradSchemes
{
    default         Gauss linear;
    grad(U)         Gauss linear;
    grad(alpha1)     Gauss linear;
}

divSchemes
{
    div(rhoPhi,U)  Gauss limitedLinearV 1;
    div(((rho*nuEff)*dev2(T(grad(U))))) Gauss linear;
    div(phi,alpha)  Gauss MUSCL;
    div(phirb,alpha) Gauss interfaceCompression;

    div(phi,thermo:rho.water) Gauss upwind;
    div(phi,thermo:rho.air) Gauss upwind;
    div(rhoPhi,K)  Gauss upwind;
    div(phi,p)      Gauss upwind;
    div(rhoPhi,T)  Gauss upwind;

    div(phid1,p_rgh)  Gauss upwind; //added
    div(phid2,p_rgh)  Gauss upwind; //added
}

laplacianSchemes
{
```

```
    default         Gauss linear corrected;
}

interpolationSchemes
{
    default         linear;
}

snGradSchemes
{
    default         corrected;
}

fluxRequired
{
    default         no;
    p_rgh;
    pcorr;
    alpha.water;
}

//
*************************************************************
*** //
```

- *fvSolution*

```
/*--------------------------------*- C++ -*----------------------------
-------*\
| =========                 |
|
| \\      /  F ield         | OpenFOAM: The Open Source CFD Toolbox
|
|  \\    /   O peration     | Version:  1.5
|
|   \\  /    A nd           | Web:      http://www.OpenFOAM.org
|
|    \\/     M anipulation  |
|
\*---------------------------------------------------------------------
-------*/
FoamFile
{
    version     2.0;
    format      ascii;
    class       dictionary;
    object      fvSolution;
}
// * * * * * * * * * * * * * * * * * * * * * * * * * * * * * * * * * * *
* * * //

solvers
{
    "alpha.water.*"
    {
        nAlphaCorr      1;
        nAlphaSubCycles 1;
        alphaOuterCorrectors yes;
        cAlpha          1;
```

155

```
    MULESCorr        yes;
    nLimiterIter     3;

    solver           smoothSolver;
    smoother         symGaussSeidel;
    tolerance        1e-8;
    relTol           0;
}

".*(rho|rhoFinal)"
{
    solver           diagonal;
}

pcorr PBiCG //changed wrt GAMG
{
    preconditioner   DILU;//added
    tolerance        1e-7;
    relTol           0.0;

    smoother         DIC;//GaussSeidel;
    nPreSweeps       0;
    nPostSweeps      2;
    nFinestSweeps    2;

    cacheAgglomeration true;
    nCellsInCoarsestLevel 10;
    agglomerator     faceAreaPair;
    mergeLevels      1;
};

p_rgh PBiCG //changed wrt GAMG
{
    preconditioner   DILU;//added
    tolerance        1e-7;
    relTol           0.0;

    smoother         GaussSeidel;//GaussSeidel;
    nPreSweeps       0;
    nPostSweeps      2;
    nFinestSweeps    2;

    cacheAgglomeration true;
    nCellsInCoarsestLevel 10;
    agglomerator     faceAreaPair;
    mergeLevels      1;
};

p_rghFinal PBiCG //changed wrt GAMG
{
    preconditioner   DILU;//added
    tolerance        1e-8;
    relTol           0.0;

    smoother         GaussSeidel;//GaussSeidel;
    nPreSweeps       0;
    nPostSweeps      2;
    nFinestSweeps    2;

    cacheAgglomeration true;
```

```
        nCellsInCoarsestLevel 10;
        agglomerator     faceAreaPair;
        mergeLevels      1;
    };

    U PBiCG//changed wrt GAMG
    {
        preconditioner  DILU;//added
        tolerance        1e-09;
        relTol           0;
        smoother         DILU;//GaussSeidel;
    };

    UFinal PBiCG //changed wrt GAMG
    {
        preconditioner  DILU;//added
        tolerance        1e-09;
        relTol           0;
        smoother         DILU;//GaussSeidel;
    };

  "(T|k|B|nuTilda).*"
    {
        solver           smoothSolver;
        smoother         symGaussSeidel;
        tolerance        1e-08;
        relTol           0;
    }

    gamma PBiCG
    {
        preconditioner  DILU;
        tolerance        1e-07;
        relTol           0;
    };
}


PIMPLE
{
    momentumPredictor no;
    nCorrectors      3;
    nNonOrthogonalCorrectors 0;
    transonic yes;
}

relaxationFactors
{
    fields
    {
    }
    equations
    {
        ".*" 1;
    }
}


//
****************************************************************
*** //
```

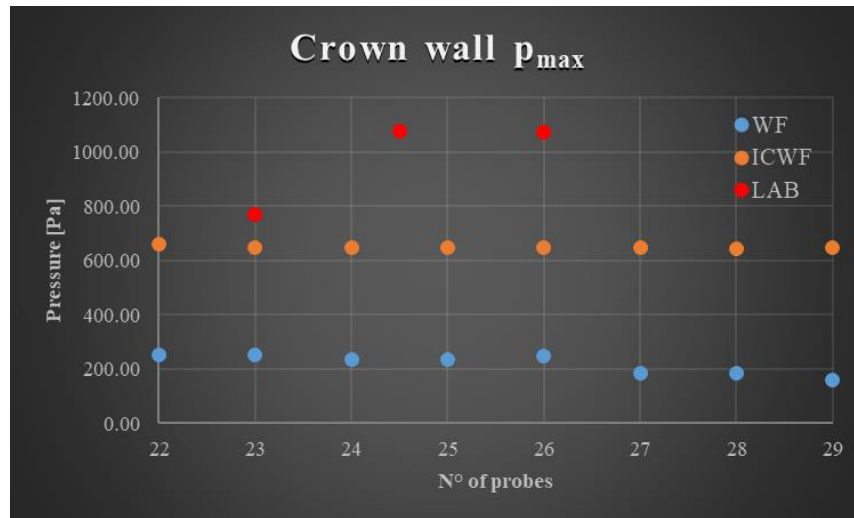# Appendix E → *Results related to ICWF*

Figure 89. Comparison between the values of p_{max}, acting against the crown wall, in case of *waveFoam* and *IsoCompressibleWaveFoam* for the test case 2 in Table 25, i.e. R00H05s4G30c4W4.
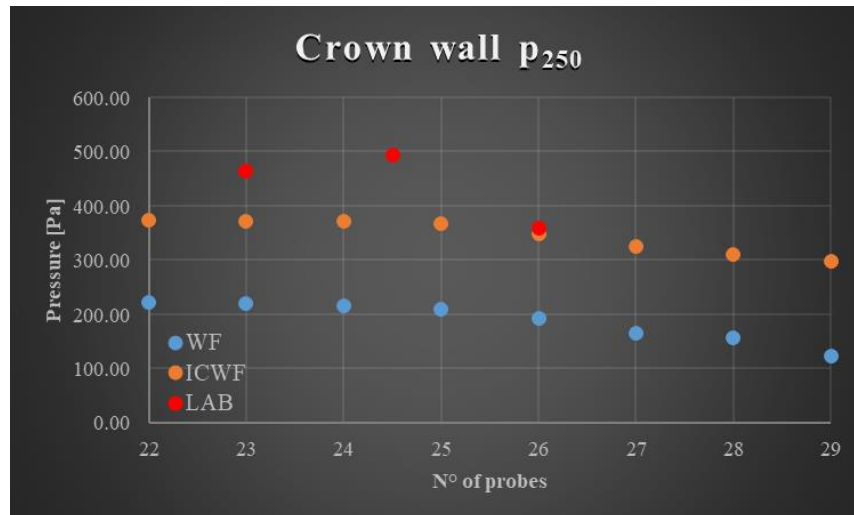

Figure 90. Comparison between the values of p_{100}, acting against the crown wall, in case of *waveFoam* and *IsoCompressibleWaveFoam* for the test case 2 in Table 25, i.e. R00H05s4G30c4W4.

Figure 91. Comparison between the values of p_{100}, acting against the crown wall, in case of *waveFoam* and *IsoCompressibleWaveFoam* for the test case 2 in Table 25, i.e. R00H05s4G30c4W4.
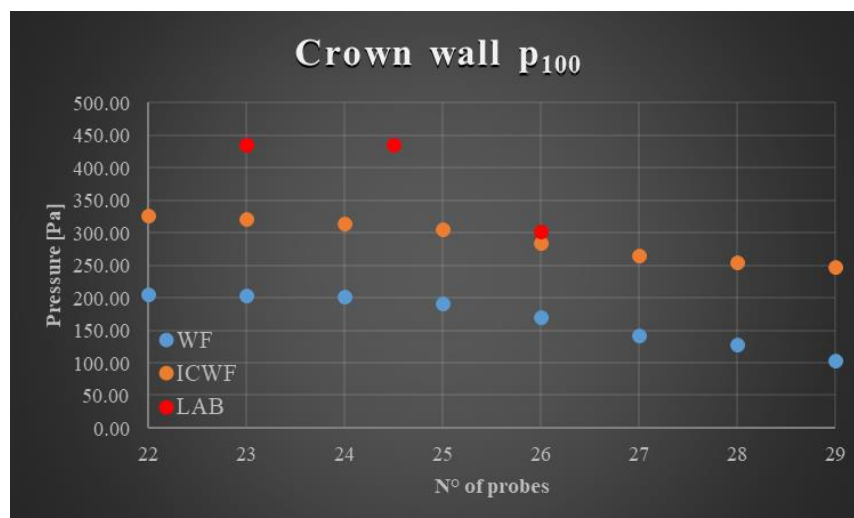
Figure 92. Comparison between the values of p_{max}, acting against the crown wall, in case of *waveFoam* and *IsoCompressibleWaveFoam* for the test case 2 in Table 25, i.e. R00H05s4G30c4W4.

Figure 93. Comparison between the values of p_{250}, acting against the crown wall, in case of *waveFoam* and *IsoCompressibleWaveFoam* for the test case 2 in Table 25, i.e. R00H05s4G30c4W4.
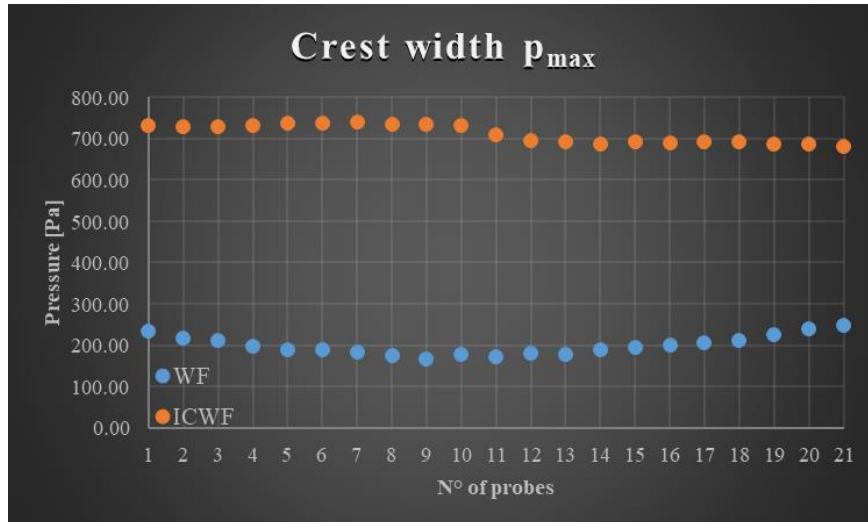

Figure 94. Comparison between the values of p_{100}, acting against the crown wall, in case of *waveFoam* and *IsoCompressibleWaveFoam* for the test case 2 in Table 25, i.e. R00H05s4G30c4W4.

Figure 95. Comparison between the values of p_{max}, acting against the crown wall, in case of *waveFoam* and *IsoCompressibleWaveFoam* for the test case 3 in Table 25, i.e. R00H06s3G30c4W4.
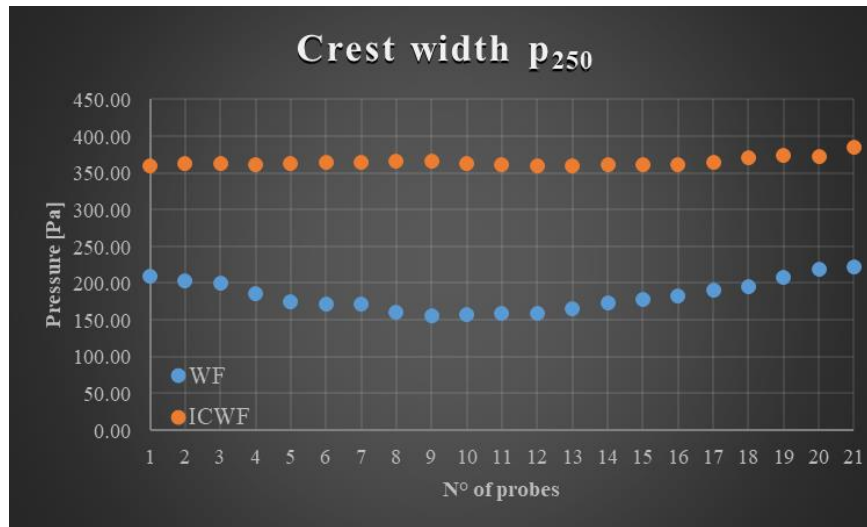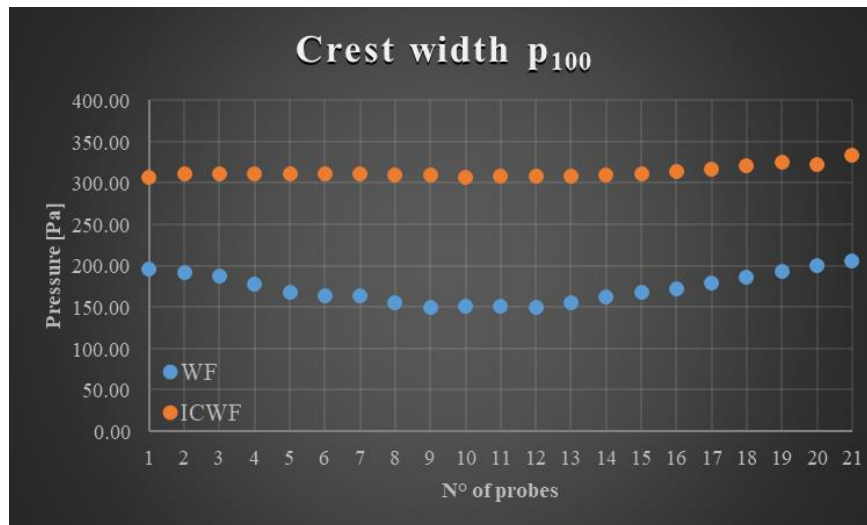

Figure 96. Comparison between the values of p_{250}, acting along the crest width, in case of *waveFoam* and *IsoCompressibleWaveFoam* for the test case 3 in Table 25, i.e. R00H06s3G30c4W4.

Figure 97. Comparison between the values of p_{100}, acting along the crest width, in case of *waveFoam* and *IsoCompressibleWaveFoam* for the test case 3 in Table 25, i.e. R00H06s3G30c4W4.
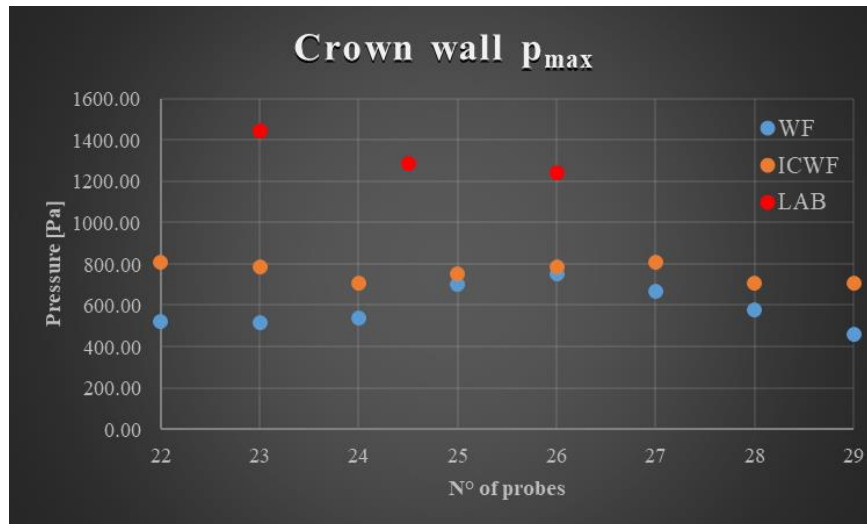
Figure 98. Comparison between the values of p_{max}, acting along the crest width, in case of *waveFoam* and *IsoCompressibleWaveFoam* for the test case 3 in Table 25, i.e. R00H06s3G30c4W4.

Figure 99. Comparison between the values of p_{250}, acting along the crest width, in case of *waveFoam* and *IsoCompressibleWaveFoam* for the test case 3 in Table 25, i.e. R00H06s3G30c4W4.
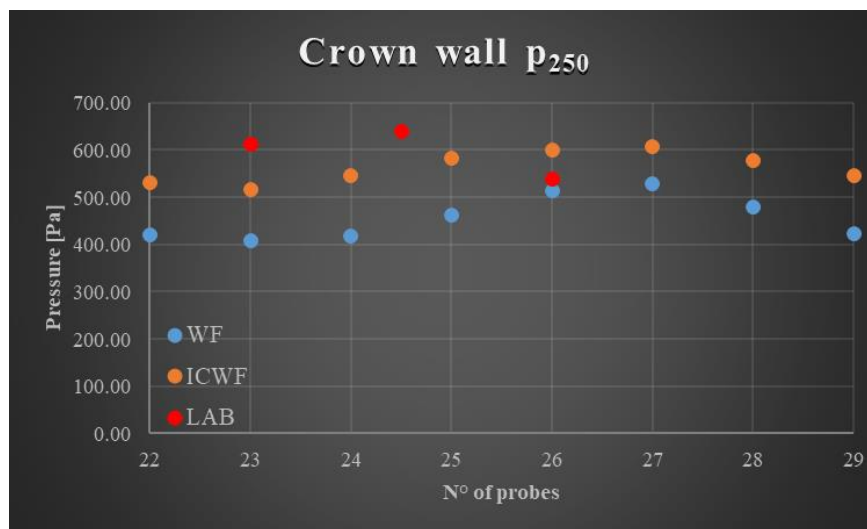

Figure 100. Comparison between the values of p_{100}, acting along the crest width, in case of *waveFoam* and *IsoCompressibleWaveFoam* for the test case 3 in Table 25, i.e. R00H06s3G30c4W4.
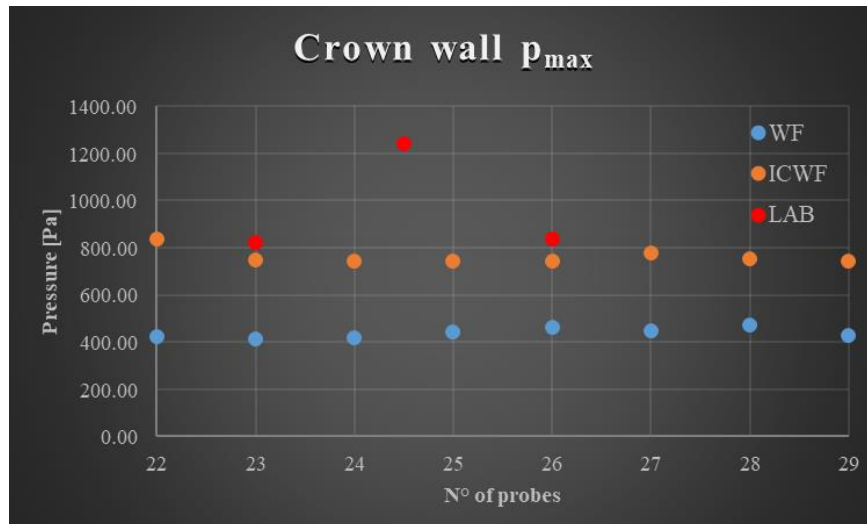
Figure 101. Comparison between the values of p_{max}, acting along the crest width, in case of *waveFoam* and *IsoCompressibleWaveFoam* for the test case 4 in Table 25, i.e. R05H05s3G30c4W4.
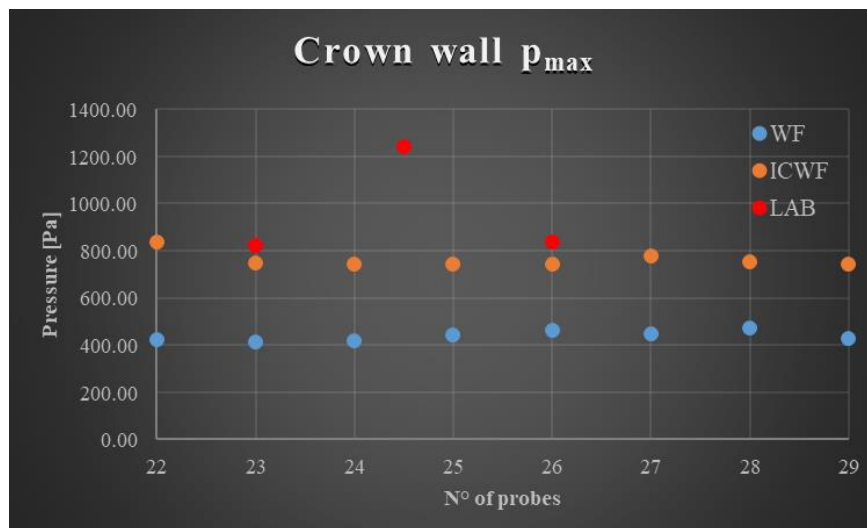
Figure 102. Comparison between the values of p_{250} acting along the crest width, in case of *waveFoam* and *IsoCompressibleWaveFoam* for the test case 4 in Table 25, i.e. R05H05s3G30c4W4.
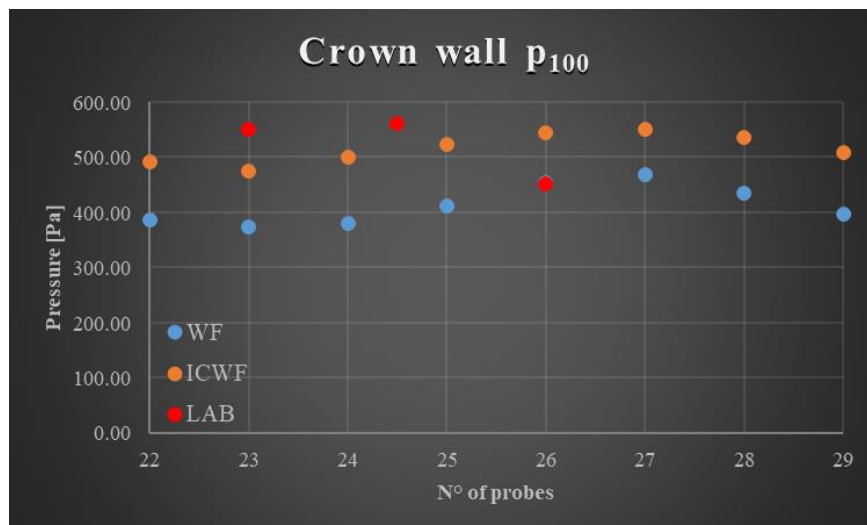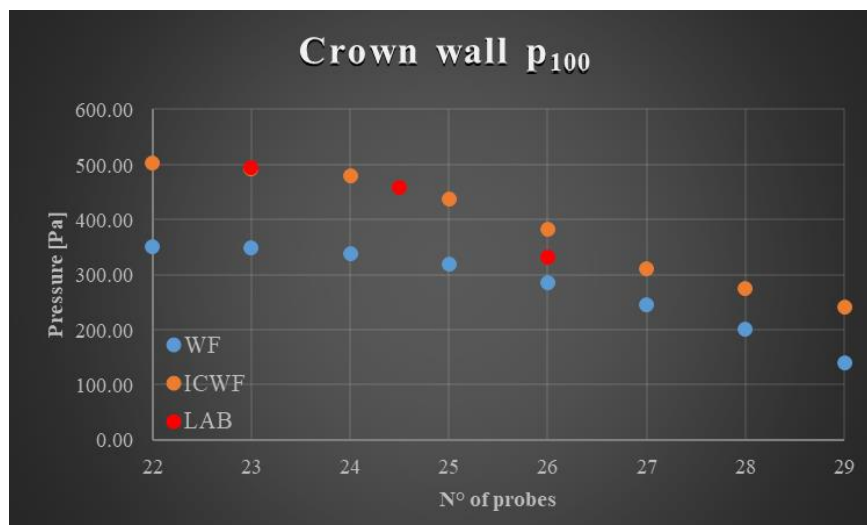

Figure 103. Comparison between the values of p_{100}, acting along the crest width, in case of *waveFoam* and *IsoCompressibleWaveFoam* for the test case 4 in Table 25, i.e. R05H05s3G30c4W4.
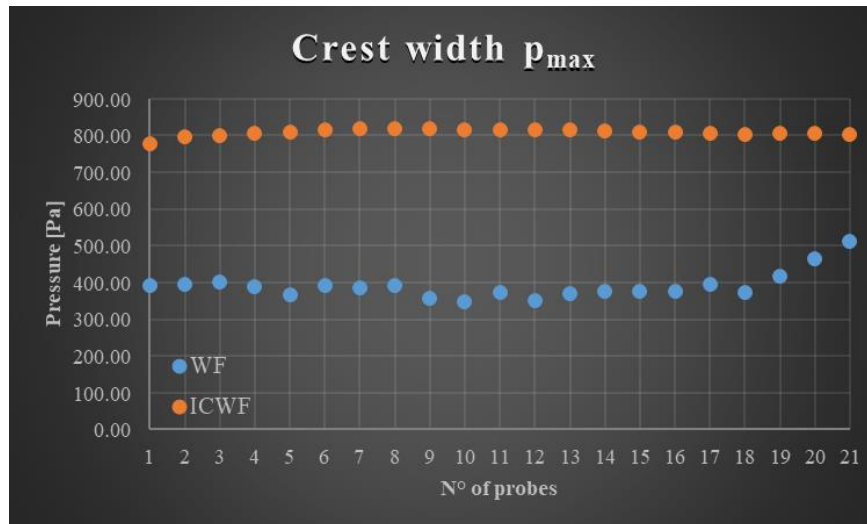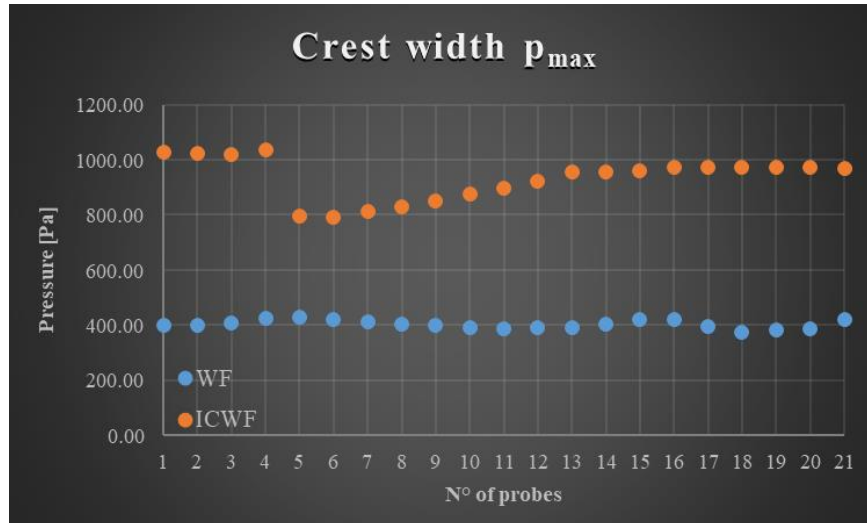
Figure 104. Comparison between the values of p_{max}, acting along the crest width, in case of *waveFoam* and *IsoCompressibleWaveFoam* for the test case 4 in Table 25, i.e. R05H05s3G30c4W4.
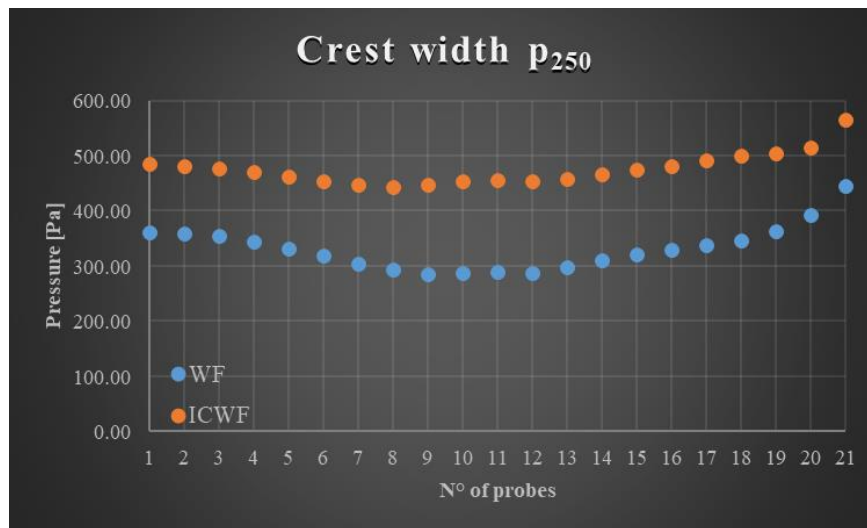

Figure 105. Comparison between the values of p_{250}, acting along the crest width, in case of *waveFoam* and *IsoCompressibleWaveFoam* for the test case 4 in Table 25, i.e. R05H05s3G30c4W4.
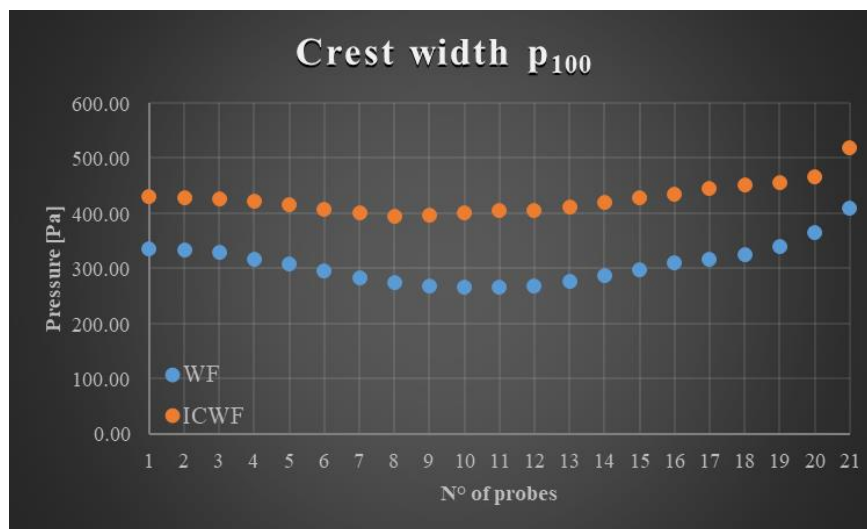

Figure 106. Comparison between the values of p_{100}, acting along the crest width, in case of *waveFoam* and *IsoCompressibleWaveFoam* for the test case 4 in Table 25, i.e. R05H05s3G30c4W4.
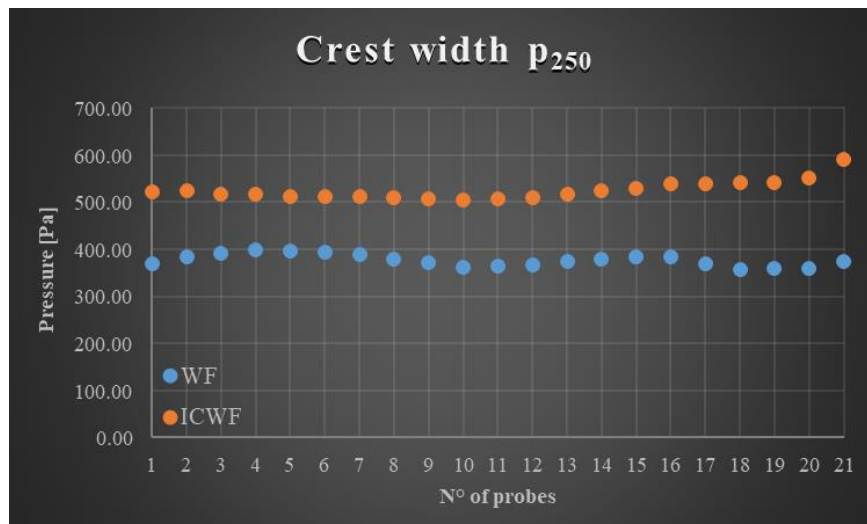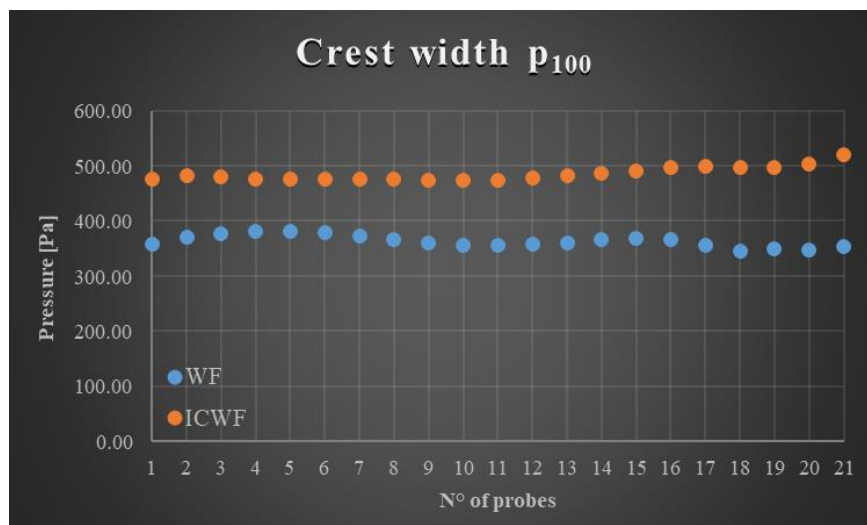
References

[1] Ahrens, J.P., & Heimbaugh, M.S. (1986). Irregular wave overtopping of seawalls. *In Proceedings of the OCEANS'86, Washington, DC, USA, 23–25; pp. 96–103.*

[2] Allsop, N. W. H. (1991). Reflection performance of rock armoured slopes in random waves. *In Coastal Engineering (pp. 1460-1472).*

[3] Allsop, N.W.H., McKenna, J.E., Vicinanza, D., & Whittaker, T.J.T. (1996). New design formulae for wave loadings on vertical breakwaters and seawalls. *Proc 25th Int. Conf. Coastal Engineering, pp 2508−2521, ASCE, New York.*

[4] Allsop, N.W.H. & Vicinanza, D. (1996). Wave impact loadings on vertical breakwaters: development of new prediction formulae. *Proc. 11th Int. Harbour Congress, Antewerp, Belgium.*

[5] Bagnold, R.A. (1938-39). Interim report on wave – pressure research. *Jour. Institution of Civil Engineers, vol. 12, pp. 202-226.*

[6] Balk, D., Montgomery M. R., McGranahan, G., Kim, D., Mara, V., Todd, M., et al. (2009). Mapping urban settlements and the risks of climate change in Africa, Asia and South America. *In: Guzmán J. M., Martine McGranahan G., G., Schensul D. and Tacoli C., editors. Population Dynamics and Climate Change. NewYork, London: United Nations Population Fund (UNFPA), International Institute for Environment and Development (IIED). pp. 80–103. 2.*

[7] Blackmore, P.A. & Hewson, P.J. (1984). Experiments on full – scale wave impact pressures. *Coastal Engineering 8, 331−346.*

[8] Boake, C.B., Whittaker, T.J., Folley, M. & Ellen, H. (2002). Overview and initial operational experience of the LIMPET wave energy plant. *In Proceedings of the 12th International Offshore and Polar Engineering Conference, Kitakyushu, Japan, 26–31.*

[9] Boccotti, P. (2007). Caisson breakwaters embodying an OWC with a small opening–Part I: Theory. *Ocean Eng., 34, 806–819.*

[10] Brown S., Nicholls R., Woodroffe C., Hanson S., Hinkel J., Kebede A.S., et al. (2013). Sea – Level Rise Impacts and Responses: A Global Perspective. *In: FinklCW, editor. Coastal Hazards. Netherlands: Springer; pp.117–149. 9.*

[11] Buccino, M., Dentale, F., Salerno, D., Contestabile, P. & Calabrese, M. (2016). The use of CFD in the analysis of wave loadings acting on seawave slot – cone generators. *Sustainability, 8, 1255.*

[12] Bullock, G. N., Obhrai, C., Peregrine, D. H. & Bredmose, H. (2007). Violent breaking wave impacts. Part 1: Results from large – scale regular wave tests on vertical and sloping walls. *Coastal Engineering*, *54*(8*), 602-617.*

[13] Burger, W., Oumeraci, H. & Partenscky, H. W. (1988). Ceohydraulic investigations of rubble mound breakwaters. *Coastal Engineering Proceedings, 1(21).*

[14] Castellino M., Sammarco P., Romano A., Martinelli L., Ruol P., Franco L., & De Girolamo, P. (2018). Large impulsive forces on recurved parapets under non – breaking waves. A numerical study. *Coastal Engineering 136, 1-15.*

[15] Centurioni L., Braasch L., Di Lauro E., Contestabile P., De Leo F., Casotti R., & Vicinanza D. (2017). A new strategic wave measurement station off Naples port main breakwater. *Coastal Engineering Proceedings, 1(35), 36.*

[16] Christensen, E. D., & Deigaard, R. (2001). Large eddy simulation of breaking waves. *Coastal engineering, 42(1), 53-86.*

[17] Clarke, D. K., Hassan, H. A., & Salas, M. D. (1986). Euler calculations for multielement airfoils using Cartesian grids. *AIAA journal, 24(3), 353-358.*

[18] Contestabile, C., Crispino, G., Di Lauro, E., Ferrante, V., Gisonni, C., Vicinanza, D. (2020). Overtopping breakwater for wave energy conversion: Review of state of art, recent advancements and what lies ahead. *Renew. Energy*.

[19] Contestabile P., Di Lauro E., Buccino M., & Vicinanza D. (2016). Economic assessment of Overtopping BReakwater for Energy Conversion (OBREC): a case study in Western Australia. *Sustainability, 9 (1) pp. 51.*

[20] Contestabile, P., Iuppa, C., Di Lauro, E., Cavallaro, L., Andersen, T. L., & Vicinanza, D. (2017). Wave loadings acting on innovative rubble mound breakwater for overtopping wave energy conversion. *Coastal Engineering, 122, 60-74.*

[21] Contestabile, P., Ferrante, V., Di Lauro, E., & Vicinanza, D. (2017). Full – scale prototype of an overtopping breakwater for wave energy conversion. *Coast. Eng. Proc., 1, 12.*

[22] Contestabile, P., Ferrante, V., Di Lauro, E., & Vicinanza, D. (2016). Prototype Overtopping Breakwater for Wave Energy Conversion at Port of Naples. *In Proceedings of the 26th International Conference ISOPE, Rhodes, Greece, 26 June–1 July; pp. 616–621.*

[23] Contestabile, P., Vicinanza, D. (2018). Coastal Defence Integrating Wave-Energy-Based Desalination: A Case Study in Madagascar. *Journal of Marine Science and Engineering, 6(2), 64.*

[24] Crossland C., Baird D., Ducrotoy J-P, Lindeboom H, Buddemeier R, Dennison W et al. (2005). The Coastal Zone – a Domain of Global Interactions. *In: Crossland C, Kremer H, Lindeboom H, Marshall Crossland J , Tissier M A, editors. Coastal Fluxes in the Anthropocene. Berlin, Heidelberg: Springer; pp. 1– 37.*

[25] Cuomo, G. (2005). Dynamics of wave – induced loads and their effects on coastal structures. *PhD thesis, Science of Civil Engineering, University of Roma Tre, Italy.*

[26] Cuomo G., Allsop W., Bruce T., & Pearson, J. (2010a). Breaking wave loads at vertical seawalls and breakwaters. *Coastal Engineering 57, 424-439.*

[27] Cuomo G., Allsop W, & Takahashi, S. (2010b). Scaling wave impact pressure on vertical walls. *Coastal Engineering 57, 604-609.*

[28] d'Angremond, K., Van Der Meer, J. W., & De Jong, R. J. (1997). Wave transmission at low – crested structures. *In Coastal Engineering (pp. 2418-2427).*

[29] Di Lauro, E., Lara, J. L., Maza, M., Losada, I. J., Contestabile, P., & Vicinanza, D. (2019). Stability analysis of a non-conventional breakwater for wave energy conversion. *Coastal Engineering, 145, 36-52.*

[30] Engelund, F. (1953). On the laminar and turbulent flow of ground water through homogeneous sand. *Trans. Danish academy of Technical sciences, 3.*

[31] Ergun, S. (1952).Fluid flow through packed columns. *Chemical Engineering Progress 48(2): 89-94.*

[32] EurOtop. (2018). Manual on wave overtopping of sea defences and related Structures. An overtopping manual largely based on European research, but for worldwide application. *Second Edition. N.W.H. Allsop, T. Bruce, J. DeRouck, A. Kortenhaus, T. Pullen, H. Schüttrumpf, P. Troch, J.W. van der Meer and B. Zanuttigh. www.overtopping-manual.com.*

[33] Falcao, A. (2010). Wave energy utilization: A review of the technologies. *Renewable and sustainable energy reviews, 14(3), 899-918.*

[34] Forchheimer. P. (1901). Wasserbewegung durch Boden. Zeitschrift des Vereines DeutscherIngenieuer, *45 edition.*

[35] Formentin, S.M., Palma, G., Contestabile, P., Vicinanza, D., & Zanuttigh, B. (2017). 2DV RANS – VOF numerical modeling of a multi – functional harbor structure. *Coast. Eng. Proc., 1, 3.*

[36] Franco, L. (1994). Vertical breakwaters: the Italian experience. *Coastal Engineering, 22(1-2), 31-55.*

[37] García, N., Lara J. L., & Losada I. J. (2004). 2-D numerical analysis of near-field flow at lowcrested permeable breakwaters. *Coastal Engineering 51(10): 991-1020.*

[38] Geuzaine, C., & Remacle, J.-F. (2009). Gmsh: A 3 – D finite element mesh generator with built-in pre- and post-processing facilities. *Int. J. Numer. Meth. Engng. 79: 1309–1331.*

[39] Goda, Y. (1973) A new method of wave pressure calculation for the design of composite breakwater. *Rep. Port Harb. Res. Inst., 12, 31–70. (In Japanese).*

[40] Greenshields, C. J. (2015). Openfoam user guide. *OpenFOAM Foundation Ltd, version, 3(1), e2888.*

[41] Higuera, P., Lara, J. L., & Losada, I. J. (2014). Three-dimensional interaction of waves and porous coastal structures using OpenFOAM®. Part I: formulation and validation. Coastal Engineering, 83, 243-258.

[42] Higuera, P., Lara, J. L., & Losada, I. J. (2014). Three-dimensional interaction of waves and porous coastal structures using OpenFOAM®. Part II: Application. Coastal Engineering, 83, 259-270.

[43] Higuera, P., Lara, J. L., & Losada, I. J. (2013). Simulating coastal engineering processes with OpenFOAM®. Coastal Engineering, 71, 119-134.

[44] Hiroi, I. (1920). The force and power of waves. *The Engineer, August, pp184.*

[45] Hirsch, C. (2007). Numerical computation of internal and external flows. *The fundamentals of computational fluid dynamics. Elsevier.*

[46] Hsu, T. J., Sakakiyama, T., & Liu, P. L. F. (2002). A numerical model for wave motions and turbulence flows in front of a composite breakwater. *Coastal Engineering, 46(1), 25-50.*

[47] Huerta, J. C. A., & Oumeraci, H. (2014). CFD – CSD numerical modelling of wave – induced pressures in open – pored PBA – revetments. *Coastal Engineering Proceedings, 1(34), 18.*

[48] Iuppa, C., Contestabile, P., Cavallaro, L., Foti, E., & Vicinanza, D. (2016). Hydraulic performance of an innovative breakwater for overtopping wave energy conversion. *Sustainability, 8(12), 1226.*

[49] Jasak, H., Jemcov, A., & Tukovic, Z. (2007). OpenFOAM: A C++ library for complex physics simulations. *In International workshop on coupled methods in numerical dynamics (Vol. 1000, pp. 1-20). IUC Dubrovnik Croatia.*

[50] Jacobsen, N.G., Fuhrman, D.R., & Fredsoe, J. (2012). A wave generation toolbox for the open – source CFD library: OpenFoam. *Int. J. Numer. Methods Fluids, 70. pp. 1073-1088.*

[51] Jensen B., Jacobsen N. G., Damgaard E., & Christensen. (2014). Investigations on the porous media equations and resistance coefficients for coastal structures. *Coastal Engineering, Volume 84, Pages 56-72.*

[52] Kirkgoz M.S. (1995) Breaking wave impact on vertical and sloping coastal structures. *Ocean Engineering, Vol 22, No1, pp. 35 - 48, Elsevier Science, Oxfor.*

[53] Klopman, G., & van der Meer, J.W. (1999). Random wave measurements in front of reflective structures. *Journal Waterw. Port Coastal Ocean Engineering, 125 (1), 39–45.*

[54] Kofoed J. P. (2002). Wave Overtopping of Marine Structures – Utilization of Wave Energy. *Ph. D. Thesis, Hydraulics & Coastal Engineering Laboratory, Department of Civil Engineering, Aalborg University, December.*

[55] Kofoed, J.P., Frigaard, P., Friis-Madsen, E., & H.C. Sørensen. (2006). Prototype testing of the wave energy converter Wave Dragon. *Renewable Energy, 31, 181–189.*

[56] Kortenhaus, A., & Oumeraci, H. (1999). Classification of wave loading on monolithic coastal structures. *In Coastal Engineering, pp. 867-880.*

[57] Kortenhaus, A., Pearson, J., Bruce, T., Allsop, N., & Van der Meer, J. (2003). Influence of parapets and recurves on wave overtopping and wave loading of complex vertical walls. *Proc. Coast. Struct. 2003, 369–381.*

[58] Kothe, D. B., Mjolsness, R. C., & Torrey, M. D. (1991). RIPPLE: a computer program for incompressible flows with free surfaces, *Los Alamos National Lab. LA-10612-MS, Los Alamos, NM.*

[59] Lara J.L., Ruju A., & Losada I.J.. (2010). Reynolds averaged navier–stokes modelling of long waves induced by a transient wave group on a beach. *Proceedings of the Royal Society A, 467:1215– 1242, 2011*

[60] Lara, J., Losada, I. J., del Jesus, M., Barajas, G., & Guanche, R. (2011). IH – 3VOF: a three – dimensional Navier – Stokes model for wave and structure interaction. *Coastal Engineering Proceedings, 1(32), 55.*

[61] Liu, P. L. F., Lin, P., Chang, K. A., & Sakakiyama, T. (1999). Numerical modeling of wave interaction with porous structures. *Journal of waterway, port, coastal, and ocean engineering, 125(6), 322-330.*

[62] Liu, P. L. F., & Losada I. J. (2002). Wave propagation modelling in coastal engineering. *Journal of Hydraulic Research 40(3).*

[63] Losada, I. J., Lara, J. L., Guanche, R., & Gonzalez-Ondina, J. M. (2008). Numerical analysis of wave overtopping of rubble mound breakwaters. *Coastal engineering, 55(1), 47-62.*

[64] Lynett, P. J., Liu, P. L.-F., Losada, I. J. & Vidal, C. (2000). Solitary Wave Interaction with Porous Breakwater, *Waterway, Port, Coastal and Ocean Engineering, 314-322.*

[65] Mansard, E.P., & Funke, E.R. (1980).The measurement of incident and reflected spectra using a least squares method. *In Coastal Engineering; American Society of Civil Engineers: Reston, VA, USA, 1980; pp. 154–172.*

[66] Margheritini, L., Vicinanza, D., & Frigaard, P. (2009). SSG wave energy converter: Design, reliability and hydraulic performance of an innovative overtopping device, *Journal of Renewable Energy, 34, 1371–1380.*

[67] Marqués, J., López de Aguileta, L.I., & Torre-Enciso, Y. (2010). Mutriku. Lessons learnt. *In Proceedings of the 3rd International Conference on Ocean Energy, Bilbao, Spain, 6–8 October.*

[68] Martin F. L. (1999). Experimental study of wave forces on rubble mound breakwater crown walls. *PIANC Bulletin, vol. 102, pp. 5-17.*

[69] McKenna, J., & Allsop, W. (1999). Statistical distribution of horizontal wave forces on vertical breakwaters. *In Coastal Engineering 1998 (pp. 2082-2095).*

[70] Nam, B. W., Shin, S. H., Hong, K. Y., & Hong, S. W. (2008). Numerical simulation of wave flow over the spiral – reef overtopping device. *In The Eighth ISOPE Pacific/Asia Offshore Mechanics Symposium. International Society of Offshore and Polar Engineers.*

[71] NAUE (2012). Geotextile Filter und Kolkschutzmatten-Terrafix. Producktbeschreibung. *NAUE.*

[72] Neumann, B., Vafeidis, A. T., Zimmermann, J., & Nicholls, R. J. (2015). Future coastal population growth and exposure to sea – level rise and coastal flooding – a global assessment. *PloS one*, *10*(3), e0118571.

[73] Nørgaard, J.Q.H., Andersen T.L., & Burcharth, H.F. (2013) .Wave loads on rubble mound breakwater crown walls in deep and shallow water wave conditions. *Coastal Engineering, vol. 80, pp. 137-147,.*

[74] Oumeraci, H., Allsop N. W. H., M. B. de Groot, C. R.S., & JVrijling,. K. (1999). MAST III/PROVERBS Probabilistic design tools for vertical breakwaters. *European Union.*

[75] Oumeraci, H., Klammer, P., & Partenscky, H.W. (1993). Classification of breaking wave loads on vertical structures' *Journal of Waterway, Port, Coastal and Ocean Eng. v 119, n 4, 381-397.*

[76] Oumeraci, H., Staal, T., Pfoertner, S., Ludwigs, G., & Kudella, M. (2010). Hydraulic performance, wave loading and response of Elastocoast revetments and their foundation-A large scale model study.

[77] Palma, G., Contestabile, P., Mizar Formentin, S., Vicinanza, D., & Zanuttigh, B. (2016*). Design optimization of a multifunctional wave energy device. In Progress in Renewable Energies Offshore, *Proceedings of the 2nd International Conference on Renewable Energies Offshore (RENEW2016), Lisbon, Portugal, 24–26 October; CRC Press: Boca Raton, FL, USA, 2016; p. 235.*

[78] Patterson, M., & Hardy, D. (2008). Economic Drivers of Change and their Oceanic-Coastal Ecological Impacts. In: Patterson M., Glavovic B.C., editors. *Ecological economics of the oceans and coasts. Edward Elgar Publishing; pp. 187–209. 15.*

[79] Pecher, A., & Kofoed, J. P. (Eds.). (2017). Handbook of ocean wave energy. *London: Springer.*

[80] Pecher, A., Kofoed, J.P., Le Crom, I., Neumann, F., & Azevedo, E.D.B. (2011). Performance assessment of the Pico OWC power plant following the EquiMar Methodology. *In Proceedings of the Twenty-First International Offshore and Polar Engineering Conference, Maui, HI, USA, 19–24 June.*

[81] Pedersen, J., & Burcharth, H. F. (1993). Wave forces on crown walls. *In Coastal Engineering 1992, pages 1489–1502.*

[82] Peregrine, D. H., Bredmose, H., Bullock, G., Obrhai, C., Müller, G., & Wolters, G. (2005). Water wave impact on walls and the role of air. *In Coastal Engineering 2004: (In 4 Volumes) (pp. 4005-4017).*

[83] Plumerault, L. R., Astruc, D., & Maron, P. (2012). The influence of air on the impact of a plunging breaking wave on a vertical wall using a multifluid model. *Coastal Engineering, 62, 62-74.*

[84] Postma, G. M. (1989). Wave reflection from rock slopes under random wave attack. *MS thesis, Delft University of Technology, Department of Civil Engingineering.*

[85] Romano, A., Bellotti, G., Briganti, R., & Franco, L. (2014). Uncertainties in the physical modelling of the wave overtopping over a rubble mound breakwater: The role of the seeding number and of the test duration. *Coast. Eng., 103, 15–21.*

[86] Sainflou, G. (1928). Essai sur les digues maritimes verticales. *Annales des Ponts et Chausse'es Paris 98, 11, pp: 5−48 (in French),*

[87] Seiffert, B. R. (2014). Tsunami and storm wave impacts on coastal bridges. *Doctoral dissertation, [Honolulu]: [University of Hawaii at Manoa][December 2014].*

[88] Seto K C. (2011). Exploring the dynamics of migration to mega-delta cities in Asia and Africa: Contemporary drivers and future scenarios. *Global Environmental Change; 21, Supplement1: S94–S107.*

[89] Simonetti, I. (2017). Optimization of Oscillating Water Column Wave Energy Converters: A Numerical Study. *Doctoral dissertation, Technische Universität Braunschweig.*

[90] Small C., & Nicholls R.J. (2003). A global analysis of human settlement in coastal zones. *Journal of Coastal Research; 19:584–599.*

[91] Tanimoto, K., & Kimura, K. (1985). A hydraulic experiment study on trapezoidal caisson breakwaters. *Technical Note, (528), 193-226.*

[92] Takahashi, S. & Hosoyamada, S. (1994). Hydrodynamic characteristics of sloping top caissons. *Proc. Int. Conf. on Hydro-Technical Eng. for Port and Harbour Construction. Port and Harbour Research Institute, Yokosuka, Japan, pp733−746.*

[93] Takahashi, S., Tanimoto, K. & Shimosako, K. (1993). Experimental study of impulsive pressures on composite breakwaters – Foundamental feature of impulsive pressure and the impulsive pressure coefficient. *Rept. of Port and Harbour Research institute 31,.5, pp33−72 (in Japanese).*

[94] Tanimoto, K., Moto, K., Ishizuka, S. & Goda, Y. (1976). An investigation on design wave force formulae of composite – type breakwaters. *Proc. 23rd Japanese Conf. on Coastal Eng. pp11−16 (in Japanese)*

[95] Têtu, A. (2017). Power take-off systems for WECs. *In Handbook of Ocean Wave Energy (pp. 203-220). Springer, Cham.*

[96] Torre-Enciso, Y., Ortubia, I., López de Aguileta, LI., & Marqués, J. (2009). Mutriku wave power plant: From the thinking out to the reality. *In Proceedings of the 8th European Wave Tidal Energy Conference, Uppsala, Sweden, 7–10 September; pp. 319–329. 28.*

[97] Van der Meer, J. W. (1995). Conceptual design of rubble mound breakwaters. In Advances *In Coastal And Ocean Engineering: (Volume 1), pages 221–315. World Scientific.*

[98] Van der Meer, J.M. (1998). Wave run – up and overtopping. *Chapter 8 in: Pilarczyk, K. W. Ed., Seawall, Dikes and Revetments. Balkema. Rotterdam.*

[99] Van der Meer, J. W., & Stam, C. J. M. (1992). Wave runup on smooth and rock slopes of coastal structures. *Journal of Waterway, Port, Coastal, and Ocean Engineering, 118(5), 534-550.*

[100] Van Doorslaer, K., De Rouck, J., & Audenaert SDuquet, V. (2015). Crest modifications to reduce wave overtopping of non – breaking waves over a smooth dike slope. *Coast. Eng., 101, 69–88.*

[101] Van Doorslaer, K., Romano, A., Bellotti, G., Altomare, C., Cáceres, I., De Rouck, J. & van der Meer, J. (2015). Force measurements on storm walls due to overtopping waves: a middle-scale model experiment. *In Coastal structures 2015 (pp. 1-12). ASCE.*

[102] Van Doorslaer, K., Romano, A., De Rouck, J., & Kortenhaus, A. (2017). Impacts on a storm wall caused by non – breaking waves overtopping a smooth dike slope. *Coastal Engineering, 120, 93-111.*

[103] Van Gent, M. R. (1993). Stationary and oscillatory flow through coarse porous media. *Ph.D., Delft University of Technology, Communications on Hydraulic and Geotechnical Engineering.*

[104] Van Gent, M.R.A. (1995). Porous flow though rubble mound material, *J. of Waterway, Port, Coastal and Ocean Engineering, 121 (3), 176-181, ASCE, New York.*

[105] Vicinanza, D., Cappietti, L., Ferrante, V., & Contestabile, P. (2011). Estimation of the wave energy in the Italian offshore. *Journal of Coastal Research, vol. 64(12), pp. 613-617.*

[106] Vicinanza D., Contestabile P., Harck Nørgaard J., & Lykke Andersen T. (2014). Innovative rubble mound breakwaters for overtopping wave energy conversion. *Coastal Eng., 88, 154–170.*

[107] Vicinanza, D., & Frigaard, P. (2008) Wave pressure acting on a seawave slot – cone generator. *Coast. Eng., 55, 553–568.*

[108] Victor, L., & Troch, P. (2012). Wave overtopping at smooth impermeable steep slopes with low crest freeboards. *Journal of Waterway, Port, Coastal, and Ocean Engineering, 138(5), 372-385.*

[109] VLH Turbine. (2018) *Available online: http://www.vlh-turbine.com/products/vlh-turbine/.*

[110] Weber, J. (2012). WEC Technology Readiness and Performance Matrix–finding the best research technology development trajectory. *In Int. Conf. Ocean Energy Dublin Irel.*

[111] Willmott, C.J. (1981). On the validation of models. *Phys. Geogr., 2, 184–194.*

[112] Witte, H. H. (1988). Wave – induced impact loading in deterministic and stochastic reflection. *Leichtweiss Institut für Wasserbau, Technische Universität Braunschweig: 1-227.*

[113] Wong, PP, Losada, I.J., Gattuso, J. – P., Hinkel, J. Khattabi, A., McInnes, K.L., Saito, Y., & Sallenger, A. (2014). Coastal systems and low – lying areas. *In: Field, C.B., Barros, V.R. Dokken, D.J., Mach, K.J., Mastrandrea, M.D. Bilir, T.E. et al. (Eds.), Climate change 2014: Impacts, Adaptation and Vulnerability. Part A: Global and Sectoral Aspects. Contributon of Working Group II to the Fifth Assessment Report of the Intergovernamental Panel on Climate Change. Cambridge University Press Cambridge, United Kingdom and New York, NY, USA, pp. 361-409.*

[114] Wood, D. J., Peregrine, D. H., & Bruce, T. (2000). Study of wave impact against a wall with pressure-impulse theory. Part 1: trapped air. *Journal of Waterway, Port, Coastal, and Ocean Engineering, 126(4), 182-190.*

[115] Zanuttigh B., & Formentin S.M. (2018). Reduction of the wave overtopping discharge at dikes in presence of crown walls with parapets. *In: Proceedings of the XXXVI ICCE, Baltimore (MD).*

[116] Zanuttigh, B., Nicholls, R. J., Vanderlinden, J. P., Thompson, R. C., & Burcharth, H. F. (Eds.). (2014). Coastal risk management in a changing climate. *Butterworth-Heinemann.*

[117] Zanuttigh, B., & Van der Meer, J. W. (2008). Wave reflection from coastal structures in design conditions. *Coastal engineering, 55(10), 771-779.*

[118] Zanuttigh, B., Van Der Meer, J.W., Andersen, T.L., Lara, J.L., & Losada, I.J. (2009). Analysis of wave reflection from structures with berms through an extensive database and 2DV numerical modelling. *In Proceedings of the Coastal Engineering, Hamburg, Germany, 31 August–5 September 2008; Volume 5, pp. 3285–3297.*

[119] Zelt, J.A., & Skjelbreia, J.E. (1992). Estimating incident and reflected wave field using an arbitrary number of wave gauges. *Proc. 23rd International Conference of Coastal Engineering, vol I, 777–789.*